

**Nanocomposites of Nickel Phthalocyanines  
as Electrocatalysts for the Oxidation of  
Chlorophenols: An Experimental and  
Theoretical Approach**

A thesis submitted in fulfillment of the requirement for the degree of

**DOCTOR OF PHILOSOPHY**

Of

**RHODES UNIVERSITY**

By

**MIELIE SAMSON KHENE**

**January 2012**

**DEDICATION**

**TO MY WIFE**

**CAROLINE KHENE**

**MOTHER**

**CONSTANCE KHENE**

**AND GRANDMOTHER**

**JULIA RADEBE**

# ACKNOWLEDGEMENTS

I would like to thank my supervisor, Prof Tebello Nyokong, all your patience, commitment, guidance and training have greatly contributed to every accomplishment presented in this thesis. Thank you for the opportunity to travel to the UK (Norwich) and Japan (Sendai). I have benefited immensely from these two visits. Thank you for the time and energy you have put in to reading my thesis. Thank you to my co-supervisor, Dr Kevin Lobb, thank you for all your help with DFT calculations and reading my thesis.

I would like to thank my darling wife, Caroline Khene, for all the support, sacrifices and understanding you have given me without any reservation throughout this PhD. I am the person I am today because you have been there to support my every step of the way.

I would also like to send my gratitude to the following:

- The Chemistry department (academic and technical staff) for every kind and encouraging words.
- S22 group “a family away from home”. I am grateful for all the friendship and encouragement you all have given me.
- My friends (no man is an island), Mosiuoa Tsietsi, Mamello Thinyane, Vongani Chauke, Nolwazi Nimbona, Wadzanai Chidawanyika and Olomola Temitope. Without you guys I would have gone insane.
- NRF, Atlantic Philanthropy and Rhodes University for financial support. Without your financial support life would have been very difficult indeed.

## Abstract

In this work the interaction between peripherally ( $\beta$ ) substituted nickel tetrahydroxyphthalocyanines ( $\beta$ -NiPc(OH)<sub>4</sub> and *poly*- $\beta$ -Ni(O)Pc(OH)<sub>4</sub>) with 4-chlorophenol is theoretically rationalized by performing calculations at the B3LYP/6-31G(d) level. Density functional theory (DFT) and molecular orbital theory are used to calculate the condensed Fukui function for phthalocyanine derivatives and 4-chlorophenol, in order to determine the reactive sites involved when 4-chlorophenol is oxidized, and to compare theoretically predicted reactivity to experimentally determined electrocatalytic activity. Electrocatalytic activities of adsorbed NiPc derivatives: OPGE- $\alpha$ -NiPc(OH)<sub>8</sub> (OPGE = ordinary pyrolytic graphite electrode,  $\alpha$  = nonperipheral substitution), OPGE- $\alpha$ -NiPc(OH)<sub>4</sub> and OPGE- $\beta$ -NiPc(OH)<sub>4</sub> are compared with those of the polymerized counterparts: OPGE-*poly*- $\alpha$ -Ni(O)Pc(OH)<sub>8</sub>, OPGE *poly*- $\alpha$ -NiPc(OH)<sub>4</sub> and OPGE-*poly*- $\beta$ -NiPc(OH)<sub>4</sub>, respectively.

$\beta$ -NiPc(NH<sub>2</sub>)<sub>4</sub>,  $\beta$ -NiPc(OH)<sub>4</sub>,  $\alpha$ -NiPc(OH)<sub>4</sub>,  $\alpha$ -NiPc(OH)<sub>8</sub>,  $\alpha$ -NiPc(C<sub>10</sub>H<sub>21</sub>)<sub>8</sub> are adsorbed on singled walled carbon nanotube (SWCNT) and  $\beta$ -NiPc(NH<sub>2</sub>)<sub>4</sub>-SWCNT (linked to SWCNT), are used to modify glassy carbon electrode (GCE) and employed for the electro oxidation of chlorophenols. The  $\beta$ -NiPc(NH<sub>2</sub>)<sub>4</sub>-SWCNT gave the best current response for the oxidation of 4-chlorophenol.  $\alpha$ -NiPc(OH)<sub>8</sub>-SWCNT and  $\alpha$ -NiPc(C<sub>10</sub>H<sub>21</sub>)<sub>8</sub> gave the best resistance to electrode fouling due to oxidation by product of 4-chlorophenol.

The synthesis of conjugates of cadmium telluride quantum dots (CdTe-QDs) capped with thioglycolic acid and peripherally substituted nickel tetraamino phthalocyanine ( $\beta$ -NiPc(NH<sub>2</sub>)<sub>4</sub>) complex were also employed for the oxidation of chlorophenols.

Separation of one of the diastereomers of 1, 2-subnaphthalocyanine (SubNPc) was achieved as well as separation of the enantiomers. The absorption and magnetic circular dichroism spectra, together with theoretical calculations, reveal rather small variations in the frontier molecular orbitals of the SubNPc compared to conventional subphthalocyanine (SubPc), except for the destabilization of the highest occupied molecular orbital (HOMO), which results in a characteristic absorption in the Soret band region. The chirality of SubNPc, including the cyclic dichroism (CD) signs and intensities, are discussed in detail.

**TABLE OF CONTENTS**

Title page.....	i
Dedication.....	ii
Acknowledgement.....	iii
Abstract.....	iv
Table of Contents.....	vi
List of Abbreviation.....	xi
List of Symbols.....	xiv
List of Figures.....	xvi
List of Schemes.....	xxi
List of Tables.....	xxii

**CHAPTER ONE: INTRODUCTION**

1. Introduction.....	2
1.1. Phthalocyanines and Subphthalocyanines .....	2
1.1.1. Phthalocyanine synthesis .....	4
1.1.1.1. Peripherally tetrasubstituted phthalocyanine.....	5
1.1.1.2. Non-Peripherally tetrasubstituted phthalocyanine.....	6
1.1.1.3. Peripherally octasubstituted phthalocyanine.....	7
1.1.1.4. Non-peripherally octasubstituted phthalocyanine.....	8
1.1.2. Syntheses of Subphthalocyanines (SubPcs) and Subnaphthalocyanines (SubNPcs) ....	13
1.1.3. Spectroscopic properties of phthalocyanines.....	18
1.1.3.1. UV-vis spectra.....	18
1.1.3.2. Raman spectra.....	20
1.1.4. Spectroscopic properties of subphthalocyanines .....	23
1.1.5. Electrode modification and characterisation.....	26
1.1.5.1. Modification methods.....	26
1.1.5.2. Voltammetric characterization of modified electrode.....	27
1.1.5.3. Electrochemical Impedance Spectroscopy (EIS) characterization.....	28

1.1.6. Electrocatalysis .....	32
1.1.6.1. Definition.....	32
1.1.6.2. General electrocatalytic behavior of Pcs.....	33
1.1.6.3. Chlorophenols.....	34
1.1.6.4. NiPc as an electrocatalyst.....	35
1.1.7. Theoretical consideration and computational method .....	38
1.1.7.1. Density functional theory.....	38
1.1.7.2. The Fukui function.....	39
1.1.7.3. Computational aspects and calculation procedure.....	42
1.1.7.4. Computation of interaction between molecules.....	43
1.2. Nanostructured materials .....	45
1.2.1. Singled-walled carbon nanotubes (SWCNT).....	45
1.2.1.1. Basics of structure.....	45
1.2.1.2. Electrocatalytic behaviour of phthalocyanines in the presence of SWCNT.....	46
1.2.2. Quantum dots (QDs).....	50
1.2.2.1. Basics of spectra and size.....	50
1.2.2.2. Electrocatalytic behaviour of QDs.....	52
1.2.2.3. QDs-SWCNT-MPc conjugate.....	53
1.3. Summary of Aims of thesis.....	54

**CHAPTER TWO: EXPERIMENTAL**

2. Experimental.....	58
2.1. Materials .....	58
2.2. Equipment.....	58
2.3. Electrochemical methods.....	60
2.4. Density functional theory calculations.....	61
2.5. Synthesis .....	61
2.5.1. $\alpha$ -Nickel(II)tetrahydroxylphthalocyanine ( $\alpha$ -NiPc(OH) <sub>4</sub> ), Scheme 3.1.....	62
2.5.2. The synthesis of non-peripherally octahydroxy nickel phthalocyanine ( $\alpha$ -NiPc(OH) <sub>8</sub> ), Scheme 3.2.....	62

2.5.3. 1, 4, 8, 11, 15, 18, 22, 25-Octadecylphthalocyanine nickel(II) ( $\alpha$ -NiPc(C <sub>10</sub> H <sub>21</sub> ) <sub>8</sub> ) (Scheme 3.3). .....	63
2.5.4. Synthesis of 1,2-subnaphthalocyanine (SubNPc) (Scheme 3.4).....	63
2.5.5. Functionalization of singled walled carbon nanotubes (SWCNT) .....	64
2.5.6. CdTe-QDs- $\beta$ -NiPc conjugates .....	65

**CHAPTER THREE: RESULTS AND DISCUSSION**

3. Synthesis and Characterization .....	70
3.1. NiPc derivatives .....	71
3.1.1. Synthesis .....	71
3.1.2. Synthesis of nickel octadecylphthalocyanine ( $\alpha$ -NiPc(C <sub>10</sub> H <sub>21</sub> ) <sub>8</sub> ).....	73
3.1.3. Modelling of IR spectra .....	74
3.1.4. Modelling of Raman spectra.....	77
3.1.5. Solution cyclic voltammetry characterization .....	80
3.2. NiPc-SWCNT Conjugates .....	80
3.2.1. IR spectra .....	82
3.2.2. Raman spectra.....	83
3.2.3. UV-Vis spectra.....	85
3.2.4. Microscopic study.....	85
3.2.5. XPS of NiPc-SWCNT.....	88
3.3. CdTe-QDs- $\beta$ -NiPc(NH <sub>4</sub> ) <sub>2</sub> conjugate.....	90
3.3.1. XRD spectra.....	90
3.3.2. UV-Vis spectra.....	91
3.3.3. Fluorescence lifetimes .....	91
3.3.4. IR Spectra.....	94
3.3.5. Raman spectra.....	95
3.3.6. AFM.....	96

3.4. NiPc-SWCNT-QD conjugate.....	97
3.4.1. UV-Vis spectra.....	98
3.4.2. Raman spectral characterization of $\alpha$ -NiPc(C <sub>10</sub> H <sub>21</sub> ) <sub>8</sub> -SWCNT-QDs conjugate .....	99
3.4.3. XPS analysis of $\alpha$ -NiPc(C <sub>10</sub> H <sub>21</sub> ) <sub>8</sub> -SWCNT-QDs conjugate .....	100
3.5. SubNPc .....	104
3.5.1. Synthesis .....	104
3.5.2. UV/vis , CD, and MCD spectra .....	105
3.5.3. Electronic structures and theoretical absorption spectra.....	107

## **CHAPTER FOUR: ELECTRODE MODIFICATION AND CHARACTERIZATION**

4.1. NiPc derivatives and their conjugates with SWCNT.....	112
4.1.1. NiPc derivatives .....	112
4.1.2. Electrode modification NiPc-SWCNT conjugates .....	122
4.1.3. Surfaces characterization behaviour of electrodes in [Fe(CN) <sub>6</sub> ] <sup>3-/4-</sup> .....	125
4.2. QDs and their conjugates with $\beta$ -NiPc(NH <sub>2</sub> ) <sub>4</sub> .....	130
4.2.1. Pre-adsorbed CdTe-QDs on Au electrode .....	130
4.2.1.1. CV .....	130
4.2.1.2. DPV .....	133
4.2.2. Pre-adsorbed CdTe-QDs- $\beta$ -NiPc(NH <sub>2</sub> ) <sub>4</sub> conjugate.....	137
4.2.2.1. CV .....	137
4.2.2.2. DPV .....	139
4.2.3. Electrochemical impedance spectroscopy .....	142

## **CHAPTER FIVE: ELECTROCATALYSIS**

5.1. 4-Chlorophenol (4-CP) .....	147
5.1.1. NiPc derivatives in the absence of nanomaterials.....	147
5.1.1.1. $\beta$ -NiPc(OH) <sub>4</sub> .....	147
5.1.1.2. $\alpha$ -NiPc(OH) <sub>4</sub> .....	149
5.1.1.3. $\alpha$ -NiPc(OH) <sub>8</sub> .....	153



5.1.1.4. $\alpha$ -NiPc(C <sub>10</sub> H <sub>21</sub> ) <sub>8</sub> and NiPc.....	154
5.1.1.5. Mechanism.....	155
5.1.2. NiPc-SWCNT conjugates on GCE.....	156
5.1.2.1. NiPc(OH) <sub>n</sub> derivatives.....	156
5.1.2.2. $\alpha$ -NiPc(C <sub>10</sub> H <sub>21</sub> ) <sub>8</sub> and NiPc.....	158
5.1.3. Electrode stability .....	160
5.2. 2,4-Dichlorophenol (DCP).....	162
5.2.1. NiPc derivatives without SWCNT.....	162
5.2.2. NiPc-SWCNT conjugates: $\alpha$ -NiPc(C <sub>10</sub> H <sub>21</sub> ) <sub>8</sub> and NiPc used as examples.....	164
5.2.3. CdTe-QDs and its conjugates .....	166
5.2.3.1. CdTe-QDs without $\beta$ -NiPc(NH <sub>2</sub> ) <sub>4</sub> .....	166
5.2.3.2. CdTe-QDs and $\beta$ -NiPc(NH <sub>2</sub> ) <sub>4</sub> .....	169
5.3. Pentachlorophenol (PCP).....	170
5.3.1. CdTe-QDs .....	170
5.3.2. CdTe-QDs- $\beta$ -NiPc(NH <sub>2</sub> ) <sub>4</sub> conjugate.....	171
5.3.3. NiPc-SWCNT-QDs conjugate.....	174
5.4. Theoretical prediction of the interaction between NiPc complexes and 4-chlorophenol. .....	177
6.1. General Conclusion.....	190
References.....	193

**LIST OF ABBREVIATIONS**

<b>Abs</b>	-	<b>absorbance</b>
<b>Anal</b>	-	<b>analyte</b>
<b>Ar</b>	-	<b>aromatic</b>
<b>Au</b>	-	<b>gold working electrode</b>
<b>C E</b>	-	<b>counter electrode</b>
<b>CPE</b>	-	<b>constant phase element</b>
<b>CV</b>	-	<b>cyclic voltammogram</b>
<b>DCC</b>	-	<b>dicyclohexylcarbodiimide</b>
<b>DCM</b>	-	<b>dichloromethane</b>
<b>DFT</b>	-	<b>Density functional theory</b>
<b>DMF</b>	-	<b>N, N-dimethylformamide</b>
<b>DMSO</b>	-	<b>dimethylsulphoxide</b>
<b>DPV</b>	-	<b>Differential pulse voltammetry</b>
<b>EIS</b>	-	<b>electrochemical impedance spectroscopy</b>
<b>EA<sub>A</sub></b>	-	<b>Electron affinities</b>
<b>F</b>	-	<b>fluorescence</b>
<b>FFT</b>	-	<b>fast fourier transform</b>
<b>FMO</b>	-	<b>Frontier molecular orbital</b>
<b>GCE</b>	-	<b>glassy carbon electrode</b>
<b>GPES</b>	-	<b>general purpose electrochemical systems</b>
<b>H<sub>2</sub>Pc</b>	-	<b>metal-free phthalocyanine</b>
<b><sup>1</sup>H-NMR</b>	-	<b>proton nuclear magnetic resonance</b>
<b>HOMO</b>	-	<b>highest occupied molecular orbital</b>
<b>HPLC</b>	-	<b>high performance liquid chromatography</b>
<b>ICP</b>	-	<b>inductively coupled plasma</b>
<b>IP<sub>A</sub></b>	-	<b>Ionization potential</b>
<b>IR</b>	-	<b>infrared</b>
<b>IUPAC</b>	-	<b>International Union of Pure and Applied Chemistry</b>
<b>LUMO</b>	-	<b>lowest unoccupied molecular orbital</b>
<b>M</b>	-	<b>metal</b>
<b>m</b>	-	<b>multiplet</b>
<b>MCD</b>	-	<b>Magnetic circular dichroism</b>
<b>MCPBA</b>	-	<b>m-chloroperoxy-Ibenzoic acid</b>
<b>MPc</b>	-	<b>metallophthalocyanine</b>
<b>MS</b>	-	<b>mass spectroscopy</b>

## Preliminaries

---

<b>MTSPc</b>	-	<b>tetra-sulfonated metallophthalocyanine</b>
<b>NLO</b>	-	<b>non-linear optics</b>
<b>NMR</b>	-	<b>nuclear magnetic resonance</b>
<b>OPG</b>	-	<b>Ordinary pyrolytic graphite</b>
<b>OSWV</b>	-	<b>Osteryoung square wave voltammetry</b>
<b>OTos</b>	-	<b>tosyl</b>
<b>OTf</b>	-	<b>triflate</b>
<b>PBS</b>	-	<b>phosphate buffer solution</b>
<b>Pc</b>	-	<b>phthalocyanine</b>
<b>PDT</b>	-	<b>photodynamic therapy</b>
<b>Ph</b>	-	<b>phenyl</b>
<b>PPh<sub>3</sub></b>	-	<b>triphenylphosphine</b>
<b>R</b>	-	<b>any functional group</b>
<b>RBr</b>	-	<b>alkyl bromide</b>
<b>R E</b>	-	<b>reference electrode</b>
<b>ROH</b>	-	<b>alcohol</b>
<b>RSH</b>	-	<b>thiol</b>
<b>RT</b>	-	<b>Room temperature</b>
<b>S<sub>0</sub></b>	-	<b>ground singlet state</b>
<b>S<sub>1</sub></b>	-	<b>excited singlet state</b>
<b>SCE</b>	-	<b>Saturated calomel electrode</b>
<b>SubPc</b>	-	<b>subphthalocyanine</b>
<b>SubNc</b>	-	<b>subnaphthalocyanine</b>
<b>SWV</b>	-	<b>square wave voltametry</b>
<b>T<sub>1</sub></b>	-	<b>excited triplet state</b>
<b>TDDFT</b>	-	<b>Time dependent density functional theory</b>
<b>TpPc</b>	-	<b>Tetra-4-(pyrrol-1-yl) phenoxy phthalocyanine</b>
<b>TPhPyPc</b>	-	<b>Tetra(pyrro-1-yl) phenoxy phthalocyanine</b>
<b>TBABF<sub>4</sub></b>	-	<b>tetrabutylammonium tetrafluoroborate</b>
<b>TBC</b>	-	<b>triazatertrabenzcorrole</b>
<b>TBMPC</b>	-	<b>Tetrakis (benzylmercapto) phthalocyanine</b>
<b>TBTAP</b>	-	<b>tetrabenzotriazaporphyrin</b>
<b>TDMPC</b>	-	<b>Tetrakis (dodecyl mercapto) phthalocyanine</b>
<b>THF</b>	-	<b>tetrahydrofuran</b>
<b>TLC</b>	-	<b>thin column chromatography</b>
<b>TNPc</b>	-	<b>tetranitrophthalocyanine</b>

## **Preliminaries**

---

<b>TSPc</b>	-	<b>tetra sulfonated phthalocyanine</b>
<b>UV/Vis</b>	-	<b>ultraviolet/visible</b>
<b>VCE</b>	-	<b>Vitreous carbon electrode</b>
<b>WE</b>	-	<b>working electrode</b>

**LIST OF SYMBOLS**

<b>A</b>	-	<b>geometric or real surface area</b>
<b>C</b>	-	<b>concentration</b>
<b>D</b>	-	<b>diffusion coefficient</b>
<b>E</b>	-	<b>potential</b>
<b>E<sub>1/2</sub></b>	-	<b>half-wave potential</b>
<b>E<sub>pa</sub></b>	-	<b>anodic peak potential</b>
<b>E<sub>pc</sub></b>	-	<b>cathodic peak potential</b>
<b>F</b>	-	<b>Faradays constant</b>
<b>f</b>	-	<b>frequency</b>
<b>hν</b>	-	<b>absorption energy</b>
<b>Hz</b>	-	<b>hertz</b>
<b>I</b>	-	<b>current</b>
<b>I</b>	-	<b>intensity</b>
<b>I(t)</b>	-	<b>sinusoidal current</b>
<b>I<sub>0</sub></b>	-	<b>incident intensity</b>
<b>I<sub>0</sub></b>	-	<b>maximum current amplitude</b>
<b>I<sub>p</sub></b>	-	<b>peak current</b>
<b>I<sub>pa</sub></b>	-	<b>anodic peak current</b>
<b>I<sub>pc</sub></b>	-	<b>cathodic peak current</b>
<b>j</b>	-	<b>complex number</b>
<b>K</b>	-	<b>Kelvin</b>
<b>n</b>	-	<b>Number of electrons</b>
<b>Q</b>	-	<b>charge</b>
<b>R</b>	-	<b>universal gas constant</b>
<b>R<sub>ct</sub></b>	-	<b>charge transfer resistance</b>
<b>R<sub>E</sub></b>	-	<b>electrolyte or solution resistance</b>
<b>T</b>	-	<b>double layer capacitance quantity</b>
<b>ν<sub>max</sub></b>	-	<b>wavenumber of maximum absorption</b>
<b>v</b>	-	<b>scan rate</b>
<b>V</b>	-	<b>volts</b>
<b>V</b>	-	<b>volume</b>
<b>V(t)</b>	-	<b>sinusoidal potential</b>
<b>V<sub>0</sub></b>	-	<b>maximum potential amplitude</b>
<b>Z</b>	-	<b>impedance (or complex resistance)</b>

## Preliminaries

---

$Z'$	-	real component
$Z''$	-	imaginary component
$Z_w$	-	Warburg impedance
$\alpha$	-	alpha
$\beta$	-	beta
$\Delta E_p$	-	anodic to cathodic peak potential separation
$\varepsilon$	-	extinction coefficient
$\omega$	-	radial frequency
$\Gamma$	-	surface coverage
$\theta$	-	phase angle
$\theta$	-	surface coverage
$\pi (\pi^*)$	-	pi bonding (anti-pi bonding)
$\Delta G_{ads}$	-	Gibbs free energy of adsorption
$\sigma$	-	Warburg coefficient
$\Omega$	-	ohm
$\delta$	-	interaction parameter between adsorbed molecules
$q_{Ak}$	-	Mulliken charges on $k^{th}$ atom
$\tau_0$	-	absorption band area
$\tau_F$	-	fluorescence life time
$\tau_T$	-	triplet life time

### Figure Caption

**Figure 1.1:** Phthalocyanine.

**Figure 1.2:** Unsubstituted Subphthalocyanine

**Figure 1.3:** The NiPc derivatives synthesized in this work

**Figure 1.4:** Selection of SubPc's which have been reported in literature

**Figure 1.5:** Absorption spectra of unmetallated phthalocyanine (i) and metallated (ii).

**Figure 1.6:** Schematic representation of energy levels and origins of Q and B band.

**Figure 1.7:** The 1350-1550  $\text{cm}^{-1}$  region of NiPc, CoPc, ZnPc and PbPc illustrating the Raman band that exhibit unique patterns for each phthalocyanine

**Figure 1.8:** UV-vis spectrum of subphthalocyanine (thick line) compared to the one of nickel phthalocyanine (thin line) both in chloroform

**Figure 1.9:** The three Faraday terms  $\mathcal{A}_1$ ,  $\mathcal{B}_0$  and  $C_0$

**Figure 1.10:** Electronic (bottom) and circular dichroism (top) spectra of subPc in chloroform

**Figure 1.11:** Model of Glassy carbon electrode GCE (A) and Structure of planes of ordinary pyrolytic graphite (OPGE) (B).

**Figure 1.12:** (a) Applied sinusoidal voltage and resulting sinusoid current response (b) vector representation of real ( $Z'$ ) and imaginary ( $Z''$ ) part of impedance ( $Z$ ).

**Figure 1.13:** Flow diagram for the measurement and characterization of a material-electrode system.

**Figure 1.14:** Erschler-Randles circuit for the electrochemical system with diffusion-limited behaviour.

**Figure 1.15:** Nyquist plot for the electrochemical system with diffusion-limited behavior.

**Figure 1.16:** Bode plot for the Randles equivalent circuit with diffusion-limited behavior.

**Figure 1.17:** A schematic representation of an electrocatalytic reaction. (S = substrate and O/R = redox couple).

**Figure 1.18:** Molecular structure of chlorophenols

**Figure 1.19:** Schematic representation of a 2-dimensional graphite layer sheet with the resultant SWCNT tubular structures

**Figure 1.20:** Absorption and Photoluminescence (PL) of typical CdTe-QDs, (a), (b) and (c) correspond to the growth time of 90, 150, and 360 minute respectively

**Figure 1.21:** Band gap in bulk crystals and QDs

**Figure 1.22:** Voltammograms of the Au electrode with preadsorbed CdTe-QDs in blank buffer solution

**Figure 1.23:** Nickel tetra amino conjugate (CdTe-QDs- $\beta$ -NiPc(NH<sub>2</sub>)<sub>4</sub>)

**Figure 3.1:** Ground state absorption spectra of  $\alpha$ -NiPc(C<sub>10</sub>H<sub>21</sub>)<sub>8</sub> (A) and  $\alpha$ -NiPc(C<sub>10</sub>H<sub>21</sub>)<sub>8</sub>-SWCNT (B) in THF.

**Figure 3.2:** IR spectrum of  $\beta$ -H<sub>2</sub>Pc(OH)<sub>4</sub> (a) Experimental (b) and Theoretical .

**Figure 3.3:** (a) N-Ni: stretch:  $\nu=336.87$  - $336.85$  cm<sup>-1</sup> in plane stretches, (b) C-H: stretch:  $\nu=3236.48$  - $3226.98$  cm<sup>-1</sup> in plane stretches and (c) O-H stretch:  $\nu=3749.64$  cm<sup>-1</sup> in plane stretches

**Figure 3.4:** IR spectrum of  $\beta$ -NiPc(OH)<sub>4</sub> (a) Experimental and (b) Theoretical

**Figure 3.5:** Raman spectrum of  $\beta$ -H<sub>2</sub>Pc(OH)<sub>4</sub> (a) Experimental and (b) Theoretical.

**Figure 3.6:** Raman spectrum of  $\beta$ -NiPc(OH)<sub>4</sub> (a) Experimental and (b) Theoretical.

**Figure 3.7:** Cyclic voltammograms of  $\alpha$ -NiPc(C<sub>10</sub>H<sub>21</sub>)<sub>8</sub> in THF with TBABF<sub>4</sub> as electrolyte.

**Figure 3.8:** (a) possible structures formed on linking  $\beta$ -NiPc(NH<sub>2</sub>)<sub>4</sub> to SWCNT (b) and representation of  $\beta$ -NiPc(NH<sub>2</sub>)<sub>4</sub> adsorbed on SWCNT.

**Figure 3.9:** FT-IR spectra of SWCNT (A),  $\alpha$ -NiPc(OH)<sub>4</sub> (B) and  $\alpha$ -NiPc(OH)<sub>4</sub>-SWCNT (C) adsorbed conjugate.

**Figure 3.10:** IR spectra of SWCNT (A),  $\alpha$ -NiPc(C<sub>10</sub>H<sub>21</sub>)<sub>8</sub> (B) and  $\alpha$ -NiPc(C<sub>10</sub>H<sub>21</sub>)<sub>8</sub>-SWCNT(ads) (C).

**Figure 3.11:** Raman spectra of SWCNT (A),  $\alpha$ -NiPc(OH)<sub>4</sub> (B) and  $\alpha$ -NiPc(OH)<sub>4</sub>-SWCNT(ads).

**Figure 3.12:** Raman spectra of SWCNT (A),  $\alpha$ -NiPc(C<sub>10</sub>H<sub>21</sub>)<sub>8</sub> (B) and  $\alpha$ -NiPc(C<sub>10</sub>H<sub>21</sub>)<sub>8</sub>-SWCNT (C).

**Figure 3.13:** TEM image of SWCNT before (a) and after (b) functionalization with  $\alpha$ -NiPc(OH)<sub>8</sub> at 200 nm resolution

**Figure 3.14:** TEM images of  $\alpha$ -NiPc(C<sub>10</sub>H<sub>21</sub>)<sub>8</sub> (A) film and  $\alpha$ -NiPc(C<sub>10</sub>H<sub>21</sub>)<sub>8</sub>-SWCNT (B) at 200 nm resolution.

**Figure 3.15:** AFM images of  $\alpha$ -NiPc(C<sub>10</sub>H<sub>21</sub>)<sub>8</sub>-SWCNT

**Figure 3.16:** XPS spectra of SWCNT (A) and  $\alpha$ -NiPc(C<sub>10</sub>H<sub>21</sub>)<sub>8</sub>-SWCNT(B)

**Figure 3.17:** XRD spectrum of CdTe-QDs.

**Figure 3.18:** Absorption (a) and Emission (b) spectra of CdTe-QDs- $\beta$ -NiPc(NH<sub>2</sub>)<sub>4</sub> in pH 9.2 buffer solution.

**Figure 3.19:** Photoluminescence decay curves of (A) CdTe-QDs-NiPc(NH<sub>2</sub>)<sub>4</sub> and (B)



CdTe QDs in a buffer solution of pH 9.2. Excitation wavelength = 480 nm.

**Figure 3.20:** Infrared (IR) Spectra of (A) CdTe-QDs, (B)  $\beta$ -NiPc(NH<sub>2</sub>)<sub>4</sub> and (C) CdTe-QDs- $\beta$ -NiPc(NH<sub>2</sub>)<sub>4</sub>

**Figure 3.21:** Far Infrared (FIR) Spectra of (A)  $\beta$ -NiPc(NH<sub>2</sub>)<sub>4</sub>, (B) CdTe-QDs- $\beta$ -NiPc(NH<sub>2</sub>)<sub>4</sub> and (C) CdTe-QDs

**Figure 3.22:** Raman spectra of (A) CdTe-QDs- $\beta$ -NiPc(NH<sub>2</sub>)<sub>4</sub>, (B) CdTe-QDs and (C)  $\beta$ -NiPc(NH<sub>2</sub>)<sub>4</sub>

**Figure 3.23:** AFM image of (A) CdTe-QDs and (B) CdTe-QDs- $\beta$ -NiPc(NH<sub>2</sub>)<sub>4</sub>.

**Figure 3.24:** Ground state absorption spectra of  $\alpha$ -NiPc(C<sub>10</sub>H<sub>21</sub>)<sub>8</sub> (A) and  $\alpha$ -NiPc(C<sub>10</sub>H<sub>21</sub>)<sub>8</sub>-SWCNT (B) and  $\alpha$ -NiPc(C<sub>10</sub>H<sub>21</sub>)<sub>8</sub>-SWCNT-QDs (C) in THF.

**Figure 3.25:** Raman spectra of SWCNT (A),  $\alpha$ -NiPc(C<sub>10</sub>H<sub>21</sub>)<sub>8</sub> (B),  $\alpha$ -NiPc(C<sub>10</sub>H<sub>21</sub>)<sub>8</sub>-SWCNT (C) and  $\alpha$ -NiPc(C<sub>10</sub>H<sub>21</sub>)<sub>8</sub>-SWCNT-QDs conjugate (D).

**Figure 3.26:** XPS spectra of SWCNT (A),  $\alpha$ -NiPc(C<sub>10</sub>H<sub>21</sub>)<sub>8</sub>-SWCNT(ads) (B) and  $\alpha$ -NiPc(C<sub>10</sub>H<sub>21</sub>)<sub>8</sub>-SWCNT-QDs conjugate (C).

**Figure 3.27:** Subnaphthalocaynine enantiomers

**Figure 3.28:** HPLC trace of Fraction 1: Solvent: Chloroform: Hexane (2:3) Flow rate (1mL/Min).

**Figure 3.29:** MCD, CD and electronic absorption spectra of SubNPc (Fraction 1) measured in CHCl<sub>3</sub> at room temperature. ( $\epsilon = 3.42 \times 10^{-5}$  M)

**Figure 3.30:** Partial molecular diagram of SubPc (left) and SubNPc (right).

**Figure 3.31:** Theoretical absorption and CD spectra of clockwise isomer (left) and anti-clockwise isomer (right) of Fraction 1 based on TDDFT calculation.

**Figure 4.1:** Cyclic voltammograms of  $\beta$ -NiPc(OH)<sub>4</sub>, adsorbed on the OPG electrode in 0.1 M NaOH, forming *poly*- $\beta$ -Ni(O)Pc(OH)<sub>4</sub>, Scan rate = 100 mVs<sup>-1</sup>.

**Figure 4.2:** Cyclic voltammograms of *poly*- $\beta$ -Ni(O)Pc(OH)<sub>4</sub> on OPG electrode at (i) pH 7 and (ii) in 0.1 M NaOH, Scan rate=100 mVs<sup>-1</sup>.

**Figure 4.3:** Cyclic voltammograms of (A)  $\alpha$ -NiPc(OH)<sub>4</sub>, and (B)  $\alpha$ -NiPc(OH)<sub>8</sub> adsorbed on the OPG electrode in 0.1 M NaOH, forming *poly*- $\alpha$ -Ni(O)Pc(OH)<sub>n</sub>.

**Figure 4.4:** Cyclic voltammograms of (i) *poly*- $\beta$ -Ni(O)Pc(OH)<sub>4</sub>, (ii) *poly*- $\alpha$ -Ni(O)Pc(OH)<sub>4</sub> and (iii) *poly*- $\alpha$ -Ni(O)Pc(OH)<sub>8</sub> on OPG electrode.

**Figure 4.5:** Cyclic voltammogram of GCE- $\beta$ -NiPc(OH)<sub>4</sub> electrode in buffer solution of pH 9.2.

**Figure 4.6:** (A) Cyclic voltammogram of  $\alpha$ -NiPc(C<sub>10</sub>H<sub>21</sub>)<sub>8</sub>-SWCNT, (B) Square wave voltammogram of  $\alpha$ -NiPc(C<sub>10</sub>H<sub>21</sub>)<sub>8</sub>-SWCNT

**Figure 4.7:** Cyclic voltammograms of 1mM [Fe(CN)<sub>6</sub>]<sup>3-</sup>/[Fe(CN)<sub>6</sub>]<sup>4-</sup> in 0.1 M KCl on (A) GCE- $\beta$ -NiPc(OH)<sub>4</sub>-SWCNT

**Figure 4.8:** (A) Cyclic voltammograms of Au electrode with pre-adsorbed ((a) and (b)) CdTe-QDs And (c) bare Au electrode in blank buffer pH 9.2;

**Figure 4.9:** DPV scans of (A) CdTe-QDs 1<sup>st</sup> scan to 6<sup>th</sup> scan, (B) 6<sup>th</sup> scan to 14<sup>th</sup> scan. (C) the last scan in (B) following rinsing in pH 9.2 buffer

**Figure 4.10:** (A) Cyclic Voltammograms of Au electrode with pre-adsorbed (a) CdTe-QDs and (b) CdTe-QDs- $\beta$ -NiPc(NH<sub>2</sub>)<sub>4</sub> in blank buffer pH 9.2.

**Figure 4.11:** (A) DPV scans of CdTe-QDs- $\beta$ -NiPc(NH<sub>2</sub>)<sub>4</sub> in pH 9.2 buffer solution with 0.1 M Na<sub>2</sub>SO<sub>4</sub> as an electrolyte.

**Figure 4.12:** DPV scans of (A) CdTe-QDs and (B) CdTe-QDs- $\beta$ -NiPc(NH<sub>2</sub>)<sub>4</sub> in pH 9.2 buffer solution containing Na<sub>2</sub>SO<sub>4</sub>.

**Figure 4.13:** (a) Nyquist plots, (b) Bode plots and (c) Equivalent circuit used in this work.

**Figure 5.1:** Cyclic voltammograms of 0.7 mM 4-chlorophenol in 0.1 M NaOH on (i) bare OPGE, (ii)  $\beta$ -NiPc(OH)<sub>4</sub> on OPGE and (iii) *poly*- $\beta$ -Ni(O)Pc(OH)<sub>4</sub>-OPGE.

**Figure 5.2:** Comparison of cyclic voltammogram of *poly*- $\beta$ -Ni(O)Pc(OH)<sub>4</sub>-OPGE in the absence (i) and presence (ii) of 4-chlorophenol in 0.1 M NaOH.

**Figure 5.3:** Cyclic voltammograms of  $7 \times 10^{-4}$  M 4-chlorophenol in 0.1 M NaOH on OPGE modified with (A)  $\alpha$ -NiPc(OH)<sub>4</sub> and (B)  $\alpha$ -NiPc(OH)<sub>8</sub>.

**Figure 5.4:** Cyclic voltammograms of 0.7 mM 4-chlorophenol in 0.1 M NaOH on GCE-*poly*- $\alpha$ -Ni(O)Pc(C<sub>10</sub>H<sub>21</sub>)<sub>8</sub> and GCE-*poly*- $\alpha$ -Ni(O)Pc.

**Figure 5.5:** Oxidation of 0.7 mM of 4-chlorophenol in 0.1 mM NaOH aqueous solution on GCE- $\beta$ -NiPc(NH<sub>2</sub>)<sub>4</sub>-SWCNT(linked), GCE- $\beta$ -NiPc(NH<sub>2</sub>)<sub>4</sub>-SWCNT.

**Figure 5.6:** Cyclic voltammograms of 0.7 mM 4-chlorophenol in 0.1 M NaOH on (i) bare GCE, (ii) GCE-SWCNT and (iii) GCE- $\alpha$ -NiPc(C<sub>10</sub>H<sub>21</sub>)<sub>8</sub>-SWCNT

**Figure 5.7:** Variation of peak current with scan number for the voltammetric responses in 0.7 mM 4-chlorophenol in 0.1 M NaOH for GCE- $\beta$  NiPc(OH)<sub>4</sub> and SWCNT.

**Figure 5.8:** Cyclic voltammograms of 0.7 mM 4-chlorophenol in 0.1 M NaOH solution catalysed by GCE- $\alpha$ -NiPc(OH)<sub>4</sub>-SWCNT .

**Figure 5.9:** Cyclic voltammograms of 0.7 mM 2,4-dichlorophenol in 0.1 M NaOH on *poly*- $\alpha$ -Ni(O)Pc(C<sub>10</sub>H<sub>21</sub>)<sub>8</sub> and GCE and GCE-*poly*-Ni(O)Pc.

**Figure 5.10:** Cyclic voltammograms of 0.7 mM 2,4-dichlorophenol in 0.1 M NaOH on GCE-SWCNT, GCE- $\alpha$ -Ni(O)Pc(C<sub>10</sub>H<sub>21</sub>)<sub>8</sub> and GCE- $\alpha$ -NiPc(C<sub>10</sub>H<sub>21</sub>)<sub>8</sub>-SWCNT

**Figure 5.11:** DPV scans for detection of 0.7 mM 2, 4-dichlorophenol in pH 9.2 buffer on: (A) bare Au electrode in the absence (a) and presence (b) of 2, 4-dichlorophenol.

**Figure 5.12:** Electrodep-CdTe-QDs- $\beta$ -NiPc(NH<sub>2</sub>)<sub>4</sub> in the absence (a) and presence (b) of 0.7 mM 2, 4-dichlorophenol.

**Figure 5.13:** DPV scans for detection of 0.7 mM pentachlorophenol in pH 9.2 buffer on: (A) bare Au electrode in the absence (a) and presence (b) of 2, 4-dichlorophenol.

**Figure 5.14:** DPV scans for detection of 0.7 mM pentachlorophenol in pH 9.2 buffer on (A) electrodep-CdTe-QDs- $\beta$ -NiPc(NH<sub>2</sub>)<sub>4</sub>.

**Figure 5.15:** Oxidation of 0.7 mM of pentachlorophenol in 0.1 M NaOH aqueous solution on (a) GCE- $\alpha$ -NiPc(C<sub>10</sub>H<sub>21</sub>)<sub>8</sub>-SWCNT-QDs, (b) GCE- $\alpha$ -NiPc(C<sub>10</sub>H<sub>21</sub>)<sub>8</sub>-SWCNT, (c) GCE- $\alpha$ -NiPc(C<sub>10</sub>H<sub>21</sub>)<sub>8</sub>.

**Figure 5.16:** Plot of the change in peak current,  $I_p$ , versus cycle number for GCE- $\alpha$ -NiPc(C<sub>10</sub>H<sub>21</sub>)<sub>8</sub>-SWCNT-QDs (a), GCE-SWCNT (b), GCE bare (c).

**Figure 5.17:** Fully optimized molecular structures at the B3LYP/DFT 6-31G(d) level of calculations of (a)  $\beta$ -H<sub>2</sub>Pc(OH)<sub>4</sub>, (b)  $\beta$ -NiPc(OH)<sub>4</sub>

**Figure 5.18:** Orbital energy diagrams for  $D_{4h}$  configuration of (A)  $\beta$ -NiPc(OH)<sub>4</sub> and (B)  $\beta$ -Ni(O)Pc(OH)<sub>4</sub>.

**Figure 5.19:** Orbital energy diagrams for 4-chlorophenol

**Figure 5.20:** (A) Optimised structure of  $\beta$ -NiPc(OH)<sub>4</sub> and 4-chlorophenol using B3LYP/6-3g(d). (B) Electron density distribution of  $\beta$ -NiPc(OH)<sub>4</sub>.

**Figure 5.21:**  $\beta$ -NiPc(OH)<sub>4</sub> (a),  $\beta$ -NiPc(OH)<sub>4</sub>/4-chlorophenol (b),  $\beta$ -Ni(O)Pc(OH)<sub>4</sub>/4-chlorophenol (c) and  $\beta$ -Ni(O)Pc(OH)<sub>4</sub> (d) frontier molecular orbitals (LUMO).

**Figure 5.22:** Fukui 2D plots of condensed softness for maximum softness.

### Schemes

**Scheme 1.1:** General phthalocyanine synthesis. M = metal, MX = metal salt, DBN = 1,5-Diazabicyclo[4.3.0]non-5-ene, ROH = alcohol.

**Scheme 1.2:** Synthesis of a peripherally tetrasubstituted phthalocyanine. R= any functional group.

**Scheme 1.3:** Synthesis of non-peripherally tetrasubstituted phthalocyanine. (R = any substituent, Ac<sub>2</sub>O = Acetic anhydride).

**Scheme 1.4:** Synthesis of tetra and octa substituted β-phthalocyanines. (R = any functional group, Ac<sub>2</sub>O = Acetic anhydride).

**Scheme 1.5:** Preparation of 3, 6-dialkylphthalonitrile. (R = alkyl, MCPBA = m-chloroperoxy-Ibenzoic acid, RBr = alkyl bromide).

**Scheme 1.6:** Cross coupling reactions of aryl triflate. (DCM = dichloromethane, and RT = room temperature and CF<sub>3</sub>SO<sub>2</sub>)<sub>2</sub>O = triflate ester.

**Scheme 1.7:** Formation of an aryl triflate (28).

**Scheme 1.8:** Negishi coupling reaction. (R = aryl or alkyl, X = Halogen, Ph =phenyl)

**Scheme 1.9:** Preparation of unsubstituted subphthalocyanine

**Scheme 1.10:** Subphthalocyanine regio- and enantiomers (R = can be any functional group)

**Scheme 3.1:** Preparation of nickel(II) 2,9,16,23-tetrahydroxy phthalocyanine, α-NiPc(OH)<sub>4</sub>.

**Scheme 3.2:** Synthesis pathway for non-peripherally substituted α-NiPc(OH)<sub>8</sub>.

**Scheme 3.3:** 1, 4, 8, 11, 15, 18, 22, 25-Octadecylphthalocyanine Nickel(II)

**Scheme 3.4:** Synthesis of 1,2-subnaphthalocyanines

### Tables

**Table 1.1:** A selection of all known hydroxy phthalocyanine complexes

**Table 1.2:** List of known Subnaphthalocyanines and chiral Subphthalocyanine, see Figure 1.4.

**Table 1.3:** Raman and spectral data of known NiPcs

**Table 1.4:** Electrocalysis of chlorophenols using NiPc electrodes.

**Table 1.5:** Known MPc-SWCNT conjugate used for electrocatalysis

**Table 3.1:**List of Synthesised phthalocyanine, SubNPc and and NiPc-Nanomaterial

**Table 3.2:** Gross Mulliken populations and atomic charge (Q)

**Table 3.3:** Calculated parameters (bond length R in Å, bond angle  $\theta$  in deg)

**Table 3.4:** Fluorescence lifetimes of QDs linked to  $\beta$ -NiPc(NH<sub>2</sub>)<sub>4</sub>  $\lambda_{Exc} = 480$  nm. pH 9.2 buffer

**Table 3.5:** Mass concentration percentage (%)

**Table 3.6:** Selected transition energies and wave functions of Faction 1 and SubPc calculated by the TDDFT (B3LYP/6-31G(d)) method.

**Table 4.1.** Electrochemical parameters for NiPc derivatives in 0.1 M NaOH.

**Table 4.2:** Electrochemical parameters for electrode characterization (using [Fe(CN)<sub>6</sub>]<sup>3-</sup>/[Fe(CN)<sub>6</sub>]<sup>4-</sup> in 0.1 M KCl. Potentials versus Ag|AgCl on GCE.

**Table 4.3:** Impedance data adsorbed CdTe QDs and CdTe-QDs- $\beta$ -NiPc(NH<sub>2</sub>)<sub>4</sub>. pH 9.2 buffer. Fe(CN)<sub>6</sub><sup>4-</sup>/[Fe(CN)<sub>6</sub>]<sup>3-</sup> in 1M KCl solution.

**Table 5.1:** Electrochemical parameters for the detection 0.7 mM 4-chlorophenols in 0.1 M NaOH. Potentials versus Ag|AgCl on GCE.

**Table 5.2:** Electrochemical parameters for the detection dichlorophenol in 0.1 M NaOH. Potentials versus Ag|AgCl.

**Table 5.3:** Oxidation potentials for 2, 4-dichlorophenol and pentachlorophenol and current percentage loss after second scan in pH 9.2 buffer.

**Table 5.4:** Peak potential for PCP oxidation and Current drop percentage from first scan for the detection of pentachlorophenol in 0.7 mM in 0.1M NaOH.

**Table 5.5:** Calculated energy gaps (eV) between HOMO and LUMO and Molecular hardness( $\eta$ ) in gas phase.

**Table 5.6:** Calculated HOMO-LUMO energy gaps (eV) in gas phase.

# **Chapter 1: Introduction**

## 1. Introduction

The main focus of the work is on the study of nickel phthalocyanines (NiPc) as electrocatalysts using chlorophenols as test pollutants. The theoretical and experimental study of the electrocatalysis is presented. The other small part of the thesis is on the isolation of isomers of Subnaphthalocyanines (SubNPc). Thus the introduction will include both SubNPc and NiPc.

### 1.1. Phthalocyanines and Subphthalocyanines

Phthalocyanines (Pcs) are remarkable 18  $\pi$  electron macrocyclic compounds that possess interesting physical and chemical properties. Their bright colours, conductivity, chemical and thermal stability have made them very desirable for many applications. Phthalocyanines continually find their usefulness in contemporary and emerging technologies such as catalysis [1], photodynamic therapy (PDT) [2], nonlinear optics [3], electrochemical sensors [4], thermal writing displays [5] and solar cells [6].

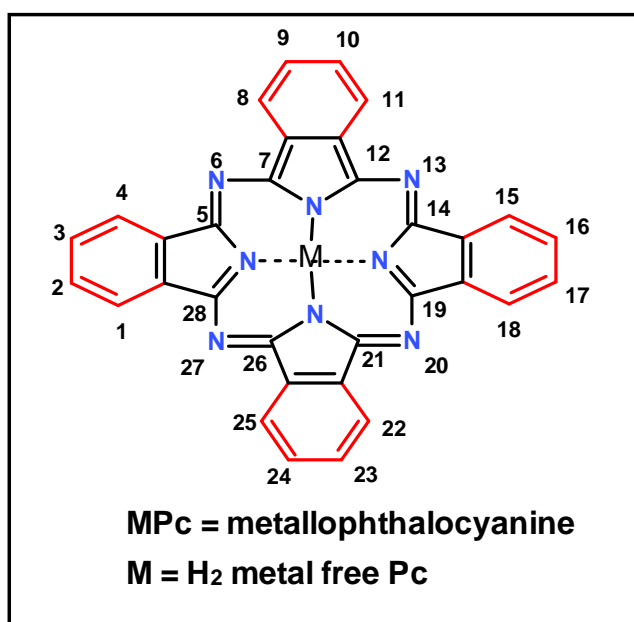


**Figure 1.1: Phthalocyanine.**

The inner aromatic ring shown in black (**Figure 1.1**) is responsible for the intense blue-green colour of these macrocycles ( $\pi-\pi^*$  transition occurring in the visible region). The phthalocyanine ring is numbered following the International Union of Pure and Applied Chemistry (IUPAC) nomenclature of tetrapyrroles (**Figure 1.1**) [7]. The presence of four

benzene groups causes solubility and aggregation problems. By substituting functional groups on these benzene groups, solubility can be improved considerably. When a phthalocyanine is coordinated to a central metal it is referred to as metallophthalocyanine (MPc). Substituting with electron donating or withdrawing functional groups on the periphery of the phthalocyanine molecule alters electrochemical and physical properties of the macrocycle.

Subphthalocyanine (SubPc) is a ring-contracted congener of phthalocyanine (Pc), comprising of three isoindole units linked by three nitrogen atoms (**Figure 1.2**) [8, 9].

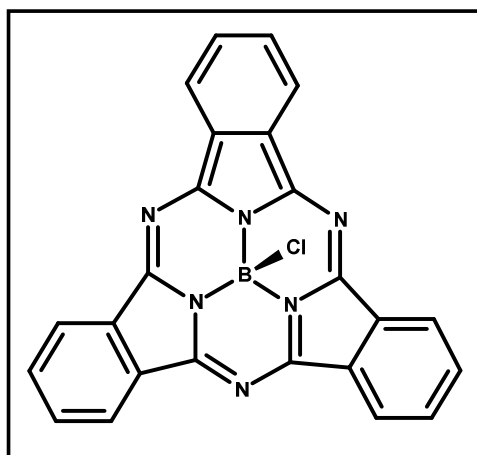


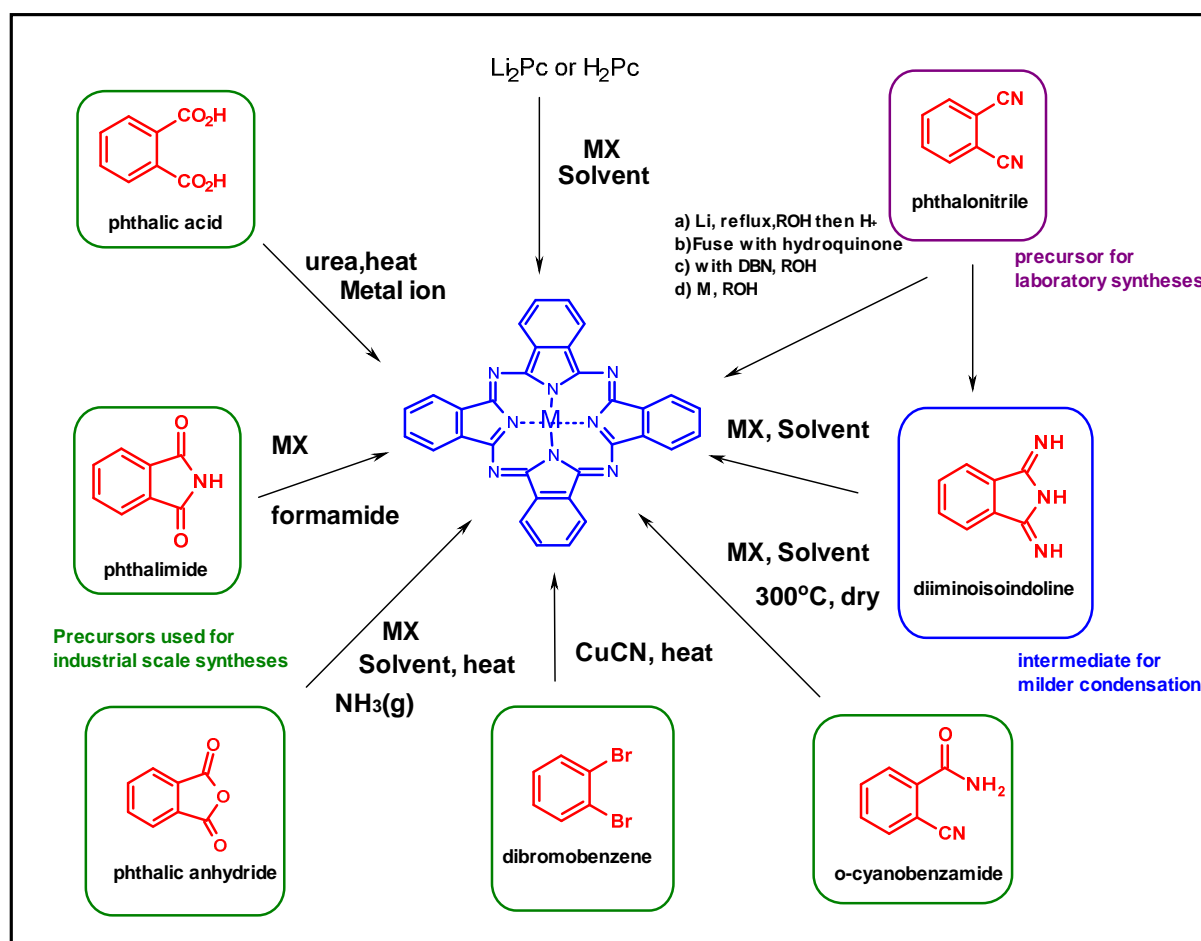
**Figure 1.2: Unsubstituted Subphthalocyanine.**

As a result of the  $C_{3v}$ -symmetric bowl-shaped structure [10] with boron atom at the center and the 14  $\pi$ -electron aromatic conjugate system, SubPc exhibits unique optical properties, such as strong absorption in the UV/vis region, intense fluorescence with moderate quantum yields, and unique nonlinear optical properties [8, 11, 12]. The central boron atom plays a critical role in maintaining the bowl-shaped structure, as well as enabling further functionalization by linking other functional units at the axial position [13-17]. Due to the proximity of the lowest unoccupied molecular orbital (LUMO) energy levels of SubPc to a fullerene ( $C_{60}$ ), hybrid materials of SubPc and  $C_{60}$  have received extensive interest in the fields of organic solar cells [18-21], organic transistor devices [22] and photo-induced energy and electron-transfer processes [23, 24]. The bowl-shaped molecular structure of SubPc is also beneficial for constructing supramolecular architectures with fullerenes both in solution [25] and the solid state [26].



### 1.1.1. Phthalocyanine synthesis

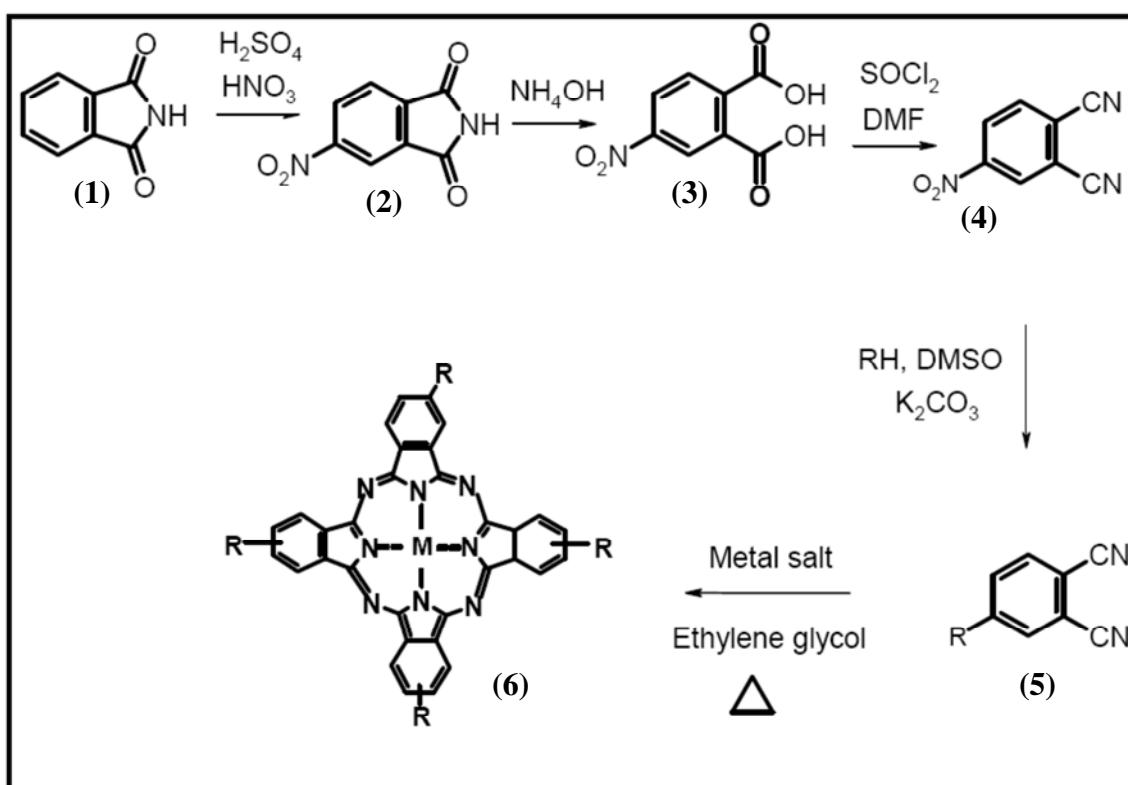
Pc complexes may be synthesised from a wide variety of starting materials, **Scheme 1.1**. The synthetic route that is generally used in the laboratory involves the use of unsubstituted or substituted phthalonitrile (or dicyanobenzene) derivatives as starting materials to produce unsubstituted Pc or peripherally and non-peripherally substituted molecules. Monosubstitution at the 3-position will lead to four isomers of ( $C_{4h}$ ) 1, 8, 15, 22-, ( $D_{2h}$ ) 1, 11, 15, 25-, ( $C_{2v}$ ) 1, 11, 18, 22 and ( $C_s$ ) 1, 8, 18, 22- non-peripherally ( $\alpha$ ) tetrasubstituted Pc complexes. When substitution is at the 4-position, isomers of peripherally ( $\beta$ ) tetrasubstituted complexes are obtained (( $C_{4h}$ ) 2, 9, 16, 23-, ( $D_{2h}$ ) 2, 10, 16, 24-, ( $C_{2v}$ ) 2, 9, 17, 24- and ( $C_s$ ) 2, 9, 16, 24-). In this thesis Pcs that are non-peripherally ( $\alpha$ ) and peripherally ( $\beta$ ) substituted with OH or alkyl groups are reported, hence the general synthesis for these Pcs are presented.



**Scheme 1.1: General phthalocyanine synthesis.** M = metal, MX = metal salt, DBN = 1,5-Diazabicyclo[4.3.0]non-5-ene, ROH = alcohol.

### 1.1.1.1. Peripherally tetrasubstituted phthalocyanine

**Scheme 1.2** shows a general synthetic route of peripherally tetrasubstituted phthalocyanine (**6**) involving the nucleophilic aromatic substitution of 4-nitrophthalonitrile (**4**). The phthalonitrile derivative (**4**) is commercially available or can be easily prepared following literature method [27]. Nucleophilic aromatic substitution of 4-nitrophthalonitrile (**4**) results in the substituted phthalonitrile (**5**).

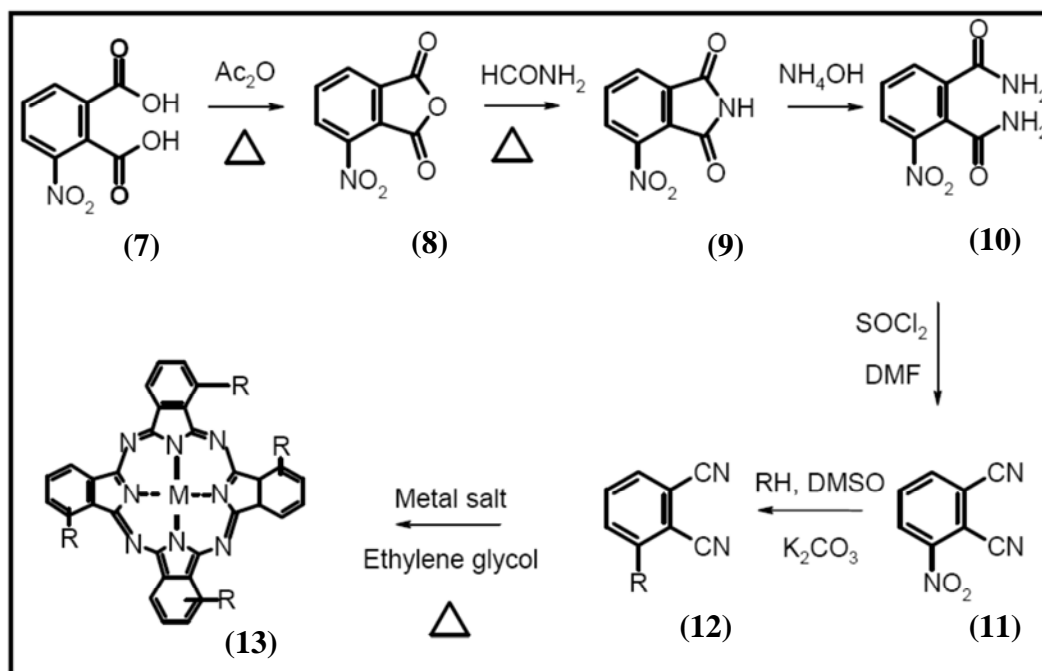


**Scheme 1.2: Synthesis of a peripherally tetrasubstituted phthalocyanine. R= any functional group.**

A strong nucleophile can effectively displace the good leaving nitro group (**4**) from its activated aromatic substituent in the presence of a base [28] and dry polar aprotic solvents such as dimethyl formamide (DMF) or dimethylsulfoxide (DMSO). Reaction of the substituted phthalonitrile (**5**) with a metal salt in the presence of ethylene glycol, through a metal assisted cyclotetramerisation process, gives the peripherally tetrasubstituted phthalocyanine (**6**).

### 1.1.1.2. Non-Peripherally tetrasubstituted phthalocyanine

The synthesis of non-peripherally tetrasubstituted phthalocyanines is similar to that of their peripherally substituted counterparts except for the initial steps, as outlined in **Scheme 1.3**.

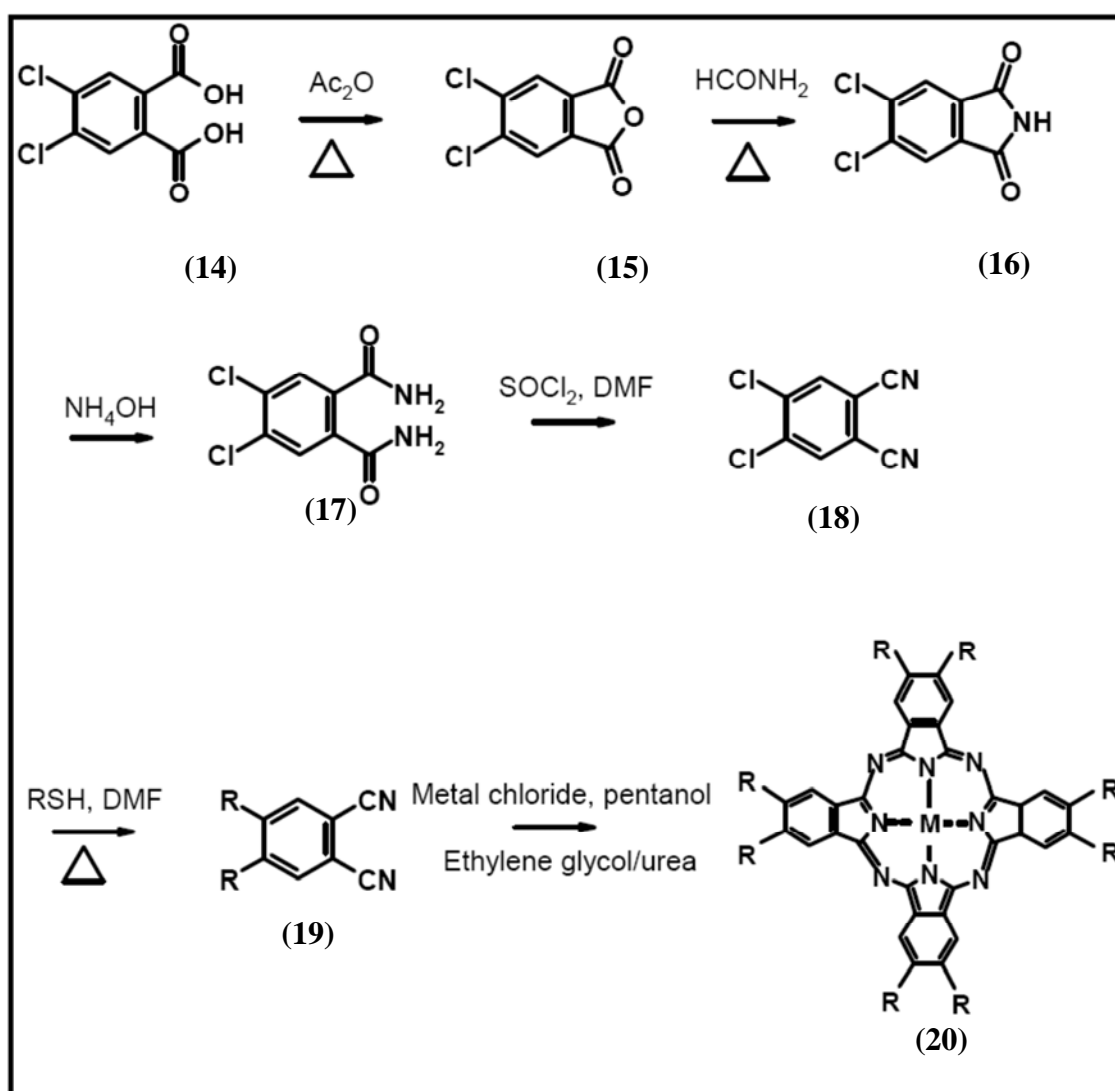


**Scheme 1.3: Synthesis of non-peripherally tetrasubstituted phthalocyanine. (R = any substituent,  $\text{Ac}_2\text{O}$  = Acetic anhydride).**

Non-peripherally tetrasubstituted phthalocyanine synthesis involves the nucleophilic aromatic substitution of 3-nitrophthalonitrile (11). The phthalonitrile derivative is commercially available or maybe synthesised following the synthetic route in **Scheme 1.3** [29] and maybe transformed into substituted phthalonitrile (12) as mentioned for the peripherally tetrasubstituted phthalocyanine. The non-peripherally substituted Pc (13) is then formed by cyclotetramerisation of substituted phthalonitrile (12) as explained above.

### 1.1.1.3. Peripherally octasubstituted phthalocyanine

**Scheme 1.4** shows the synthetic method for octasubstituted Pc. For the preparation of 4,5-disubstituted phthalonitriles (**18**), 1, 2-dichlorophthalic acid (**14**) is commonly used as the precursor [30]. Nucleophilic aromatic substitution of 4,5-dichlorophthalonitrile (**18**) with any functional group (R), results in the substituted phthalonitrile (**19**). The final step involves reacting the 4,5-disubstituted phthalonitrile (**19**) with a metal salt in the presence of 1,8-diazabicyclo-[5.4.0]-undec-7-ene (DBU) and solvent (or urea) to yield the peripherally octasubstituted MPc (**20**), **Scheme 1.4**.

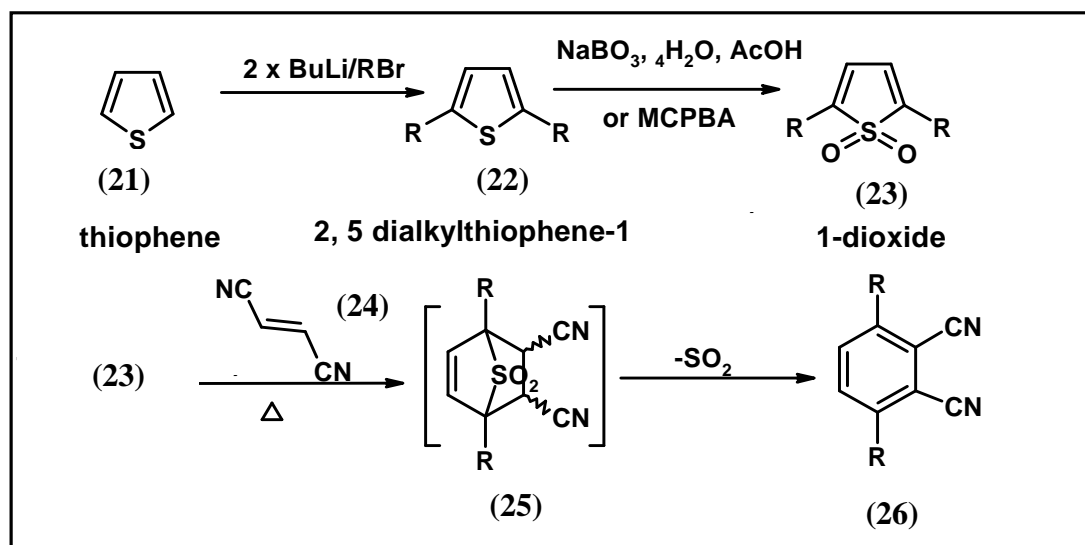


**Scheme 1.4:** Synthesis of tetra and octa substituted  $\beta$ -phthalocyanines. (R = any functional group,  $\text{Ac}_2\text{O}$  = Acetic anhydride).

### 1.1.1.4. Non-peripherally octasubstituted phthalocyanine

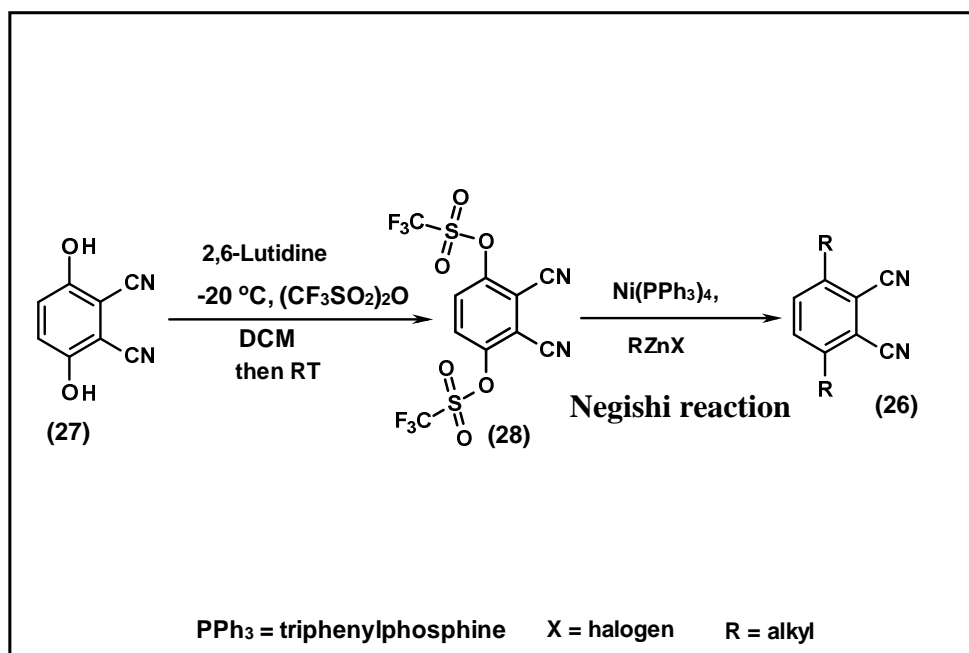
In this thesis a Pc possessing C-C bonds at the non-peripheral position is developed, hence the general synthetic procedure of these Pcs is presented.

For the synthesis of 3,6-disubstituted phthalonitriles containing C-C bonds (alkyl substituted), [4+2] cycloaddition reactions have been successfully developed [31, 32]. Fumaronitrile (**24**) is used as dienophile and heterocyclic systems (five membered) such as thiophene (**21**) or furan can be used as a source of diene (**Scheme 1.5**). To prepare 3, 6-disubstituted phthalonitrile (**26**), (**21**) is first reacted with BuLi (butyllithium) /RBr to form 2, 5-dialkylthiophene-1 (**22**). Oxidation of the thiophene ring (**22**) to the 1,1-dioxide (**23**) is required to break the aromaticity of this system which can then undergo Diels-Alder reaction with fumaronitrile (**24**). Compound (**23**) is known to form unstable cycloaddition adduct (**25**) with (**24**). Thermally or by treating with a non-nucleophilic base, (**25**) will self aromatize to yield (**26**).



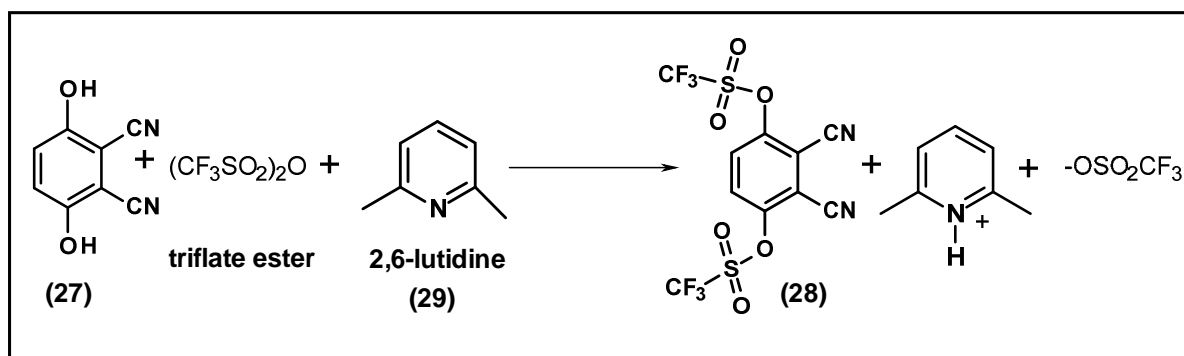
**Scheme 1.5: Preparation of 3, 6-dialkylphthalonitrile. (R = alkyl, MCPBA = m-chloroperoxy-Ibenzoic acid, RBr = alkyl bromide).**

Another synthetic route of 3,6-dialkylphthalonitrile (**26**) involves the use of 3,6-bis(trifluoromethanesulfonyloxy)phthalonitrile (**28**) as a precursor (**Scheme 1.6**). This method was developed by Cook's group [33, 34].



**Scheme 1.6:** Cross coupling reactions of aryl triflate. (DCM = dichloromethane, and RT = room temperature and  $\text{CF}_3\text{SO}_2)_2\text{O}$  = triflate ester.

Compound (28) is synthesised by reacting 2,3-dicyanohydroquinone (27) with  $(\text{CF}_3\text{SO}_2)_2\text{O}$ , using 2,6-lutidine as a base and a solvent, expanded in **Scheme 1.6**. For the synthesis of 3,6-dialkylphthalonitrile (26) a Suzuki [35] coupling is used.



**Scheme 1.7:** Formation of an aryl triflate (28).

The role of the 2,6-lutidine (29) (a base) is to neutralize triflic acid generated by the reaction of (27) with triflate ester, **Scheme 1.7**.

A Negishi coupling is a cross coupling reaction between an organometallic reagent  $\text{RMX}$  ( $\text{M}=\text{Sn}, \text{Zn}, \text{Mg}$  and  $\text{X} = \text{halogen}$  for example) and a triflate (28) in **Scheme 1.6**, and is one of the most important methods for forming a new carbon-carbon  $\sigma$  bond. Negishi and co-workers [36] developed the first transition-metal catalysed cross-coupling reaction between

an aryl halide and an organozinc reagent. However Cook *et al.* used the triflate method, which will be employed in this thesis (**Scheme 1.6**).

Different functional groups can be incorporated into the organozincs used by Negishi (RZnX) [37, 38]. Due to the low-lying p orbitals of zinc, organozincs can undergo smooth transmetallations with a variety of transition metal salts or complexes (**Scheme 1.6**).

#### Sub Aims of thesis:

The aim of this thesis is to synthesise tetra- and octa- substituted nickel phthalocyanine complexes. The Negishi method (**Scheme 1.6**) will be employed to synthesise phthalonitrile for NiPc containing C-C bonds. The NiPc derivatives which will be synthesised in this work are shown in **Figure 1.3** as complexes  $\beta$ -NiPc(OH)<sub>4</sub>,  $\alpha$ -NiPc(OH)<sub>4</sub>,  $\alpha$ -NiPc(OH)<sub>8</sub>,  $\alpha$ -NiPc(C<sub>10</sub>H<sub>21</sub>)<sub>8</sub> and  $\beta$ -NiPc(NH<sub>2</sub>)<sub>4</sub>.

**Table 1.1**, lists a selection of known MPc(OH) complexes [39-42]. As shown, only  $\beta$ -NiPc(OH)<sub>4</sub> complexes is known. OH functional groups are very important for applications such as photodynamic therapy (PDT) where OH increases potency [2], hence synthesis of a wide range of OH substituted Pc's with multiple points of OH substitution is of importance, even though the Ni atom is not good for PDT. The simplicity of the OH substituent also allows for the ease of modelling of the substituted Pc. Ni is chosen because NiPc derivatives readily form O-Ni-O oxo bridges which have proven to be good in electrocatalysis, which will be discussed later. The long alkyl chain C<sub>10</sub>H<sub>21</sub> was chosen for comparison purposes in electrocatalysis compared to OH ligands.  $\beta$ -NiPc(NH<sub>2</sub>)<sub>4</sub> is chosen because NH<sub>2</sub> groups can be linked to functionalized carbon nanotubes (CNT) and quantum dots (QDs) to form amide bonds.

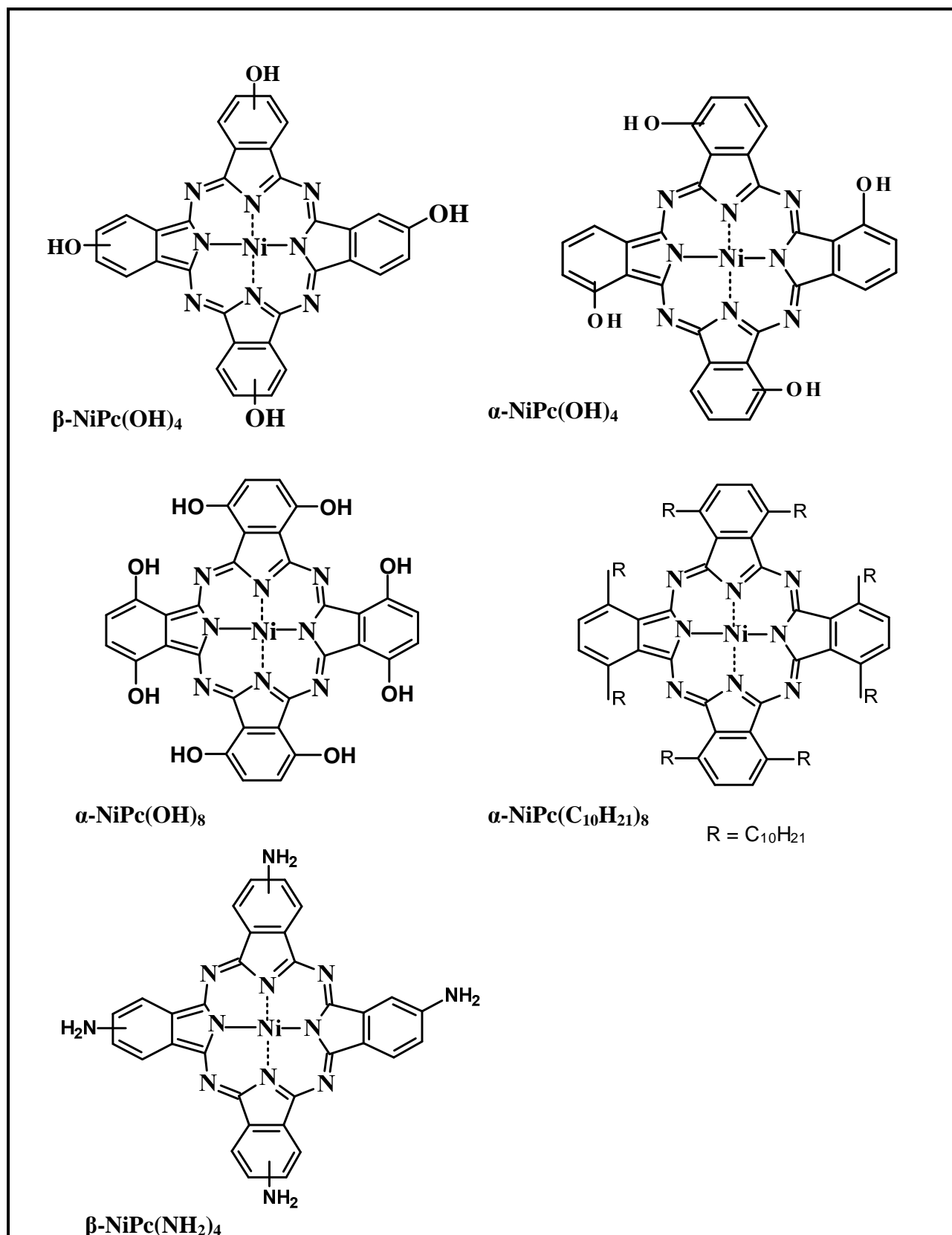


Figure 1.3: The NiPc derivatives synthesised in this work

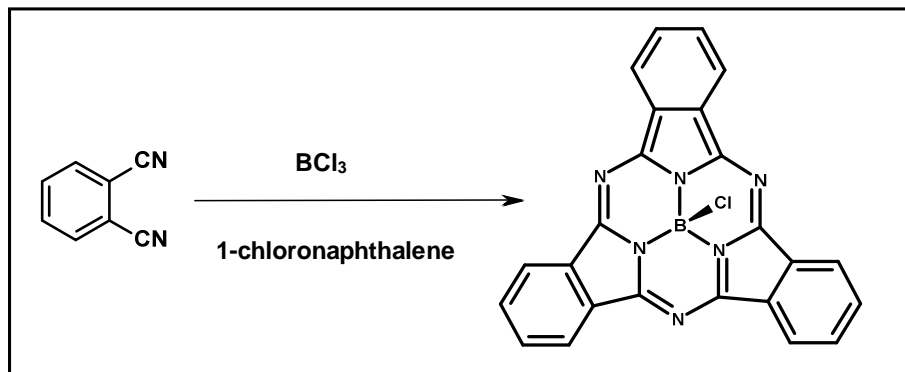


Table 1.1: A selection of all known hydroxy phthalocyanine complexes

Phthalocyanine	References
$\beta$ -NiPc(OH) <sub>4</sub>	[39]
$\beta$ -Fe(Cl)Pc(OH) <sub>4</sub>	[40]
$\alpha$ -Fe(Cl)Pc(OH) <sub>4</sub>	[40]
$\beta$ -Al(Cl)Pc(OH) <sub>4</sub>	[41]
$\beta$ -In(Cl)Pc(OH) <sub>4</sub>	[41]
$\beta$ -Cr(Cl)Pc(OH) <sub>4</sub>	[41]
$\beta$ -Sn(Cl)Pc(OH) <sub>4</sub>	[41]
$\beta$ -Hf(Cl)Pc(OH) <sub>4</sub>	[41]
$\alpha$ -Al(OH)Pc(OH) <sub>4</sub>	[41]
$\alpha$ -Cr(OH)Pc(OH) <sub>4</sub>	[41]
$\alpha$ -Ga(OH)Pc(OH) <sub>4</sub>	[41]
$\beta$ -ZnPc(OH) <sub>8</sub>	[42]

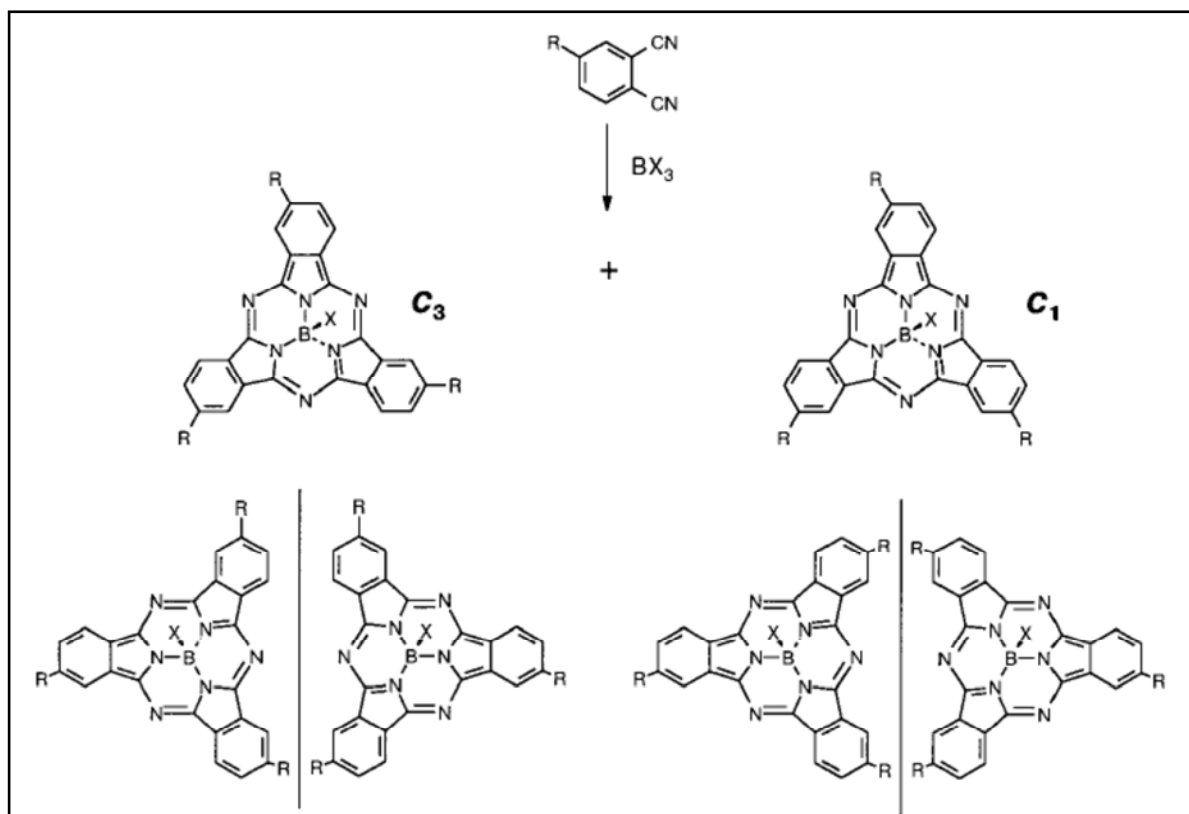
**1.1.2. Syntheses of Subphthalocyanines (SubPcs) and Subnaphthalocyanines (SubNPcs)**

Subphthalocyanines are synthesised in good yields by the cyclotrimerization reaction of phthalonitrile precursors in the presence of boron derivative (typically a boron trihalide), **Scheme 1.8** [8].



**Scheme 1.8: Preparation of unsubstituted subphthalocyanine** [8]

SubPcs are obtained as a mixture of  $C_1$  and  $C_3$  constitutional isomers, when the starting material (substituted dinitrile) does not belong to the  $C_{2v}$  symmetry group [43]. Each of these isomers is in turn a racemic mixture of enantiomers. Inherent molecular chirality, which was suggested by Torres and Claessens [44, 45], is obtained when SubPc molecule is asymmetrically substituted. From reactions of asymmetrically substituted phthalonitriles, such as 4-iodophthalonitrile [45] and 3-nitro-5-*tert*-butylphthalonitrile [46], two structural isomers having  $C_3$  and  $C_1$  molecular symmetries with respect to the arrangement of substituents are obtained, and each structural isomer is inherently chiral due to the absence of any mirror plane in their structures. **Scheme 1.9** shows general synthetic procedure of asymmetrically substituted subphthalocyanines and distribution of products.



**Scheme 1.9: Subphthalocyanine regio- and enantiomers (R = can be any functional group)[8].**

Preparative high performance liquid chromatography (HPLC) was first used by Hanack and coworkers to resolve the  $C_1$  and  $C_3$  enantiomers [43]. Very few  $C_3$  organic compounds have been obtained in optically active forms. The resolution of aromatic chiral  $C_3$  molecules has been described only in the case of a subphthalocyanine. Torres and coworkers used column chromatography on silica gel to separate constitutional isomers of a series of 3-substituted [44] and 4-substituted [45] subphthalocyanines.

#### **Sub aim of thesis:**

To synthesise, separate and characterise novel chiral 1,2-subnaphthalocyanine (SubNPc) having  $C_3$  and  $C_1$  molecular symmetries relative to the arrangement of the fused benzene rings. **Table 1.2** and **Figure 1.4** lists a selection of known SubNPcs and SubPcs [46-56], no chiral SubNPcs derivatives haven been separated hence the aim of this thesis.

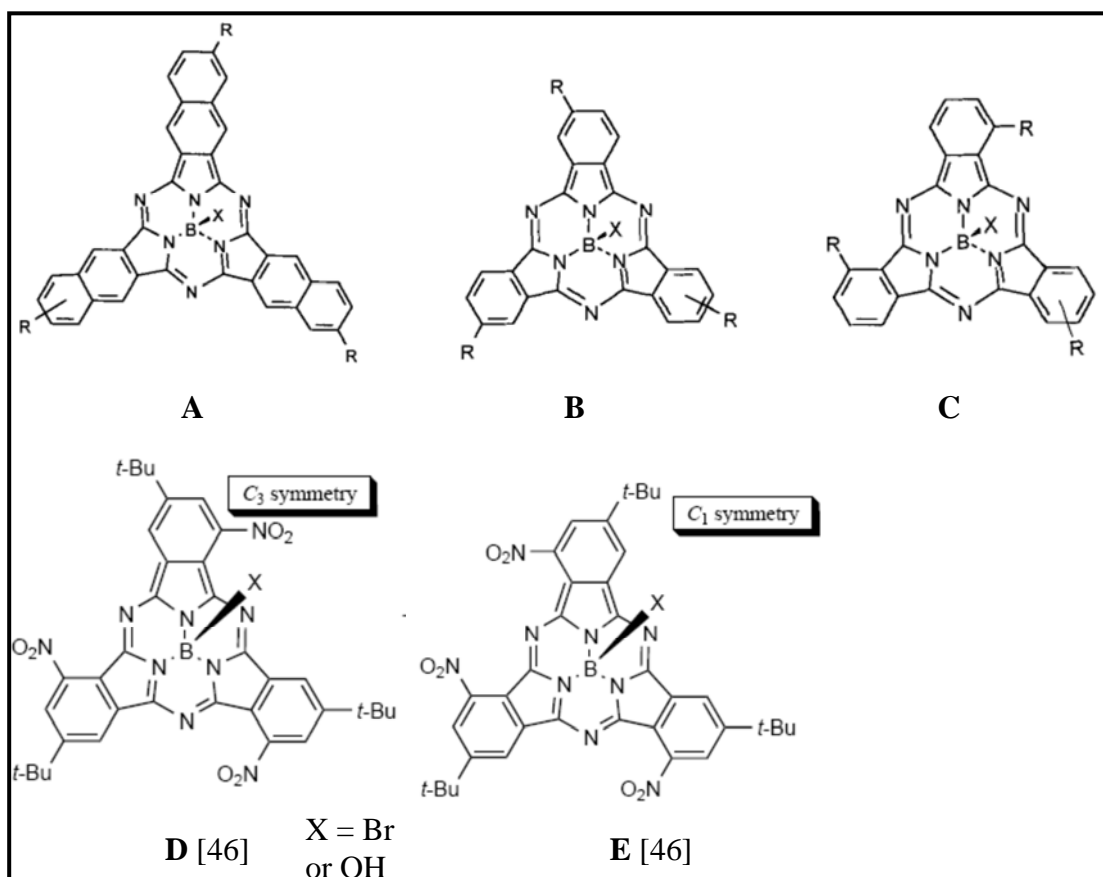


Figure 1.4: Selection of SubPcs which have been reported in literature

**Table 1.2: List of known Subnaphthalocyanines and chiral Subphthalocyanine, see Figure 1.4.**

Subnaphthalocyanine	R : peripheral	X : axial	Reference
A	H	Ph	[47, 48]
A	tetr-butyl	Ph	[47, 48]
A	H	Cl	[49, 50]
A	H	Br	[51]
<b>Chiral SubPcs</b>			
B	tert-butyl	Ph	[48]
B	tert-butyl	Cl	[48]
B	tert-butyl	Br	[52]
B	NO <sub>2</sub>	Cl	[48]
B	NO <sub>2</sub>	Br	[53]
B	I	Cl	[48]
B	SO <sub>2</sub> Cl	Br	[54]
B	SC <sub>8</sub> H <sub>17</sub>	Cl	[55]
B	SO <sub>2</sub> C <sub>8</sub> H <sub>17</sub>	Cl	[56]

---

C	I	Cl	[48]
C	SC <sub>3</sub> H <sub>7</sub>	Cl	[44]
C	SO <sub>2</sub> C <sub>3</sub> H <sub>7</sub>	Cl	[44]
C	NO <sub>2</sub>	Cl	[48]

### 1.1.3. Spectroscopic properties of phthalocyanines

#### 1.1.3.1. UV-vis spectra

The electronic structure of MPc is known to have a strong effect on its electrocatalytic activity. **Figure 1.5** shows ultraviolet/visible (UV/Vis) spectra that are typical of unmetallated (**i**) and metallated (**ii**) Pc. An intense and isolated absorption band is found near 700 nm (systematically labelled as the Q band). The next absorption bands are much less intense and lie at considerably higher energies near 340 nm (systematically labelled the B bands). The Q band and the B bands occur due to  $\pi - \pi^*$  transitions (see **Figure 1.6**). The Q band arises from  $a_{1u} \longrightarrow e_g$  transition and the B bands arise from  $a_{2u} \longrightarrow e_g$  and  $b_{2u} \longrightarrow e_g$  transitions. The B band is broad compared to the Q band due to the superimposition of the B<sub>1</sub> and B<sub>2</sub> bands. It is known that the introduction of a metal ion inside the cavity will generate a slight blue shift in the Q band. This occurs because the introduction of a metal ion reduces the electronic density of the phthalocyanine ring system. It has been demonstrated that the more electronegative the metal ion is, the greater the blue shift. Some compounds which have their metal ions outside the cavity, for example PbPcs, often show a red shifted Q band.

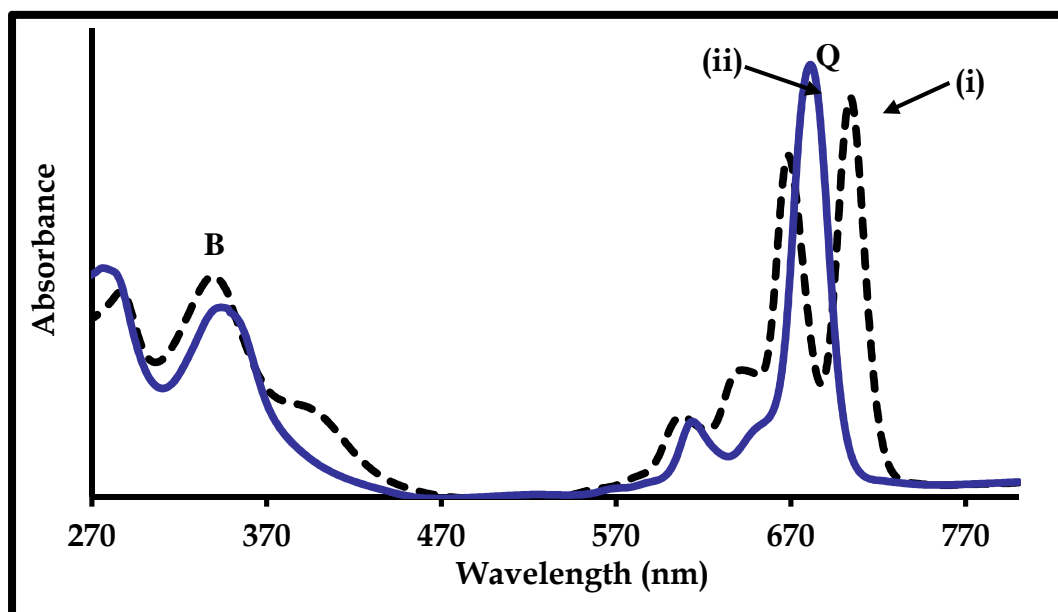


**Figure 1.5:** Absorption spectra of unmetallated phthalocyanine (**i**) and metallated (**ii**).

An unmetallated Pc is of lower,  $D_{2h}$ , symmetry while a metallated Pc is of higher,  $D_{4h}$ , symmetry. Due to the lower symmetry of unmetallated phthalocyanine, the  $e_g$  energy levels are not degenerate, giving rise to a split Q band. The symmetry of the metallated

phthalocyanine causes the energy level to be degenerate, therefore the Q band is not split (**Figure 1.5**). Substitution on the benzene ring gives rise to a shift (bathochromic or hypsochromic shift depending on the type of substituent) of the Q-band relative to the unsubstituted Pc. Non-peripheral substitutions show greater shifts than peripheral substitution [57].

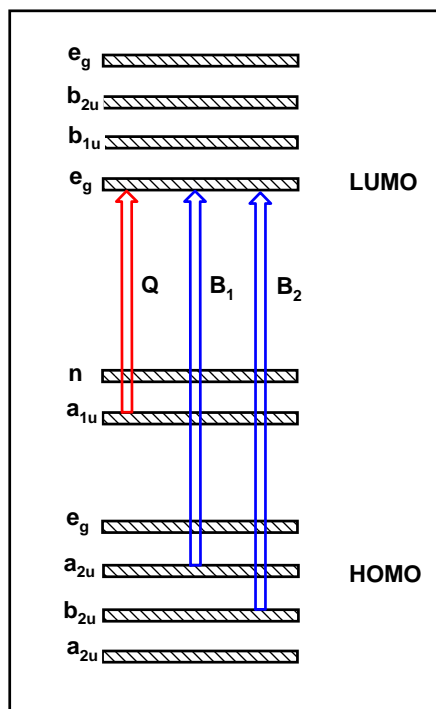


**Figure 1.6: Schematic representation of energy levels and origins of Q and B band.**

Theoretical interpretation of MPCs electronic spectra has been a subject of great interest for a long time [58-60]. In the past, calculations which made use of semi-empirical methods with questionable accuracy were used. Recently more accurate high level density functional theory (DFT) calculations have been used [61-63]. Global and local reactivity of MPC complexes involved in electrocatalytic processes have been predicted by use of DFT methods [64-66]. In this work, DFT calculations are carried out in order to understand the effect on the electron density due to substituents at the peripheral and nonperipheral positions of NiPcs, with the aim of explaining electrocatalytic activity. DFT calculations are also used in this thesis to describe the molecular structure, atomic charges, IR and Raman spectra of these NiPc complexes.



### 1.1.3.2. Raman spectra

Raman spectroscopy measures the scattering of radiation by the sample rather than the absorption process [67, 68]. Raman spectroscopy provides structural information about the molecules based on the vibrational energy bands. This technique exploits the Raman effect which is due to inelastic light scattering [67, 68].

An example of its use is in the study of the intermolecular interaction of copper phthalocyanine aggregates [69]. In CuPc films, CuPc molecules have been shown to pile up in a direction almost perpendicular to the molecular plane due to strong  $\pi$  electronic interactions between adjacent molecules [69]. Metallated phthalocyanine complexes may belong to a  $C_{4v}$  point group (in this case the metal atom is located above or below the molecular plane), or  $D_{4h}$  point group when the metal is on the plane.

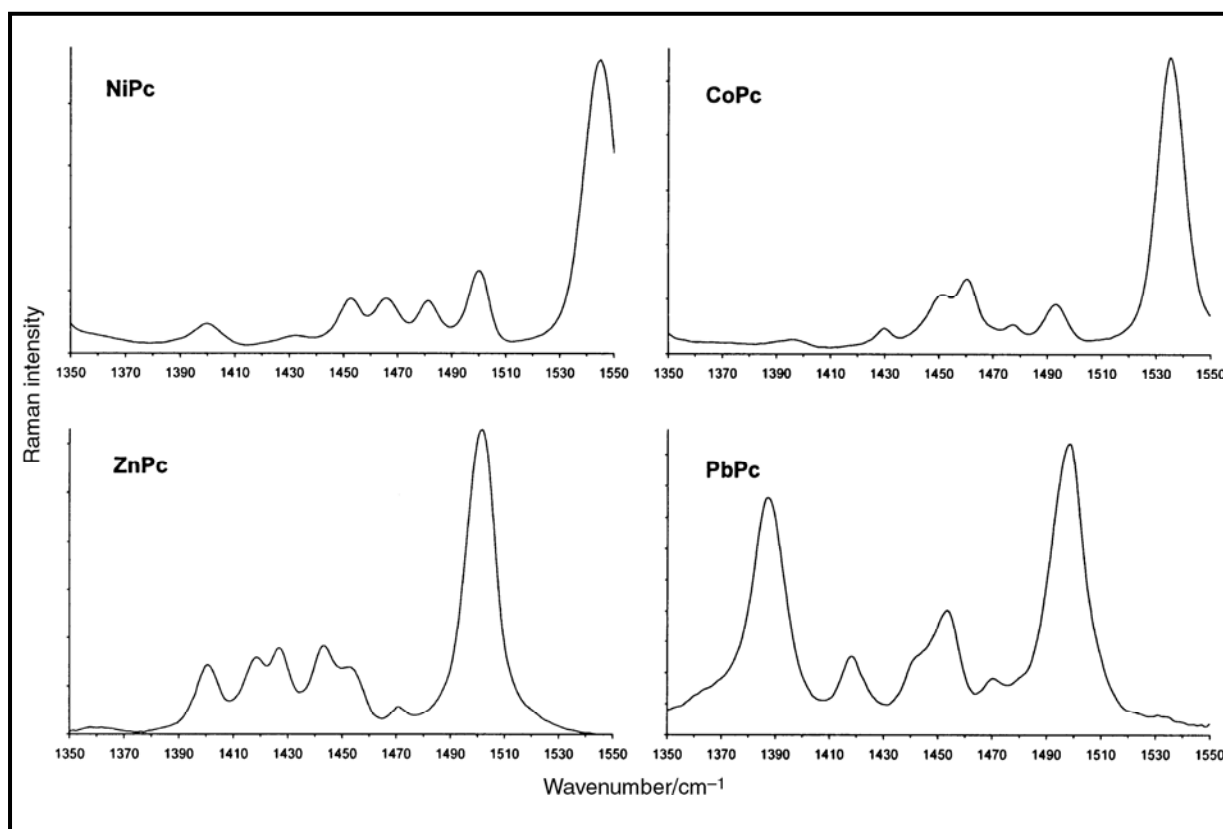


**Figure 1.7:** The 1350-1550  $\text{cm}^{-1}$  region of NiPc, CoPc, ZnPc and PbPc illustrating the Raman band that exhibit unique patterns for each phthalocyanine [71].

One band in Raman spectrum has been identified as highly sensitive to the metal ion present [70]. **Figure 1.7** [71] shows that this is the most intense band near  $1500 \text{ cm}^{-1}$  in the Raman

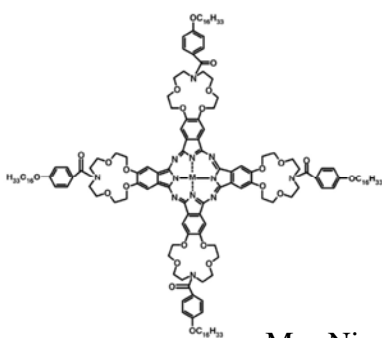
spectra of MPc compounds. This band has been found to shift by up to  $50\text{ cm}^{-1}$  depending on the metal present (see **Figure 1.7**). The major feature of this vibration is the displacements of the C-N-C bridge bonds of the phthalocyanine macrocycle.

For the purpose of understanding the effect of substitution on the spectroscopic characteristics of phthalocyanines, DFT and TD-DFT calculations can be performed to comparatively describe their molecular structures using infrared (IR) and Raman spectra [72-75].

**Sub aim of thesis:**

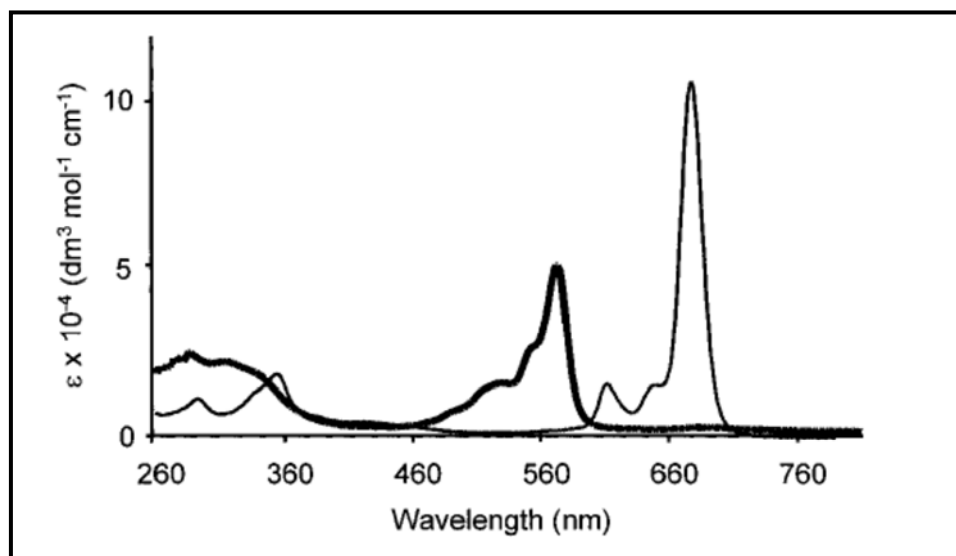
In this work DFT and TD-DFT are used to study the effect of number of hydroxyl substituents on the C-N-C Raman stretch of NiPcs. **Table 1.3** [70, 71, 76] shows the Raman spectral data of known NiPc C-N-C stretch. Even though these studies have been reported on NiPc derivatives, **Table 1.3**, the effect of number of substituents has not been explored and is addressed by this work.

Table 1.3: Raman and spectral data of known NiPcs

Phthalocyanine	C-N-C(Raman stretch) /cm <sup>-1</sup>	Reference
NiPc	1545	[71]
$\beta$ -NiPc(S(CH <sub>2</sub> ) <sub>5</sub> CH <sub>3</sub> ) <sub>8</sub>	1576	[70]
$\beta$ -NiPc(S(CH <sub>2</sub> ) <sub>11</sub> CH <sub>3</sub> ) <sub>8</sub>	1576	[70]
$\beta$ -NiPc(S(CH <sub>2</sub> CH <sub>2</sub> O) <sub>3</sub> CH <sub>3</sub> ) <sub>8</sub>	1576	[70]
$\beta$ -NiPc(SCH(CH <sub>2</sub> OC <sub>12</sub> H <sub>25</sub> ) <sub>2</sub> ) <sub>8</sub>	1576	[70]
 <p>M = Ni</p>	1548	[76]

### 1.1.4. Spectroscopic properties of subphthalocyanines

UV-vis spectra of subphthalocyanines (SubPcs) are comparable to the ones obtained for Pcs in that they both show a Q-band and a Soret (B) band as in other aza aromatic macrocyclic compounds. The Q band (560 nm) and Soret band (660 nm) of SubPcs tend to shift to shorter wavelength with respect to the Pcs as a consequence of the decrease of the  $\pi$ -conjugation system, **Figure 1.8**.



**Figure 1.8:** UV-vis spectrum of subphthalocyanine (thick line) compared to the one of nickel phthalocyanine (thin line) both in chloroform [8].

The absorption coefficients of both the Q-band and Soret band also decrease on going from Pcs to SubPcs. The non-planer structure of SubPcs compared to Pcs may contribute to the small Q band observed for SubPcs [51, 77]. Peripheral donor substituents tend to shift the Q-band of SubPcs toward longer wavelengths, while axial substituents have no or only a very small effect on the position of the band.

To complement the UV-vis spectroscopy, magnetic circular dichroism (MCD) is usually employed to retrieve valuable information about the nature of UV-Vis transitions such as position (energy) and number of transitions. MCD will be employed in this work to characterise SubPc complexes hence the basis of MCD are discussed briefly below.

MCD peaks in the Q-band region are approximately at the same position as the absorption peaks. The  $Q_{0-0}$  band corresponds to a transition to an orbitally degenerate state that could only be fitted with a Faraday  $\mathcal{A}$  term in both Pcs and SubPcs. The Soret region contains the Faraday  $\mathcal{B}$  terms (in both Pcs and SubPcs) [51, 77, 78]. MCD is based on the wavelength dependent differential absorption of left (lcp) and right (rcp) circularly polarised light in the presence of a magnetic field to form excited electronic states. MCD intensity is dependent on the coupling of the ground and excited states through the electric (m) and magnetic dipole moments ( $\mu$ ), while the intensity in the UV-vis absorption is dominated by the electric dipole moment (m) [79, 80]. The MCD intensity is given in terms of **Equation 1.1**:

$$\frac{\Delta\mathcal{A}_{l-r}}{E} = 152.5\mathcal{B}cl \left[ \mathcal{A}_1 \left( \frac{df}{dE} \right) + \left( \mathcal{B}_0 + \frac{C_0}{kT} \right) f \right] \quad 1.1$$

where  $\mathcal{B}$  is the field strength (in Tesla),  $cl$  is the product of the concentration in  $\text{mol L}^{-1}$  and path length in  $\text{cm}^{-1}$ ,  $E$  represents the energy coordinate in  $\text{cm}^{-1}$ ,  $f$  refers to the normalized band shape function (Gaussian shaped curve). Analysis of the MCD spectra is thus a function of an estimation of the magnitudes of the three Faraday terms  $\mathcal{A}_1$ ,  $\mathcal{B}_0$  and  $C_0$ , see **Figure 1.9**.

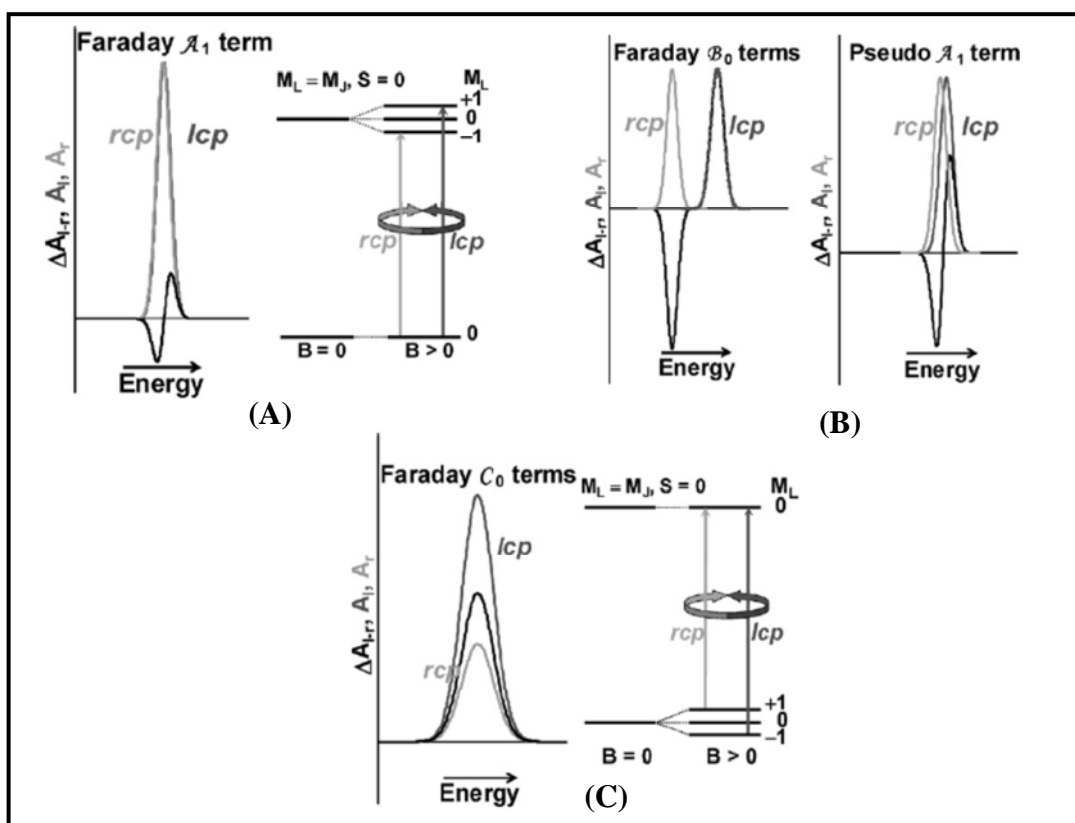


**Figure 1.9:** The three Faraday terms  $\mathcal{A}_1$ ,  $\mathcal{B}_0$  and  $C_0$  [80]

The  $\mathcal{A}_1$  term intensity is due to the relative magnitudes of the combined orbital ( $L_z$ ) and spin ( $S_z$ ) angular momenta of electrons within the ground excited states, **Figure 1.9 (A)**[80]. The  $\mathcal{B}_0$  term is due to second order effects based on the field induced mixing of the zero-field states via magnetic dipole transition moments, **Figure 1.9 (B)** [80]. Pseudo- $\mathcal{A}$  term often occur as a result of small splitting of the x/y-polarised transitions. The  $C_0$  term is due to the Boltzmann population distribution across a degenerate ground state and as a result shows a strong  $1/kT$  temperature dependence, **Figure 1.9 (C)** [80].

For chiral SubPcs CD spectra is a useful tool to differentiate between the enantiomers (**Figure 1.10**). Absorption of a photon by dissymmetric molecules with a chiral center is due to both magnetic and electric dipoles, because there is a helical redistribution of electronic charge [80]. Enantiomers preferably absorb left (lcp) and right (rcp) circularly polarised light based on the handedness of the helical electron redistribution.

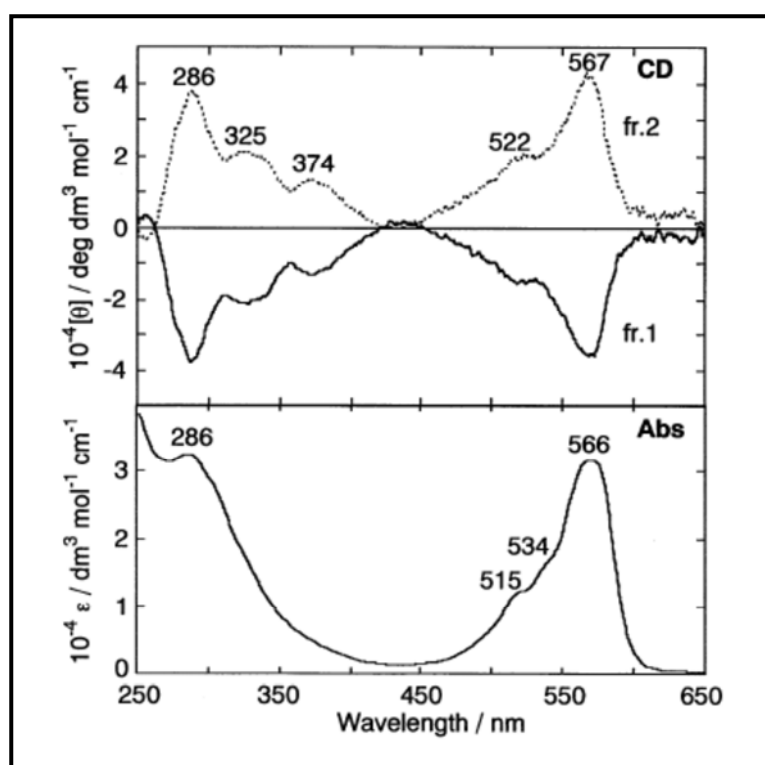


**Figure 1.10: Electronic (bottom) and circular dichroism (top) spectra of subPc in chloroform** [46].

This inherent chirality of the asymmetrically substituted SubPc can be regarded as a type of “bowl chirality” [81], which has recently been of intense study for fullerenes [82] and carbon

nanotubes [83], since molecules containing three-dimensional chiral  $\pi$ -surfaces can provide a chiral three-dimensional space for chiral recognition and asymmetric catalytic reactions. Although the use of chiral SubPcs towards these applications has been anticipated, the chirality of SubPcs is still at an early stage of its chemistry due to a lack of general information on a relationship between absolute molecular structure, signs and intensities of their CD spectra, hence in this work the MCD spectra of chiral SubNPs are studied.

### 1.1.5. Electrode modification and characterisation

#### 1.1.5.1. Modification methods

Over the past several decades, substantial interest in the field of electrochemistry has been focused on the development of modified electrodes [84-90]. The modification of carbon electrodes with macromolecules which act as electrocatalysts is currently an area commanding wide attention in electrochemistry. Modification of the electrode surface can alter the reactivity of the surface [91], and can offer extensive control over heterogeneous kinetics and the molecular recognition processes. The resulting electrodes are termed chemically modified electrode (CME).

Various methods can be used to modify electrodes, these include covalent bonding [92, 93], composite method [94, 95], dip dry [96-100], drop dry [96], self assembled monolayer (SAM) and electropolymerisation [84, 85-88]. In this work electropolymerisation, dip dry and drop dry methods are used to modify glassy carbon (GCE), ordinary pyrolytic graphite (OPGE) and Au electrodes. Drop dry method involves dropping of a known volume of Pc solution on to the electrode surface and rinsing off after known time interval. The Pc strongly adsorbs on to the electrode material and the bulk of the material is held by  $\pi$ - $\pi$  interaction between the  $N_4$  macrocycles [101]. Dip dry involves dipping the electrode in the Pc solution and allowing spontaneous adsorption to occur. Electropolymerisation involves repetitive oxidative or reductive cycling of suitable MPc monomer process resulting in the coating of the polymeric MPc film on the electrode.

GCE is the most commonly used type of carbon electrode. It is made up of an amorphous form of carbon, which is denser than natural graphite. GCE (**Figure 1.11 A**) has an unknown composition, is non-homogenous, hard and resistant to chemical attack and thus more

mechanically durable. OPGE (**Figure 1.11 B**) is made up of ordered sheets of hexagonally bonded carbon atoms arranged in the same direction. The OPGE basal plane surface is non ionic, hydrophobic, slightly denser than natural graphite, very reproducible and rich in  $\pi$ -electrons density. The high electron density makes strong chemisorption possible, and due to its porosity, electrode modifiers are easily adsorbed.

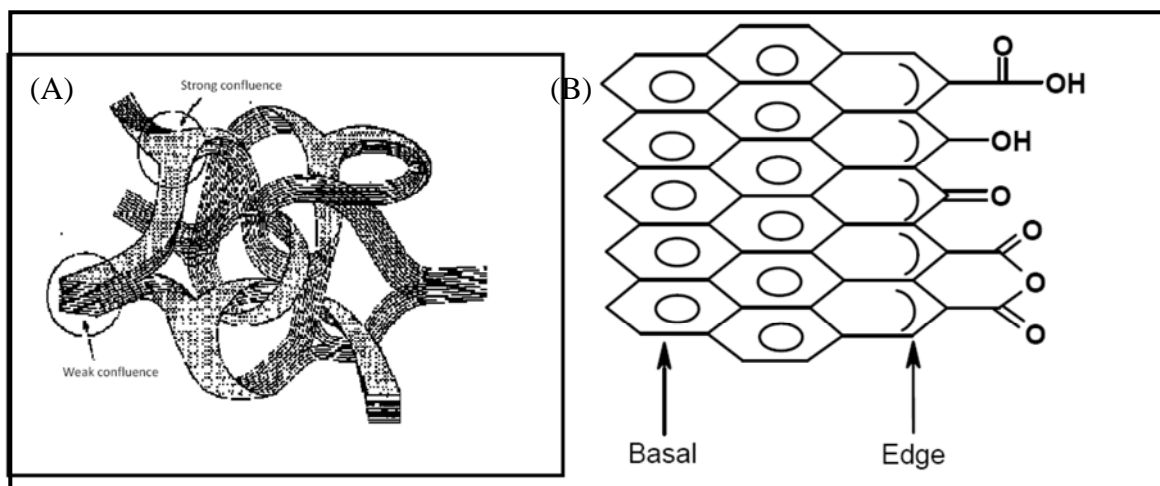


**Figure 1.11: Model of Glassy carbon electrode GCE (A) and Structure of planes of ordinary pyrolytic graphite (OPGE) (B).**

Gold electrodes are highly conductive and exhibit negligible background currents, high sensitivity and reproducibility. However, they are prone to corrosion and passivation.

### 1.1.5.2. Voltammetric characterization of modified electrodes

Cyclic voltammetry (CV) is the most widely used electrochemical technique in order to probe and study electron transfer mechanisms in reactions. The technique can also provide information about formal oxidation and reduction potentials, reversibility and kinetics of the system [102-106].

Differential pulse voltammetry (DPV) is a more sensitive technique compared to CV, because DPV technique rejects capacitive currents and the differential nature of faradaic current measurements [107]. Under optimal conditions DPV allows the detection of electroactive species at concentrations as low as  $10^{-8}$  M. Thus this technique is useful for voltammetric studies with species available in very limited supply. The peak-shaped output of DPV technique favors the resolution of voltammetric features having close  $E^{\circ}$  values.



### 1.1.5.3. Electrochemical Impedance Spectroscopy (EIS) characterization

Electrochemical impedance spectroscopy (EIS) is an important tool that is used to characterize or study materials and electrochemical processes. Materials whose external parameter or property has an influence on the conductivity of an electrochemical system can be studied by use of impedance spectroscopy [108]. EIS has vast applications, such as characterization of thin films, corrosion and kinetics studies.

Electrochemical impedance spectroscopy makes use of a three electrode set up, similar to a voltammetric analysis cell set up. In performing a basic EIS experiment, a general approach involves applying an electrical stimulus (voltage or current) to the electrode and observing the response (the resulting current or voltage). The overall electronic response is due to the microscopic process taking place throughout the cell. The spectroscopic processes include transport of electrons through the electronic conductor and the movement of charged particles towards the electrode through a concentration gradient. The flow rate of the charged particles depends on the ohmic resistance, electrolyte and on reaction rates at the electrode-electrolyte interfaces [109].

In EIS spectroscopy a general stimulus used to measure impedance is a single-frequency sinusoidal voltage signal. The response measured is the phase shift and amplitude, or real and imaginary parts, of the resulting current at that particular frequency using fast Fourier transform (FFT) analysis of the response. FFT analysis converts measurements in the time domain into the frequency domain. The results or response can be related to the physical and chemical properties of the material [108].

Impedance is a complex resistance and differs from ordinary Ohm's law resistance ( $R$ ) which is defined in terms of ratio between voltage ( $V$ ) and current ( $I$ ) (**Equation 1.2**).

$$R = \frac{V}{I} \quad 1.2$$

Impedance ( $Z$ ) is defined as a ratio of the alternating potential and the alternating-current signal:

$$Z(\omega) = \frac{E(t)}{I(t)} = \frac{E_m}{I_m} e^{j(\alpha-\beta)} = \frac{E_m}{I_m} e^{j\theta} = |Z| e^{j\theta} \quad 1.3$$

where

$$E(t) = E_m e^{j(\omega t + \alpha)} \quad 1.4$$

and

$$I(t) = I_m e^{j(\omega t + \beta)} \quad 1.5$$

with

$$j^2 = -1$$

where **Equations 1.4** and **1.5** represent a sinusoidal wave with amplitude of potential  $E_m$  and current  $I_m$  and an angular frequency  $\omega$  (where  $\omega = 2\pi f$  ( $f$  in Hz)),  $t$  is time and  $\alpha$  and  $\beta$  in radians are phase angles (**Figure 1.12 (a)**). From **Equation 1.3** it can be seen that impedance is dependent on frequency and has a phase angle  $\theta$ . This impedance (**Equation 1.3**) can be presented as a vector in the complex plane with modulus  $|Z| = E_m / I_m$  and argument  $\theta = \alpha - \beta$ . The resistance  $Z'$  (real part) and reactance  $Z''$  (the imaginary part) are the x and y axis of the complex plane (**Figure 1.12 (b)**) and **Equation 1.6**.

$$Z(\omega) = Z'(\omega) + jZ''(\omega) \quad 1.6$$

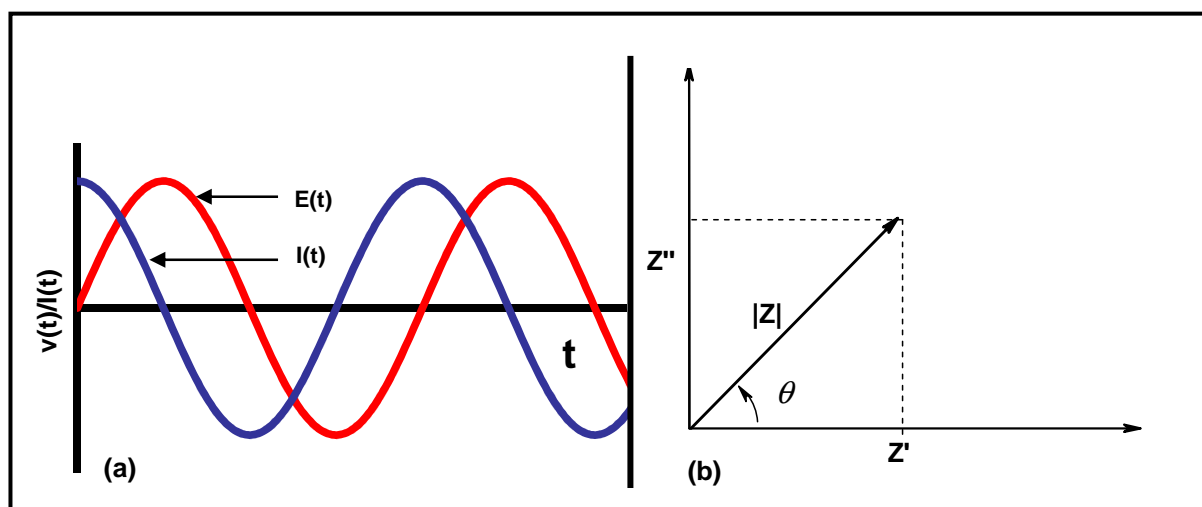


**Figure 1.12: (a) Applied sinusoidal voltage and resulting sinusoid current response (b) vector representation of real ( $Z'$ ) and imaginary ( $Z''$ ) part of impedance ( $Z$ ).**

EIS is becoming a popular analytical tool in materials research and development because simple electrical measurements can be made and the results can often be correlated with the material variables. These variables include: mass transport [110], rates of chemical reactions [111], corrosion [112], dielectric properties [113], and defects [114]. A flow diagram of a general characterization procedure using EIS is represented in **Figure 1.13**. Experimentally obtained impedance data for a given electrode-materials system may be analyzed by using

electrical equivalent circuits. These circuits (RC circuits) consist of simple elements such as resistance (R) and capacitance (C) which are connected to model the electrochemical processes [108, 109]. The resistance in the equivalent circuit represents the electrical conductivity of the electrolyte (bulk resistance) and the capacitance (double-layer capacitance) caused by the charge which is in excess at the electrode-electrolyte interface. The most commonly used equivalent circuit in EIS is the Ershler-Randles circuit [109]. This circuit is equivalent to an electrode to which a chemical reaction,  $O + ne^- \leftrightarrow R$  occurs (Figure 1.14).

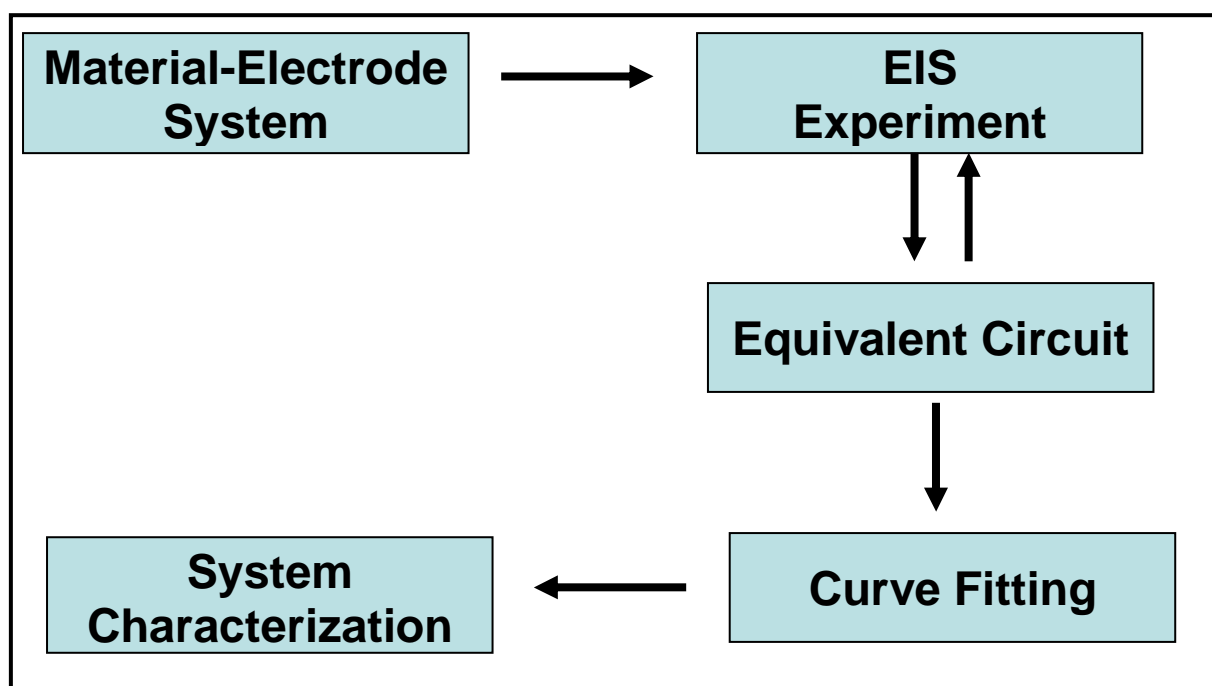


**Figure 1.13: Flow diagram for the measurement and characterization of a material-electrode system.**

In Randles equivalent circuit the electrolyte resistance ( $R_E$ ) is connected in series to the parallel connections of charge transfer resistance ( $R_{CT}$ ) and the double layer capacitance ( $C_d$ ). Randles equivalent circuit also takes into account the fact that the reaction rate might be controlled by the transport phenomenon of electroactive species [108], by having an extra component called Warburg impedance ( $Z_W$ ). This component is connected in series with the charge transfer resistance.

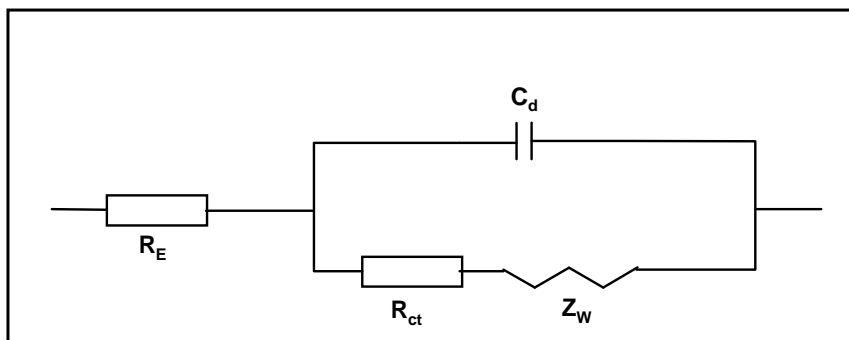


**Figure 1.14:** Ershler-Randles circuit for the electrochemical system with diffusion-limited behaviour.

Impedance data is graphically represented as a Nyquist and Bode plots. Nyquist plot, is a plot of the imaginary part ( $-Z''$ , y-axis) versus the real part ( $Z'$ , x-axis) of impedance (**Figure 1.15**). In this representation of impedance data there is no clear indication of the dependence of impedance and phase angle to frequency. For this reason Bode plots are used to monitor the real part of impedance and phase angle ( $\theta$ ) as a function of frequency. Bode data representation is a plot of the phase angle ( $\theta$ ) and the logarithm of impedance magnitude ( $\log Z$ ) versus the logarithm of the frequency ( $\log f$ ) (**Figure 1.16**).

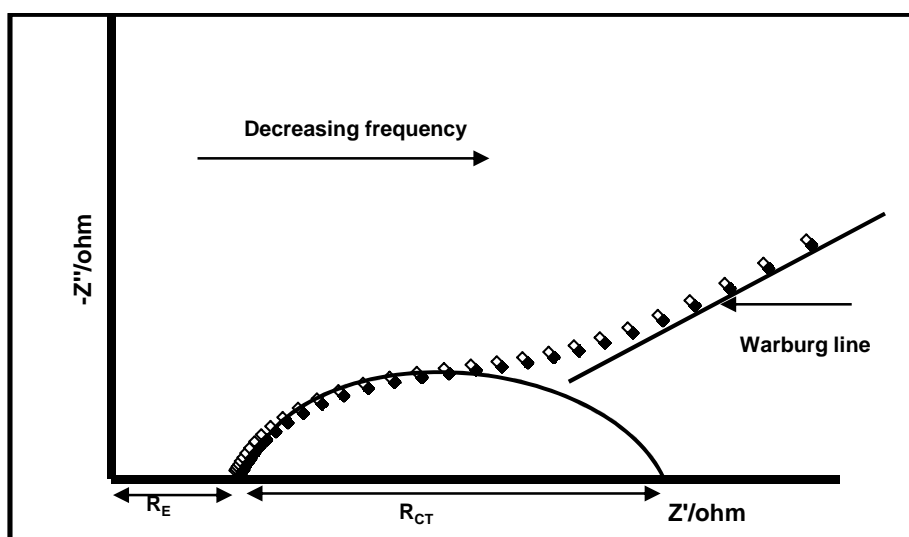


**Figure 1.15:** Nyquist plot for the electrochemical system with diffusion-limited behavior.

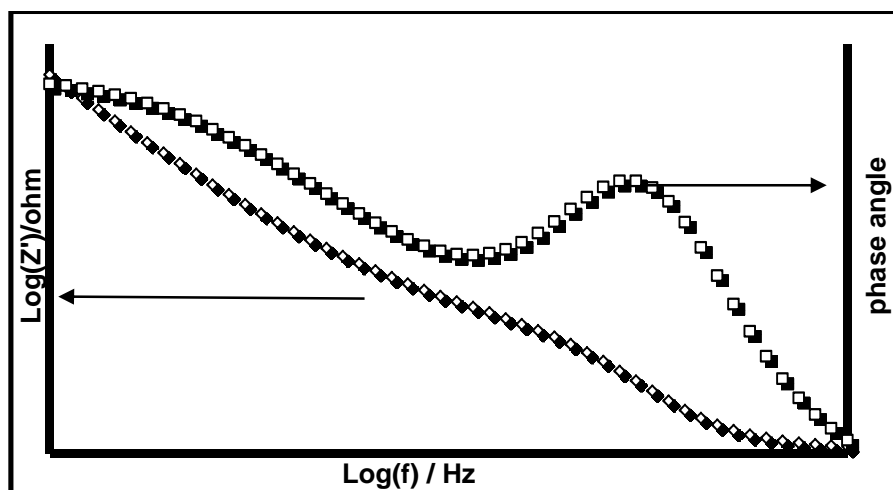


Figure 1.16: Bode plot for the Randles equivalent circuit with diffusion-limited behavior.

### 1.1.6. Electrocatalysis

#### 1.1.6.1. Definition

Electrocatalysis is defined as the increase in electron transfer rate of electrochemical reactions by using a catalyst. The catalyst acts as a mediator thus it takes part in the reaction but it is not consumed. MPc containing transitional metals are known to have good electrocatalytic properties. During electron transfer, MPcs show chemical and physical stability, this property makes them superior electrocatalysts compared to metal and metal oxides. MPcs have been used to modify electrodes such as glassy carbon and gold electrodes and therefore act as electron mediators during electrocatalysis. In general metal based redox processes mediate the catalytic reaction of MPcs [115-118], but ring based catalysis have been reported [119]. MPc containing metals such as nickel, cobalt, iron and manganese show enhanced electroactivity. Substituents on different positions of the Pc ring can also contribute to the overall electrocatalytic efficiency of the Pc, due to the effect they have on the electron density. In order that electrocatalysis should occur, initially there must be some interaction of the catalyst with the analyte, i.e. adsorption of the latter on the catalyst [120]. MPcs are known to achieve this effectively thereby facilitating electron transfer processes; as a consequence reactions would occur at reduced potentials with increased current densities [121, 122].

Cyclic voltammetry (CV) can be used to study electrocatalysis, by comparing the CV of an analyte on modified electrode with that on the bare electrode; higher catalytic current ( $I_p$ ) and lowering of overpotentials in CV of the former compared to the latter is an indication of electrocatalysis.

The redox couple of the electrocatalyst (O/R) mediates and improves electron transfer process between the electrode and the substrate, **Figure 1.17**.

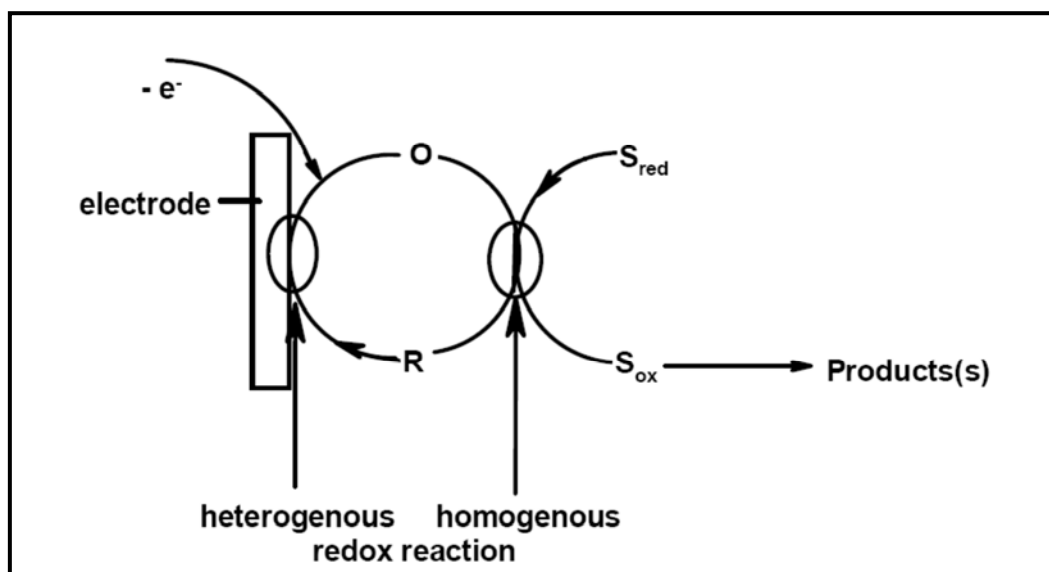


**Figure 1.17: A schematic representation of an electrocatalytic reaction. (S = substrate and O/R = redox couple).**

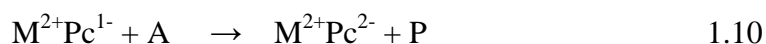
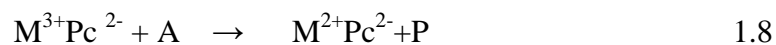
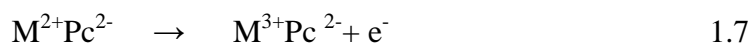
The electrochemical reaction undergone by the substrate will occur at a potential close to the O/R formal potential,  $E^\circ$ , of the electrocatalyst. The return peak of the O/R couple will not be observed because the oxidized species would have interacted with the substrate.

#### 1.1.6.2. General electrocatalytic behavior of Pcs

MPcs are also well known electrocatalysts for the oxidation of a variety of analytes including chlorophenols [123-125]. NiPc complexes have received less attention as electrocatalysts for degradation of chlorophenols, hence extending the range of Ni macrocyclic compounds for use in chlorophenol oxidation deserves attention. The interest in NiPc complexes is due to the formation of O-Ni-O bridges [116,117], for adsorbed NiPc complexes which results in increased sensitivity and reduced electrode fouling. Electrooxidation of chlorophenols on glassy carbon electrode (GCE) modified with nickel based cyclam, porphyrin and

tetrasulfonated phthalocyanine has been reported [124, 126, 127]. These electrodes were found to reduce fouling of electrodes (to different extents) towards the detection of chlorophenols. It has been observed that the nature of the ring substituents on the Ni macrocyclic complexes affects the stability of the modified electrodes [125].

The mechanism for electro oxidation using MPcs for catalysis is shown in **Equations 1.7 to 1.10**. **Equations 1.7 and 1.9** suggest that the metal or ring oxidation occurs first followed by a chemical process leading to oxidation of the analyte by the reactive oxidised catalyst, the latter is then regenerated. **Equations 1.7 and 1.8** are metal based oxidation reactions and **Equations 1.9 and 1.10** are ring based oxidation process.



A is the analyte and P is the product.

### 1.1.6.3. Chlorophenols

Rapid industrial and agricultural growth worldwide has led to increasing discharge of toxic substances such as chlorophenols as effluents. Chlorinated phenols such as 4-chlorophenol, 2,4-dichlorophenol, and pentachlorophenol (**Figure 1.18**) are classified as priority pollutants by both the European Union (EU) and the United State Environmental Protection Agency (USEPA) [128, 129]. Their toxicity depends on degree of chlorination and the positions of chlorine atoms relative to the hydroxyl group and it increases as the chlorine atom is further away from the hydroxyl group [130, 131]. Chlorophenol toxicity also depends on pH and the presence of some other compounds accompanying them in the environment [130-132].

Unmodified electrodes such as glassy carbon [133], platinum (Pt) [134-136] and gold [137] have been used for electro oxidation of chlorophenols but they showed instability towards electrode fouling.

Catalysis of chlorophenol oxidation requires the interaction between the catalyst and the chlorophenol. It is to be expected that the type of oxidation process would depend on the properties of the adduct formed. There are relatively few models, if any, proposed to explain a specific aspect of chlorophenol interacting with metal chelates. In this work density functional theory (DFT) calculations are carried out in order to describe the molecular orbitals of 4-chlorophenol and metal chelate and to describe their interactions. The possible consequences of the electronic structure of the 4-chlorophenol adduct on the reduction mechanism are also discussed.

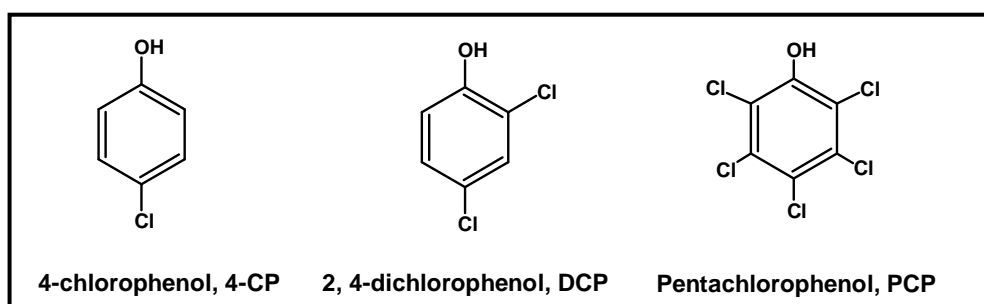


**Figure: 1.18. Molecular structure of chlorophenols**

#### 1.1.6.4. NiPc as an electrocatalyst

Oxidation of chlorophenols results in the formation of polyphenols. Several factors such as concentration of the phenol, the structure of the phenolic compounds and the operational conditions play an important role in the extent of electrode passivation. In addition for unmodified electrodes the oxidation potential of chlorinated phenol are very high. When Au or Pt electrodes are used, the chlorophenol oxidation potentials are at the region where the metal oxides are formed [133-137]. Development of electrochemical sensors which are stable and are able to prevent electrode fouling is a major area of research and this has led to the use of macromolecular complexes for electrode modification. Macromolecular complexes with transition metals are known to improve the performance of solid electrodes because of their robust nature and provision of catalytic sites at the electrode/solution interface [138, 139]. The nickel macro molecular complexes have been shown to be the most effective in improving stability and electrocatalytic abilities towards chlorophenols [127, 140]. Repetitive cycling of nickel macro molecular complexes in strong alkaline media, results in the formation of O-Ni-O bridges between the macro molecular complexes (represented as Ni(O)Pc) [141-143], which play an important role in the improvement of their catalytic



efficiency. **Table 1.4** [144 -148] shows a list of known NiPc modified electrode used for the detection of 4-CP. As this table shows all the NiPc complexes studied are tetra substituted at the  $\beta$  position. There have been no studies on octasubstituted NiPc and those of  $\alpha$  substitution. This thesis presents a systematic study on the effect of number and points of substitution on the electrocatalytic behavior of NiPc derivatives towards the oxidation of chlorophenols.

Table 1.4: Electrocalysis of chlorophenols using NiPc electrodes.

NiPc	Electrode	Analyte	Ep/V SCE	vs	Medium	Reference
NiTpPc	VCE or Pt	4-CP	0.39		0.1M NaOH	[144]
Ni(O)TpPc	VCE or Pt	4-CP	0.33		0.1 M NaOH	[144]
NiPc(SO <sub>3</sub> ) <sub>4</sub>	GCE/ITO	2-CP	0.16		pH 11	[145]
<i>Poly</i> -NiTBMPC	Au	4-CP	0.34		0.1 M NaOH	[146]
<i>Poly</i> -Ni(O)TBMPC	Au	4-CP	0.33		0.1 M NaOH	[146]
<i>Poly</i> -NiTDMPC	Au	4-CP	0.34		0.1 M NaOH	[146]
<i>Poly</i> -Ni(O)TDMPC	Au	4-CP	0.33		0.1 M NaOH	[146]
<i>Poly</i> -NiTBMPC	Au	TCP	0.55		0.1 M NaOH	[146]
<i>Poly</i> -Ni(O)TBMPC	Au	TCP	0.53		0.1 M NaOH	[146]
<i>Poly</i> -NiTDMPC	Au	TCP	0.55		0.1 M NaOH	[146]
<i>Poly</i> -Ni(O)TDMPC	Au	TCP	0.50		0.1 M NaOH	[146]
NiTPhPyPc	VCE	4-CP	0.43		0.1 M NaOH	[147]
Ni(O)TPhPyPc	VCE	4-CP	0.35		0.1 M NaOH	[147]

**TpPc = tetra-4-(pyrrol-1-yl) phenoxy phthalocyanine, TPhPyPc = tetra (pyrro-1-yl) phenoxy phthalocyanine, TDMPC = tetrakis (dodecyl mercapto) phthalocyanine, TBMPC = tetrakis (benzylmercapto) phthalocyanine, SCE = saturated calomel electrode, VCE = Vitreous carbon electrode, GCE = glassy carbon electrode, to convert potential vs. Ag|AgCl to SCE, a correction factor of -0.0045V is applied [148].**

### 1.1.7. Theoretical consideration and computational method

#### 1.1.7.1. Density functional theory

Density functional theory (DFT) provides a very convenient framework for the discussion of chemical reactivity. Most of the frontier orbital theory of chemical reactivity can be rationalized from the DFT described electronic structure of molecules [149, 150]. DFT theory is a branch of quantum mechanics in which the emphasis is on the one electron density function, rather than on the more usual wave function. Many useful and important concepts in chemistry have been identified by and derived from DFT. Among these DFT-derived concepts, the Fukui function, as derived by Parr and co-workers [151-155], is related to the electron density in the frontier molecular orbitals (FMO) and thus plays a vital role in describing chemical selectivity. DFT methods are based on the density-functional theory of Hohenberg, and co-workers, and allow for the theoretical study of material properties [150, 156]. The functional employed is computed separately into several components according to the Kohn-Sham equation. Electron correlation is computed as a functional of the electron density **Equation 1.11**.

$$E = E^T + E^V + E^J + E^{XC} \quad 1.11$$

where  $E^T$  is the kinetic energy term that contains the motion of electrons,  $E^V$  is the potential energy term that includes nuclear-nuclear and nuclear-electron interactions.  $E^J$  is the electron-electron repulsion term and  $E^{XC}$  is the exchange-correlation term that includes the electron-electron interaction. A diversity of functionals have been defined according to the treatment of the exchange-correlation components, including both traditional and hybrid functionals. The local and the gradient-corrected or non local functionals are the traditional functionals. The gradient-corrected exchange functional proposed by Becke (B) [157] and the gradient-corrected correlation function proposed by Lee, Yang and Parr (LYP) [158] are the most popular functionals used. Hybrid functionals define the exchange functional as a linear combination of Hartree-Fock, local and non-local exchange terms; and the correlation function as a local and/or non-local correlation term. A widely used hybrid functional is the Becke's three-parameter formulation, B3LYP.

### 1.1.7.2. The Fukui function

Electronegativity and chemical hardness are two important qualitative chemical concepts, formulated by DFT of many electron systems. In this work an energy perturbation method within DFT formalism is used to discuss chemical reactivity and selectivity.

The fundamental DFT differential equation for a virtual change of the ground state is defined by **Equation 1.12**:

$$dE = \mu dN + \int \rho(r) dv(r) dr \quad 1.12$$

where E is the total electronic energy, N is the number of electrons,  $\rho(r)$  is the electron density,  $v(r)$  is the external electrostatic potential an electron at r experiences due to the nuclei and  $\mu$  the chemical potential defined by **Equation 1.13**, according to Koopman's theorem [159-162]:

$$\mu = \left( \frac{\partial E}{\partial N} \right)_{v(r)} \approx \frac{1}{2} (\epsilon_{HOMO} + \epsilon_{LUMO}) \quad 1.13$$

where  $\epsilon_{HOMO}$  is the energy of the highest occupied molecular orbital (HOMO) and  $\epsilon_{LUMO}$  is the energy of the lowest unoccupied molecular orbital (LUMO).

Electronegativity  $\chi$  is defined by **Equation 1.14** [152] as

$$\chi = -\mu = - \left( \frac{\partial E}{\partial N} \right)_{v(r)} \quad 1.14$$

When studying the chemical activity of two systems of interest, it is the difference in chemical potential that will drive the given reaction between them. A finite difference approximation for **Equation 1.14** yields the Mullikan electronegativity, **Equation 1.15**:

$$\chi_M = \frac{I + A}{2} \approx \chi = -\mu \quad 1.15$$

where  $I$  and  $A$  are the ionization potential and the electron affinity of the system of interest. When studying the chemical reactivity of two interacting molecules the chemical potential ( $\mu$ ) has an important role to play. In order for a reaction to proceed via a low-energy path, an electron should be transferred from a molecule with higher chemical potential to a molecule with a lower chemical potential [160]. This means that the larger the difference in the chemical potential between the two molecules, the easier the reaction will be.

If a reaction is to take place, the driving force in a reaction is the equalization of the chemical potential between the two reacting species. Changes in the number of electrons and the external potential will cause the chemical potential of a system to change. If only infinitesimal changes in  $\mu$  are considered, the following relation is established, **Equation 1.16**:

$$d\mu = \left( \frac{\partial^2 E}{\partial N^2} \right)_{v(r)} dN + \int \left( \frac{\delta\mu}{\delta v(r)} \right)_N \delta v(r) dr \quad 1.16$$

The first term gives the chemical hardness ( $\eta$ ) shown in **Equation 1.17**, which is an important factor governing the reactivity of two chemical species.

$$\eta = \frac{1}{2} \left( \frac{\partial\mu}{\partial N} \right)_{v(r)} = \frac{1}{2} \left( \frac{\partial^2 E}{\partial N^2} \right)_{v(r)} \approx \frac{1}{2} (\epsilon_{LUMO} - \epsilon_{HOMO}) = \frac{I - A}{2} \quad 1.17$$

The final relation of the ionization potential ( $I$ ) and the electron affinity ( $A$ ) is arrived at by finite difference approximation of the differential. The molecular hardness gives account of the molecular reactivity and is associated with the energy gap between the lowest unoccupied molecular orbital (LUMO) and the highest occupied molecular orbital (HOMO) in a DFT framework. The chemical hardness of a given system is a resistance of the chemical potential to change in the number of electrons [159]. Chemical hardness ( $\eta$ ) governs reactivity [159, 160]. A higher  $\eta$  implies that a molecule has a higher ability to attract electrons, hence a good catalytic activity towards oxidation. The concept of hardness is used in this work to explain the reactivity in electrodic reactions occurring on the OPGE. The global chemical softness ( $S$ ) is defined by **Equation 1.18**, which is as inverse of the chemical hardness:

$$S = \left( \frac{\partial N}{\partial \mu} \right)_{v(r)} = \frac{1}{2\eta} \quad 1.18$$

Chemical potential ( $\mu$ ), chemical hardness ( $\eta$ ) and chemical softness (S) are three useful molecular indices in the DFT framework.

The second term in **Equation 1.16** is related to the Fukui function  $f(r)$  which is defined by **Equations 1.19 and 1.20**:

$$f(r) = \left( \frac{\delta \mu}{\delta v(r)} \right)_N = \left( \frac{\partial \rho(r)}{\partial N} \right)_{v(r)} \quad 1.19$$

$$\rho(r) = \left( \frac{\partial E}{\partial v(r)} \right)_N \quad 1.20$$

In the DFT framework, the Fukui function is a local reactivity descriptor and provides the reactive site where the reaction occurs. The Fukui function gives the site of higher reactivity because the function gives the largest variation in the electronic density for a molecular system when it accepts or donates electrons.

The Fukui function (**Equation 1.19**) is a quantity involving the electron density of the atom or molecule in its frontier orbitals and has a local quantity which has different values at different points [159-163]. This function is indicative of how the electronic density varies at a constant external potential when there is a change in the number of electrons in the system. When electrons are added to the LUMO or removed from the HOMO, the density as a function of N has slope discontinuities, hence three different reaction indices can be defined,  $f^+(r)$ ,  $f^-(r)$  and  $f^0(r)$ ; which are the Fukui functions for nucleophilic attack, electrophilic attack and radical attack, respectively. They are defined by **Equations 1.21-1.23**:

$$f^+(r) = \left( \frac{\partial \rho(r)}{\partial N^+} \right)_{v(r)} \approx \rho_{N+1}(r) - \rho_N(r) \quad 1.21$$

$$f^-(r) = - \left( \frac{\partial \rho(r)}{\partial N^-} \right)_{v(r)} \approx \rho_N(r) - \rho_{N-1}(r) \quad 1.22$$

$$f^0(r) = \left( \frac{\partial \rho(r)}{\partial N^0} \right)_{v(r)} \approx \frac{1}{2} [\rho_{N+1}(r) - \rho_{N-1}(r)] = \frac{1}{2} [f^+(r) + f^-(r)] \quad 1.23$$

where  $f^-(r)$ , measures the reactivity towards an electrophile,  $f^+(r)$ , measures reactivity towards a nucleophile and  $f^0(r)$  measures reactivity towards radical attack. The quantities  $\rho_{N+1}(r)$ ,  $\rho_N(r)$  and  $\rho_{N-1}(r)$  are the electronic densities for the system with N+1, N and N-1 electrons, respectively.

When charges of two interacting molecules are small or may be zero, for example in a reaction between two neutral molecules, the maximal Fukui function ( $f(r)$ ) site is preferred for the reaction [159-162]. When the charges of the molecules are relatively large, then the Fukui function ( $f(r)$ ) needs to be minimised in order for the reaction to proceed smoothly [161].

### 1.1.7.3. Computational aspects and calculation procedure

In this work, the Gaussian 03 program [164] running on an Intel/Linux cluster was used to perform all DFT calculations. The calculations were done at the B3LYP level with basis set 6-31G(d) for both optimization and excited energy calculations (using time dependent density functional theory, TD-DFT). The Gaussview 4.1 program was used for all visualization [164].

Geometry optimization for the ground state of a given molecule A (e.g.  $\beta$ -NiPc(OH)<sub>4</sub>) was obtained. From this calculation, the value of the energy for molecule A with N electrons ( $E_A(N)$ ) and the Mulliken charges on the k<sup>th</sup> atom of the molecule ( $q_{Ak}(N)$ ) were obtained. Single point energy calculations were performed on molecule A with N-1 and N+1 electrons. Accordingly  $E_A(N-1)$ ,  $q_{Ak}(N-1)$  and  $E_A(N+1)$ ,  $q_{Ak}(N+1)$  are obtained from the calculations. Ionization potentials ( $IP_A$ ) and electron affinities ( $EA_A$ ) for molecule A, are calculated using **Equations 1.24 and 1.25** of Koopman's theorem:

$$IP_A = E_A(N-1) - E_A(N) \quad 1.24$$

$$EA_A = E_A(N+1) - E_A(N) \quad 1.25$$

From the values obtained for A, absolute electronegativity, absolute hardness and absolute softness values  $\chi_A$ ,  $\eta_A$  and  $S_A$ , respectively can be calculated using **Equations 1.26-1.28**:

$$\chi_A = \frac{1}{2}(IP_A + EA_A) \quad 1.26$$

$$\eta_A = \frac{1}{2}(IP_A - EA_A) \quad 1.27$$

$$S_A = \frac{1}{2\eta_A} \quad 1.28$$

Mulliken charges for each of the  $k^{\text{th}}$  atoms in A with N, N-1 and N+1 electrons, allow for the calculation of the condensed Fukui function according to **Equations 1.29-1.31**:

$$f_{Ak}^+ = q_{Ak}(N_A + 1) - q_{Ak}(N_A) \quad 1.29$$

$$f_{Ak}^- = q_{Ak}(N_A) - q_{Ak}(N - 1) \quad 1.30$$

$$f_{Ak}^0 = \frac{1}{2}[q_{Ak}(N_{Ak} + 1) - q_{Ak}(N_A - 1)] = \frac{1}{2}[f_{Ak}^+ + f_{Ak}^-] \quad 1.31$$

Condensed local softness is represented by **Equations 1.32-1.34**:

$$S_{Ak}^+ = S_A f_{Ak}^+ \quad 1.32$$

$$S_{Ak}^- = S_A f_{Ak}^- \quad 1.33$$

$$S_{Ak}^0 = S_A f_{Ak}^0 \quad 1.34$$

#### 1.1.7.4. Computation of interactions between molecules

In this work the focus is on the noncovalent intermolecular interactions between NiPcs and chlorophenols.

Intermolecular interactions range from strong, long-distance electrical attractions and repulsions between ions to relatively weak dispersion forces which have not yet been completely explained. According to the different origins of these interactions, they are categorized as dispersions, electrostatic, polarization and repulsion-exchange interactions.

Therefore, the total intermolecular interaction energy for a system is defined as the sum of these four intermolecular energies, **Equation 1.35**:

$$E_{\text{int}} = E_{es} + E_{pol} + E_{dis} + E_{ex} \quad 1.35$$

where,  $E_{es}$ ,  $E_{pol}$ ,  $E_{dis}$ ,  $E_{ex}$  are electrostatic, polarization, dispersion and exchange respectively. Repulsion – exchange interactions originates from charge overlap of occupied orbitals and exchange effects. Electrostatic interactions are between two molecules with permanent dipole. Some types of electrostatic interaction are charge-charge, charge-dipole, dipole-dipole.



For intermolecular interaction energy calculation, the *ab-initio* methods are the most accurate. *Ab-initio* methods make use of the perturbation and supermolecular methods to study the intermolecular interaction energy. The perturbation method [150] treat the interaction between the subsystem wave function as a perturbation and the interaction energy is evaluated by the perturbation theory. The different interaction energies, electrostatic energy, polarization energy, dispersion energy and exchange energy, are calculated separately. Therefore the total energy is a summation of these contributions. The supermolecular method has been the most common procedure for the calculation of the interaction energies, when dealing with large molecules.

Consider a chemical system AB composed of two interacting fragment A and B. The interaction can be defined by **Equation 1.36** [149]

$$E_{\text{int}} = E_{\text{complex}} - \sum E_{\text{molecule}} \quad 1.36$$

where,  $E_{\text{int}}$  is the intermolecular interaction energy or binding energy,  $E_{\text{complex}}$  the energy of complex AB and  $\sum E_{\text{molecule}}$ , is the total energy of isolated molecules A and B. Several *ab initio* methods such as Hartree-Fock (HF), Moller-Plesset theory (MP2), and DFT can be employed for intermolecular interaction energy calculation, using the supermolecular approach. However not all of them can describe interaction energy. HF method does not take into account the dispersion energy, which is involved in electron correlation between electrons on different molecules. In the post HF methods, the electron correlation is evaluated. Therefore the accuracy of the interaction energy should be better. The post HF method such as the second-order MP2, with greater computational cost, gives accurate intermolecular interaction energies. DFT method contains the exchange-correlation function and is less demanding computationally compared to post HF. However the method has a disadvantage of not being able to evaluate the dispersion energy, because DFT method does not have the correlation function that can describe dispersion [149].

## 1.2. Nanostructured materials

### 1.2.1. Singled-walled carbon nanotubes (SWCNT)

#### 1.2.1.1. Basics of structure

Carbon nanotubes (CNTs) were discovered in the early 90s independently by Iijima (Japanese electron microscopist) [165, 166] and Bethune [167], although Oberlin and coworkers [168] observed a similar structure in 1976. To date CNTs have generated great interest for several applications based on their high mechanical strength [169], chemical properties, field emission and electronic transport properties [170, 171] such as nanoscale transistors [172, 173], tips for scanning microscopy [174], and component for composite material [175]. These properties have made CNTs to be one of the most commonly used building blocks of nanotechnology. CNTs include both single walled and multi walled structures. A single-wall carbon nanotube (SWCNT) is a rolled-up tubular shell of sheet which is made up of benzene-type hexagonal rings of carbon atoms ( $sp^2$  hybridised) (**Figure. 1.19**). The  $(m, n)$  indices determine the diameter (0.4 – 2 nm), the length (of several microns) and chirality, which are key parameters of a nanotube [176]. SWCNT are defined as quasi-1-dimensional (1-D) quantum structures or pseudo-quantum wires due to the spatial confinement of the electrons in 2-dimensions [177, 178].

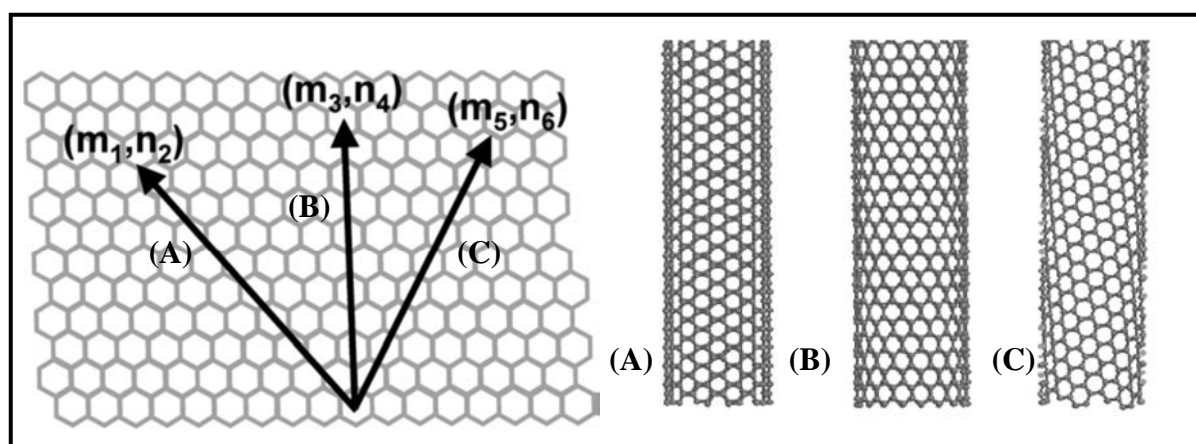


**Figure: 1.19** Schematic representation of a 2-dimensional graphite layer sheet with the resultant SWCNT tubular structures [176].

### 1.2.1.2. Electrocatalytic behaviour of phthalocyanines in the presence of SWCNT

Single walled carbon nanotube's (SWCNT) remarkable electrical, chemical, mechanical and structural properties have found their applications in various disciplines, such as electrochemistry [179], materials science [180] and surface science (imaging) [181]. SWCNT are ideal material to use for fabrication of electrochemical sensors because of their electrical conductivity, large surface area, low surface fouling and ability to reduce overpotentials [182-185]. It has been demonstrated that chemically modified SWCNT electrodes enhance the reactivity of reactions involved in electrocatalysis [186-188]. Metallophthalocyanines are used to functionalized SWCNT, covalently [189] or noncovalent ( $\pi-\pi$  interaction) [190], in order to improve electron transfer process in electrocatalysis. The main advantage of the noncovalent functionalization of CNTs is that it fully preserves the electronic network of these tubular structures. This approach of functionalisation is useful and important for developing new nanomaterials. The immobilization of MPc molecules onto CNTs may give rise to novel nanodevices where the photophysical and conducting properties of the Pcs are coupled to the unspoiled electronic properties of the nanotubes. The immobilization of the Pc cores onto the CNT sidewalls results from the  $\pi-\pi$  interaction between the conjugated surface of the CNTs and the aromatic Pc macrocycles.

Application of SWCNT in various fields is limited due to their lack of solubility. The most classical approach to the covalent functionalization of the surface of the SWCNT involves the reaction of the nanotubes with strong acids, usually mixtures of concentrated sulfuric and nitric acids [191-193]. This oxidizing treatment opens the SWCNT, giving rise to short uncapped CNTs (pipes with an average length of 100-300 nm) bearing oxygen-containing groups, such as carboxylates at the end of the pipes and at defective sites of the sidewalls. The carboxyl groups can be readily derivatized to acid chlorides by treatment with  $\text{SOCl}_2$  and subsequently coupled to amines or alcohols. The preparation of covalent Pc-SWCNT ensembles by the oxidative route was reported by several groups [194-197]. In their study, SWCNT with carboxylic moieties at the open ends were used to prepare a hybrid Zn(II)Pc-SWCNT system by means of amide bond formation. Covalent functionalization alters the conjugated  $sp^2$ -hybridised system to  $sp^3$ , which is seldom a desired characteristic as many of the optical, electrical and thermal properties are dependent on the extended  $\pi$ -conjugated system. The SWCNT bound to Pc may be characterized by Fourier transform infrared (FT-

IR), ultraviolet-visible (UV-Vis) electronic absorption and Raman spectroscopy [186, 193-208].

In this work, carboxylic acid functionalised SWCNT are used for the attachment of nickel based phthalocyanine (Pc) units. **Table 1.5** [209-217] shows known MPc-SWCNT conjugates, adsorbed and linked, and used for electrocatalysis. As **Table 1.5** shows only the most common NiPc derivatives, which have been studied in the presence of SWCNT. None of the NiPc-SWCNTs have been used for detection of chlorophenols. In this work  $\alpha$ -NiPc(C<sub>10</sub>H<sub>21</sub>)<sub>8</sub>,  $\beta$ -NiPc(OH)<sub>4</sub>,  $\alpha$ -NiPc(OH)<sub>4</sub> or  $\alpha$ -NiPc(OH)<sub>8</sub> and  $\beta$ -NiPc(NH<sub>2</sub>)<sub>4</sub> are adsorbed and linked (only for  $\beta$ -NiPc(NH<sub>2</sub>)<sub>4</sub> ) to SWCNT and employed for the detection of chlorophenols.  $\alpha$ -NiPc(C<sub>10</sub>H<sub>21</sub>)<sub>8</sub> is added because long chains have been found be better electrode modifiers than aryl substituents [218].

Table 1.5: Known MPc-SWCNT conjugate used for electrocatalysis

<b>Metallophthalocyanine-SWCNT conjugates</b>	<b>Electrode</b>	<b>Analyte detected</b>	<b>References</b>
CoPc(SO <sub>3</sub> ) <sub>4</sub> /SWCNT (adsorbed)	GCE	Thiocholine	[209]
NiPc(SO <sub>3</sub> ) <sub>4</sub> /SWCNT (adsorbed)	GCE	Nitric oxide	[210]
NiPc(SO <sub>3</sub> ) <sub>4</sub> /SWCNT (adsorbed)	GCE	2-ME	[211]
NiPc(SO <sub>3</sub> ) <sub>4</sub> /SWCNT (adsorbed)	GCE	Nitric oxide	[211]
CoPc(SO <sub>3</sub> ) <sub>4</sub> /SWCNT (adsorbed)	GCE	2-ME	[211]
CoPc(SO <sub>3</sub> ) <sub>4</sub> /SWCNT (adsorbed)	GCE	Nitric oxide	[211]
CoPc/SWCNT(adsorbed)	GCE	Hydrazine	[192]
NiPc(NH <sub>2</sub> ) <sub>4</sub> /SWCNT (linked)	GCE	2-ME	[212]
FePc(NH <sub>2</sub> ) <sub>4</sub> -SWCNT (linked)	GCE	Amitrole	[213]
CoPc(NH <sub>2</sub> ) <sub>4</sub> -EA-SWCNT (linked)	GCE	Amitrole	[214]

CoPc(COOH) <sub>4</sub> -SWCNT (linked)	GCE	Amitrole	[215]
NiPc(NH <sub>2</sub> ) <sub>4</sub> -SWCNT (linked)	Au-AE	Dopamine	[216]
CoOBCPPc-SWCNT (linked)	GCE	NADH	[217]

**OBCP = octa [(3,5-biscarboxylate)-phenoxy], 2-ME = 2-mercaptoethanol, NADH =  $\beta$ -nicotinamide adenine dinucleotide, and EA = ethylene amine.**

## 1.2.2. Quantum dots (QDs)

### 1.2.2.1. Basics of spectra and size

Quantum dots are defined as 0-dimensional semiconductor material as result of quantum confinement of electrons in three dimensions [177, 178]. QDs are generally synthesised from elements in the periodic table belonging to groups 12-14 or 13-15 to form clusters which have dimensions smaller than the exciton Bohr radius; which is about 10 nm [178, 198, 219-221]. Over the past two decades there has been a rapid growth in research of nanometer sized conducting and semiconducting structures such as QDs [222, 223]. QDs' unique electronic properties, which depend on their size, have sparked intense interest and quantized electronic behavior of these nanoparticles have been explored by electrochemical means [224-231].

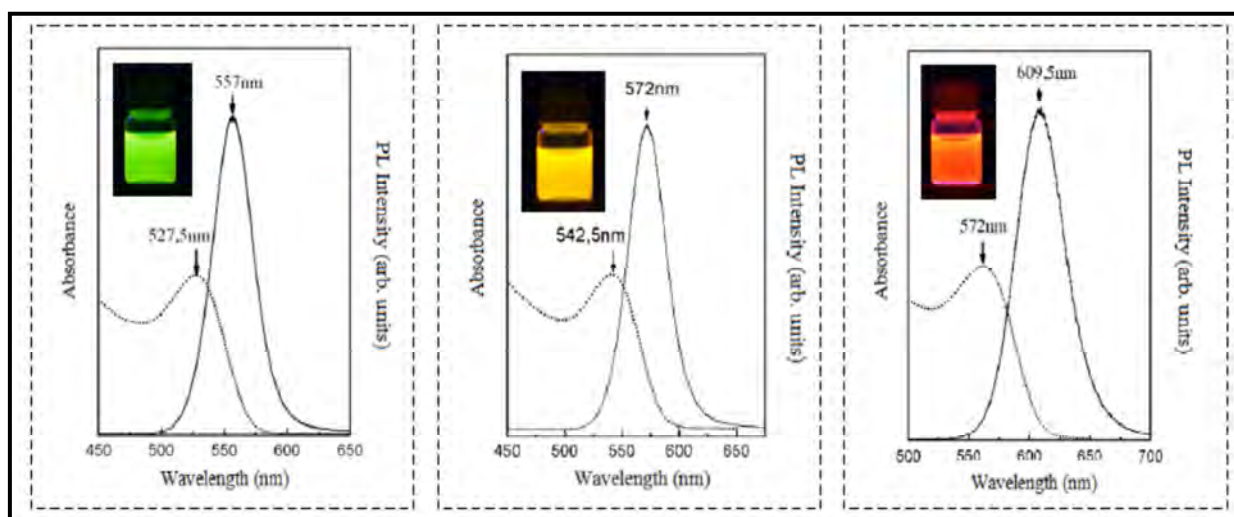


**Figure 1.20: Absorption and Photoluminescence(PL) of typical CdTe-QDs, (a), (b) and (c) correspond to the growth time of 90, 150, and 360 minute respectively[231].**

Cyclic voltammetry has been used to correlate the optical band gap of QDs to band gap estimated from the oxidation and reduction peak position [224, 226, 228]. QDs quantised energy gives them their unique optical properties, which lie between those of bulk and atomic materials [232]. QDs possess broad absorption spectrum and narrow emission spectrum spanning the ultraviolet region (UV) to infrared region, see **Figure 1.20**. Fluorescence emission or photoluminescence (PL) in QDs arises from the radiative recombination of electron-hole pairs. The recombination of the charge carries can follow different processes such as, radiative recombination (band gap emission), recombination via trap state or annihilation of the exciton [233]. Slight defects in the solid, such as a vacancies, impurities,

or adsorbates at the surface cause the formation of “trap” states into which the photo-excited electron can fall. The electron recombination from these surface traps (defects sites) on the surface of the QDs results in radiative emission of low intensity. Some of the recombinations of the electrons and hole from surface states result in non-radiative (NR) emission [233, 234].

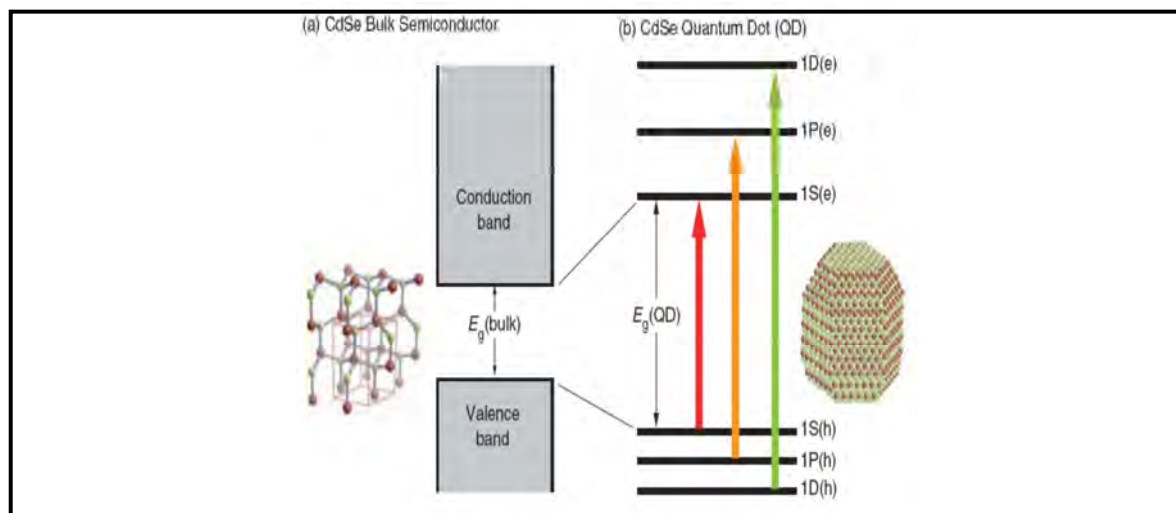


**Figure 1.21: Band gap in bulk crystals and QDs showing (a) continuous conduction and valence energy bands separated by a fixed energy gap,  $E_g(\text{bulk})$  (b) QD characterized by discrete atomic-like states with energies that are determined by the QD’s radius [232].**

At this small dimension there is what is called quantum confinement for which the spatial extent of the electronic wave function is comparable with the dot size [232]. As a result, the electronic structure is altered from the continuous electronic band to discrete atomic-like states with energies that are determined by the QDs radius, **Figure 1.21**. This behaviour is known as the quantum size effect. The band gap energy decreases with increasing particle size, whereby the absorption profile shifts towards higher wavelengths of the electromagnetic spectrum. In addition to the band gap, the absorption spectrum depends on the shape fluctuation of the nanocrystals [235], the crystalline defects, concentration and the environmental inhomogeneities.

CV and DPV methods provide useful information on the surface of QDs. In this work these two methods are used to investigate whether phthalocyanine linked to QDs will improve the stability of QDs from electrochemical degradation.



### 1.2.2.2. Electrocatalytic behaviour of QDs

**Figure 1.22** shows CdTe-QDs preadsorbed on Au electrode cycled in buffer (pH 9.2) solution. Three main peaks  $A_1$ ,  $A_2$  and  $C_1$  are observed from **Figure 1.22**. Peak  $A_1$  and  $A_2$  are due to oxidation and peaks  $C_1$ ,  $C_2$  and  $C_3$  are due to reduction of CdTe-QDs. These peaks are similar to the peaks belonging to Au oxidation. The peak positions are known to depend on the CdTe-QDs size [177, 178].  $A_2$  is due to intact QDs,  $A_1$  due to defects.

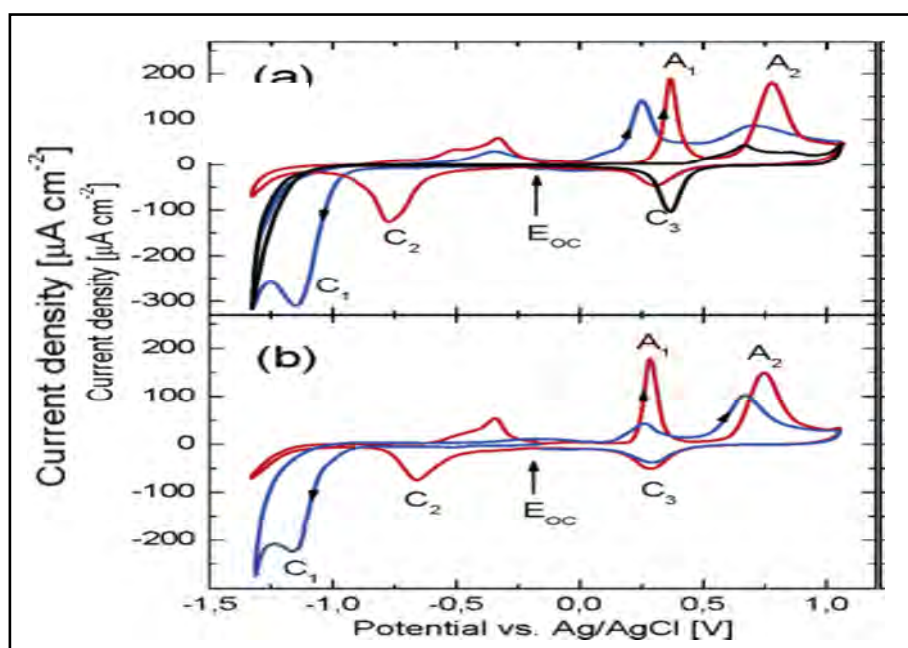


**Figure 1.22:** Voltammograms of the Au electrode with preadsorbed CdTe-QDs in blank buffer solution [225].

Due to high surface area-to-volume ratio and good interfacial properties, QDs have been used to modify electrode surfaces for electrochemical detection of analytes such as magnesium ions, glutathione and glucose [236-239]. The focus of this thesis is to investigate the electrochemical stability of QDs on electrode surfaces alone or when coordinated to  $\beta$ -NiPc(NH<sub>2</sub>)<sub>4</sub>, making use of CV and DPV techniques. NiPc complexes are also well known electrocatalysts, however the use of these two electrocatalysts together has not been explored. Therefore the synergetic effect of their electrocatalysis is explored [125, 240,241]. Oxidation of 2, 4-dichlorophenol and pentachlorophenol on bare Au, and on Au modified with CdTe-QDs, CdTe-QDs- $\beta$ -NiPc(NH<sub>2</sub>)<sub>4</sub> and  $\beta$ -NiPc(NH<sub>2</sub>)<sub>4</sub> electrode is comparatively studied, for the first time.

QDs capping consisting of carboxylic acid functionalities (such as glycolic acid, TGA, used in this work) could be used to covalently attach amino functionalized molecules. A number of structures have been reported where QDs are linked to MPc [189, 242-246], but the Pc contained electro-inactive zinc and the conjugate were for photophysical studies. In this work the aim is to investigate the effect of linking the nickel tetraamino phthalocyanine ( $\beta$ -NiPc(NH<sub>2</sub>)<sub>4</sub>, **Figure. 1.23**) complex to QDs (forming: CdTe-QDs- $\beta$ -NiPc(NH<sub>2</sub>)<sub>4</sub> conjugates) on the redox properties of QDs,  $\beta$ -NiPc(NH<sub>2</sub>)<sub>4</sub> is linked via an amide bond to CdTe-QDs.  $\beta$ -NiPc(NH<sub>2</sub>)<sub>4</sub> is chosen due to the presence of amino groups on the periphery which can form an amide bond with the carboxylic acid group of the TGA capped CdTe-QDs. Electrocatalytic behavior of the MPc-QDs conjugates was explored for the first time.

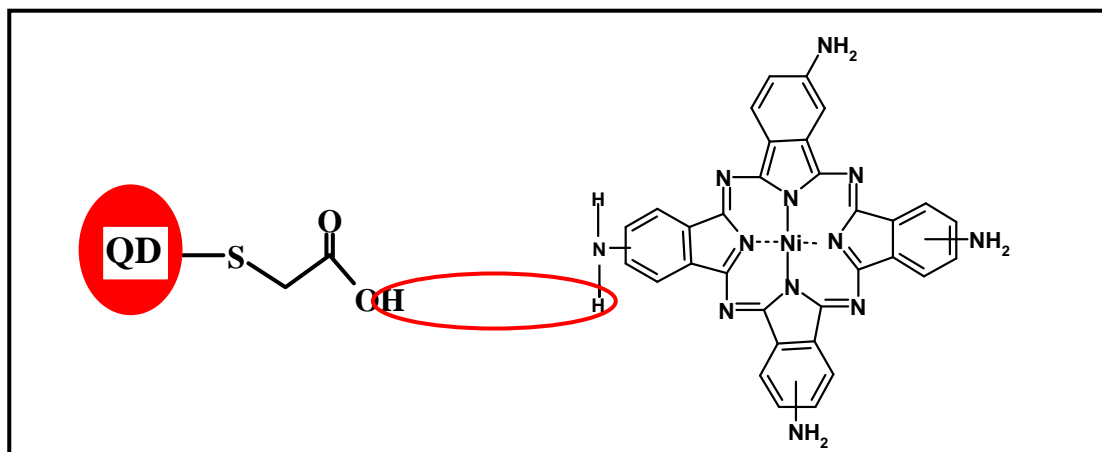


**Figure 1.23: Nickel tetra amino conjugate (CdTe-QDs- $\beta$ -NiPc(NH<sub>2</sub>)<sub>4</sub>)**

### 1.2.2.3. QDs-SWCNT-MPc conjugate

An extensive research of literature has not revealed any QDs-MPc conjugates that have been used for electrocatalysis. SWCNT-MPc conjugates have been used for detection of various analytes as discussed above and in **Table 1.5**. This work reports on QDs/SWCNT/MPc conjugates for the first time for electrocatalysis of chlorophenols. Deliberate combination of these three electrochemical sensors (SWCNT, QDs and MPc complexes) may have a synergistic effect on each other.

### 1.3. Summary of Aims of thesis

This thesis presents the following:

Ordinary pyrolytic graphite electrode (OPGE) surface is easily renewed and offers a better  $\pi$ - $\pi$  interaction compared to GC electrode, thus allows easy adsorption of electrode modifiers. However, OPGE is not readily available compared to GC electrodes, due to this limitation OPGE was employed only for  $\beta$ -NiPc(OH)<sub>4</sub>,  $\alpha$ -NiPc(OH)<sub>4</sub> and  $\alpha$ -NiPc(OH)<sub>8</sub>.

- (i) The electro-oxidation of 4-chlorophenol (4-CP) on OPGE coated with films of adsorbed  $\beta$ -NiPc(OH)<sub>4</sub> which was polymerised (in 0.1 M NaOH) to form (*poly*- $\beta$ -Ni(O)Pc(OH)<sub>4</sub>) containing Ni-O-Ni bridges. The concept of donor-acceptor hardness ( $\eta_{DA}$ ) is used to explain the reactivity of electrodeposited  $\beta$ -NiPc(OH)<sub>4</sub> and films of *poly*- $\beta$ -Ni(O)Pc(OH)<sub>4</sub> on OPGE electrode for catalysis of chlorophenols, assuming that the distance is kept constant between the  $\beta$ -NiPc(OH)<sub>4</sub>, *poly*- $\beta$ -Ni(O)Pc(OH)<sub>4</sub> and the 4-chlorophenol.
- (ii) The use of the Fukui function in order to theoretically investigate if there is any effect on selectivity and reactivity of the ring, due hydroxy groups substituted at different positions on Ni phthalocyanines. The Fukui function gives information on possible reactive sites on the metallo phthalocyanine, where electrocatalytic oxidation of analytes such as 4-chlorophenol may occur. The Fukui function plots of three differently substituted metallo phthalocyanines {non-peripherally-( $\alpha$ -NiPc(OH)<sub>4</sub>) and peripherally tetrasubstituted ( $\beta$ -NiPc(OH)<sub>4</sub>) and non-peripherally octasubstituted ( $\alpha$ -NiPc(OH)<sub>8</sub>), **Figure 1.3**} are comparatively studied and the information used to explain the catalytic activity of 4-chlorophenol. The molecules are adsorbed on ordinary poly graphite electrode (OPGE). Electrocatalytic activities of adsorbed OPGE- $\alpha$ -NiPc(OH)<sub>8</sub> and OPGE-*poly*- $\alpha$ -Ni(OH)Pc(OH)<sub>8</sub> are compared with adsorbed OPGE- $\beta$ -NiPc(OH)<sub>4</sub> and OPGE-*poly*- $\beta$ -NiPc(OH)<sub>4</sub>.
- (iii) The electro-oxidation of 4-chlorophenol (4-CP) and 2, 4-dichlorophenol (2,4-DCP) on glassy carbon electrodes modified with SWCNT which are non-

covalently functionalized with the  $\alpha$ -NiPc(C<sub>10</sub>H<sub>21</sub>)<sub>8</sub> complex. The activity of this complex is compared with that of unsubstituted NiPc.

- (iv) Also studied are the effects of linking nickel tetraaminophthalocyanine ( $\beta$ -NiPc(NH<sub>2</sub>)<sub>4</sub>), **Figure 1.23**) complex to QDs (forming: CdTe-QDs- $\beta$ -NiPc(NH<sub>2</sub>)<sub>4</sub> conjugates) on the redox properties of QDs,  $\beta$ -NiPc(NH<sub>2</sub>)<sub>4</sub> is linked via an amide bond to CdTe-QDs. The electrochemistry of QDs,  $\beta$ -NiPc(NH<sub>2</sub>)<sub>4</sub> and CdTe-QDs- $\beta$ -NiPc(NH<sub>2</sub>)<sub>4</sub> are carried out when adsorbed on the electrode and also when in solution. The electrochemical stability of QDs on electrode surfaces alone or when coordinated to  $\beta$ -NiPc(NH<sub>2</sub>)<sub>4</sub> is of particular importance.
- (v) CdTe-QDs easily adsorb on Au electrode surface compared to OPGE and GCE, hence this electrode was used to study the redox properties of QDs. The electrochemical stability of QDs on electrode surfaces alone or when coordinated to  $\beta$ -NiPc(NH<sub>2</sub>)<sub>4</sub>, making use of CV and DPV techniques. Oxidation of 2, 4-dichlorophenol and pentachlorophenol on bare Au, and on Au modified with CdTe-QDs, CdTe-QDs- $\beta$ -NiPc(NH<sub>2</sub>)<sub>4</sub> and  $\beta$ -NiPc(NH<sub>2</sub>)<sub>4</sub> electrodes is comparatively studied.
- (vi) The interaction of  $\beta$ -NiPc(OH)<sub>4</sub>,  $\alpha$ -NiPc(OH)<sub>4</sub> and  $\alpha$ -NiPc(OH)<sub>8</sub> with SWCNT and electrochemical oxidation of 4-chlorophenol on glassy carbon electrode modified with SWCNT which is non-covalently and covalently functionalized with  $\beta$ -NiPc(NH<sub>2</sub>)<sub>4</sub> complex.
- (vii) The deliberate combination of SWCNT, QDs and  $\alpha$ -NiPc(C<sub>10</sub>H<sub>21</sub>)<sub>8</sub> complexes thus forming conjugates composed of all three complexes. SWCNT,  $\alpha$ -NiPc(C<sub>10</sub>H<sub>21</sub>)<sub>8</sub>, SWCNT- $\alpha$ -NiPc(C<sub>10</sub>H<sub>21</sub>)<sub>8</sub> and  $\alpha$ -NiPc(C<sub>10</sub>H<sub>21</sub>)<sub>8</sub>-SWCNT-QDs complexes are used to modify glassy carbon electrode (GCE) and used for the electro-oxidation of pentachlorophenol.  $\alpha$ -NiPc(C<sub>10</sub>H<sub>21</sub>)<sub>8</sub> is converted to  $\alpha$ -Ni(O)Pc(C<sub>10</sub>H<sub>21</sub>)<sub>8</sub> on GCE and comparatively studied with other electrodes.

- (viii) The synthesis, separation and characterisation of novel chiral 1,2-subnaphthalocyanine (SubNPc) having  $C_3$  and  $C_1$  molecular symmetries relative to the arrangement of the fused benzene rings.

## Chapter 2: Experimental

## 2. Experimental

### 2.1. Materials

Acetone, dimethylformamide (DMF), dichloromethane (DCM), tetrahydrofuran (THF), toluene, hydrogen peroxide, sulfuric acid, potassium hydroxide pellets were obtained from SAARCHEM. 1.8-diazabicyclo[5, 4, 0] undec-7-ene (DBU), 3-nitrophthalic acid, 2, 3-dicyanohydroquinone, dibromoethane, p-toluenesulfonyl chloride,  $K_3Fe(CN)_6$ ,  $K_4Fe(CN)_6$ , potassium chloride, dodacanethiol, potassium carbonate, buffer tablets, cerium chloride, nickel chloride, nickel acetate tetrahydrate, tetraethylammonium perchlorate (TEAP), dicyclohexylcarbodiimide (DCC), N-hydroxy succinimide (NHS), thiol glycolic acid (TGA),  $CdCl_2$ ,  $H_2Te$ ,  $NaBH_4$ , SWCNT (diameter of 2-10 nm and length of 1-5  $\mu m$ ) and nickel phthalocyanine (NiPc) were purchased from Sigma-Aldrich. 2,6-Lutidine, iododecane, bis(triphenylphosphine)nickel(II) dichloride and lithium chloride were from Alfa Aesar. Triphenylphosphine, Zn dust and n-butyllithium (2.5 M hexane) were procured from Lancaster. Trifluoromethanesulfonic acid anhydride and trimethylsilyl chloride were from Apollo. Decyl iodide (for making  $C_{10}H_{21}ZnI$ , respectively) according to reference [49] was from Aldrich. Glacial acetic acid and Li metal were obtained from commercial suppliers. Column chromatography was performed on silica gel 60 (0.04-0.063 mm). DMF was stored over alumina, distilled and stored dry over molecular sieves before use.

### 2.2. Equipment

Fluorescence emission spectra were recorded on a Varian Eclipse spectrofluorimeter. UV-visible spectra were recorded on a Shimadzu UV-vis/NIR spectrophotometer or JASCO V-570 spectrophotometer.

X-ray powder diffraction (XRD) patterns were recorded on a Bruker D8 Discover equipped with a proportional counter, using Cu-K $\alpha$  radiation ( $\lambda = 1.5405 \text{ \AA}$ , nickel filter). Data were collected in the range from  $2\theta = 5^\circ$  to  $60^\circ$ , scanning at  $1^\circ \text{ min}^{-1}$  with a filter time-constant of 2.5s per step and a slit width of 6.0 mm. Samples were placed on a silicon wafer slide. The X-ray diffraction data were treated using the freely-available Eva (evaluation curve fitting) software. Baseline correction was performed on each diffraction pattern by subtracting a spline fitted to the curved background and the full-width at half-maximum values used in this study were obtained from the fitted curves.

Atomic force microscopy (AFM) images were recorded in the non-contact mode in air with a CP-11 Scanning Probe Microscope from Veeco Instruments (Carl Zeiss, South Africa) at a scan rate of 1 Hz. Samples for AFM were prepared by placing a drop of a colloidal suspension of QDs in a volatile solvent, tetrahydrofuran (THF) and dried. The samples were ultrasonicated for 30 minutes in THF, before being dropped on a glass plate. Transmission electron microscope (TEM) images were recorded using, JEOL JEM 1210 at 100 KV accelerating voltage.

FT-IR spectra (Nujol and KBr pellets) were recorded on a Perkin-Elmer spectrum 100 ATR spectrometer. Raman spectra were acquired with Bruker Vertex 70 - Ram II spectrometer (equipped with a 1064 nm Nd:YAG laser and a liquid nitrogen cooled germanium detector). Solid samples containing KBr were employed.

Fluorescence lifetimes were measured using a time correlated single photon counting (TCSPC) setup (FluoTime 200, Picoquant GmbH). The excitation source was a diode laser (LDH-P-C-485 driven by PDL 800-B, 480 nm, with 10 MHz repetition rate, 88 ps pulse width). Fluorescence was detected under the magic angle with a peltier cooled photomultiplier tube (PMT) (PMA-C 192-N-M, Picoquant) and integrated electronics (PicoHarp 300E, Picoquant GmbH). A monochromator with a spectral width of about 8 nm was used to select the required emission wavelength band. The response function of the system, which was measured with a scattering Ludox solution (DuPont), had a full width at half-maximum (FWHM) of about 300 ps. The ratio of stop to start pulses was kept low (below 0.05) to ensure good statistics. All luminescence decay curves were measured at the maximum of the emission peak. The data were analyzed with the program FluoFit (Picoquant). The support plane approach was used to estimate the errors of the decay times.

X-ray photoelectron spectroscopy (XPS) experiments were recorded with 75 W power source using hybrid-slot spectral acquisition mode and an angular acceptance angle of  $\pm 20^\circ$ . The analyzer axis made an angle of  $90^\circ$  with the specimen surface, with the specimen surface making an angle of  $45^\circ$  with the X-ray angle. Charge neutraliser was used due to the insulating surface used to prepare the sample. The elemental analysis and metal core level



were recorded with a step of 1eV and pass energy of 160 eV. XPS data analysis was performed with Kratos version 2 program.

Circular dichroism (CD) and magnetic circular dichroism (MCD) spectra were recorded on a JASCO J-725 spectrodichrometer equipped with a JASCO electromagnet, which produces magnetic fields of up to 1.09 T (1T = 1 tesla) with both parallel and antiparallel fields. The magnitudes were expressed in terms of molar ellipticity ( $[\theta]$  / deg dm<sup>3</sup> mol<sup>-1</sup> cm<sup>-1</sup>) and molar ellipticity per tesla ( $[\theta]_M$  / deg dm<sup>3</sup> mol<sup>-1</sup> cm<sup>-1</sup> T<sup>-1</sup>).

<sup>1</sup>H NMR spectra were recorded on a JEOL ECA-600 spectrometer (operating as 594.17 MHz for <sup>1</sup>H) using the residual solvent as the internal reference for <sup>1</sup>H ( $\delta$  = 7.260 ppm for CDCl<sub>3</sub>) or a Bruker AMX 400 MHz NMR spectrometer.

Mass spectra data were collected with a Bruker AutoFLEX III Smart-beam TOF/TOF mass spectrometer. The instrument was operated in positive ion mode using a m/z range of 400–3000 amu. The voltage of the ion sources were set at 19 and 16.7 kV for ion sources 1 and 2, respectively, while the lens was set at 8.50 kV. The reflector 1 and 2 voltages were set at 21 and 9.7 kV, respectively. The spectra were acquired using dithranol as the MALDI matrix, using a 354 nm nitrogen laser.

Preparative separations were performed by silica gel column chromatography (Merck Kieselegel 60H for thin layer chromatography). Separation of all the enantiomers was carried out by high-performance liquid chromatography (HPLC) with a preparative CHIRALPAK IA column.

### 2.3. Electrochemical methods

Cyclic (CV) and differential pulse (DPV) voltammetry data were obtained with an Autolab potentiostat PGSTAT 30 (Eco Chemie, Utrecht, The Netherlands) driven by the General Purpose Electrochemical Systems data processing software (GPES, software version 4.9, Eco Chemie), using a conventional three-electrode set-up with gold electrode (Au, 3 mm diameter), glassy carbon electrode (GCE) or ordinary polygraphite electrode (OPGE) as working electrodes, platinum wire as a counter electrode and Ag|AgCl wire as a pseudo-reference electrode. The potential of the pseudo reference electrode was less than that of

Ag|AgCl (3M KCl) by  $0.015 \pm 0.003$  V. The OPGE was constructed in house. Conduction between the copper wire and OPGE material was facilitated by making use of high purity silver paint and Teflon was used for the outer casing.

Electrochemical impedance spectroscopy (EIS) experiments were performed on an Autolab potentiostat PGSTAT 30, controlled by FRA software which was used for the acquisition and analysis of the impedance data. EIS experiments were recorded in the frequency range between 100 mHz to 10 KHz at a formal potential of 150 mV ( $E_{1/2}$  of  $\text{Fe}(\text{CN})_6^{3-/4-}$  redox couple on bare gold electrode) and with an amplitude 5mV sinusoidal modulation.

Electrochemical experiments for detection of phenols were performed in phosphate buffer (pH = 9.2) containing 0.1 M sodium sulfate ( $\text{Na}_2\text{SO}_4$ ) as a supporting electrolyte. Prior to scans, the working electrodes were polished with alumina paste on a Buehler felt pad, followed by washing with milli-pore water.

#### 2.4. Density functional theory calculations

In this work, The Gaussian 03 program [164] running on an Intel/Linux cluster was used to perform all DFT calculations. The calculations were done at the B3LYP level with basis set 6-31G(d) for both optimization and excited energy calculations (using time dependent density functional theory (TDDFT)). The Gausview 4.1 program was used for all visualization [164]. B3LYP employs Becke's method of using Lee-Yang-Parr's gradient-correction, exchange-correlation density functional, which includes a hybrid of the Hartree-Fock exchange and the DFT exchange.

#### 2.5. Synthesis

The preparation of 3, 6-bis(trifluoromethanesulfonyloxy) phthalonitrile (**28**), 3, 6-didecylphthalonitrile (**26**), 3, 6-bis(4-methylphenylsulfonyloxy) phthalonitrile (**30**) (Scheme 3.2), 3-nitrophthalonitrile (**11**) and 4-nitrophthalonitrile (**4**) have been reported before and will not be repeated here [30-34, 247]. The synthesis of  $\beta$ -tetraaminophthalocyanine ( $\beta$ -NiPc( $\text{NH}_2$ )<sub>4</sub>), and  $\beta$ -tetrahydroxylphthalocyanine ( $\beta$ -NiPc( $\text{OH}$ )<sub>4</sub>) have been reported [39].

### 2.5.1. $\alpha$ -Nickel(II)tetrahydroxyphthalocyanine ( $\alpha$ -NiPc(OH)<sub>4</sub>), Scheme 3.1.

A mixture of 3-nitrophthalonitrile (**11**) (1g, 5.8 mmol) in 1-pentanol (3 ml) was heated under an atmosphere of nitrogen at 180°C for 6 h. Thereafter the reaction mixture was cooled to room temperature, followed by consecutive refluxing in methanol (30 ml) for 30 min. The fine green black product was collected by filtration, washed with distilled water, methanol and petroleum ether and then air dried to give unmetallated tetranitrophthalocyanine ( $\alpha$ -H<sub>2</sub>Pc(NO<sub>2</sub>)<sub>4</sub>).  $\alpha$ -H<sub>2</sub>Pc(NO<sub>2</sub>)<sub>4</sub> (0.2 g, 0.34 mmol) was then reacted with K<sub>2</sub>CO<sub>3</sub> (0.16g, 1.16 mmol) and NaNO<sub>2</sub> (0.057g, 0.29 mmol) to afford unmetallated tetrahydroxyphthalocyanine ( $\alpha$ -H<sub>2</sub>Pc(OH)<sub>4</sub>).  $\alpha$ -H<sub>2</sub>Pc(OH)<sub>4</sub> (0.17 g, 0.29 mmol) was then reacted with nickel chloride (0.085 g, 0.34 mmol) in benzonitrile to afford  $\alpha$ -nickel tetrahydroxyphthalocyanine ( $\alpha$ -NiPc(OH)<sub>4</sub>).  $\alpha$ -NiPc(OH)<sub>4</sub> was precipitated out using methanol, filtered and purified by alternate treating with HCl and distilled water: Yield: 0.14g (63%), IR [(KBr)  $\nu_{\max}$  / cm<sup>-1</sup>]: 3291(OH), 2927 (C-H), 2854(C-H), 1631, 481, 1325, 1754. MS (ESI-MS) m/z: ( $\alpha$ -NiPc(OH)<sub>4</sub>) Calculated. 635; Found: 635 [M]<sup>+</sup>.

### 2.5.2. The synthesis of non-peripherally octahydroxy nickel phthalocyanine ( $\alpha$ -NiPc(OH)<sub>8</sub>), Scheme 3.2.

2, 3-Dicyanohydroquinone (**27**) was converted to 3, 6-bis(4-methylphenylsulfonyloxy) phthalonitrile (**30**) following literature method [247]. For the synthesis of (**30**) (1g, 2.13 mmol), and 3 ml of dry 1-pentanol were placed in a standard round bottom flask and refluxed for 30 minutes. Anhydrous nickel acetate tetrahydrate (0.13 g, 0.53 mmol) was added to the hot solution followed by a drop of DBU. The mixture was further refluxed for 7 h to afford  $\alpha$ -NiPc(OTos)<sub>8</sub> (OTos = Tosyl).  $\alpha$ -NiPc(OTos)<sub>8</sub> (0.77 g, 0.53 mmol) was stirred in NaOH (1M) solution for 24 hours to afford  $\alpha$ -NiPc(OH)<sub>8</sub>. The product was separated and purified using 1M sodium hydroxide, 1M hydrochloric acid and finally with water.  $\alpha$ -NiPc(OH)<sub>8</sub> was further stirred in hot methanol: water mixture (1:1) and finally dried at 80 °C overnight.  $\alpha$ -NiPc(OH)<sub>8</sub> was purified further on alumina column, using DMF as the eluting solvent. DMF was removed under high vacuum. Yield 0.22g (60 %). <sup>1</sup>H-NMR:  $\delta_H$  (DMSO), 7.3 – 7.8 (8H, m, Ar-CH), 5.8 (Ar-OH): IR spectrum (cm<sup>-1</sup>): 3314 (OH), 3057 (Ar-CH), 1588, (C=C), 1554 (C=N), 1491, 1474, 1361, 1286, 1172, 1142, 1081, 928, 812, 747, 704, 747. MS (ESI-MS) m/z: ( $\alpha$ -NiPc(OH)<sub>8</sub>) Calculated. 699; Found: 699 [M]<sup>+</sup>. A broad <sup>1</sup>H-NMR singlet due to hydroxy substituent at 5.8 ppm, disappeared upon addition of D<sub>2</sub>O.

### 2.5.3. 1, 4, 8, 11, 15, 18, 22, 25-Octadecylphthalocyanine nickel(II) ( $\alpha$ -NiPc(C<sub>10</sub>H<sub>21</sub>)<sub>8</sub>) (Scheme 3.3).

1, 4, 8, 11, 15, 18, 22, 25-Octadecylphthalocyanine ( $\alpha$ -H<sub>2</sub>Pc(C<sub>10</sub>H<sub>21</sub>)<sub>8</sub>) was synthesised using the lithium base catalysed method as follows: 3, 6-didecylphthalonitrile (**26**) (0.7g, 2.35 mmol) was dissolved in hot 1-pentanol (15 mL) in open atmosphere. Lithium metal was added in portions (0.28 g, 6eq) at room temperature and the yellow suspension was heated under reflux for 24 h under an atmosphere of Ar. The dark green mixture was cooled down to room temperature. Glacial acetic acid (30 mL) was added and the mixture was stirred at RT for 30 minutes, precipitated out with methanol and filtered to afford H<sub>2</sub>Pc(C<sub>10</sub>H<sub>21</sub>)<sub>8</sub> (0.65g). H<sub>2</sub>Pc(C<sub>10</sub>H<sub>21</sub>)<sub>8</sub> (0.025g, 0.015 mmol) and nickel acetate (2.65 mg, 0.015 mmol) were dissolved in hot pentanol and refluxed at 150°C for 90 min. The green product obtained was concentrated under reduced pressure and precipitated out with cold methanol. The product was recrystallized from THF and methanol to afford  $\alpha$ -NiPc(C<sub>10</sub>H<sub>21</sub>)<sub>8</sub>.

$\alpha$ -H<sub>2</sub>Pc(C<sub>10</sub>H<sub>21</sub>)<sub>8</sub> Yield: 0.65g, 68%, <sup>1</sup>H-NMR:  $\delta_H$  (CDCl<sub>3</sub>):  $\delta_H$  (300 MHz, CHCl<sub>3</sub>), 7.8 (8H, H<sub>arom</sub>), 4.4(16H, t, -CH<sub>2</sub>-Ar), 2.1 (16H, m, Ar-CH<sub>2</sub>-CH<sub>2</sub>-), 1.3 (112H, m, H<sub>aliphatic</sub>), 0.90 (24H, t, CH<sub>3</sub>-), -0.2 (2H, s, inner protons). Calc. for C<sub>112</sub>H<sub>176</sub>N<sub>8</sub>: C: 82.25 % H: 10.89 % N: 6.85 %: Found C: 82.94 H: 11.07 N: 6.96 %.

$\alpha$ -NiPc(C<sub>10</sub>H<sub>21</sub>)<sub>8</sub> Yield: 0.018g, 70%, Calc. for C<sub>112</sub>H<sub>176</sub>N<sub>8</sub>Ni C, 79.43: H, 10.40: N, 6.62 %: Found C: 80.00 H: 11.11 N: 6.69 %: Mass spec: calculated (1692). Found 1692 [M<sup>+</sup>]. IR [(KBr)  $\nu_{\max}/\text{cm}^{-1}$ ]: 3417, 2934 (C-H), 2842 (C-H), 2849, 1612, 1470, 1320, 1178, 1086.

### 2.5.4. Synthesis of 1,2-subnaphthalocyanine (SubNPc) (Scheme 3.4)

1,2-Naphthalenedicarbonitrile (178 mg, 1 mmol) was first dissolved in 1,2,4 trichlorobenzene (4 mL) followed by addition of xylene (1 mL) under stirring. The reaction flask was then cooled to 0°C (care was taken such that xylene will not solidify). Boron trichloride (BCl<sub>3</sub>) (1 mL, 0.01 mol) was added slowly under nitrogen atmosphere. The addition of BCl<sub>3</sub> resulted with an immediate change in colour of the solution to yellow. The mixture was then refluxed under nitrogen at 214 °C for 90 min. After 20 min at 192°C the colour changed from brown to red and after 40 min the mixture turned to violet. After 90 min, the violet mixture was allowed to cool to room temperature and the solvent removed by distillation under reduced pressure. The dry remaining solid was dissolved in toluene and filtered. The toluene was removed from the filtrate under low pressure at 100 mmHg at 45°C to obtain the crude

product. The crude purple product was purified by column chromatography over silica and bio-bead S-X1. The axial ligand of 1,2-subnaphthalocyanines was chloride as-synthesised, but during column chromatography using silica gel, it was gradually replaced with hydroxide. Toluene was used as the first eluting solvent followed by methanol: toluene (1:2) mixture to obtain pure isomeric mixture as the product (Fractions **1** and **2**). HPLC-GPC column (chloroform as eluent =  $3.8 \text{ mL min}^{-1}$ ) was used to separate the isomeric mixture, two isomers were collected from **Fraction 1** ((isomer **1**) 9.8 mg, 1.74 %) and ((isomer **2**) 3.32 mg, 0.6%) (**Scheme 3.4**). Optical resolution of  $C_3$  and  $C_1$  chiral isomers (**Scheme 3.4**) of isomer **1** and isomer **2** were performed by using Chiral Pak<sup>®</sup> IA LC column. Hexane: chloroform (3:2) mixture was used for isomer **1** and Hexane: Chloroform (1:9) mixture for isomer **2** with a constant flow rate of  $1 \text{ mL min}^{-1}$ . NMR data for isomer **1** and **2** gave multiplets around 10 to 10.3 ppm, corresponding to the protons attached to carbon atom of the isoindole group.

**Axial hydroxy substituted 1,2-subnaphthalocyanine (SubNPc)** (isomer **1**) and (isomer **2**):  $^1\text{H NMR}$  ( $\text{CDCl}_3$ , 400 MHz): 10.1(d, 3H, arom), 8.85 (d, 3H, arom), 8.80 (d, 3H, arom), 8.25(d, 3H, arom), 8.10(t, 3H, arom), 7.80(t, 3H, arom). UV-vis ( $\text{CHCl}_3$ ):  $\lambda_{\text{max}}$  [nm] ( $\epsilon$ ): 342 (0.92), 390 (0.96), 522 (1.30), 574 (4.44).

## 2.5.5. Functionalization of singled walled carbon nanotubes (SWCNT)

### 2.5.5.1. Purification of singled walled carbon nanotubes

SWCNTs (100 mg) were suspended in a mixture of concentrated  $\text{HNO}_3$ : $\text{H}_2\text{SO}_4$  (1:3) and stirred at  $70^\circ\text{C}$  for 2h. The SWCNT were separated from solution and washed with distilled water. The purified SWCNT were dried in the oven at  $70^\circ\text{C}$  over night. SWCNT: IR [(KBr)  $\nu_{\text{max}}/\text{cm}^{-1}$ ]: 3439 (OH), 1630 (C=O), 1382 [Raman  $\nu_{\text{max}}/\text{cm}^{-1}$ ]: 1595 (G), 1298 (D), 165 (RBM).

### 2.5.5.2. Adsorption of NiPc, derivatives to SWCNT.

SWCNT (1 mg) were functionalized with NiPc,  $\beta$ -NiPc(NH<sub>2</sub>)<sub>4</sub>,  $\beta$ -NiPc(OH)<sub>4</sub>,  $\alpha$ -NiPc(OH)<sub>4</sub>,  $\alpha$ -NiPc(OH)<sub>8</sub> or  $\alpha$ -NiPc(C<sub>10</sub>H<sub>21</sub>)<sub>8</sub> (represented as NiPc-SWCNT,  $\beta$ -NiPc(NH<sub>2</sub>)<sub>4</sub>-SWCNT,  $\beta$ -NiPc(OH)<sub>4</sub>-SWCNT,  $\alpha$ -NiPc(OH)<sub>4</sub>-SWCNT,  $\alpha$ -NiPc(OH)<sub>8</sub>-SWCNT and  $\alpha$ -NiPc(C<sub>10</sub>H<sub>21</sub>)<sub>8</sub>-SWCNT) by mixing (0.5 mg) of each in dry DMF (1.5 mL) for all NiPc derivatives with the exception of  $\alpha$ -NiPc(C<sub>10</sub>H<sub>21</sub>)<sub>8</sub> whereby dry THF (1.5 mL) was employed followed by ultrasonication for 30 min. The conjugates were washed several times with DMF or THF depending on the conjugate to remove excess catalyst.

**$\beta$ -NiPc(OH)<sub>4</sub>-SWCNT** : IR [(KBr)  $\nu_{\max}/\text{cm}^{-1}$ ]: 3719 (OH), 3058, 2955(C-H), 2867 (CH) , 1741, 1525, 1340, 1144. [Raman  $\nu_{\max}/\text{cm}^{-1}$ ]: 1596 (G), 1560 (C-N-C), 1342 (D), 753,171 (RBM = ring breathing mode).

**$\alpha$ -NiPc(OH)<sub>4</sub>-SWCNT** : IR [(KBr)  $\nu_{\max}/\text{cm}^{-1}$ ]: 3415 (OH), 3233 (C-H), 7614, 622. [Raman  $\nu_{\max}/\text{cm}^{-1}$ ]: 1596 (G), 1340, 1287 (D), 1675, 756, 171 (RBM)

**$\alpha$ -NiPc(OH)<sub>8</sub>-SWCNT** : IR [(KBr)  $\nu_{\max}/\text{cm}^{-1}$ ]: 3134 (OH), 2849(C-H), 2922 (C-H), 1558, 1729, 1507, 1402, 1287, 1084[Raman  $\nu_{\max}/\text{cm}^{-1}$ ]:1598(G), 1298(D), 770, 171 (RBM).

**$\alpha$ -NiPc(C<sub>10</sub>H<sub>21</sub>)<sub>8</sub>-SWCNT**: IR [(KBr)  $\nu_{\max}/\text{cm}^{-1}$ ]: 3444, 2934 (C-H), 2842 (C-H), 1612, 1389, [Raman  $\nu_{\max}/\text{cm}^{-1}$ ]: 1595 (G), 1298 (D), 165 (RBM).

The adsorbed and linked  **$\beta$ -NiPc(NH<sub>2</sub>)<sub>4</sub>-SWCNT** has been reported before [212].

### 2.5.6. CdTe-QDs- $\beta$ -NiPc conjugates

#### 2.5.6.1. Synthesis of CdTe-QDs

The preparation of thiol capped QD was performed from literature [248]. Briefly, 2.35 mmol of CdCl<sub>2</sub>-H<sub>2</sub>O was dissolved in 125 ml of water and 5.7 mmol of thioglycolic acid (TGA) was added under stirring. The solution was adjusted to pH 12 by addition of 0.1M NaOH dropwise. Nitrogen gas was bubbled through the solution for about 1 h. The aqueous solution was reacted with H<sub>2</sub>Te gas. H<sub>2</sub>Te gas was generated by the reaction of NaBH<sub>4</sub> with Te powder in the presence of 0.5 M H<sub>2</sub>SO<sub>4</sub> under a flow of nitrogen gas. The molar ratio of

$\text{Cd}^{2+}$ :  $\text{Te}^{2-}$ : TGA was 1: 0.5: 2.4 (Te as powder). A change of colour was observed at this stage. The solution was then refluxed under air at  $100^\circ\text{C}$  for different times to control the size of the CdTe-QDs. Different sizes are formed at different reaction times, the solution was continuously sampled to record the emission spectra of the quantum dots until the desired wavelength (hence size) was attained.

### 2.5. 6. 2. Synthesis of CdTe-QDs- $\beta$ -NiPc(NH<sub>2</sub>)<sub>4</sub> conjugates

$\beta$ -NiPc(NH<sub>2</sub>)<sub>4</sub>-CdTe-TGA conjugate was synthesised by dissolving CdTe-TGA (0.002 g) and DCC (0.1 g) in DMF: water mixture (4:1), followed by stirring for 7 h at room temperature. After this time NHS (0.1 g) was added to the solution and further stirred for 1 h, followed by addition of  $\beta$ -NiPc(NH<sub>2</sub>)<sub>4</sub> (0.02 g) to the solution. Stirring continued for four days. After this time, methanol was added to the mixture, resulting in the precipitation of linked conjugates of CdTe-QDs and  $\beta$ -NiPc(NH<sub>2</sub>)<sub>4</sub> (represented as CdTe-QDs- $\beta$ -NiPc(NH<sub>2</sub>)<sub>4</sub>(linked)). The precipitate was washed further with DMF (to remove unreacted  $\beta$ -NiPc(NH<sub>2</sub>)<sub>4</sub>(linked)) and methanol (to remove unreacted CdTe-QDs, DCC and NHS). CdTe-QDs- $\beta$ -NiPc(NH<sub>2</sub>)<sub>4</sub> is not soluble in the two solvents. The precipitate was dried at  $70^\circ\text{C}$  in an oven overnight to afford CdTe-QDs- $\beta$ -NiPc(NH<sub>2</sub>)<sub>4</sub>(linked).

**CdTe-QDs- $\beta$ -NiPc(NH<sub>2</sub>)<sub>4</sub>:** Far IR [(Nujol)  $\nu_{\text{max}}/\text{cm}^{-1}$ ]: 295, 251, 220, 197, 169, [Raman  $\nu_{\text{max}}/\text{cm}^{-1}$ ]: 1595 (G), 1298 (D), 165 (RBM).

### 2.5.6.3. Adsorption of TGA-CdTe-QDs to $\alpha$ -NiPc(C<sub>10</sub>H<sub>21</sub>)<sub>8</sub>-SWCNT conjugate

TGA CdTe-QDs were adsorbed onto SWCNT- $\alpha$ -NiPc(C<sub>10</sub>H<sub>21</sub>)<sub>8</sub> to form SWCNT- $\alpha$ -NiPc(C<sub>10</sub>H<sub>21</sub>)<sub>8</sub>-QDs as follows:  $\alpha$ -NiPc(C<sub>10</sub>H<sub>21</sub>)<sub>8</sub>-SWCNT (0.1mg) was added to an aqueous solution of TGA CdTe-QDs (0.01 mg in 5 ml) and ultrasonicated for 30 min to obtain SWCNT-NiPc(C<sub>10</sub>H<sub>21</sub>)<sub>8</sub>-QDs. The colloidal solution with  $\alpha$ -NiPc(C<sub>10</sub>H<sub>21</sub>)<sub>8</sub>-SWCNT-QDs suspension was decanted and repeatedly washed with millipore water to remove excess CdTe-QDs.  $\alpha$ -NiPc(C<sub>10</sub>H<sub>21</sub>)<sub>8</sub>-SWCNT-QDs suspension was then dried at  $80^\circ\text{C}$  in an oven.  **$\alpha$ -NiPc(C<sub>10</sub>H<sub>21</sub>)<sub>8</sub>-SWCNT-QDs:** [Raman  $\nu_{\text{max}}/\text{cm}^{-1}$ ]: 1595 (G), 1270 (D), 1170, 1073

## **Results and Discussion**

### **Chapter 3: Synthesis and Characterization**



**Papers published on the work presented in this thesis and will not be cited further.**

1. S. Shimizu, A. Miura, S. Khene, T. Nyokong, N. Kobayashi, Chiral 1,2-Subnaphthalocyanines J. Am. Chem. Soc., 2011, 133, 17322–17328.
2. S. Khene, T. Nyokong, Single walled carbon nanotubes functionalized with nickel phthalocyanines: Effects of point of substitution and nature of functionalization on the electro-oxidation of 4-chlorophenol, J. Porphyrins Phthalocyanines, 2011; In press
3. S. Khene, S. Moeno, T. Nyokong, Voltammetry and electrochemical impedance spectroscopy of gold electrodes modified with CdTe quantum dots and their conjugates with nickel tetraamino phthalocyanine, Polyhedron, 2011, 30, 2162-2170
4. S. Khene, T. Nyokong, Redox activity of CdTe quantum dots linked to nickel tetraaminophthalocyanine: Effects of adsorption versus electrodeposition on the catalytic oxidation of chlorophenols, Microchemical journal, 2011, In press
5. S. Khene, T. Nyokong Electrooxidation of Chlorophenols Catalyzed by Nickel Octadecylphthalocyanine Adsorbed on Single-Walled Carbon Nanotubes, Electroanalysis, 2011, 23, 1901-1911
6. S. Khene, K. Lobb, Nyokong, Interaction between nickel hydroxyl phthalocyanine derivatives with p-chlorophenol: linking electrochemistry experiments with theory Electrochimica Acta, 2010, 56, 706-716
7. S. Khene, K. Lobb, Nyokong, Characterisation of nickel tetrahydroxy phthalocyanine complexes and the electrocatalytic oxidation of 4-chlorophenol: Correlation of theory with experiments, Electrochimica Acta, 2009, 362, 5055-5063.
8. S. Khene, T. Nyokong, Electrode modification using conjugates of quantum dots, single walled carbon nanotubes and nickel octadecylphthalocyanine, J. Nanotechnology, Accepted .

**Other papers published in collaboration not related to this thesis**

1. R. C. George, T. Mugadza, S. Khene, Gabriel O. Egharevba, Tebello Nyokong, Porphyrin Nanorods Modified Glassy Carbon Electrode for the Electrocatalysis of Dioxygen, Methanol and Hydrazine, Electroanalysis, 2011, 23, 1699-1708.
2. I A. Akinbulu, S. Khene, T. Nyokong, The effects of point of substitution on the formation of manganese phthalocyanine-based molecular materials: Surface characterization and electrocatalysis, 2010, Thin Solid Films, 2010, 519, 911-918

3. S. Moeno, E. Antunes, S. Khene, C. Litwinski, T. Nyokong, The effect of substituents on the photoinduced energy transfer between CdTe quantum dots and mercapto substituted zinc phthalocyanine derivatives Dalton Trans. 2010, 39(14), 3460-3471
4. I. A. Akinbulu, S. Khene, T. Nyokong, Surface properties of self-assembled monolayer films of tetra-substituted cobalt, iron and manganese alkylthio phthalocyanine complexes Electrochimica acta, 2010, 55, 7085-7093.
5. R. Zügler, E. Antunes, S. Khene, Tebello Nyokong, Photooxidation of 4-chlorophenol sensitized by lutetium tetraphenoxy phthalocyanine anchored on electrospun polystyrene polymer fiber, Polyhedron. In press

## 3. Synthesis and Characterization

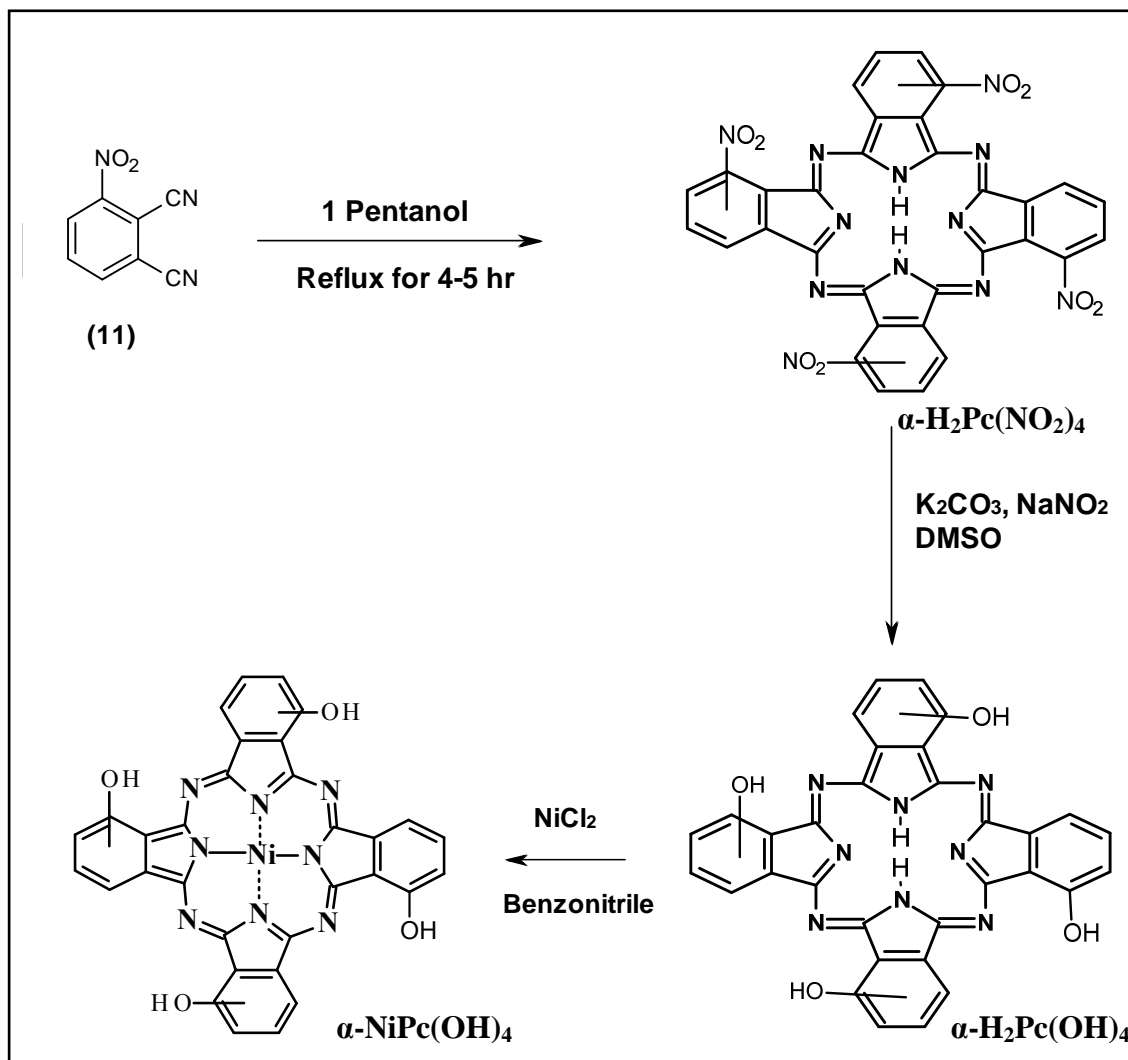
Table 3.1 List of Synthesised phthalocyanine, SubNPc and and NiPc-Nanomaterial

<b>Phthalocyanine</b>
NiPc (Known)
$\beta$ -NiPc(OH) <sub>4</sub> (Known)
$\alpha$ -NiPc(OH) <sub>4</sub>
$\alpha$ -NiPc(OH) <sub>8</sub>
$\alpha$ -NiPc(C <sub>10</sub> H <sub>21</sub> ) <sub>8</sub>
$\beta$ -NiPc(NH <sub>2</sub> ) <sub>4</sub> (Known)
SubNPc
<b>Phthalocyanine-Nanomaterial</b>
$\beta$ -NiPc(OH) <sub>4</sub> -SWCNT
$\alpha$ -NiPc(OH) <sub>4</sub> -SWCNT
$\alpha$ -NiPc(OH) <sub>8</sub> -SWCNT
$\alpha$ -NiPc(C <sub>10</sub> H <sub>21</sub> ) <sub>8</sub> -SWCNT
$\beta$ -NiPc(NH <sub>2</sub> ) <sub>4</sub> -SWCNT (linked)
QDs- $\beta$ -NiPc(NH <sub>2</sub> ) <sub>4</sub> (linked)
$\alpha$ -NiPc(C <sub>10</sub> H <sub>21</sub> ) <sub>8</sub> -SWCNT-QDs

### 3.1. NiPc derivatives

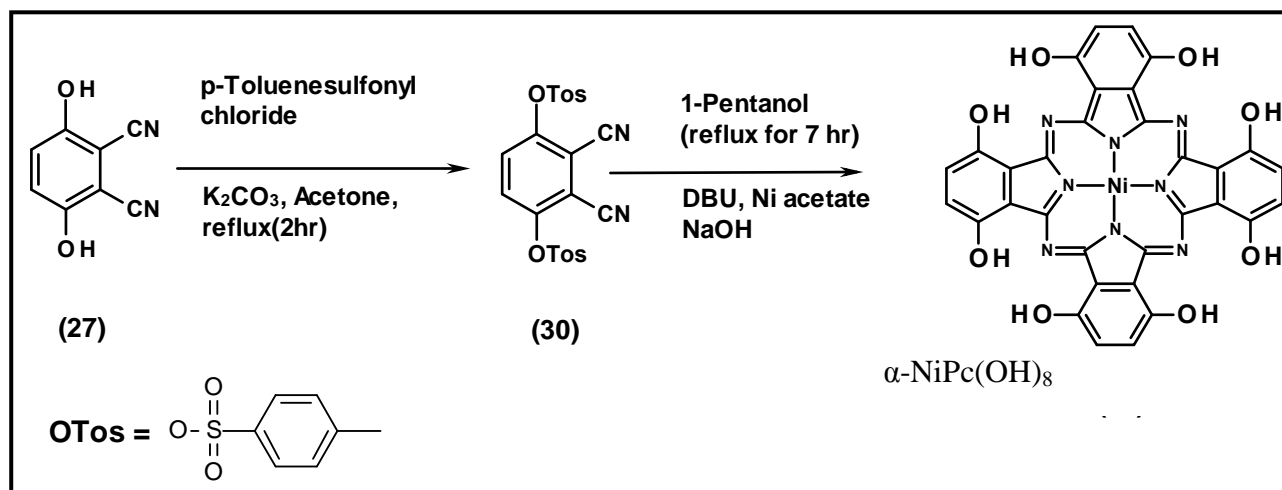
NiPc,  $\beta$ -NiPc(NH<sub>2</sub>)<sub>4</sub> and  $\beta$ -NiPc(OH)<sub>4</sub> are known and their synthesis will not be presented.

#### 3.1.1. Synthesis



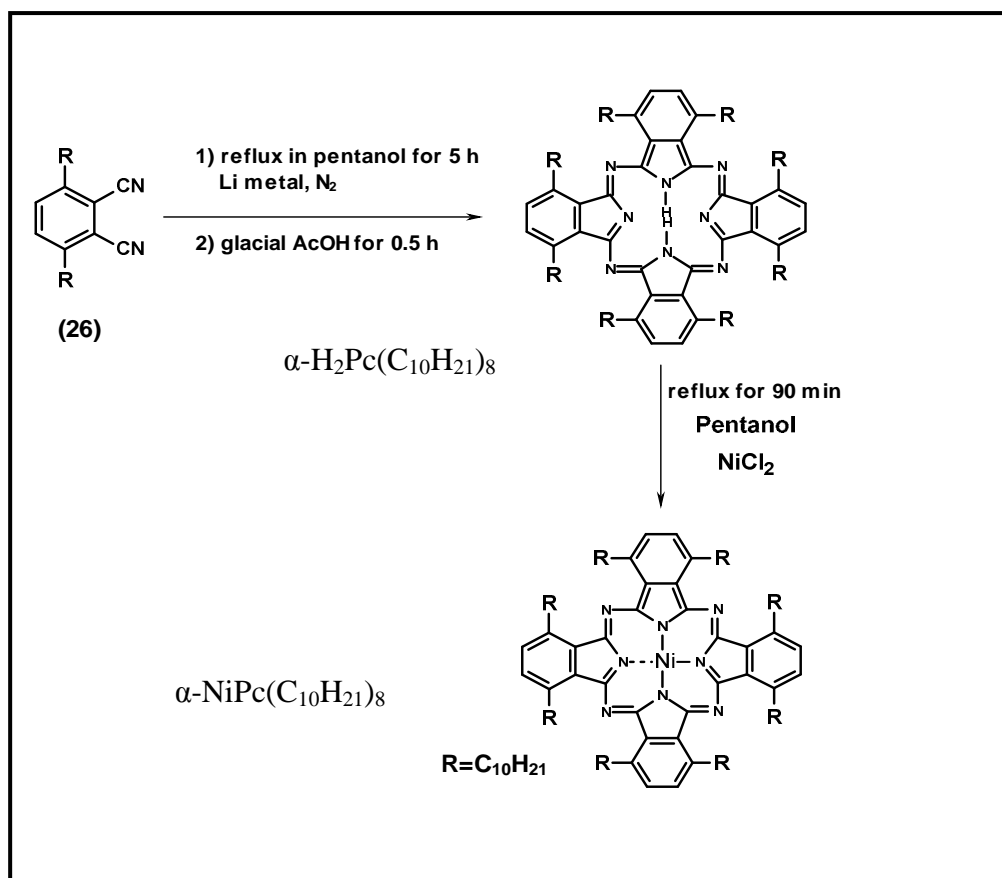
**Scheme 3.1:** Preparation of nickel(II) 2,9,16,23-tetrahydroxy phthalocyanine,  $\alpha$ -NiPc(OH)<sub>4</sub>.

Following literature methods [249]  $\alpha$ -NiPc(OH)<sub>4</sub> was synthesised from 3-nitrothalonitrile (11) (Scheme 3.1). The first step was synthesis of metal free  $\alpha$ -H<sub>2</sub>Pc(NO<sub>2</sub>)<sub>4</sub> which was converted to  $\alpha$ -H<sub>2</sub>Pc(OH)<sub>4</sub> according to Scheme 3.1 with a yield of 63%. The formation of  $\alpha$ -NiPc(OH)<sub>4</sub> was confirmed by IR and mass spectroscopy. NMR could not be done for some complexes due to poor solubility.



Scheme 3.2: Synthesis pathway for non-peripherally substituted  $\alpha\text{-NiPc(OH)}_8$ .

The synthesis of non-peripherally octahydroxy nickel phthalocyanine ( $\alpha\text{-NiPc(OH)}_8$ ) is shown in **Scheme 3.2**. The first step was to synthesise (30) from the precursor (27) following literature methods [247]. Compound (30) was then used to synthesise  $\alpha\text{-NiPc(OH)}_8$ , **Scheme 3.2**, with a yield of 60%.  $^1\text{H-NMR}$  spectrum in DMSO exhibits a broad multiple at 7.30-7.80 ppm, due to the 8 protons at the  $\beta$  position of the benzene ring (Ar-CH) and an aromatic broad OH signal at 5.80 ppm which disappeared upon addition of  $\text{D}_2\text{O}$ .  $\alpha\text{-NiPc(OH)}_8$  was confirmed by IR and mass spectroscopy.

3.1.2. Synthesis of nickel octadecylphthalocyanine ( $\alpha$ -NiPc(C<sub>10</sub>H<sub>21</sub>)<sub>8</sub>)

Scheme 3.3: 1, 4, 8, 11, 15, 18, 22, 25-Octadecylphthalocyanine Nickel(II)

Nickel octadecylphthalocyanine ( $\alpha$ -NiPc(C<sub>10</sub>H<sub>21</sub>)<sub>8</sub>) was synthesised by first synthesising  $\alpha$ -H<sub>2</sub>Pc(C<sub>10</sub>H<sub>21</sub>)<sub>8</sub>.  $\alpha$ -H<sub>2</sub>Pc(C<sub>10</sub>H<sub>21</sub>)<sub>8</sub> was metallated with nickel chloride to afford  $\alpha$ -NiPc(C<sub>10</sub>H<sub>21</sub>)<sub>8</sub> (Scheme 3.3) with a good percentage yield of 70%. The UV/vis spectra of  $\alpha$ -NiPc(C<sub>10</sub>H<sub>21</sub>)<sub>8</sub> in THF (Figure 3.1), shows a typical phthalocyanine main adsorption band (Q band) at 702 nm, vibronic band at 630 nm and a B band at 341 nm. The IR spectrum of  $\alpha$ -NiPc(C<sub>10</sub>H<sub>21</sub>)<sub>8</sub> showed C-H stretches at 2842 and 2934 cm<sup>-1</sup>. Phthalocyanine ring system stretches were observed from 400 to 1600 cm<sup>-1</sup>. Elemental analysis further confirmed the formation of this complex.

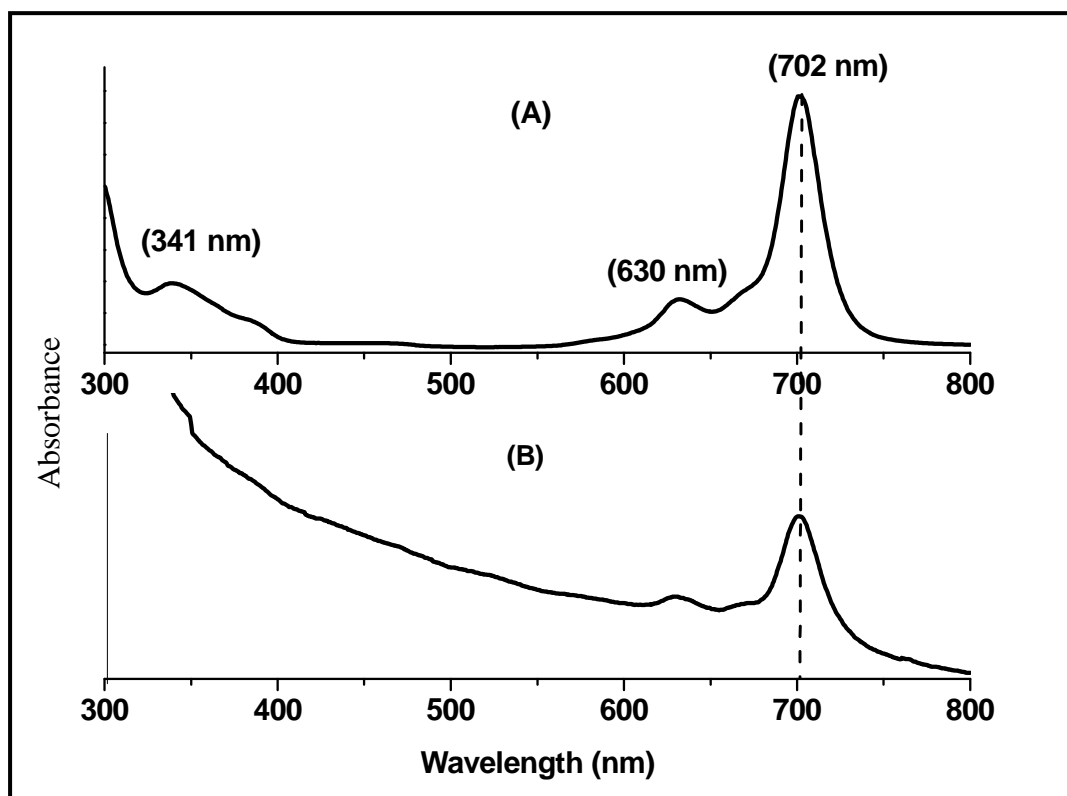
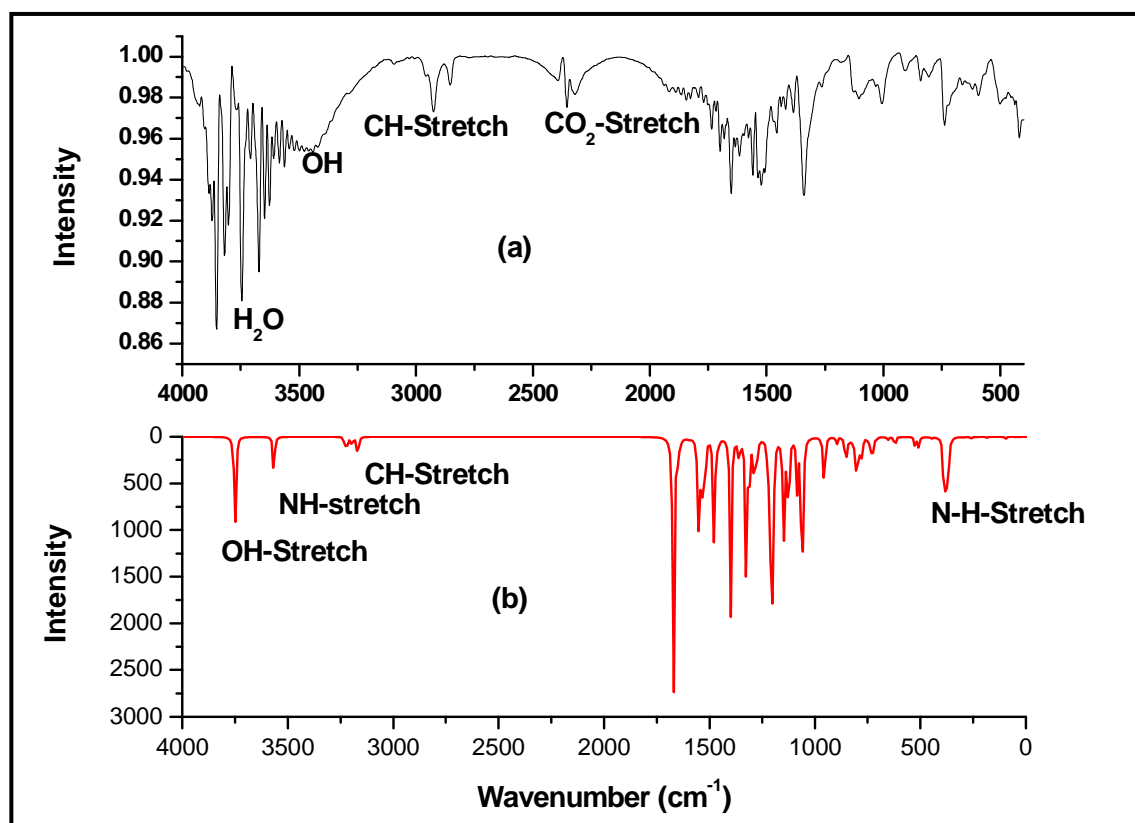


Figure 3.1: Ground state absorpuion spectra of  $\alpha$ -NiPc(C<sub>10</sub>H<sub>21</sub>)<sub>8</sub> (A) and  $\alpha$ -NiPc(C<sub>10</sub>H<sub>21</sub>)<sub>8</sub>-SWCNT (B) in THF.

### 3.1.3. Modelling of IR spectra

$\beta$ -NiPc(OH)<sub>4</sub> was chosen as model complex for theoretical modelling of IR and Raman spectra of NiPcs, in order to assign the peaks observed from experimental data. The IR and Raman spectra of  $\beta$ -NiPc(OH)<sub>4</sub> are similar to that of  $\alpha$ -NiPc(OH)<sub>4</sub> and  $\alpha$ -NiPc(OH)<sub>8</sub>.

In **Figure 3.2** the experimental FTIR spectrum (a) of  $\beta$ -H<sub>2</sub>Pc(OH)<sub>4</sub> is compared with the theoretical spectrum (b) of  $\beta$ -H<sub>2</sub>Pc(OH)<sub>4</sub>. In general, the calculated bands (gas phase) are in good agreement with the observed ones (solid phase – KBr pellets), apart from frequency variation.



**Figure 3.2:** IR spectrum of  $\beta$ -H<sub>2</sub>Pc(OH)<sub>4</sub> (a) Experimental (b) and Theoretical .

For  $\beta$ -NiPc(OH)<sub>4</sub> the Ni-N band is predicted from the theoretical calculations of IR spectra (in **Figure 3.3**) to be an in plane stretch at 337 cm<sup>-1</sup>, this band is outside the wavelength range used at experimental level, **Figure 3.4a**, but is observed as a split band for the calculated spectrum, **Figure 3.4b**. The Ni-N band is known to be dependent on the substituent position and the type of ligand substituted on the periphery of the ring [62]. The comparison of experimental (**Figure 3.2a and 3.4a**) with theoretical (**Figure 3.2b and 3.4b**) results show very good agreement.



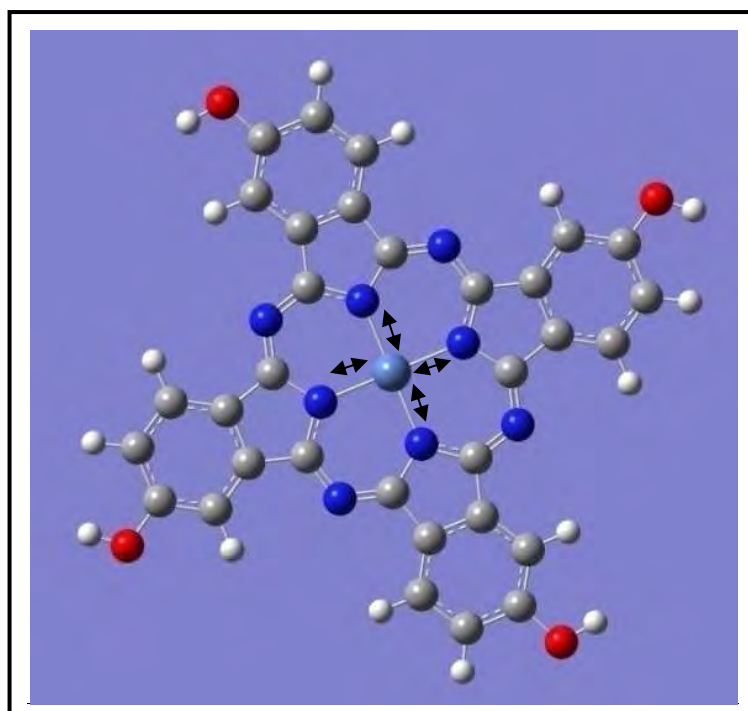


Figure 3.3: N-Ni: stretch:  $\nu=337\text{ cm}^{-1}$  in plane stretches.

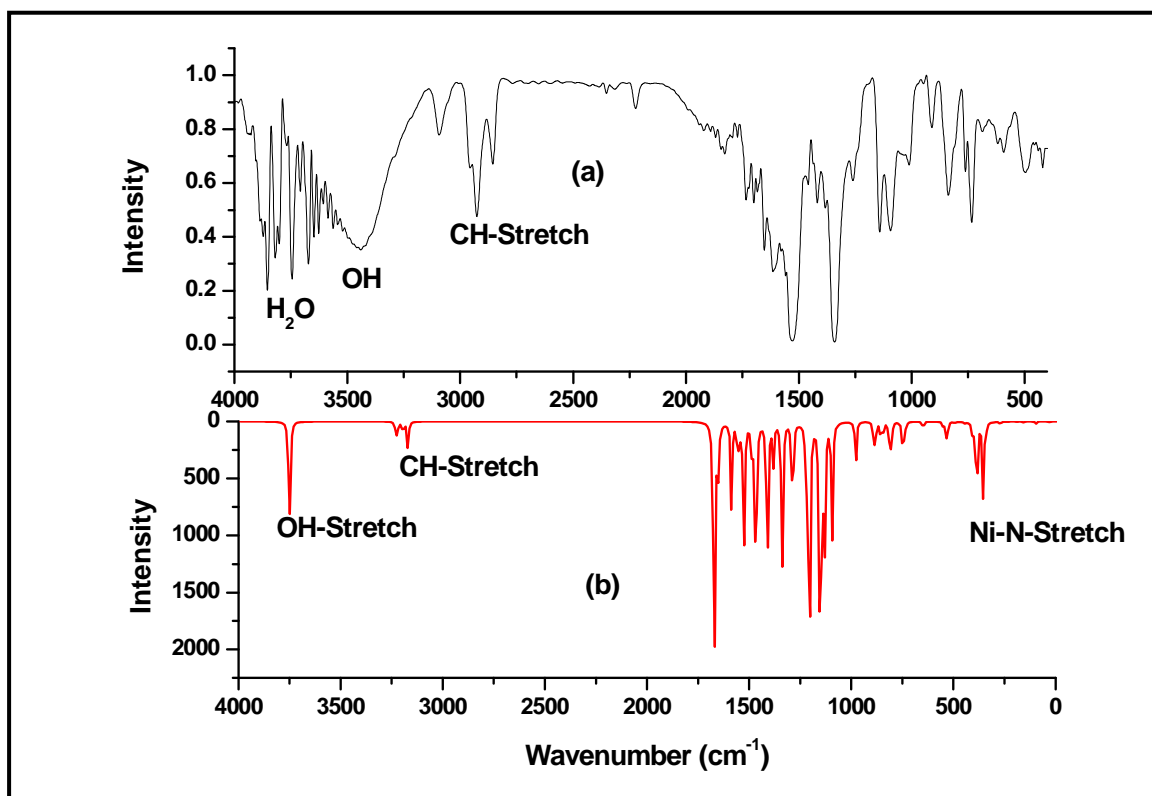
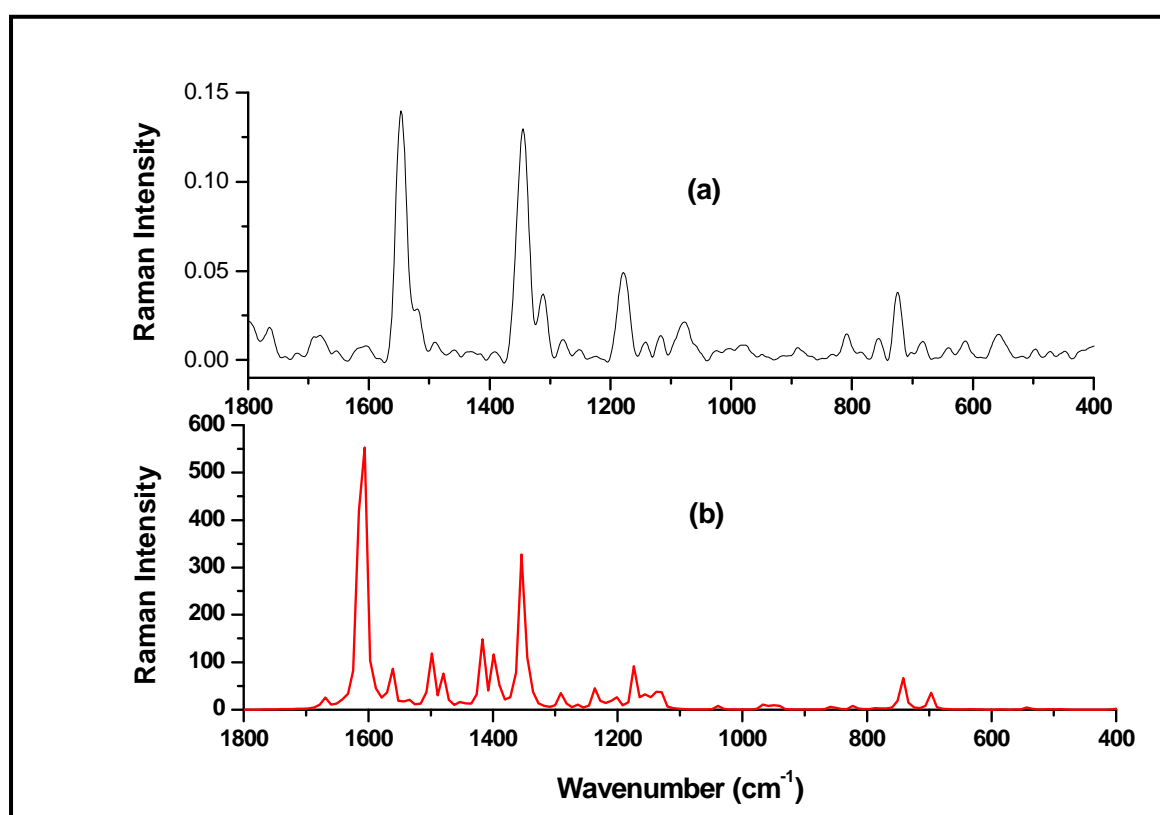


Figure 3.4: IR spectrum of  $\beta\text{-NiPc(OH)}_4$  (a) Experimental and (b) Theoretical

### 3.1.4. Modelling of Raman spectra

Raman spectra of a range of phthalocyanines are known to be related to structural data. **Figure 3.5** shows the experimental and theoretical Raman spectra for  $\beta\text{-H}_2\text{Pc(OH)}_4$  and **Figure 3.6** experimental and theoretical spectra of  $\beta\text{-NiPc(OH)}_4$ . In this work DFT method is used for vibrational assignment of  $\beta\text{-H}_2\text{Pc(OH)}_4$  and  $\beta\text{-NiPc(OH)}_4$  Raman spectra, in **Figure 3.5b**, **3.6b**. The experimental data (**Figure 3.5a**, **3.6a**) showed very good agreement with theoretical results (**Figure 3.5b**, **3.6b**, respectively). In order to minimise self absorption and to obtain a good signal-to-noise ratio, KBr powder was used to dilute  $\beta\text{-H}_2\text{Pc(OH)}_4$  and  $\beta\text{-NiPc(OH)}_4$  samples for recording of Raman experimental data.



**Figure 3.5:** Raman spectrum of  $\beta\text{-H}_2\text{Pc(OH)}_4$  (a) Experimental and (b) Theoretical.

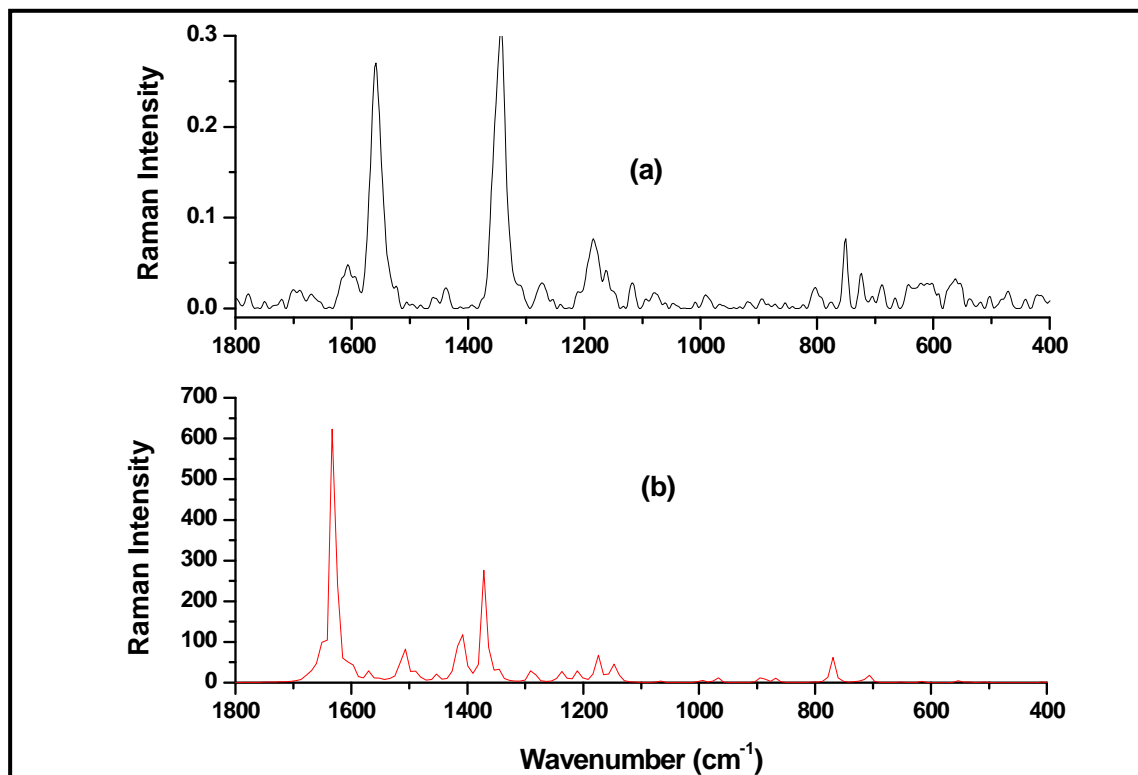


**Figure 3.6: Raman spectrum of  $\beta$ -NiPc(OH)<sub>4</sub> (a) Experimental and (b) Theoretical.**

The Raman spectra of  $\beta$ -H<sub>2</sub>Pc(OH)<sub>4</sub> and  $\beta$ -NiPc(OH)<sub>4</sub> show intense bands at 1557 and 1558 cm<sup>-1</sup>, respectively. This region is known to show a remarkable sensitivity to the metal ion present and provides a specific signature for phthalocyanine studied [63, 69, 72]. The sensitivity to the metal ion has been ascribed to a change in shape of the entire ring. This sensitivity has been correlated with the bond strength [72] and in this case the small metal ion coupled with electron donating substituent in  $\beta$ -NiPc(OH)<sub>4</sub> causes an in-plane distortion of the ring. The nickel atom has a formal charge of +2 in the neutral  $\beta$ -NiPc(OH)<sub>4</sub> complex. The calculated Mulliken atomic charges (Q in **Table 3.2**) show the effective atomic charge to be 0.82 for  $\beta$ -NiPc(OH)<sub>4</sub>. This value is almost the same as that calculated for NiPc (0.80), **Table 3.2**, suggesting a similar covalent character of metal ligand bond for both NiPc and  $\beta$ -NiPc(OH)<sub>4</sub>. Theoretical calculations shows that the bond length in  $\beta$ -NiPc(OH)<sub>4</sub> (Ni-N = 1.905 Å) is equal to the bond length of NiPc (Ni-N = 1.905 Å), **Table 3.3**, this means that the Ni-bond is not affected by the OH substituent and that there is no substantial change in the electronic delocalization of the two complexes.

Table 3.2: Gross Mulliken populations and atomic charge (Q)

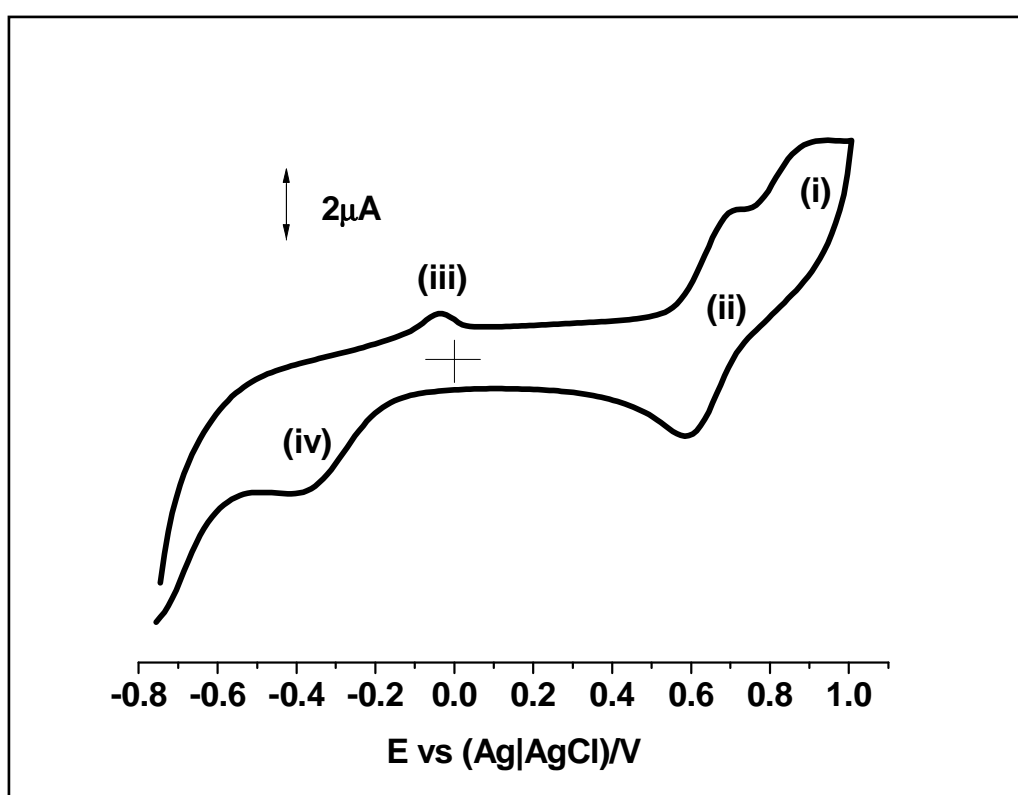
Charge	$\beta$ -H <sub>2</sub> Pc(OH) <sub>4</sub>	$\beta$ -NiPc(OH) <sub>4</sub>	NiPc
Q <sub>M</sub>	0.43	0.82	0.80
Q <sub>N1</sub>	-0.75	-0.71	-0.70
Q <sub>N2</sub>	-0.57	-0.55	-0.55
Q <sub>C1</sub>	0.51	0.52	0.48
Q <sub>C2</sub>	0.054	0.08	0.08
Q <sub>C3</sub>	-0.27	-0.22	-0.19
Q <sub>C4</sub>	0.36	0.38	-0.14
Q <sub>H1</sub>	0.15	0.19	0.16
Q <sub>H2</sub>	-0.64	-0.61	0.14

Table 3.3: Calculated parameters (bond length R in Å, bond angle  $\theta$  in deg)

	$\beta$ -H <sub>2</sub> Pc(OH) <sub>4</sub>	$\beta$ -NiPc(OH) <sub>4</sub>	NiPc
R <sub>N1-N1</sub> /R <sub>H-N1</sub>	1.0112	1.905	1.905
R <sub>N-C1</sub>	1.396	1.380	1.381
R <sub>C1-N2</sub>	1.295	1.317	1.318
R <sub>C1-C2</sub>	1.470	1.454	1.452
R <sub>C2-C2'</sub>	1.413	1.401	1.400
R <sub>C2-C3</sub>	1.393	1.392	1.396
R <sub>C3-C4</sub>	1.398	1.397	1.393
R <sub>C4-C4'</sub>	1.410	1.414	1.410
R <sub>C4-O</sub>	1.387	1.366	-
R <sub>C-H</sub>	1.087	1.084	1.081
$\theta_{C-N1-C1'}$	113.0	106.6	106.5
$\theta_{N2-C1-N1}$	129.7	127.8	127.7
$\theta_{N1-C1-C2}$	105.2	110.5	110.5
$\theta_{C4-O-H}$	106.7	109.2	-

### 3.1.5. Solution cyclic voltammetry characterization

$\alpha$ -NiPc(C<sub>10</sub>H<sub>21</sub>)<sub>8</sub> was characterized in solution. However for all other NiPc derivatives the ring based redox processes were not clear in solution, but seen when adsorbed on GCE electrode. This will be discussed in chapter 4. **Figure 3.7** shows the cyclic voltammogram for  $\alpha$ -NiPc(C<sub>10</sub>H<sub>21</sub>)<sub>8</sub> in THF containing TBABF<sub>4</sub>, with four redox processes due to ring oxidation and reduction labelled **i**, **ii**, **iii** and **iv** at 0.88 (E<sub>p</sub>), 0.65 (E<sub>1/2</sub>), -0.04(E<sub>p</sub>) and -0.34 (E<sub>p</sub>) V, respectively. The processes are generally irreversible as has been observed for other NiPc derivatives [250, 251]. All the processes are ring based for  $\alpha$ -NiPc(C<sub>10</sub>H<sub>21</sub>)<sub>8</sub> since NiPc derivatives do not show metal based processes unless transformed into O-Ni-O oxo bridge.



**Figure 3.7:** Cyclic voltammograms of  $\alpha$ -NiPc(C<sub>10</sub>H<sub>21</sub>)<sub>8</sub> in THF with TBABF<sub>4</sub> as electrolyte.

### 3.2. NiPc-SWCNT Conjugates

The first step is the functionalisation or purification of SWCNT with carboxylic acids. [191-193]. The formation of  $\beta$ -NiPc(NH<sub>2</sub>)<sub>4</sub>-SWCNT (linked) has been reported before [212], and was characterised sufficiently.

The structures formed by chemical coordination of  $\beta$ -NiPc(NH<sub>2</sub>)<sub>4</sub> to SWCNT may be represented by the dendrimer shown in **Figure 3.8a** [212]. This has been suggested before for the coordination of  $\beta$ -FePc(NH<sub>2</sub>)<sub>4</sub> to SWCNT using UV-Vis spectroscopy [212]. For adsorbed species, NiPc derivatives are adsorbed onto SWCNT through  $\pi$ - $\pi$  interactions, **Figure 3.8b**. The  $\pi$ - $\pi$  interaction preserves the sp<sup>2</sup> nanotube structure and thus their electronic characteristics.

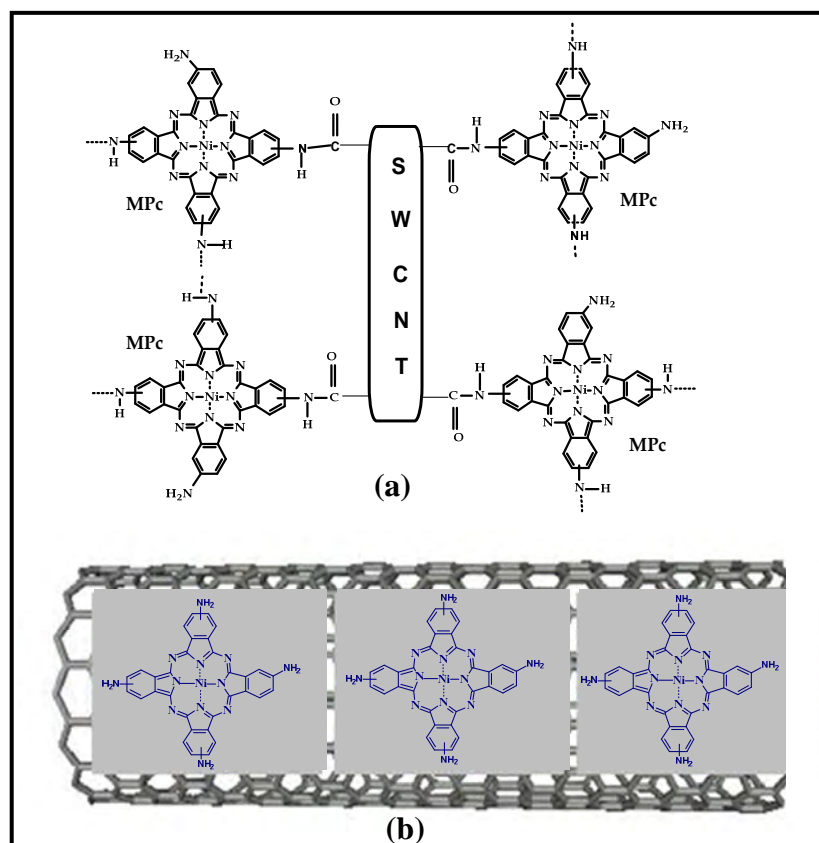


**Figure 3.8:** (a) possible structures formed on linking  $\beta$ -NiPc(NH<sub>2</sub>)<sub>4</sub> to SWCNT and (b) representation of adsorbed  $\beta$ -NiPc(NH<sub>2</sub>)<sub>4</sub> on SWCNT.

Adsorbed  $\beta$ -NiPc(NH<sub>2</sub>)<sub>4</sub>-SWCNT,  $\beta$ -NiPc(OH)<sub>4</sub>-SWCNT,  $\alpha$ -NiPc(OH)<sub>4</sub>-SWCNT and  $\alpha$ -NiPc(OH)<sub>8</sub>-SWCNT conjugates, were formed by mixing SWCNT with  $\beta$ -NiPc(OH)<sub>4</sub>,  $\alpha$ -NiPc(OH)<sub>4</sub> or  $\alpha$ -NiPc(OH)<sub>8</sub>, followed by washing with DMF, forming the structure suggested **Figure 3.8b**.

### 3.2.1. IR spectra

$\alpha$ -NiPc(OH)<sub>4</sub> and NiPc(C<sub>10</sub>H<sub>21</sub>)<sub>8</sub>-SWCNT were used as examples. **Figure 3.9** shows a FT-IR spectra of SWCNT (A),  $\alpha$ -NiPc(OH)<sub>4</sub> (B) and  $\alpha$ -NiPc(OH)<sub>4</sub>-SWCNT (C). The SWCNT shows bands at 1382 and 1630 cm<sup>-1</sup> (**Figure 3.9 A**). The band at 1630 cm<sup>-1</sup> corresponds to the carbonyl (C=O) stretch of the carboxylic acid and the band at 1382 cm<sup>-1</sup> corresponds to C-C stretch for SWCNT. **Figure 3.9 B** shows the IR spectrum of  $\alpha$ -NiPc(OH)<sub>4</sub> with OH stretches between 3000 and 3500 cm<sup>-1</sup>. Stretches from 500 to 1600 cm<sup>-1</sup> are due to the phthalocyanine ring system and are known to be the finger print region for these complexes [252]. The IR spectra of  $\alpha$ -NiPc(OH)<sub>4</sub>-SWCNT, **Figure 3.9 C**, shows peaks corresponding to both SWCNT and  $\alpha$ -NiPc(OH)<sub>4</sub> suggesting that  $\alpha$ -NiPc(OH)<sub>4</sub> is adsorbed on the SWCNT.  $\beta$ -NiPc(NH<sub>2</sub>)<sub>4</sub>-SWCNT,  $\alpha$ -NiPc(OH)<sub>8</sub>-SWCNT and  $\beta$ -NiPc(OH)<sub>4</sub>-SWCNT gave similar IR spectra as  $\alpha$ -NiPc(OH)<sub>4</sub>-SWCNT.

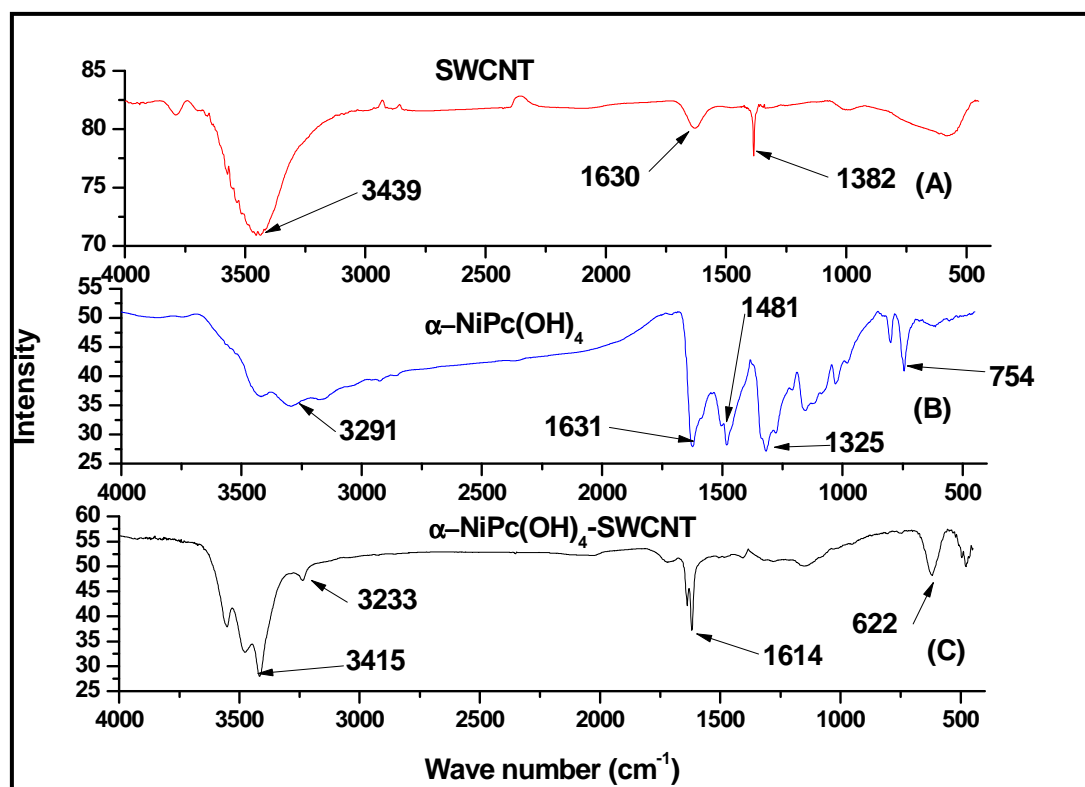


**Figure 3.9:** FT-IR spectra of SWCNT (A),  $\alpha$ -NiPc(OH)<sub>4</sub> (B) and  $\alpha$ -NiPc(OH)<sub>4</sub>-SWCNT (C) adsorbed conjugate.

**Figure 3.10** shows FT-IR spectra of SWCNT (**Figure 3.10A**),  $\alpha$ -NiPc(C<sub>10</sub>H<sub>21</sub>)<sub>8</sub> (**Figure 3.10B**) and  $\alpha$ -NiPc(C<sub>10</sub>H<sub>21</sub>)<sub>8</sub>-SWCNT conjugate (**Figure 3.10C**). **Figure 3.10B** shows the IR

spectrum of  $\text{NiPc}(\text{C}_{10}\text{H}_{21})_8$  with C-H stretches at 2842 and 2934  $\text{cm}^{-1}$ . Stretches from 400 to 1600  $\text{cm}^{-1}$  are due to the phthalocyanine ring system [252]. **Figure 3.10C** shows the IR spectrum of  $\alpha\text{-NiPc}(\text{C}_{10}\text{H}_{21})_8\text{-SWCNT}(\text{ads})$  conjugate showing peaks corresponding to both SWCNT and  $\alpha\text{-NiPc}(\text{C}_{10}\text{H}_{21})_8$  suggesting that  $\alpha\text{-NiPc}(\text{C}_{10}\text{H}_{21})_8$  is adsorbed on the SWCNT.

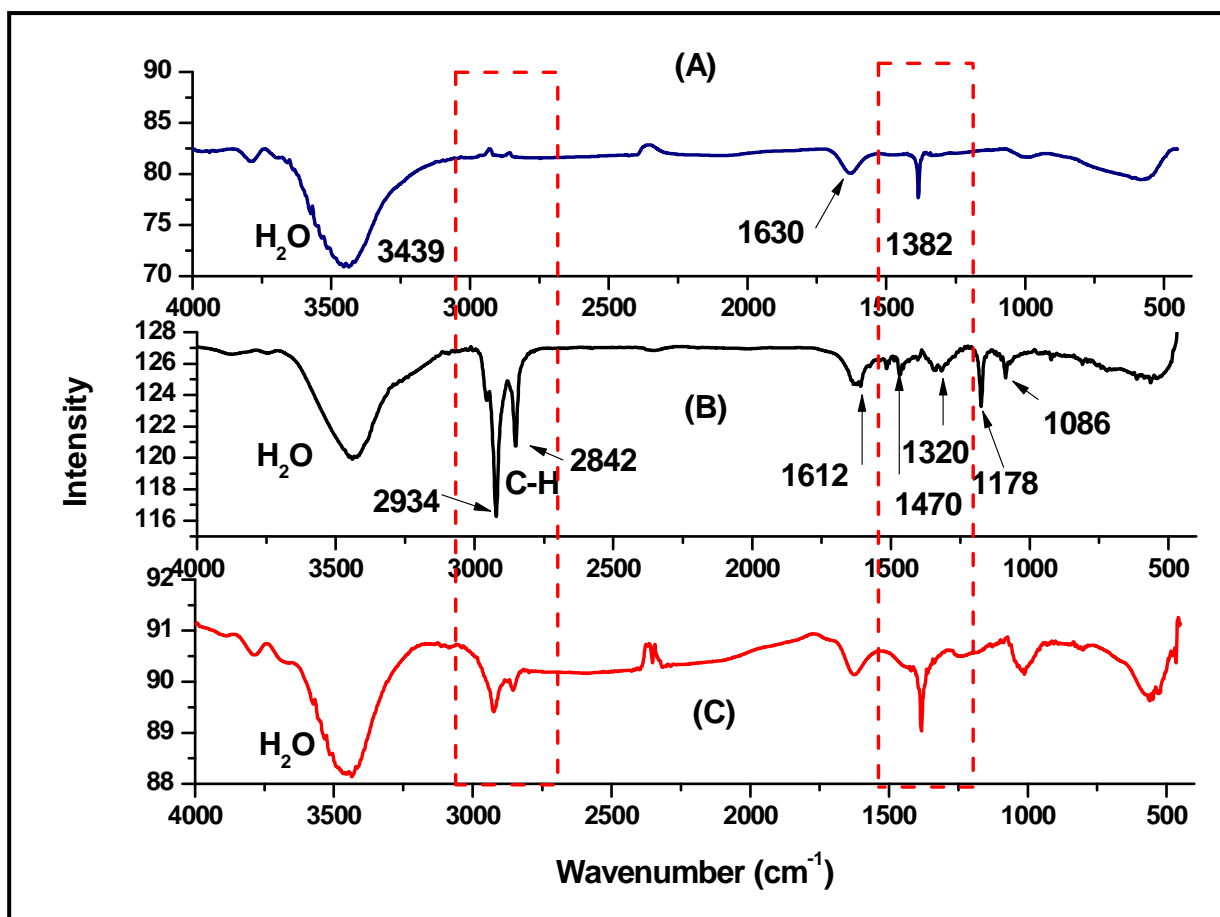


**Figure 3.10:** IR spectra of SWCNT (A),  $\alpha\text{-NiPc}(\text{C}_{10}\text{H}_{21})_8$  (B) and  $\alpha\text{-NiPc}(\text{C}_{10}\text{H}_{21})_8\text{-SWCNT}$  (C).

### 3.2.2. Raman spectra

**Figure 3.11** shows a Raman spectra of SWCNT (A),  $\alpha\text{-NiPc}(\text{OH})_4$  (B) and  $\alpha\text{-NiPc}(\text{OH})_4\text{-SWCNT}$  (C). The Raman spectra provide an insight on the extent of functionalisation of the SWCNT. The spectrum in **Figure 3.11 (A)** shows a characteristic ring breathing mode (RBM) at 165  $\text{cm}^{-1}$ , tangential vibrational mode at 1595  $\text{cm}^{-1}$  (the G band) and vibrational mode due to disorder on the hexagonal lattice on the SWCNT sidewalls at 1269  $\text{cm}^{-1}$  (the D band) [201]. The Raman spectrum of  $\alpha\text{-NiPc}(\text{OH})_4$ , **Figure 3.11 (B)**, shows intense bands at 756, 1075, 1340 and 1546  $\text{cm}^{-1}$  as discussed above. The sensitivity to the metal ion has been



ascribed to a change in shape of the entire ring. This sensitivity has been correlated with the bond strength [253] and in this case the small metal ion coupled with electron donating substituent in  $\alpha$ -NiPc(OH)<sub>4</sub> causes an in-plane distortion of the ring. The band at 1340 cm<sup>-1</sup> is due to deformation of the ring. **Figure 3.11 (C)** shows that the interaction between SWCNT and  $\alpha$ -NiPc(OH)<sub>4</sub> causes the D band to shift from 1269 cm<sup>-1</sup> to 1287 cm<sup>-1</sup>. This significant shift of 18 cm<sup>-1</sup> suggests a strong interaction between SWCNT and  $\alpha$ -NiPc(OH)<sub>4</sub>. Similar Raman spectral changes were observed for all the NiPc derivatives substituted with hydroxyl groups in the presence and absence of SWCNT.

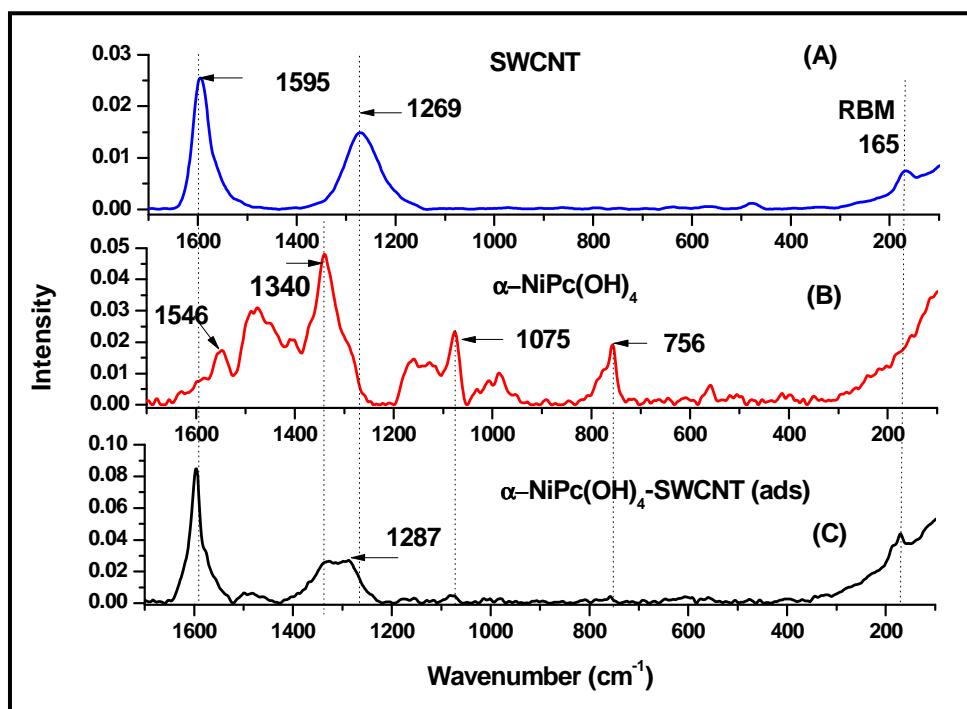


**Figure 3.11:** Raman spectra of SWCNT (A),  $\alpha$ -NiPc(OH)<sub>4</sub> (B) and  $\alpha$ -NiPc(OH)<sub>4</sub>-SWCNT.

**Figure 3.12** shows a Raman spectra of SWCNT (**Figure 3.12A**),  $\alpha$ -NiPc(C<sub>10</sub>H<sub>21</sub>)<sub>8</sub> (**Figure 3.12B**) and  $\alpha$ -NiPc(C<sub>10</sub>H<sub>21</sub>)<sub>8</sub>-SWCNT (**Figure 3.12C**). **Figure 3.12B** shows the Raman spectra of  $\alpha$ -NiPc(C<sub>10</sub>H<sub>21</sub>)<sub>8</sub> with intense bands at 165, 1277, 1549 and 1590 cm<sup>-1</sup>, respectively. A specific C-N-C stretch band of  $\alpha$ -NiPc(C<sub>10</sub>H<sub>21</sub>)<sub>8</sub> is observed in the region of 1590 cm<sup>-1</sup> [71, 253, 254]. In this region the C-N-C band overlaps with SWCNT band in the conjugate. The band at 1277 cm<sup>-1</sup> is due to deformation of the ring. **Figure 3.12C** shows that the interaction between SWCNT and  $\alpha$ -NiPc(C<sub>10</sub>H<sub>21</sub>)<sub>8</sub> causes the D band to shift from 1269 cm<sup>-1</sup> to 1298 cm<sup>-1</sup>. This significant shift of 29 cm<sup>-1</sup> suggests a very strong interaction between SWCNT and  $\alpha$ -NiPc(C<sub>10</sub>H<sub>21</sub>)<sub>8</sub>.

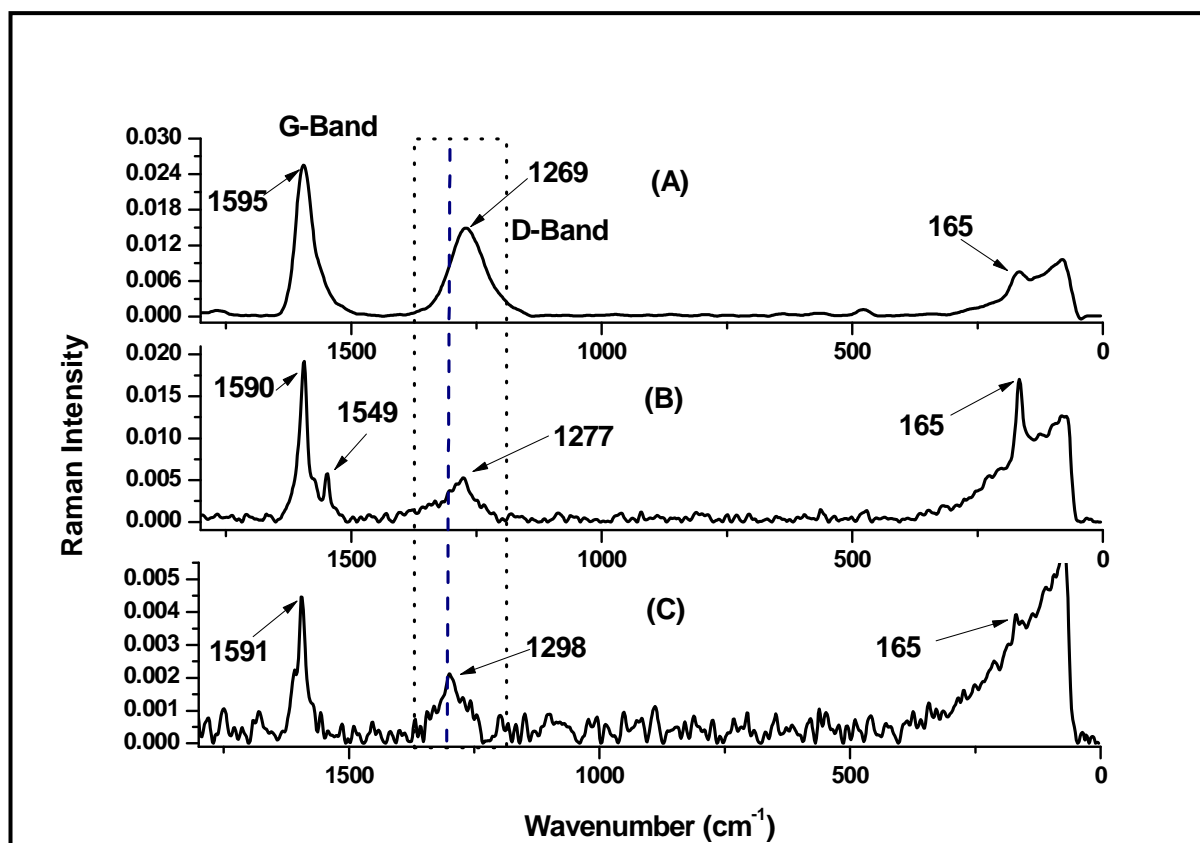


**Figure 3.12:** Raman spectra of SWCNT (A),  $\alpha$ -NiPc(C<sub>10</sub>H<sub>21</sub>)<sub>8</sub> (B) and  $\alpha$ -NiPc(C<sub>10</sub>H<sub>21</sub>)<sub>8</sub>-SWCNT (C).

### 3.2.3. UV-Vis spectra

The ground state absorption spectrum of  $\alpha$ -NiPc(C<sub>10</sub>H<sub>21</sub>)<sub>8</sub> adsorbed on SWCNT (in THF) is shown in **Figure 3.1B**. The absorption spectrum of SWCNT is typified by a broad feature that extends into the near-infrared region. In the conjugate with  $\alpha$ -NiPc(C<sub>10</sub>H<sub>21</sub>)<sub>8</sub>, the absorption of the latter appears to be riding on the broad absorption spectrum of the former. The adsorbed conjugate has peaks corresponding to the main absorption bands (Q bands) of the phthalocyanine unit at 702 nm and 330 nm which is evidence for the presence of the phthalocyanine unit on the SWCNT. Similarly no significant changes were observed for all NiPc complexes adsorbed on SWCNT.

### 3.2.4. Microscopic study

**Figure 3.13** shows the transmission electron microscopy (TEM) image of SWCNT (a),  $\beta$ -NiPc(OH)<sub>8</sub>-SWCNT (b), initially dispersed through ultrasonication in DMF. **Figure 3.13** (b) shows ropes of SWCNT coated with aggregates of  $\beta$ -NiPc(OH)<sub>8</sub> complex, thus further

confirming the structural integrity of  $\beta$ -NiPc(OH)<sub>8</sub>-SWCNT. The black spots observed on SWCNT before adsorption of NiPc are consistent with a known fact that carbon nanotubes are not 100% pure but consist of metal catalyst (which are difficult to remove) used in the synthesis of SWCNT [255].

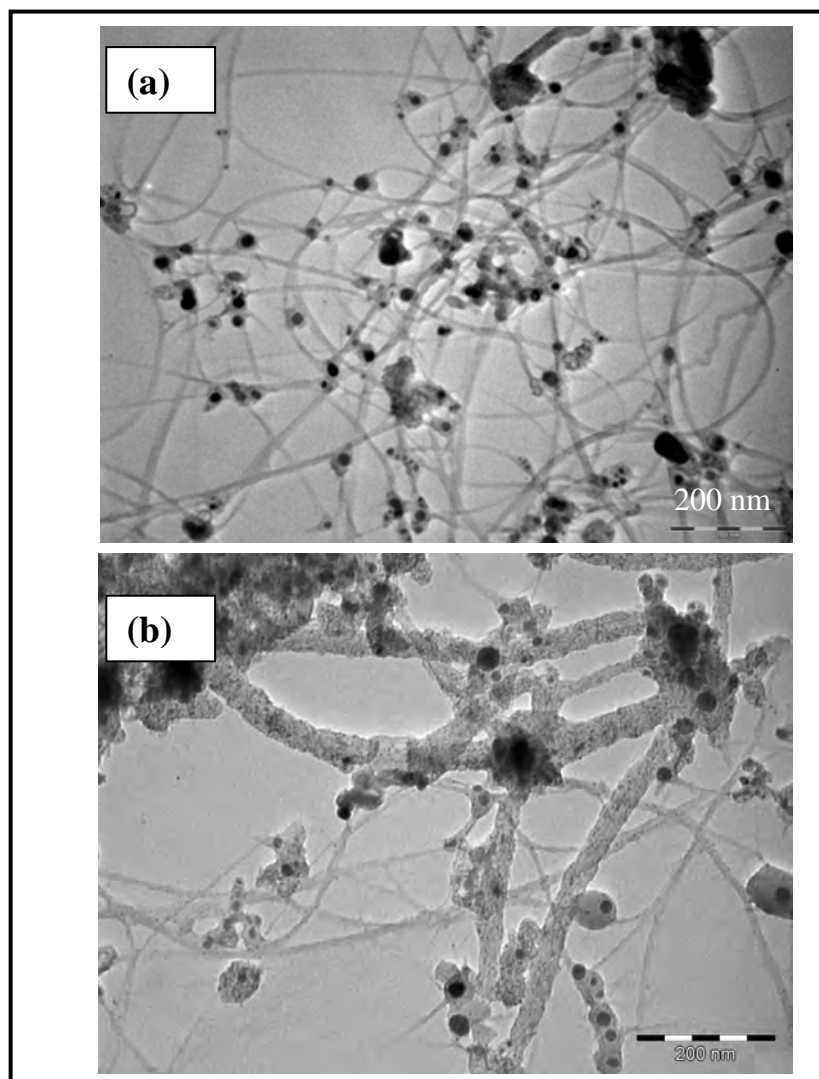


**Figure 3.13: TEM image of SWCNT before (a) and after (b) functionalization with  $\alpha$ -NiPc(OH)<sub>8</sub> at 200 nm resolution**

TEM images of  $\alpha$ -NiPc(C<sub>10</sub>H<sub>21</sub>)<sub>8</sub> and  $\alpha$ -NiPc(C<sub>10</sub>H<sub>21</sub>)<sub>8</sub>-SWCNT are shown in **Figure 3.14**. The  $\alpha$ -NiPc(C<sub>10</sub>H<sub>21</sub>)<sub>8</sub> complex shows aggregated porous film in **Figure 3.14A**. The presence of both SWCNT and  $\alpha$ -NiPc(C<sub>10</sub>H<sub>21</sub>)<sub>8</sub> in the conjugate is shown by **Figure 3.14B**. The porous film is rougher in the presence of SWCNT. AFM image of the conjugate (**Figure 3.15**) confirms the rough and compact nature of the film.

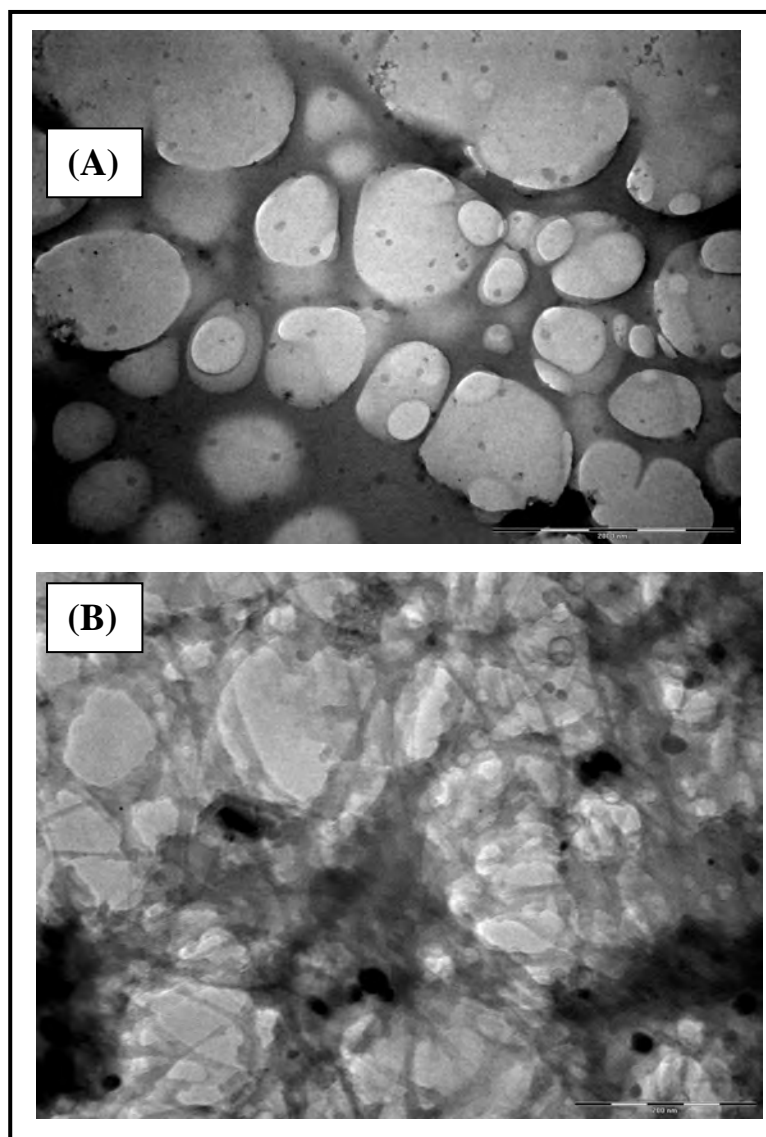


**Figure 3.14:** TEM images of  $\alpha$ -NiPc(C<sub>10</sub>H<sub>21</sub>)<sub>8</sub>(ads) (A) film and  $\alpha$ -NiPc(C<sub>10</sub>H<sub>21</sub>)<sub>8</sub>-SWCNT (B) at 200 nm resolution.

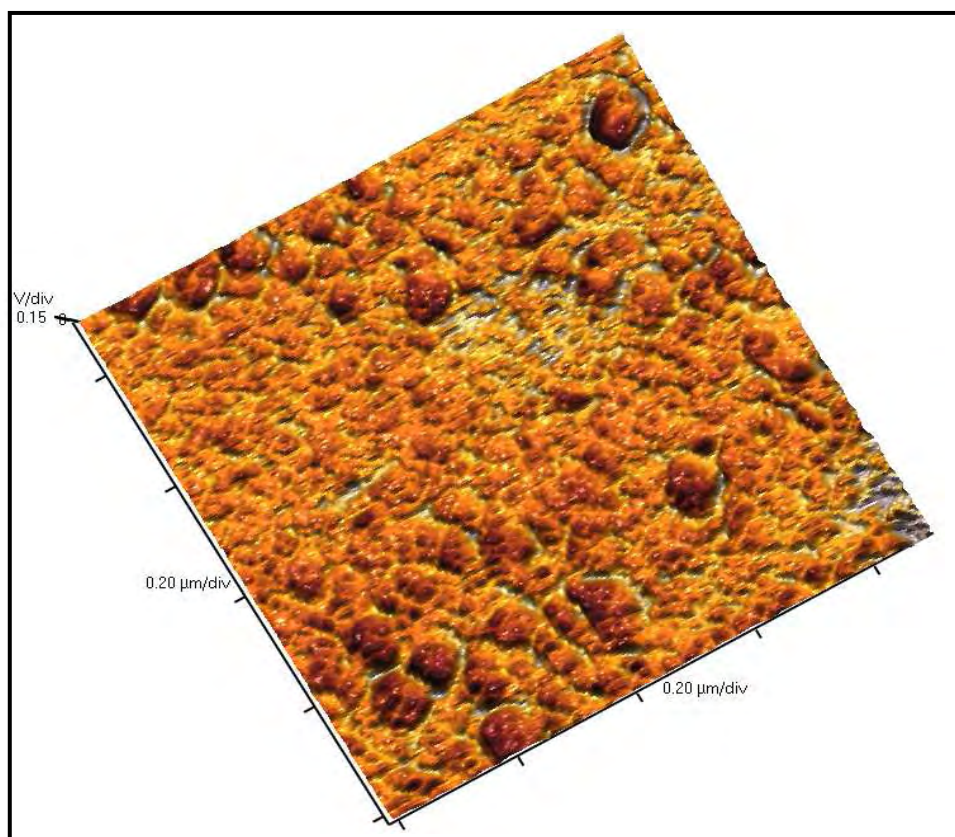


**Figure 3.15: AFM images of  $\alpha$ -NiPc(C<sub>10</sub>H<sub>21</sub>)<sub>8</sub>-SWCNT**

### 3.2.5. XPS of NiPc-SWCNT

In **Figure 3.16 (A)** the carbon and oxygen peaks are found at 283.2 and 531.1 eV respectively, and arise from SWCNT carbon atoms and the oxygen from the carboxylic acid functional groups functionalising the ends of the SWCNT. Glass was used as a substrate; hence the two peaks at 152.0 and 101.4 eV are due to silicon, the oxygen peak will also be affected by the silicon. In **Figure 3.16 (B)** the oxygen, nitrogen, carbon and nickel peaks are found at 531.1, 399.0, 283.2 and 68.6 eV respectively, which arise from  $\alpha$ -NiPc(C<sub>10</sub>H<sub>21</sub>)<sub>8</sub> adsorbed on SWCNT. The increase in the relative intensity (compared to oxygen peak) of the carbon peak, suggest an increase in number of carbon atoms in the sample compared to SWCNT alone. The increase in carbon atoms is attributed to the Pc ring carbons and carbon from the long alkyl groups attached to the  $\alpha$  position of  $\alpha$ -NiPc(C<sub>10</sub>H<sub>21</sub>)<sub>8</sub>, thus confirming the structural integrity of the complex.

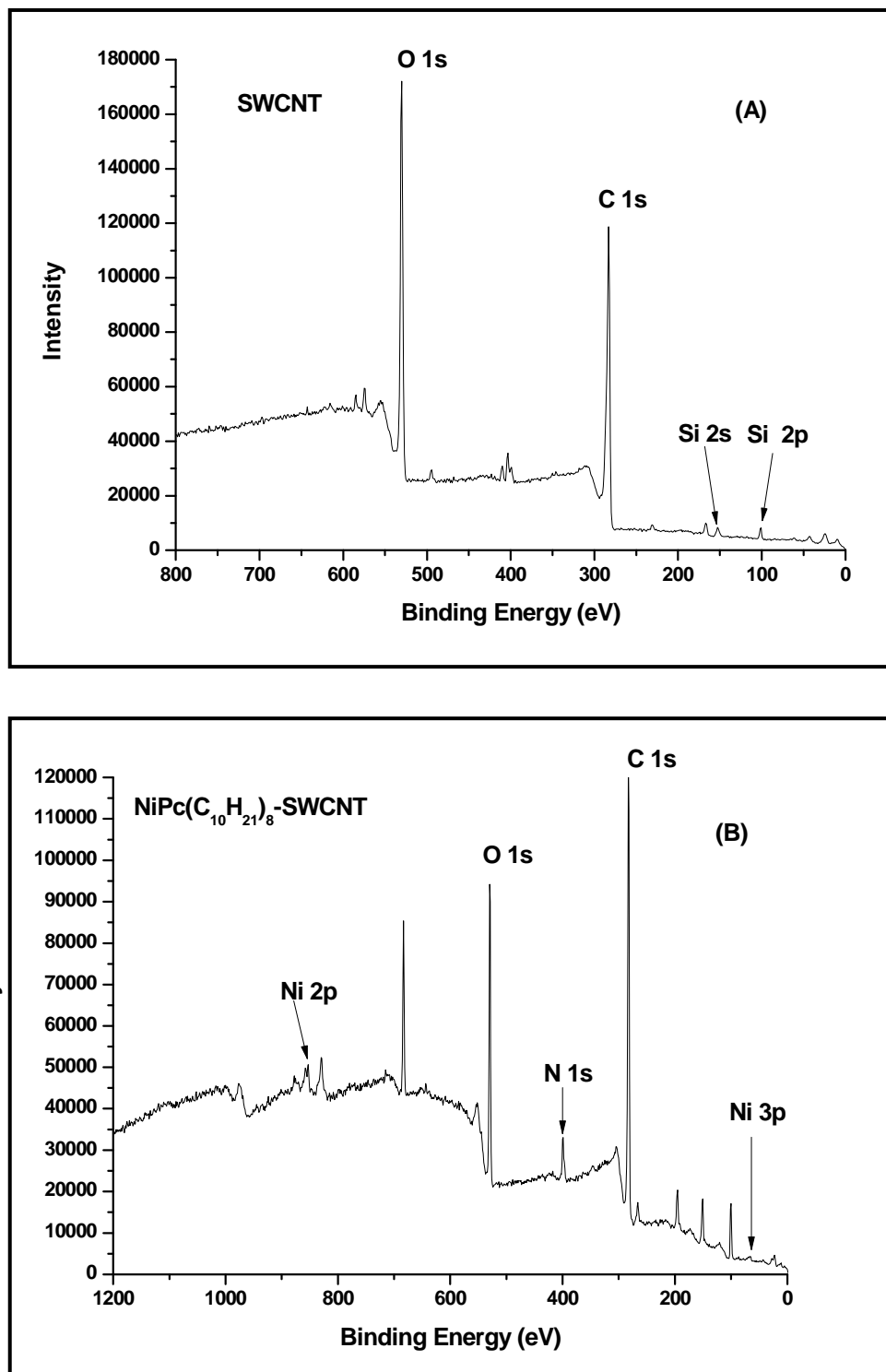


Figure 3.16: XPS spectra of SWCNT (A) and  $\alpha$ -NiPc(C<sub>10</sub>H<sub>21</sub>)<sub>8</sub>-SWCNT (B)

### 3.3. CdTe-QDs- $\beta$ -NiPc(NH<sub>4</sub>)<sub>2</sub> conjugate

$\beta$ -NiPc(NH<sub>2</sub>)<sub>4</sub> [39] and CdTe quantum dots capped with thiol glycolic acid (TGA) [248, 256, 257] were synthesised following literature methods, using DCC and NHS as coupling agents.

#### 3.3.1. XRD spectra

**Figure 3.17** shows an XRD spectrum of CdTe-QDs, which is similar to that of CdTe-QDs- $\beta$ -NiPc(NH<sub>2</sub>)<sub>4</sub>. The diffraction pattern in **Figure 3.17** corresponds well with the three characteristic peaks for bulk CdTe structure having a cubic crystalline structure.

The relative size of 2.3 nm for CdTe-QDs and 2.4 nm for CdTe-QDs-NiPc(NH<sub>2</sub>)<sub>4</sub> conjugate were obtained by fitting the XRD spectra with the, Scherrer **Equation 3.1**

$$d(\text{\AA}) = \frac{k\lambda}{\beta \cos\theta} \quad 3.1$$

where  $k$  is an empirical constant equal to 0.9,  $\lambda$  is the wavelength of the X-ray source (1.5405 Å),  $\beta$  is the full width at half maximum of the diffraction peak and  $\theta$  is the angular position of the peak.

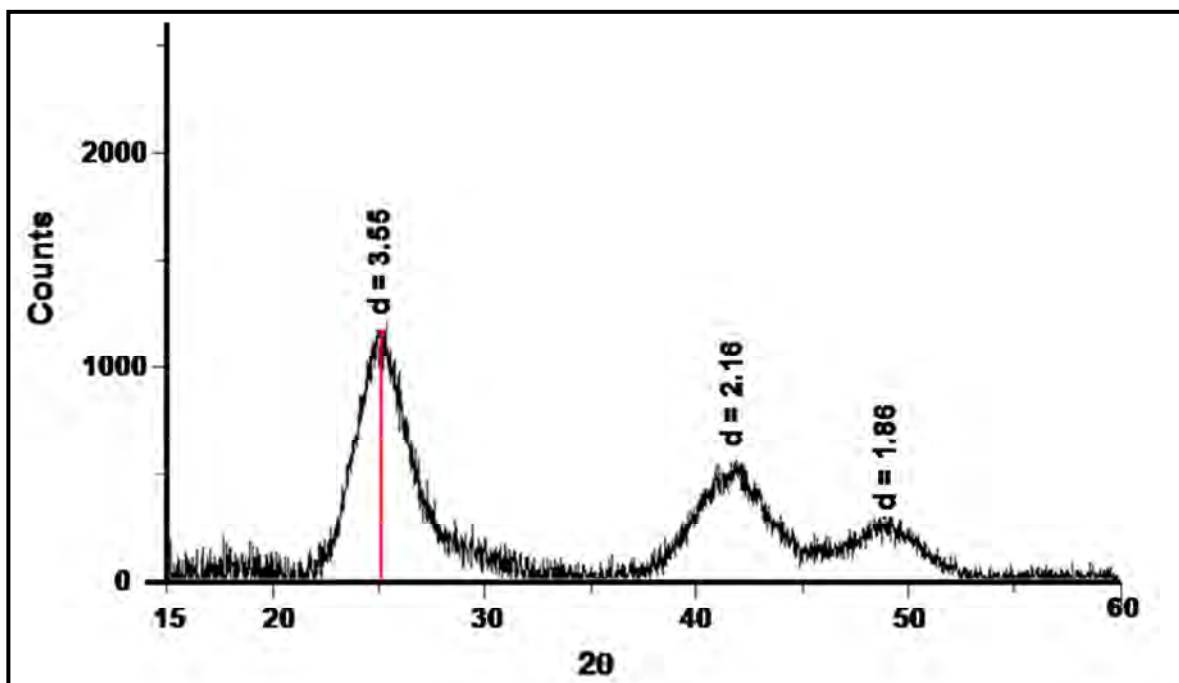


**Figure 3.17:** XRD spectrum of CdTe-QDs.

### 3.3.2. UV-Vis spectra

As is typical of QDs in general, the absorption spectrum of the CdTe-QDs is broad and the emission spectrum is narrow, **Figure 3.18**, and there were no changes in the wavelength of both emission (at 577 nm) and absorption (at 545 nm) spectra for QDs alone and when they are in a conjugate (CdTe-QDs- $\beta$ -NiPc(NH<sub>2</sub>)<sub>4</sub>). The emission and absorption spectra of QDs shift with increase in size [256]. The observation that the spectra of CdTe-QDs- $\beta$ -NiPc(NH<sub>2</sub>)<sub>4</sub> conjugate (which has a larger size) is the same as that of CdTe-QDs (with a smaller size) is expected because we are not increasing the size of the CdTe core but the radius of the capping agent.

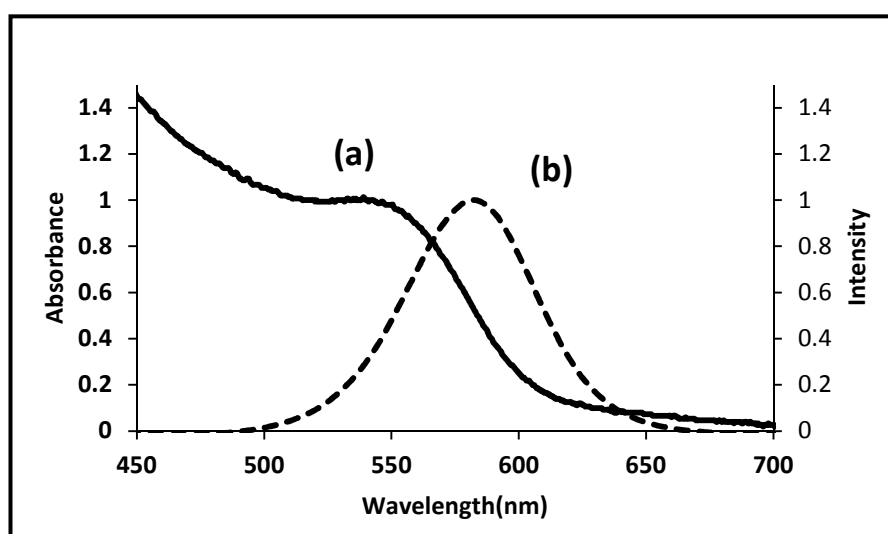


**Figure 3.18: Absorption (a) and Emission (b) spectra of CdTe-QDs- $\beta$ -NiPc(NH<sub>2</sub>)<sub>4</sub> in pH 9.2 buffer solution.**

### 3.3.3. Fluorescence lifetimes

These studies were performed in order to confirm the bonding between  $\beta$ -NiPc(NH<sub>2</sub>)<sub>4</sub> and CdTe-QDs. Attachment of MPCs on the surface of QDs is known [256] to result in quenching of fluorescence lifetimes of the latter, due to energy transfer. The fluorescence lifetimes were also used to confirm the integrity of QDs in the conjugates. **Figure 3.19** shows the photoluminescence decay curve of CdTe-QDs- $\beta$ -NiPc(NH<sub>2</sub>)<sub>4</sub> conjugate (**Figure 3.19A**) and CdTe-QDs (**Figure 3.19B**) using the time correlated single photon counting (TCSPC) technique. The quality of the fit was judged on the basis of  $\chi^2$  values which were close to unity, **Table 3.4**. The QDs showed triexponential excitonic emission decay kinetics as also observed by other researchers [258]. The origin of the longer lifetime component ( $\tau_1$ ) may be



due to the involvement of surface defects in the carrier recombination process [258]. The second fluorescence lifetime component, ( $\tau_2$ ), is a result of radiative electron-hole recombination processes due to surface states [258]. According to some researchers [259-261] the shortest component,  $\tau_3$  is caused by the band-edge recombination at the surface; but this is contradicted by other researchers who attribute this short lifetime to intrinsic recombination of initially populated core states [261-263]. Within experimental error, the fluorescence lifetime values of QDs have not changed for the CdTe-QDs- $\beta$ -NiPc(NH<sub>2</sub>)<sub>4</sub> conjugate, as would have been expected upon coordination of  $\beta$ -NiPc(NH<sub>2</sub>)<sub>4</sub> (**Table 3.4**), and as observed for other studies [189, 256, 264]. Thus the use of fluorescence lifetimes did not unequivocally prove the changes on the surface of QDs due to coordination of  $\beta$ -NiPc(NH<sub>2</sub>)<sub>4</sub>, however the data confirms the integrity of QDs in the conjugate.

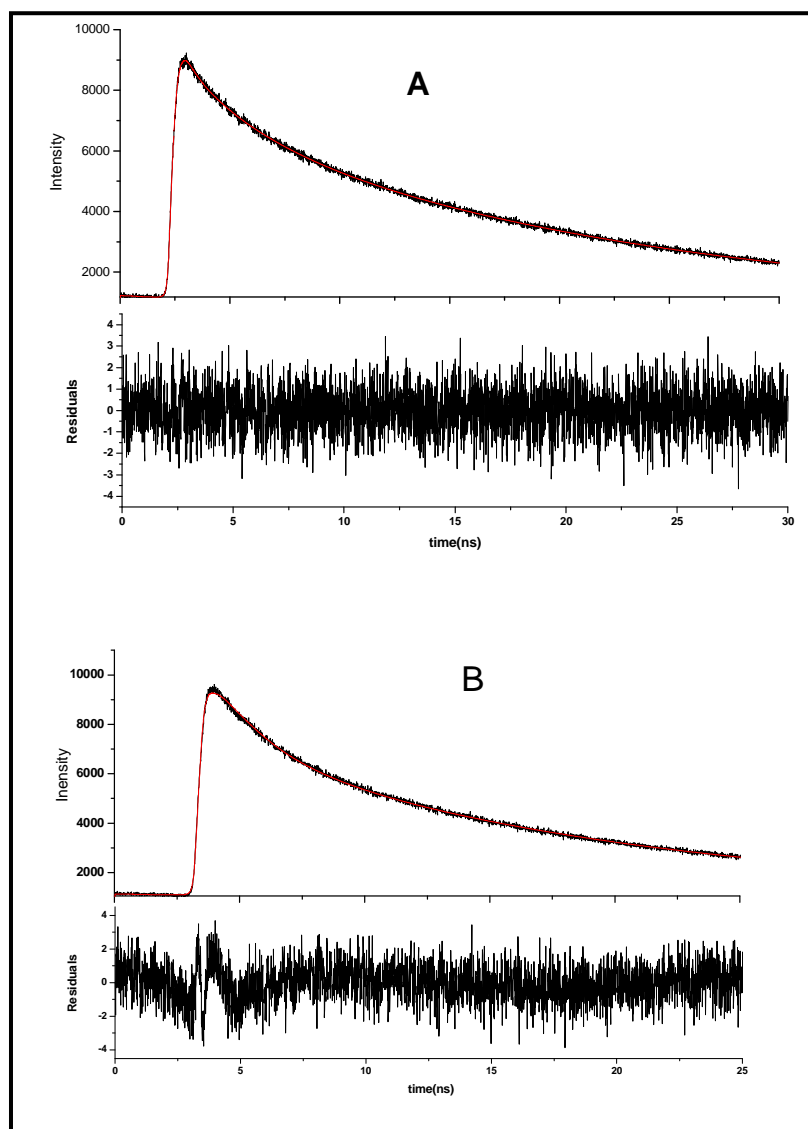


**Figure 3.19: Photoluminescence decay curves of (A) CdTe-QDs-NiPc(NH<sub>2</sub>)<sub>4</sub> and (B) CdTe QDs in a buffer solution of pH 9.2. Excitation wavelength = 480 nm.**

**Table 3.4: Fluorescence lifetimes of QDs linked to  $\beta$ -NiPc(NH<sub>2</sub>)<sub>4</sub>  $\lambda_{Exc}$  = 480 nm. pH 9.2 buffer**

Life times	$\tau_1 / ns$	$A_1$	$\tau_2 / ns$	$A_2$	$\tau_3 / ns$	$A_3$	$\chi^2$
<b>CdTe-QDs</b>	20.15 ( $\pm 2.20$ )	0.56	3.37 ( $\pm 0.43$ )	0.20	0.46 ( $\pm 0.20$ )	0.24	1.04
<b>CdTe-QDs-<math>\beta</math>-NiPc(NH<sub>2</sub>)<sub>4</sub></b>	19.25 ( $\pm 1.27$ )	0.51	3.01 ( $\pm 0.67$ )	0.28	0.49 ( $\pm 0.13$ )	0.21	1.05

### 3.3.4. IR Spectra

**Figure 3.20** shows IR spectra of CdTe-QDs (**Figure 3.20A**),  $\beta$ -NiPc(NH<sub>2</sub>)<sub>4</sub> (**Figure 3.20B**) and CdTe-QDs- $\beta$ -NiPc(NH<sub>2</sub>)<sub>4</sub> (linked) conjugate (**Figure 3.20C**). **Figure 3.20A** shows the presence C=O stretch at (1542 cm<sup>-1</sup>), due to the carboxylic acid functional group of the CdTe-QDs and a C-O at 1324 cm<sup>-1</sup>. When  $\beta$ -NiPc(NH<sub>2</sub>)<sub>4</sub> is linked to CdTe-QDs through a carboxylic group a reduction in intensity of the C-O stretch was observed, appearing as a shoulder, **Figure 3.20C**, which suggests that not all carboxylic acid on the QDs reacted with  $\beta$ -NiPc(NH<sub>2</sub>)<sub>4</sub> to form an amide bond. The band at 1200 cm<sup>-1</sup>, **Figures 3.20A** and **C**, is due to the S-C stretch from the TGA capping.

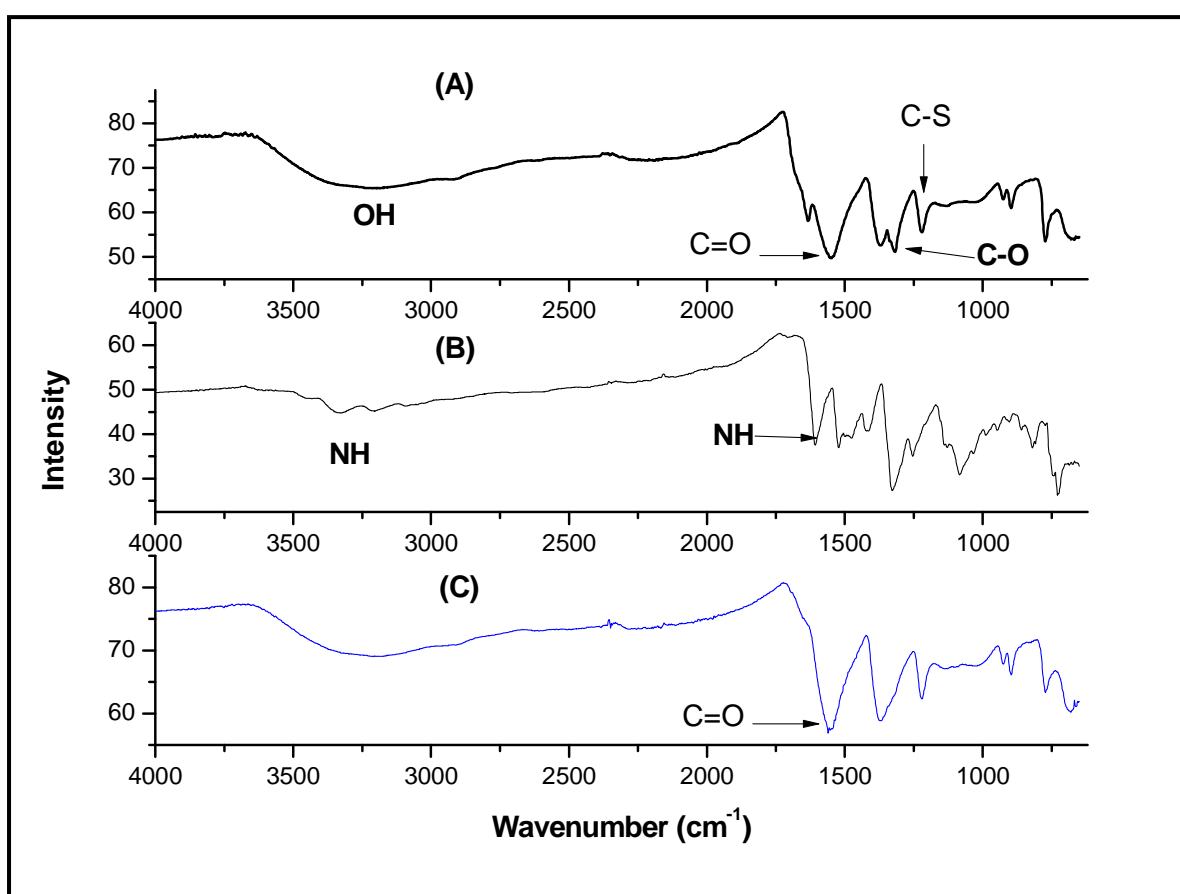


**Figure 3.20: Infrared (IR) Spectra of (A) CdTe-QDs, (B)  $\beta$ -NiPc(NH<sub>2</sub>)<sub>4</sub> and (C) CdTe-QDs- $\beta$ -NiPc(NH<sub>2</sub>)<sub>4</sub>(linked)**

**Figure 3.21** shows a far IR (FIR) spectra of  $\beta$ -NiPc(NH<sub>2</sub>)<sub>4</sub> (**Figure 3.21A**), CdTe-QDs- $\beta$ -NiPc(NH<sub>2</sub>)<sub>4</sub> (linked) conjugate (**Figure 3.21B**) and CdTe-QDs (**Figure 3.21C**). The assignment of the FIR bands for  $\beta$ -NiPc(NH<sub>2</sub>)<sub>4</sub> are based on the work done by Kobayashi et al. [265]. In **Figure 3.21A** and **B**, bands (a) around 300 cm<sup>-1</sup> are metal dependent isoindole

ring stretches. The absorption bands (b) and (c) are assigned to macrocyclic ring deformation. Band (e) around  $175\text{ cm}^{-1}$  is assigned to metal-ligand vibrations. Bands (f) around  $150$  and  $125\text{ cm}^{-1}$  are assigned as metal independent out of plane deformation vibrations. The macrocyclic metal independent absorption bands in this region are considered as those due to phthalocyanine macrocyclic ring vibrations. **Figure 3.21B** and **C** shows a band at  $104\text{ cm}^{-1}$  due to the Cd-Te bond stretch [266]. Both the bands due to QDs and to  $\beta\text{-NiPc}(\text{NH}_2)_4$  were also observed in the CdTe-QDs- $\beta\text{-NiPc}(\text{NH}_2)_4$  (linked), hence confirming the integrity of QDs and  $\beta\text{-NiPc}(\text{NH}_2)_4$  in the conjugate.

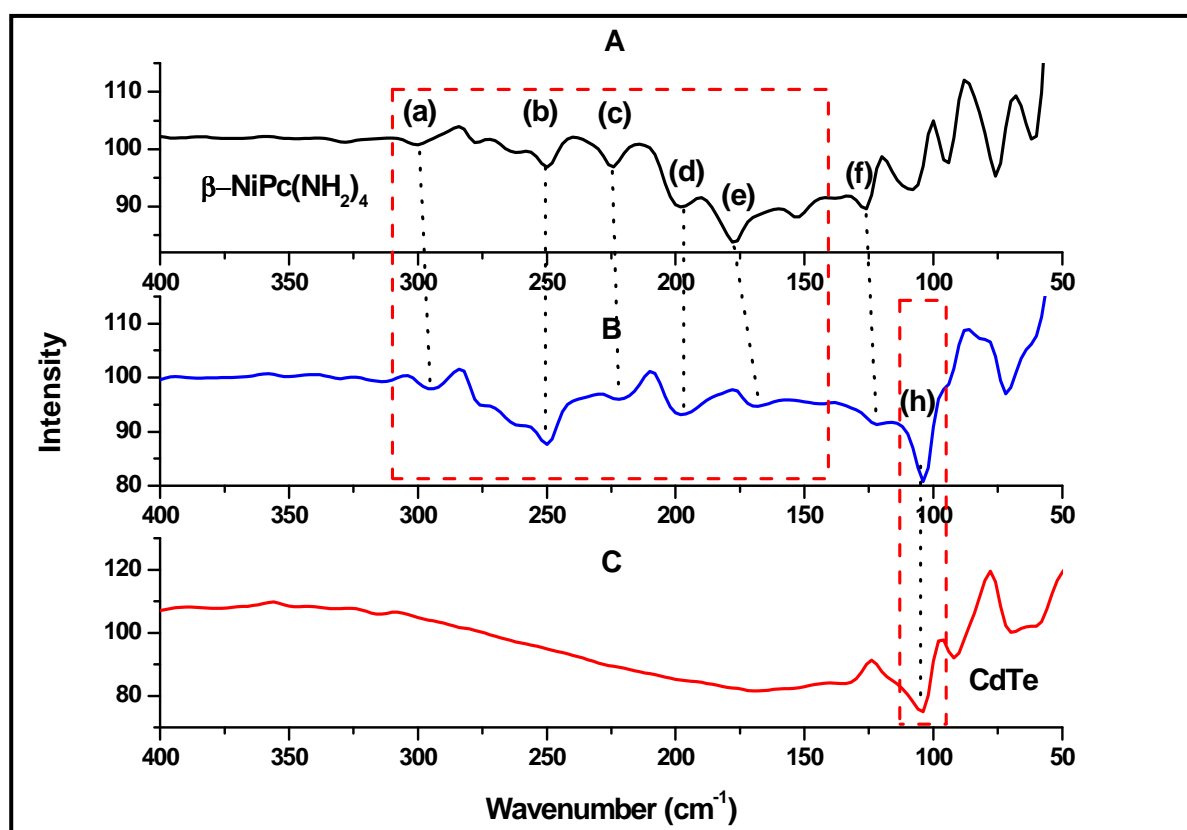


**Figure 3.21:** Far Infrared (FIR) Spectra of (A)  $\beta\text{-NiPc}(\text{NH}_2)_4$ , (B) CdTe-QDs- $\beta\text{-NiPc}(\text{NH}_2)_4$  (linked) and (C) CdTe-QDs

### 3.3.5. Raman spectra

**Figure 3.22** shows a Raman spectra of CdTe-QDs- $\beta\text{-NiPc}(\text{NH}_2)_4$  (linked) conjugates (**Figure 3.22A**), CdTe-QDs (**Figure 3.22B**) and  $\beta\text{-NiPc}(\text{NH}_2)_4$  (**Figure 3.22C**). **Figure 3.22A** Raman spectra show Raman bands at  $1595$ ,  $1561$ ,  $1481$ ,  $1402$ ,  $1364$ ,  $1333$ ,  $1275$ ,  $1105$  and  $754\text{ cm}^{-1}$ . The band at  $1595\text{ cm}^{-1}$  is due to the C-H<sub>2</sub> out of plane stretch of the TGA capping agent

(Figure 3.22B). The stretch at  $1561\text{ cm}^{-1}$  (in Figure 3.22A and C) is due to C-N-C stretch which is sensitive to the central metal and provides a specific signature for the phthalocyanine studied [71, 253, 254]. The stretch at  $754\text{ cm}^{-1}$  is due to phthalocyanine ring distortion and is present in both the conjugate (Figure 3.22A) and free  $\beta\text{-NiPc}(\text{NH}_2)_4$  (Figure 3.22C).

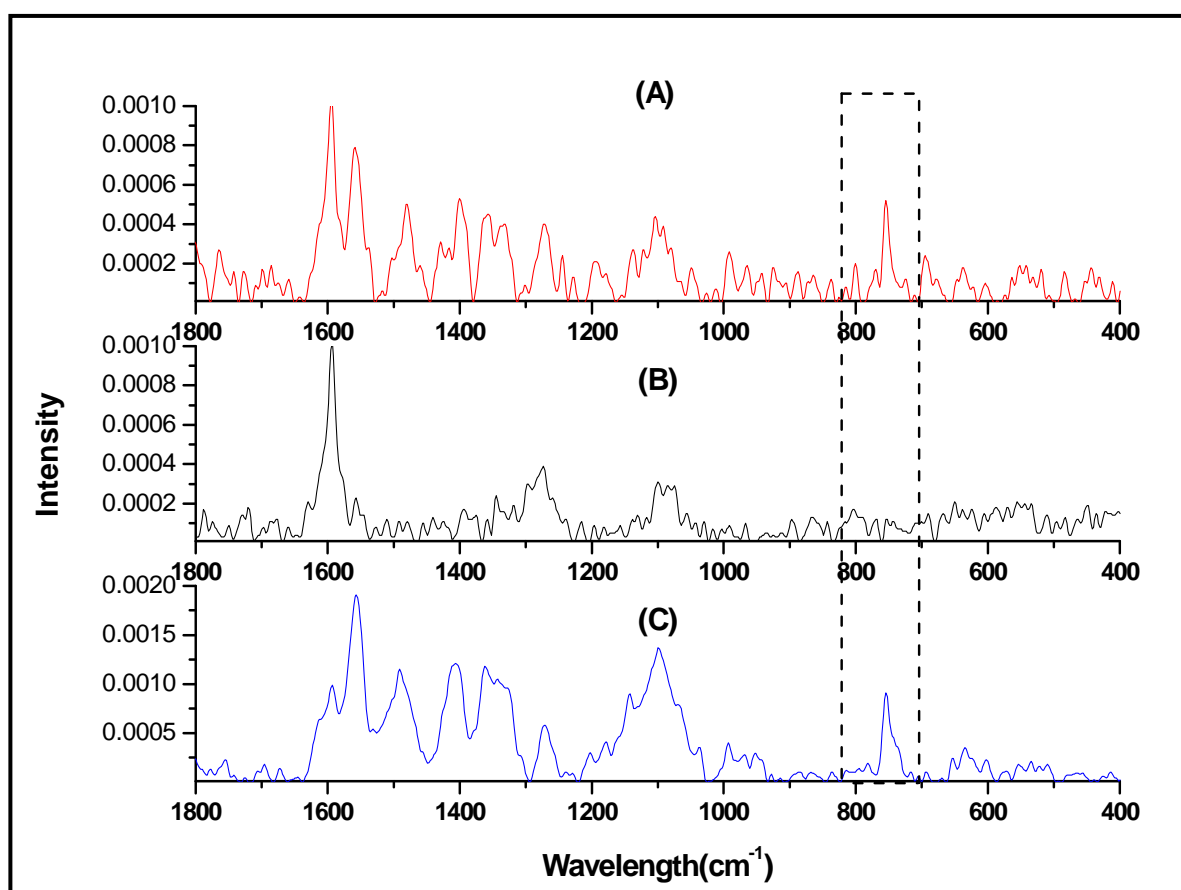


**Figure 3.22: Raman spectra of (A) CdTe-QDs- $\beta\text{-NiPc}(\text{NH}_2)_4$  (linked), (B) CdTe-QDs and (C)  $\beta\text{-NiPc}(\text{NH}_2)_4$**

### 3.3.6. AFM

Figure 3.23 shows an AFM images of CdTe-QDs (Figure 3.23A) and CdTe-QDs- $\beta\text{-NiPc}(\text{NH}_2)_4$  (linked) conjugate (Figure 3.23B). The AFM pictures show that CdTe-QDs (Figure 3.23A) are highly aggregated compared to QDs- $\beta\text{-NiPc}(\text{NH}_2)_4$  (linked) conjugates (Figure 3.23B). The aggregation problem of CdTe-QDs did not allow for the estimation of the size of an individual quantum dot. The average size measured of CdTe-QDs aggregates

(Figure 3.23A) is 5.5 nm and that of the disaggregated QDs (Figure 3.23B) is 2.2 nm. The size is very close to the size calculated from XRD spectrum for CdTe-QDs (2.3 nm).

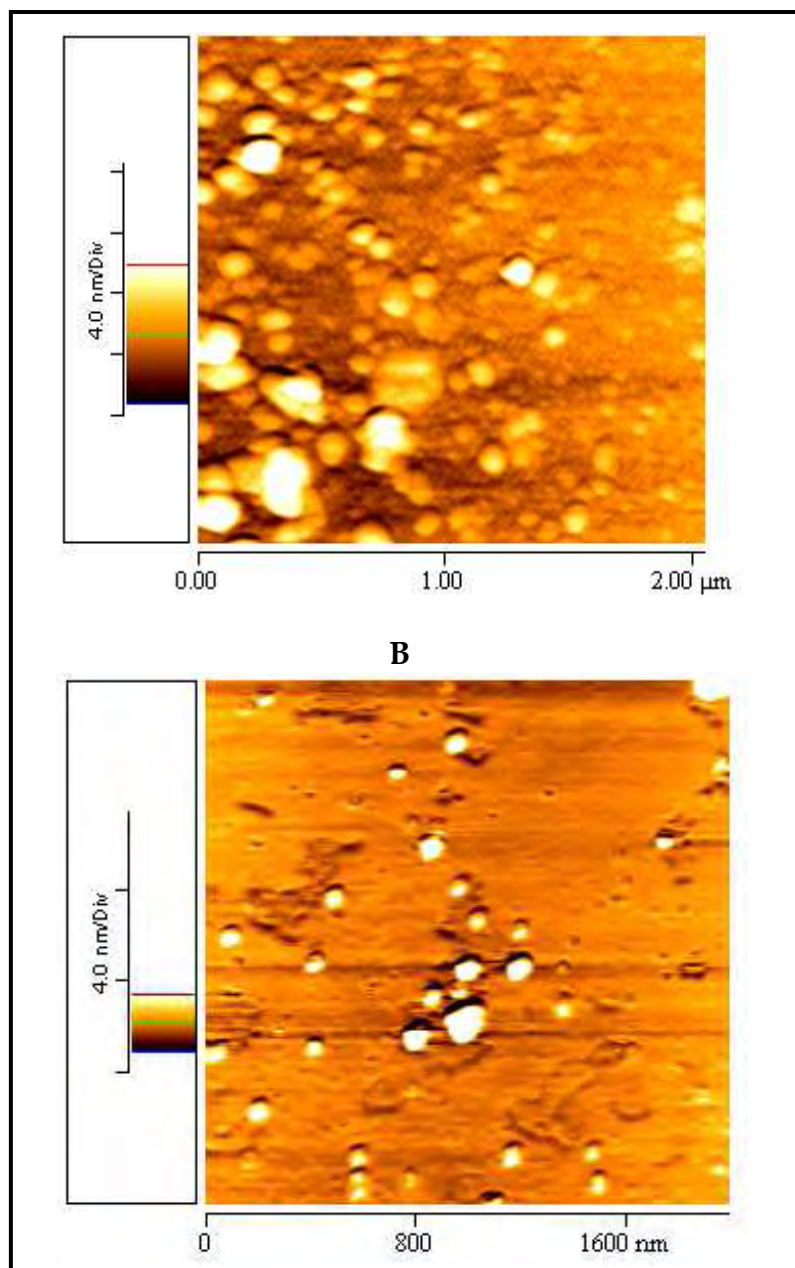


**Figure 3.23:** AFM image of (A) CdTe-QDs and (B) CdTe-QDs-β-NiPc(NH<sub>2</sub>)<sub>4</sub>.

### 3.4. NiPc-SWCNT-QD conjugate

CdSe quantum dots have been found to strongly adsorb on the surface of SWCNT by gentle heating in organic solvents [125], without the need for covalent chemical modification. The current work employs the simple method of adsorbing CdTe-QDs on SWCNT in aqueous media through sonification and without the use of heat. CdTe-QDs have been shown to play

an important role in facilitating the electron transfer between the proteins and the electrode surface, and this was attributed to the small sizes of quantum dots which allow rapid transfer of electrons to the surface, resulting to higher charge efficiency [238].  $\alpha$ -NiPc(C<sub>10</sub>H<sub>21</sub>)<sub>8</sub> was chosen as an example out of all NiPc derivatives. TGA-CdTe-QDs were adsorbed onto  $\alpha$ -NiPc(C<sub>10</sub>H<sub>21</sub>)<sub>8</sub>-SWCNT to form  $\alpha$ -NiPc(C<sub>10</sub>H<sub>21</sub>)<sub>8</sub>-SWCNT-QDs as follows: SWCNT-NiPc(C<sub>10</sub>H<sub>21</sub>)<sub>8</sub> (in THF) was added to an aqueous solution of TGA CdTe-QDs and ultrasonicated to obtain SWCNT- $\alpha$ -NiPc(C<sub>10</sub>H<sub>21</sub>)<sub>8</sub>-QDs. During ultrasonication the QDs will adsorb on vacant areas (areas which are not coated with  $\alpha$ -NiPc(C<sub>10</sub>H<sub>21</sub>)<sub>8</sub>) on SWCNT. The method is explained in the experimental section.

### 3.4.1. UV-Vis spectra

The ground state absorption spectrum of  $\alpha$ -NiPc(C<sub>10</sub>H<sub>21</sub>)<sub>8</sub> in the absence (A) and presence of SWCNT (B) and CdTe-QDs (C) is depicted in **Figure 3.24**. The absorption spectrum of SWCNT is typified by a broad feature that extends into the near-infrared region. In the conjugate with  $\alpha$ -NiPc(C<sub>10</sub>H<sub>21</sub>)<sub>8</sub>-SWCNT, the absorption of the latter appears to be riding on the broad absorption spectrum of the former. In the presence of both SWCNT and CdTe QDs (for  $\alpha$ -NiPc(C<sub>10</sub>H<sub>21</sub>)<sub>8</sub>-SWCNT-QDs), there is no change in the Q band maximum, which is evidence for the presence of the phthalocyanine unit on the SWCNT even in the presence of CdTe-QDs. It is expected that the CdTe-QDs are assembled onto SWCNT (using spaces not filled by  $\alpha$ -NiPc(C<sub>10</sub>H<sub>21</sub>)<sub>8</sub>-SWCNT as reported before [238]).

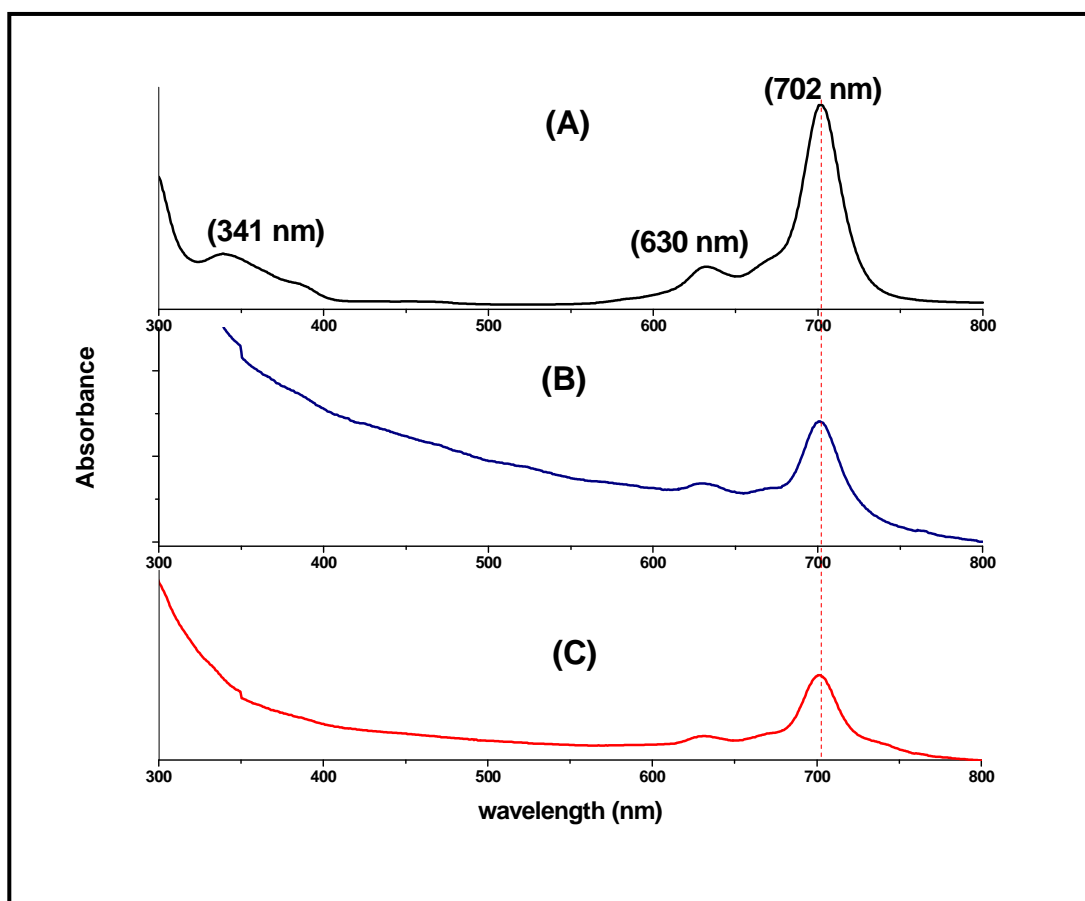
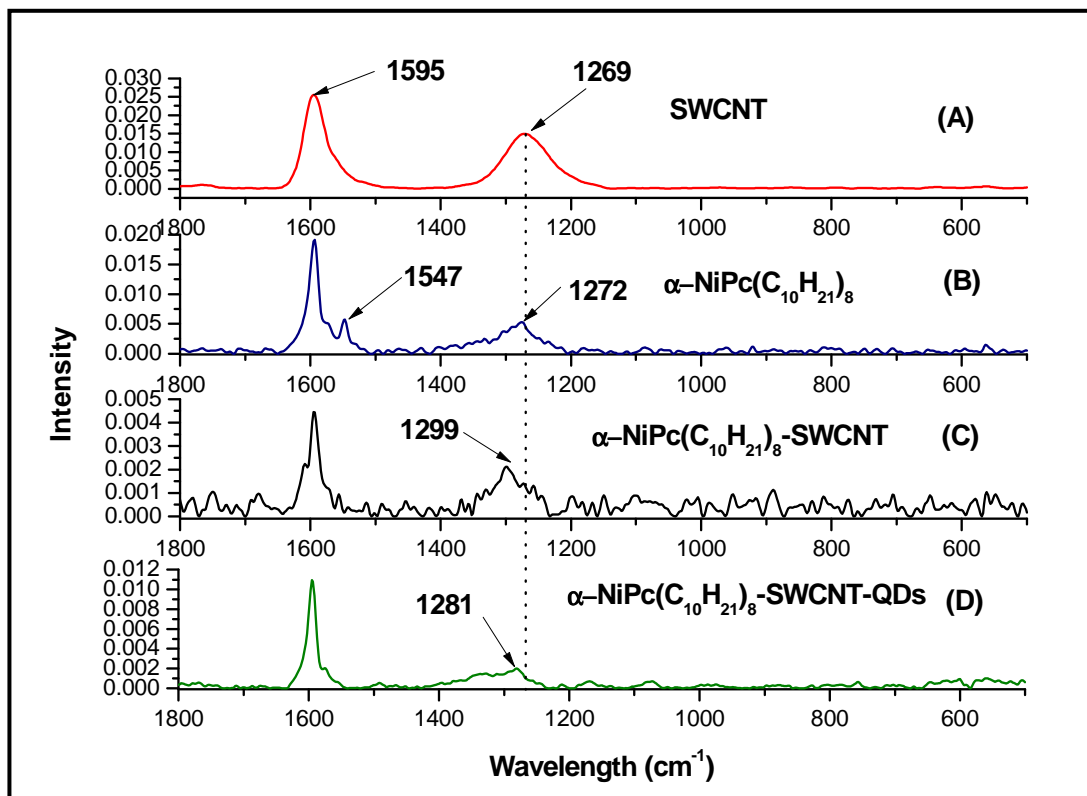


**Figure 3.24:** Ground state absorption spectra of  $\alpha$ -NiPc(C<sub>10</sub>H<sub>21</sub>)<sub>8</sub> (A) and  $\alpha$ -NiPc(C<sub>10</sub>H<sub>21</sub>)<sub>8</sub>-SWCNT (B) and  $\alpha$ -NiPc(C<sub>10</sub>H<sub>21</sub>)<sub>8</sub>-SWCNT-QDs conjugate (C) in THF.

### 3.4.2. Raman spectral characterization of $\alpha$ -NiPc(C<sub>10</sub>H<sub>21</sub>)<sub>8</sub>-SWCNT-QDs conjugate

**Figure 3.25** shows a Raman spectra of SWCNT (**Figure 3.25A**),  $\alpha$ -NiPc(C<sub>10</sub>H<sub>21</sub>)<sub>8</sub> (**Figure 3.25B**),  $\alpha$ -NiPc(C<sub>10</sub>H<sub>21</sub>)<sub>8</sub>-SWCNT (**Figure 3.25C**) and  $\alpha$ -NiPc(C<sub>10</sub>H<sub>21</sub>)<sub>8</sub>-SWCNT-QDs conjugate (**Figure 3.25D**). **Figure 3.25D** shows the Raman spectrum of  $\alpha$ -NiPc(C<sub>10</sub>H<sub>21</sub>)<sub>8</sub>-SWCNT-QDs. The D band of  $\alpha$ -NiPc(C<sub>10</sub>H<sub>21</sub>)<sub>8</sub>-SWCNT-QDs has shifted to lower wave number, from 1299 (for  $\alpha$ -NiPc(C<sub>10</sub>H<sub>21</sub>)<sub>8</sub>-SWCNT) to 1281 cm<sup>-1</sup>, with a difference of 18 cm<sup>-1</sup>. This difference suggests that the presence of QDs also interacts with the SWCNT.

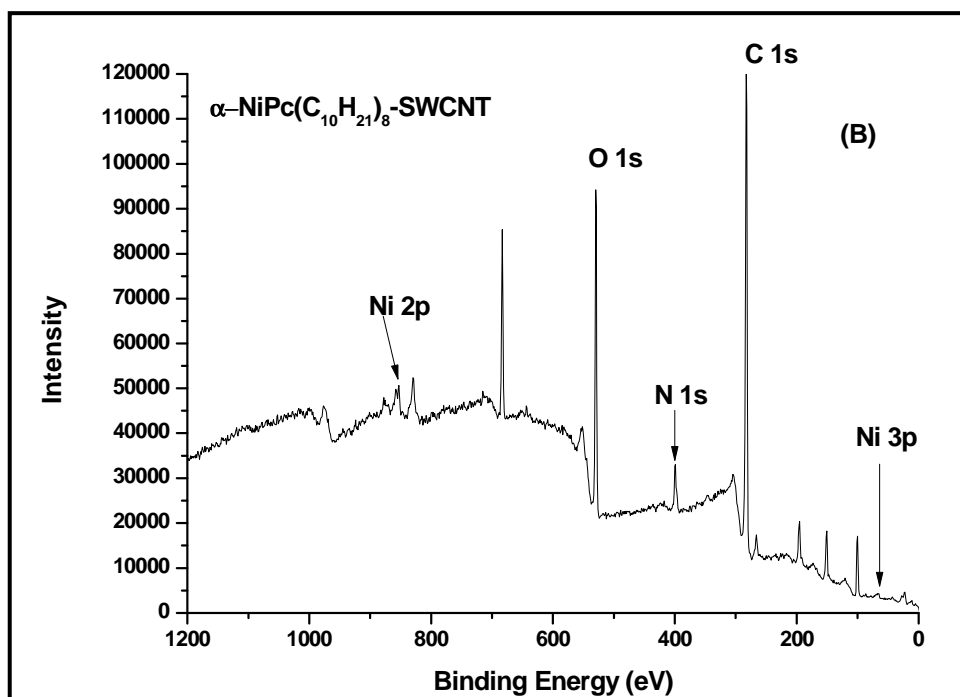
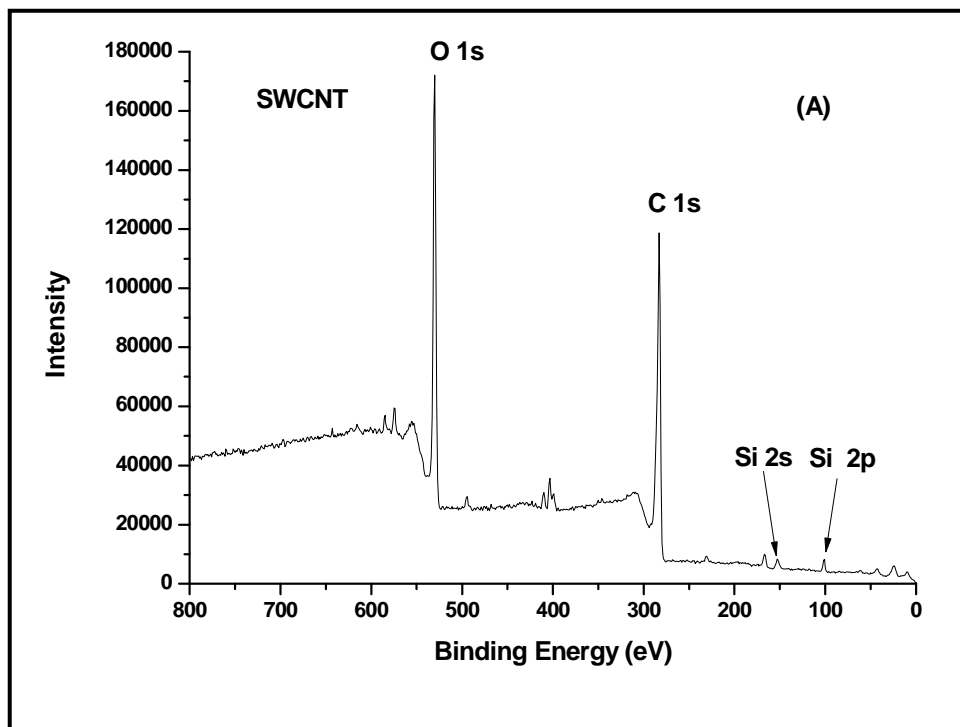




**Figure 3.25** Raman spectra of SWCNT (A),  $\alpha$ -NiPc(C<sub>10</sub>H<sub>21</sub>)<sub>8</sub> (B),  $\alpha$ -NiPc(C<sub>10</sub>H<sub>21</sub>)<sub>8</sub>-SWCNT (C) and  $\alpha$ -NiPc(C<sub>10</sub>H<sub>21</sub>)<sub>8</sub>-SWCNT-QDs conjugate (D).

### 3.4.3. XPS analysis of $\alpha$ -NiPc(C<sub>10</sub>H<sub>21</sub>)<sub>8</sub>-SWCNT-QDs conjugate

**Figure 3.26** shows XPS spectra of SWCNT (**Figure 3.26A**),  $\alpha$ -NiPc(C<sub>10</sub>H<sub>21</sub>)<sub>8</sub>-SWCNT (**Figure 3.26B**) and  $\alpha$ -NiPc(C<sub>10</sub>H<sub>21</sub>)<sub>8</sub>-SWCNT-QDs conjugate (**Figure 3.26C**). The XPS spectra for SWCNT and  $\alpha$ -NiPc(C<sub>10</sub>H<sub>21</sub>)<sub>8</sub>-SWCNT were discussed as **Figure 3.16** and are compared here with XPS of SWCNT-QDs. **Figure 3.26C** shows the XPS spectrum of  $\alpha$ -NiPc(C<sub>10</sub>H<sub>21</sub>)<sub>8</sub>-SWCNT-QDs. The elemental composition of oxygen is much higher in intensity with respect to carbon intensity (see **Figure 3.26C**), compared to **Figure 3.25 B**. The increase in intensity of the oxygen is due to the OH substituents of the carboxylic acid group surrounding the QDs. The main cadmium and telluride peaks arising from the 3d orbital are found at 403.4 and 573.4 (eV) respectively. There are other peaks observed, which arise from the 3s, 3p, 4p and 4d orbitals of these metals and are depicted in **Figure 3.26C**.



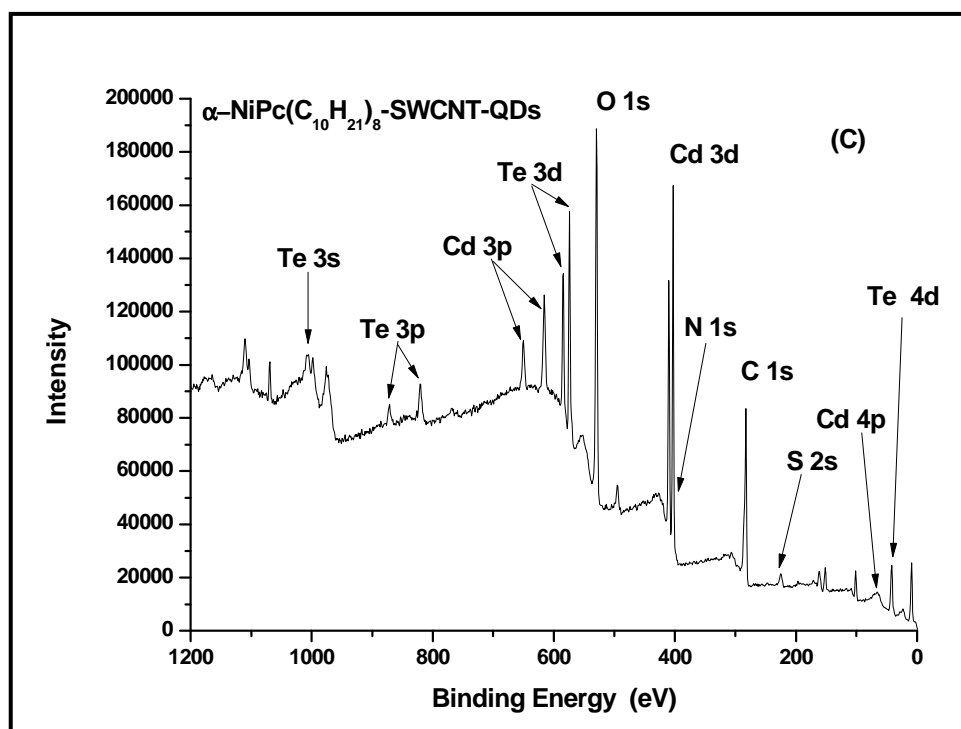


**Figure 3.26:** XPS spectra of SWCNT (A),  $\alpha$ -NiPc(C<sub>10</sub>H<sub>21</sub>)<sub>8</sub>-SWCNT (B) and  $\alpha$ -NiPc(C<sub>10</sub>H<sub>21</sub>)<sub>8</sub>-SWCNT-QDs conjugate (C).

**Table 3.5** shows mass concentration percentages of SWCNT,  $\alpha$ -NiPc(C<sub>10</sub>H<sub>21</sub>)<sub>8</sub>-SWCNT and  $\alpha$ -NiPc(C<sub>10</sub>H<sub>21</sub>)<sub>8</sub>-SWCNT-QDs. The mass concentration percentages of C (27.37%), Te (14.18%), Cd (26.71%), O (24.99 %) and Ni (1.46%) atoms are obtained for  $\alpha$ -NiPc(C<sub>10</sub>H<sub>21</sub>)<sub>8</sub>-SWCNT-QDs, the Ni peak is not clear in **Figure 3.26C**. In **Figure 3.26C** the nitrogen signal is super-imposed on the Cd 3d signal at 400 eV and thus contributes to the mass concentration of Cd. It is known that QDs which are less than 2 nm have more than 50% of their atoms residing on the surface. The size we employed in this work is slightly higher than 2 nm. The C and O will also be affected by the presence of the capping agent. The S peak from the capping is also observed, **Figure 3.26C**.

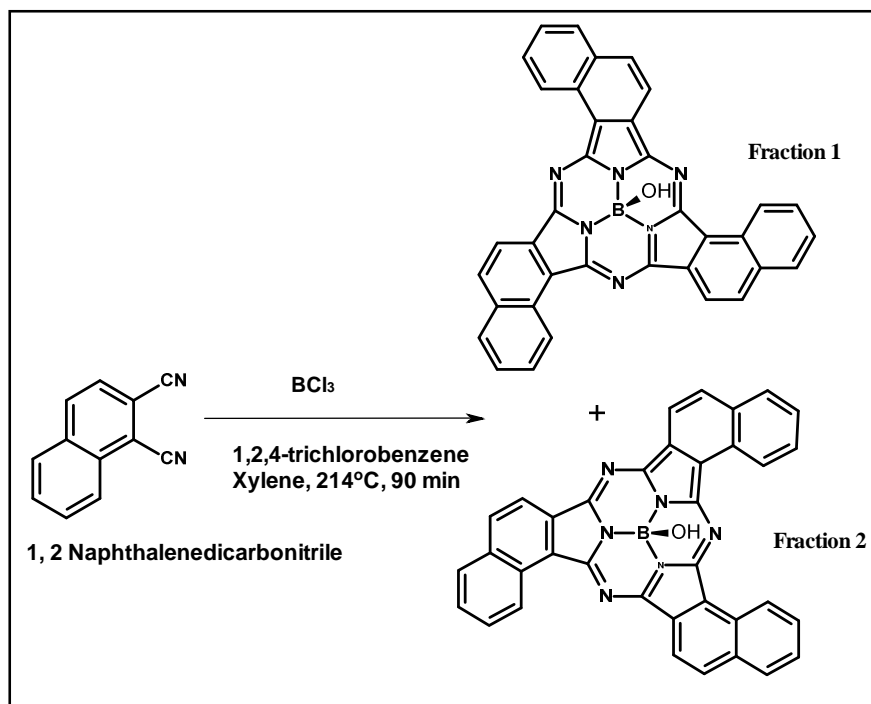
Table 3.5: Mass concentration percentage (%)

	C 1s	O 1s	N 1s	Ni 2p	Te 3d	Cd 3d
<b>SWCNT</b>	59.04	33.13	-	-	-	-
<b><math>\alpha</math>-NiPc(C<sub>10</sub>H<sub>21</sub>)<sub>8</sub>- SWCNT</b>	58.86	18.23	4.84	5.78	-	-
<b><math>\alpha</math>-NiPc(C<sub>10</sub>H<sub>21</sub>)<sub>8</sub>- SWCNT-QDs</b>	27.37	24.99	-	1.46	14.18	26.71

## 3.5. SubNPc

## 3.5.1. Synthesis

**Scheme 3.4** shows Synthesis of SubNPc. The Cl was converted to OH during the purification as shown in **Scheme 3.4**. Silica and biobeads S-X1 were employed for purification.



**Scheme 3.4:** Synthesis of 1,2-subnaphthalocyanines

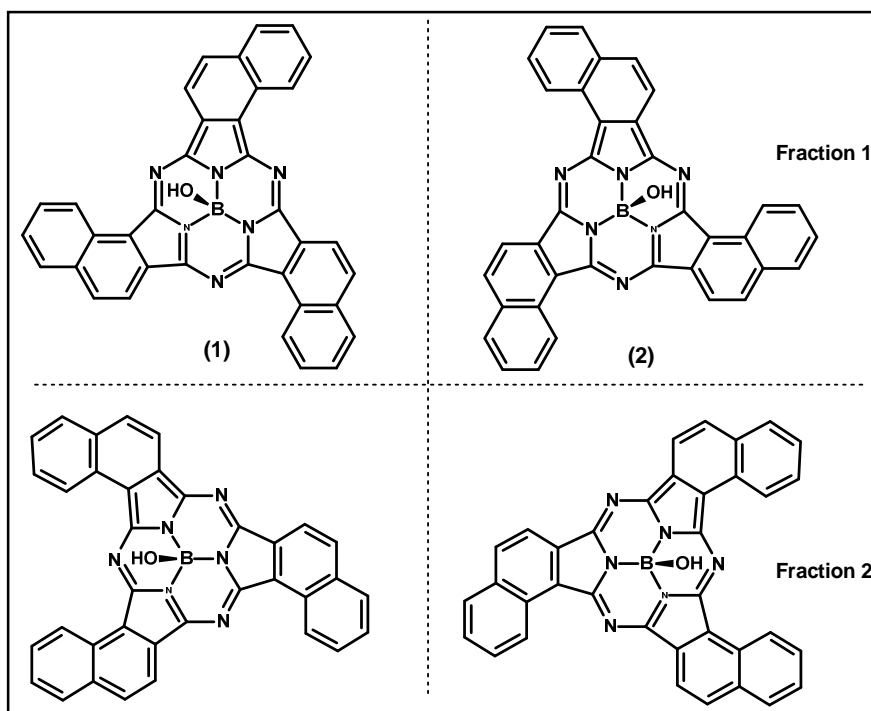


**Figure 3.27:** Subnaphthalocyanine enantiomers

High pressure liquid chromatography-gel permeation chromatography (HPLC-GPC) column (chloroform as eluent) was used to purify **Fraction 1** giving C<sub>3</sub> chiral isomers **1** and **2** (**Figure 3.27**). The chiral isomers were separated using Chiral Pak<sup>®</sup>IA LC column with a solvent mixture of hexane: chloroform (3:2) to obtain fraction (a) and (b) (**Figure 3.28**). The <sup>1</sup>H NMR spectrum of **Fraction 1** in CDCl<sub>3</sub> exhibits doublets at 10.10, 8.80, 8.85 and 8.25 ppm and two triplets at 7.90 and 7.80 ppm due to the naphthalene moieties, reflecting the C<sub>3</sub> symmetric structure.

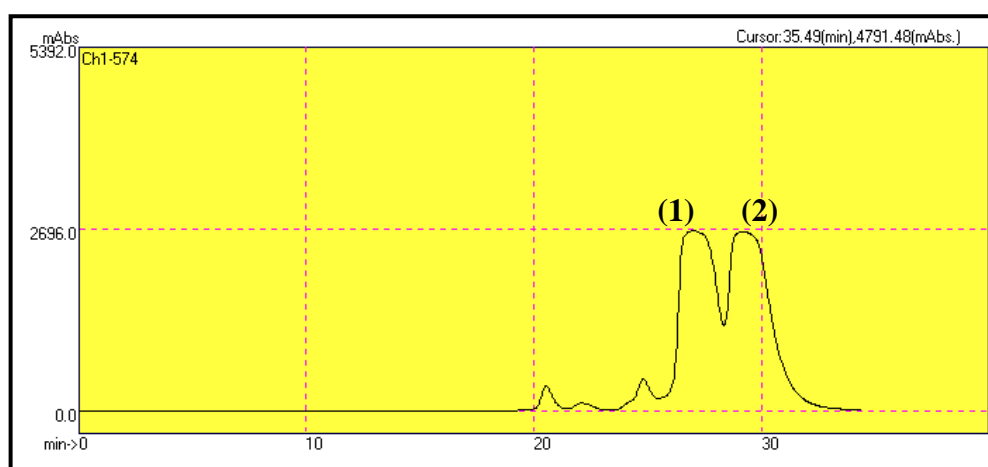


**Figure 3.28:** HPLC trace of Fraction 1: Solvent: Chloroform: Hexane (2:3) Flow rate (1mL/Pa).

### 3.5.2. UV/vis , CD, and MCD spectra

**Figure 3.29** shows the spectra of subnaphthalocyanine (**Fraction 1** in **Figure 3.27**) (SubNPc) in chloroform. The absorption spectra shows similar characteristic to that of subphthalocyanines which have a Q-band at 560 nm and a B-band at 300 nm. SubNPc absorption spectra, in **Figure 3.29C**, has a red shifted Q-band at 574 nm and a B-band at 390 nm due to the increased conjugated system. Both enantiomers (**1** and **2** in **Figure 3.29**) showed identical absorption and magnetic circular dichromism (MCD) spectrum. The absorption coefficient in both the Q and B bands is smaller in comparison to that of phthalocyanines. This decrease in the Q and B bands extinction coefficients with respect to phthalocyanines has been attributed to the non-planarity of a SubPc and SubNPc. MCD was employed as a complementary technique to UV-Vis spectroscopy in order to retrieve valuable information about the nature of UV-vis transitions. The MCD spectrum of the enantiomers (**Figure 3.29A**), showed a clear positive Faraday  $\mathcal{A}$ -term curve associated with the absorption peak at 574 nm, which means that the LUMO energy levels are degenerate.

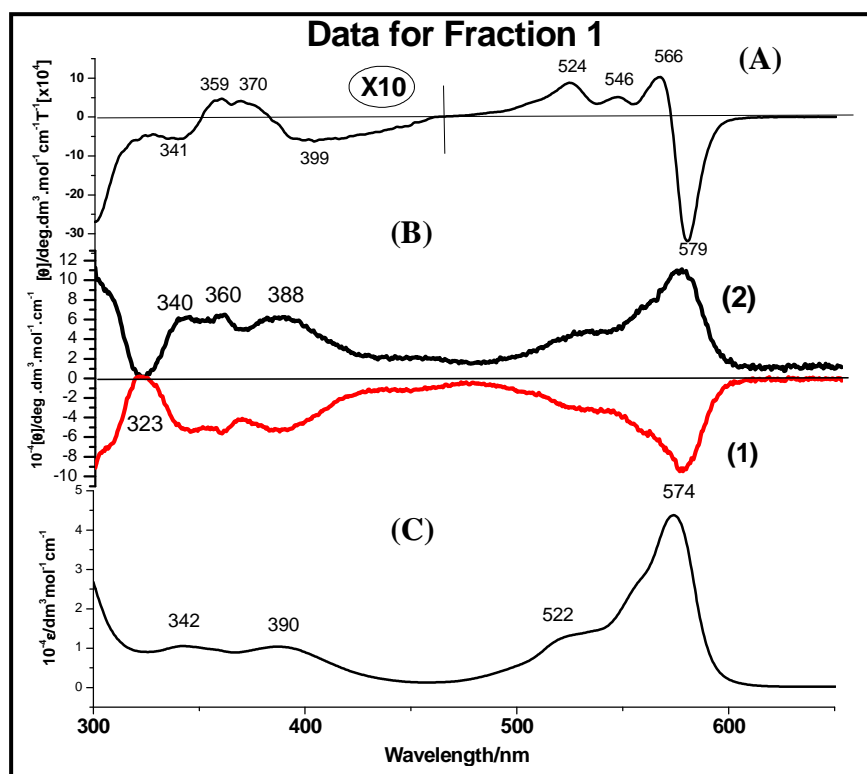


**Figure 3.29:** (A) MCD of SubNPc (Fraction 1) measured in  $\text{CHCl}_3$  at room temperature (B) CD and (C) electronic absorption spectra. ( $\epsilon = 3.42 \times 10^{-5} \text{ M}$ )

According to the following discussion based on the MCD spectra and theoretical calculations, the absorptions in the longer wavelength region of 500–600 nm are assigned as Q bands, which consist of transitions from the HOMO to the nearly degenerate, LUMO and LUMO+1.

In order to deduce further information from the absorption spectra, MCD measurements were performed on **Fraction 1** (enantiomers). The MCD spectra of isomer **1** exhibit similar spectral features over the complete region as isomer **2**. Corresponding to the Q band, derivative-shaped signals are observed with negative and positive envelopes at 579 and 566 nm. Based on the molecular symmetries of  $C_3$ , the MCD signals can be assigned as a Faraday  $\mathcal{A}$  term. In the MCD spectra of isomers **1** and **2**, the positive envelopes of the Q bands at ca.470–570 nm are significantly smaller than the negative envelopes at 570–600 nm. This is due to cancellation of the positive envelope by the edge of the negative envelope and their vibronic bands. In the higher energy region of 300–450 nm, several MCD signals correspond to the characteristic absorptions for SubNPc molecules are observed. Their smaller intensities compared to those of the Q band region are mainly due to the smaller angular momentum of these transitions. Although these signals are not easily assigned, due to the contributions of a

number of transitions and their vibronic bands, dispersion type negative to positive envelopes at 399 and 370 nm correspond to the broad absorption at 390 nm, respectively, indicates the presence of transitions to the nearly degenerate excited states. In addition to variation in shapes of the absorption spectra from those of SubPcs in the higher energy region, these MCD signals imply that the annulation of benzene rings at the  $\alpha$ , and  $\beta$  positions on going from SubPc to SubNPc cause rather significant changes in the energy level of molecular orbitals, especially for those lying lower than the HOMO and/or higher than the LUMO+1. Details of this are discussed based on theoretical calculation in the following section.

In the CD spectra (**Figures 3.29B**), isomer **1** show a negative sign between 350 and 579 nm, whereas isomer **2**, show a positive sign in the corresponding regions.

### 3.5.3. Electronic structures and theoretical absorption spectra

Theoretical calculations were performed on **Fraction 1** (isomer **1** or **2**). Structural optimization was performed based on the DFT method at the B3LYP/6-31G(d) level, and time-dependent (TD) DFT calculations were also carried out with the same hybrid functional and basis set. As a reference, DFT and TDDFT calculations were also performed on a model compound of a non-substituted SubPc, in which the axial ligand was hydroxide. With respect to the frontier molecular orbitals (MOs), **Fraction 1** (isomer **1** or **2**) of SubNPc exhibit a similar electron density distribution pattern to that of SubPc, and delocalization of electron density on the exterior benzene rings is also common to **Fraction 1** (isomer **1** or **2**) (**Figure 3.30**).



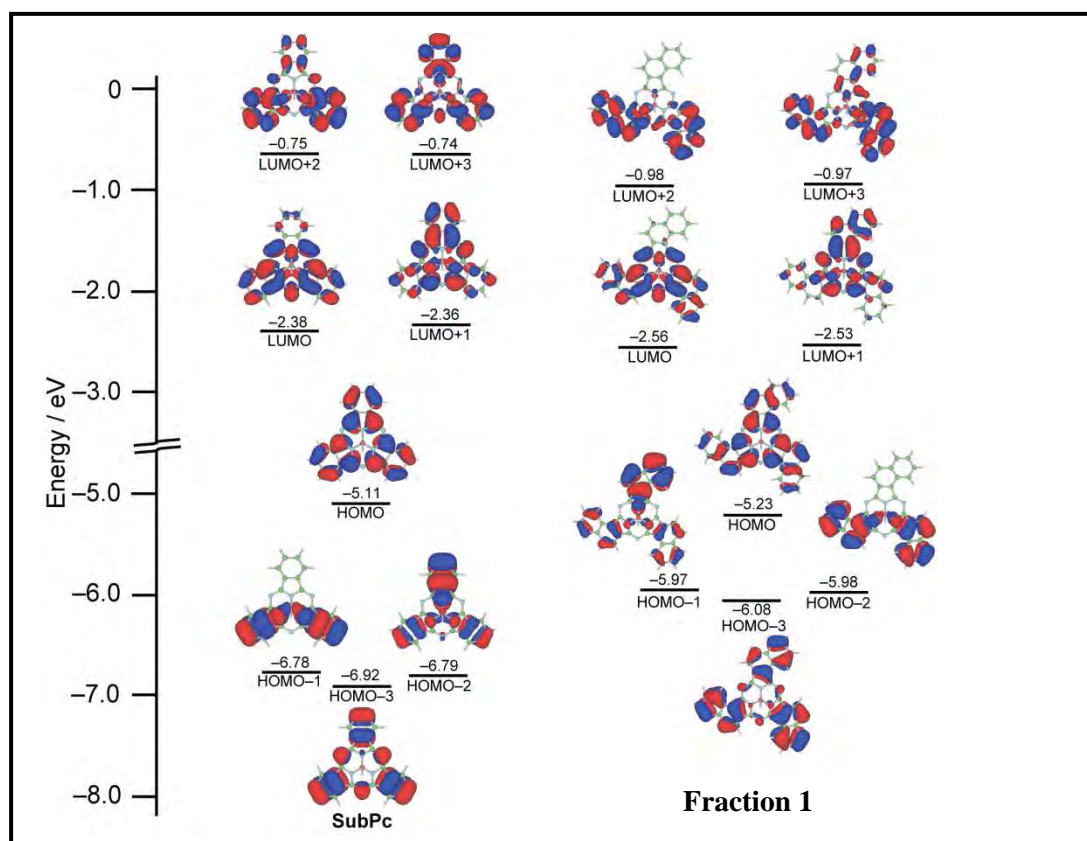


**Figure 3.30: Partial molecular diagram of SubPc (left) and SubNPc (right).**

In-depth analyses on the MOs higher than the LUMO+1 and lower than the HOMO reveals slight stabilization of the degenerate LUMO+2 and LUMO+3 and rather significant destabilization of the HOMO-3 along with the degenerate HOMO-1 and HOMO-2 compared to those of SubPc. Based on the TDDFT calculations, two main bands at 511 and 508 nm for **Fraction 1** (isomer **1** or **2**) of SubNPc which can be assigned as Q bands, are each composed of transitions from the HOMO to the nearly degenerate LUMO and LUMO+1 (**Table 3.6**). These calculation results are in good agreement with the observed small red-shift of the Q band in the absorption and dispersion-type MCD signals in the corresponding region. In the case of SubPc, the secondary main absorptions at 299 and 297 nm are composed of several transitions from MOs lower than the HOMO to the degenerate LUMO and LUMO+1 (**Table 3.6**). Meanwhile, the secondary main bands of **Fraction 1** (isomer **1** or **2**) at 399 and 395 nm are significantly red-shifted for SubNPc, and are mainly composed of transitions from the HOMO-3 to the LUMO and LUMO+1. As a result of the small mixing of bands in this region, dispersion-type MCD signals, corresponding to the absorptions at 390 nm are clearly observed in the MCD spectra of **Fraction 1** (isomer **1** or **2**). These results indicate that the main change caused by the annulation of benzene rings at the  $\alpha$ , and  $\beta$

positions of SubPc molecule is destabilization of the HOMO–3 along with the HOMO–1 and HOMO–2. Thus, the two weak bands at 350–430 nm region are fairly characteristic for the electronic structures of SubNPs, whereas conventional SubPc molecules exhibit two broad bands in the same region [8, 47, 51].

**Table 3.6: Selected transition energies and wave functions of Fraction 1(SubNPs) and SubPc calculated by the TDDFT (B3LYP/6-31G(d)) method.**

Compound	energy [nm]	$f^{[a]}$	wave function <sup>[b]</sup>
<b>Fraction 1 (SubNPs)</b>	511	0.36	+ 0.621  146 ← 145> - 0.114  147 ← 138> + 0.167  147 ← 142> ...
	508	0.35	+ 0.621  147 ← 145> + 0.116  146 ← 138> - 0.172  146 ← 142> ...
	399	0.24	+ 0.636  146 ← 142> - 0.149  147 ← 143> - 0.128  146 ← 144> + 0.112  147 ← 145> ...
	395	0.24	+ 0.658  147 ← 142> - 0.101  146 ← 143> - 0.104  146 ← 145> ...
<b>SubPc</b>	489	0.31	+ 0.617  107 ← 106> - 0.109  108 ← 100> + 0.176  108 ← 103>
	486	0.31	+ 0.618  108 ← 106> + 0.111  107 ← 100> - 0.177  107 ← 103>
	299	0.26	+ 0.225  108 ← 99> + 0.361  107 ← 101> + 0.289  108 ← 102> - 0.319  107 ← 103> + 0.100  107 ← 104> + 0.11  108 ← 105> - 0.105  109 ← 106>
	297	0.24	+ 0.225  108 ← 98> - 0.196  107 ← 99> + 0.163  108 ← 100> + 0.435  108 ← 101> - 0.123  107 ← 102> + 0.353  108 ← 103>

[a] Oscillator strength. [b] The wave functions based on the eigenvectors predicted by TDDFT. The |145> and |106> represent the HOMO of Fraction 1 and that of SubPc, respectively. Eigenvectors greater than 0.10 are included.

The theoretical CD spectra based on TDDFT calculations at the B3LYP/6-31G(d) level on model compounds of **Fraction 1** gives a first clue for assigning absolute structures (**Figure 3.31**). The model compounds having a clockwise arrangement of benzene rings exhibit negative CD bands in the Q band region (isomer **1**), while those having an anti-clockwise

arrangement show, inversely, positive CD bands (isomer **2**). The theoretical CD spectra reproduce the observed CD spectra of, compounds **Fraction 1**.

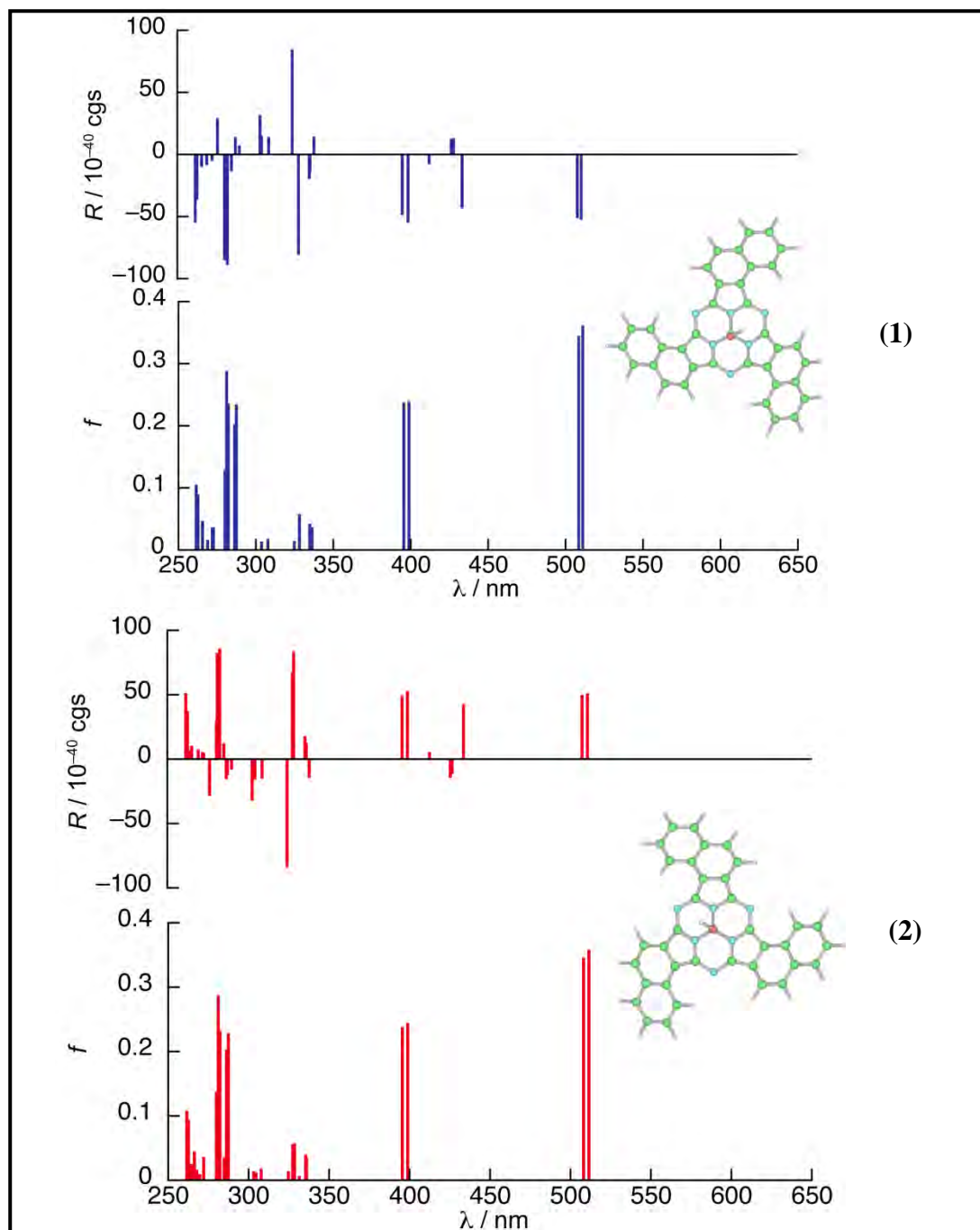


**Figure 3.31:** Theoretical absorption and CD spectra of clockwise isomer (left) and anti-clockwise isomer (right) of Fraction 1 based on TDDFT calculation.

# **Chapter 4**

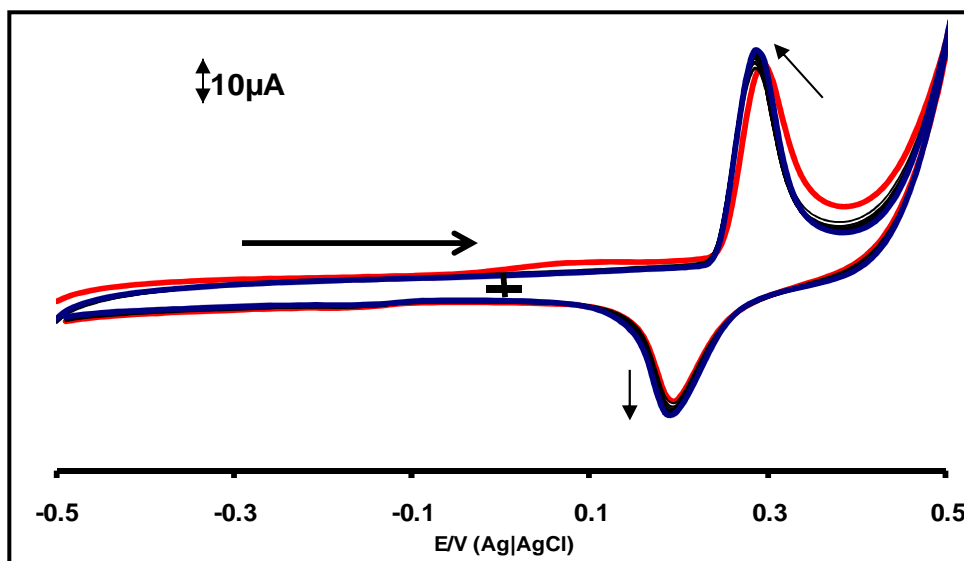
## **Electrode Modification and Characterization**

## 4.1. NiPc derivatives and their conjugates with SWCNT

### 4.1.1. NiPc derivatives

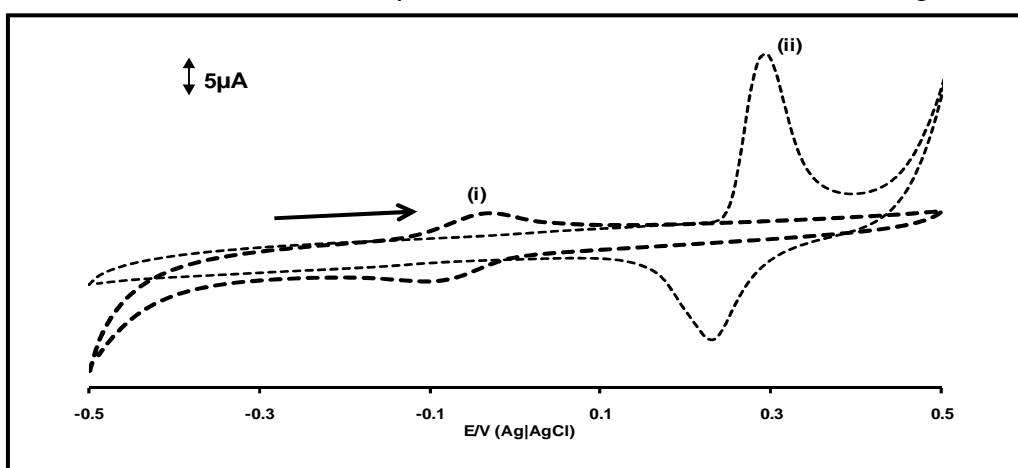
Electrode surfaces modified by MPcs can be obtained by simple adsorption on pyrolytic graphite electrode (OPGE) and glassy carbon electrodes (GCE). The simplicity of adsorbing complexes on carbon materials has been the preferred method by researchers due to its reproducibility. OPGE surface is easily renewed and offers a better  $\pi$ - $\pi$  interaction compared to GC electrode, thus allows easy adsorption of electrode modifiers. However, OPGE is not readily available compared to GC electrodes, due to this limitation, OPGE was employed only for  $\beta$ -NiPc(OH)<sub>4</sub>,  $\alpha$ -NiPc(OH)<sub>4</sub> and  $\alpha$ -NiPc(OH)<sub>8</sub>. The NiPc derivatives ( $\beta$ -NiPc,  $\beta$ -NiPc(NH<sub>2</sub>)<sub>4</sub>,  $\beta$ -NiPc(OH)<sub>4</sub>,  $\alpha$ -NiPc(OH)<sub>4</sub>,  $\alpha$ -NiPc(OH)<sub>8</sub> and  $\alpha$ -NiPc(C<sub>10</sub>H<sub>21</sub>)<sub>8</sub>) were adsorbed onto the GCE or OPGE by dipping the electrode in dry dimethylsulfoxide (DMSO) containing NiPc derivative except for  $\alpha$ -NiPc(C<sub>10</sub>H<sub>21</sub>)<sub>8</sub> (which was desolved in THF) and allowing the solvent to dry to give adsorbed derivatives. The electrochemical transformation of the NiPc derivatives in alkaline aqueous solution to form the interconnected O-Ni-O oxo bridges was achieved by cycling NiPc,  $\beta$ -NiPc(NH<sub>2</sub>)<sub>4</sub>,  $\beta$ -NiPc(OH)<sub>4</sub>,  $\alpha$ -NiPc(OH)<sub>4</sub>,  $\alpha$ -NiPc(OH)<sub>8</sub> and  $\alpha$ -NiPc(C<sub>10</sub>H<sub>21</sub>)<sub>8</sub>, respectively in 0.1 M NaOH, giving the polymerized derivatives: *poly*-Ni(O)Pc, *poly*- $\beta$ -Ni(O)Pc(NH<sub>2</sub>)<sub>4</sub>, *poly*- $\beta$ -Ni(O)Pc(OH)<sub>4</sub>, *poly*- $\alpha$ -Ni(O)Pc(OH)<sub>4</sub>, *poly*- $\alpha$ -Ni(O)Pc(OH)<sub>8</sub> and *poly*- $\alpha$ -NiPc(C<sub>10</sub>H<sub>21</sub>)<sub>8</sub>, respectively. The potential difference between OPGE and GCE for Ni<sup>III</sup>/Ni<sup>II</sup> redox process for *poly*- $\beta$ -Ni(O)Pc(OH)<sub>4</sub>, *poly*- $\alpha$ -Ni(O)Pc(OH)<sub>4</sub> and *poly*- $\alpha$ -Ni(O)Pc(OH)<sub>8</sub> was found to be ~ 0.08 V. The formation of O-Ni-O oxo bridges for  $\beta$ -NiPc(OH)<sub>4</sub>,  $\alpha$ -NiPc(OH)<sub>4</sub> and  $\alpha$ -NiPc(OH)<sub>8</sub> were easily achieved on OPGE compared to GCE. To serve as an example, the formation of O-Ni-O oxo bridge is only discussed for OPGE. For the rest of the complexes ( $\beta$ -NiPc,  $\beta$ -NiPc(NH<sub>2</sub>)<sub>4</sub> and  $\alpha$ -NiPc(C<sub>10</sub>H<sub>21</sub>)<sub>8</sub>) the readily available GCE was employed.

**Figure 4.1** shows the cyclic voltammograms of  $\beta$ -NiPc(OH)<sub>4</sub> adsorbed on OPGE in 0.1 M NaOH. There was an immediate formation of a typical pair of peaks due to Ni<sup>III</sup>/Ni<sup>II</sup> in Ni(O)Pc complexes polymerized in 0.1 M NaOH [125, 144], but instant peaks were also observed on GCE. Continuous cycling resulted in only a slight increase in current in **Figure 4.1**. Thus the cyclic voltammograms shown in **Figure 4.1** are due to *poly*- $\beta$ -Ni(O)Pc(OH)<sub>4</sub>. The peaks due to Ni<sup>III</sup>/Ni<sup>II</sup> are observed at 0.23 and 0.33 V in 0.1 M NaOH and 0.09 and -0.04V in pH 7 (**Figure 4.2**).



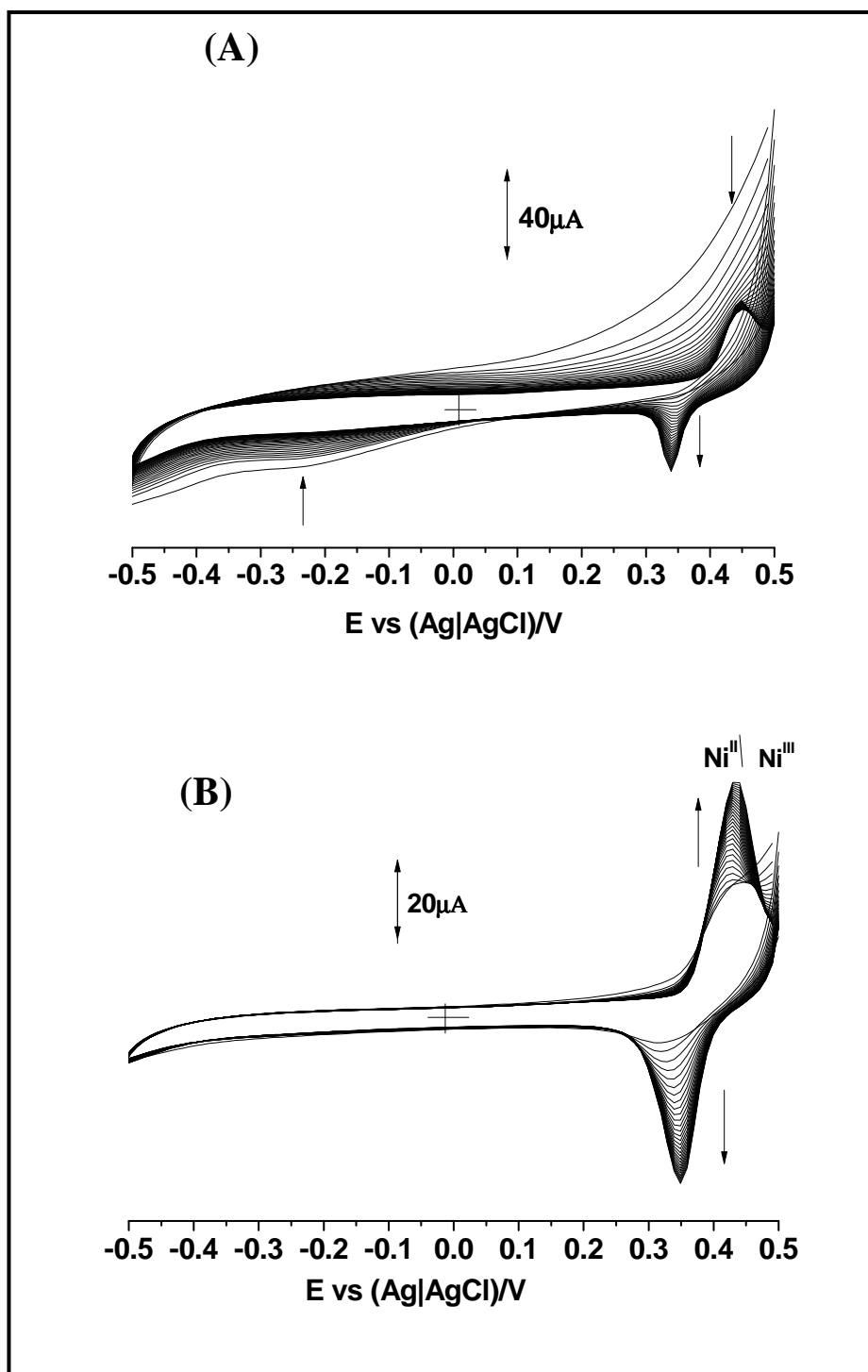
**Figure 4.1:** Cyclic voltammograms of  $\beta$ -NiPc(OH)<sub>4</sub>, adsorbed on the OPGE in 0.1 M NaOH, forming *poly*- $\beta$ -Ni(O)Pc(OH)<sub>4</sub>, Scan rate = 100 mVs<sup>-1</sup>.

The shape of the final cyclic voltammogram is very similar to those obtained with electro-transformed nickel macrocyclic-based films in alkaline aqueous solution, which are also similar to those of Ni(OH)<sub>2</sub> on electrodes [142, 143]. The formation of the peaks can be explained by the formation of the O-Ni-O oxo bridges in alkaline aqueous solution and are indication of the transformation of the  $\beta$ -NiPc(OH)<sub>4</sub> into the 'O-Ni-O oxo' bridged forms.



**Figure 4.2:** Cyclic voltammograms of *poly*- $\beta$ -Ni(O)Pc(OH)<sub>4</sub> on OPGE in (i) pH 7 buffer solution and (ii) in 0.1 M NaOH, Scan rate = 100 mVs<sup>-1</sup>.

**Figure 4.3A** shows only a weak feature at  $\sim -0.2$  V for  $\alpha$ -NiPc(OH)<sub>4</sub>, this is due to ring based reduction (NiPc<sup>2-</sup>/NiPc<sup>3-</sup>) as also observed for ring based reduction process for  $\alpha$ -NiPc(C<sub>10</sub>H<sub>21</sub>)<sub>8</sub> in solution (**Figure 3.7**). On cycling the adsorbed  $\alpha$ -NiPc(OH)<sub>4</sub> in 0.1 M NaOH solution, Ni<sup>III</sup>/Ni<sup>II</sup> couple began to form near 0.35 V. The cyclic voltammograms in **Figure 4.3A** are indication of the transformation of the  $\alpha$ -NiPc(OH)<sub>4</sub> into the O-Ni-O oxo bridged to form *poly- $\alpha$ -Ni(O)Pc(OH)<sub>4</sub>* on OPGE [125, 267, 268]. **Figure 4.3B** shows the cyclic voltammograms of  $\alpha$ -NiPc(OH)<sub>8</sub> in 0.1 M NaOH. Unlike the case with *poly- $\alpha$ -Ni(O)Pc(OH)<sub>4</sub>*, **Figure 4.3A**, there was an immediate formation of a pair of peaks associated with Ni<sup>III</sup>/Ni<sup>II</sup> for *poly- $\alpha$ -Ni(O)Pc(OH)<sub>8</sub>*, **Figure 4.3B**. This was followed by a gradual increase of the current with scanning in 0.1 M NaOH. In the case of  $\beta$ -NiPc(OH)<sub>4</sub> on OPGE (**Figure 4.1**) and  $\alpha$ -NiPc(C<sub>10</sub>H<sub>21</sub>)<sub>8</sub> the formation of Ni<sup>III</sup>/Ni<sup>II</sup> complexes on GCE was immediate (**Figure 4.3C**) compared to  $\alpha$ -NiPc(OH)<sub>4</sub> or NiPc where cycling was needed for formation of the couple as observed in **Figure 4.3A and 4.3D**. This suggests that the ease of formation of O-Ni-O bridges depends on the point of substitution, with formation being easier for the peripherally substituted derivatives, comparing  $\beta$ -NiPc(OH)<sub>4</sub> and  $\alpha$ -NiPc(OH)<sub>4</sub>. Comparing the formation of *poly- $\alpha$ -Ni(O)Pc(OH)<sub>4</sub>* with *poly- $\alpha$ -Ni(O)Pc(OH)<sub>8</sub>*, the latter forms O-Ni-O bridges more readily than the former in that the peaks were formed instantly in the latter. Thus the ease of formation of the O-Ni-O bridges also depends on the number of substituents. The scan rate dependence of the peak current was linear, suggesting surface bound redox processes. The type of substituent also plays a role in the formation of O-Ni-O bridge. For example nickel tetrasulfophthalocyanine (NiTSPc) readily forms O-Ni-O oxo bridges without the need of activation, whereas for nickel tetraaminophthalocyanine ( $\beta$ -NiPc(NH<sub>2</sub>)<sub>4</sub>), activation is needed [125, 267, 268].





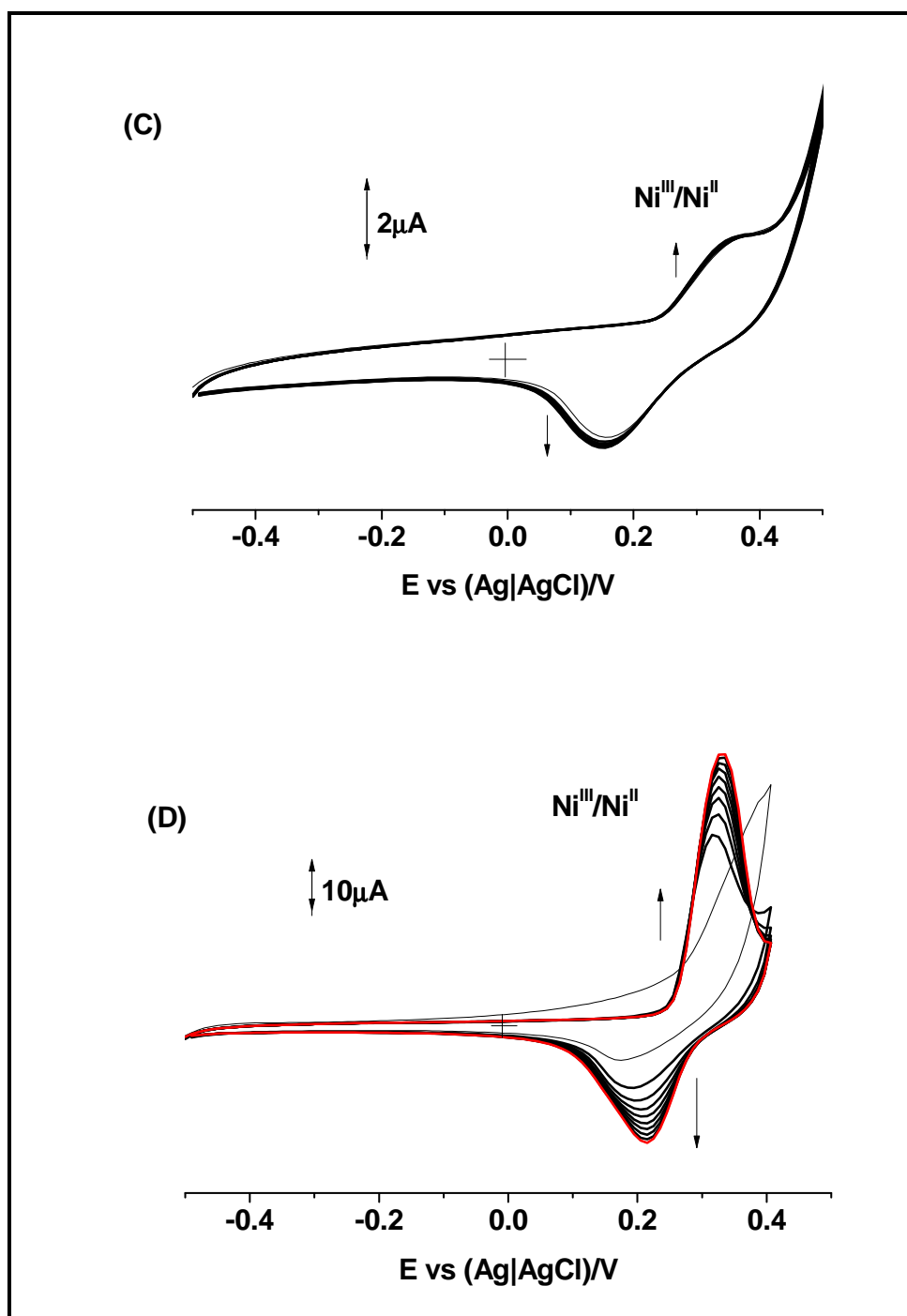
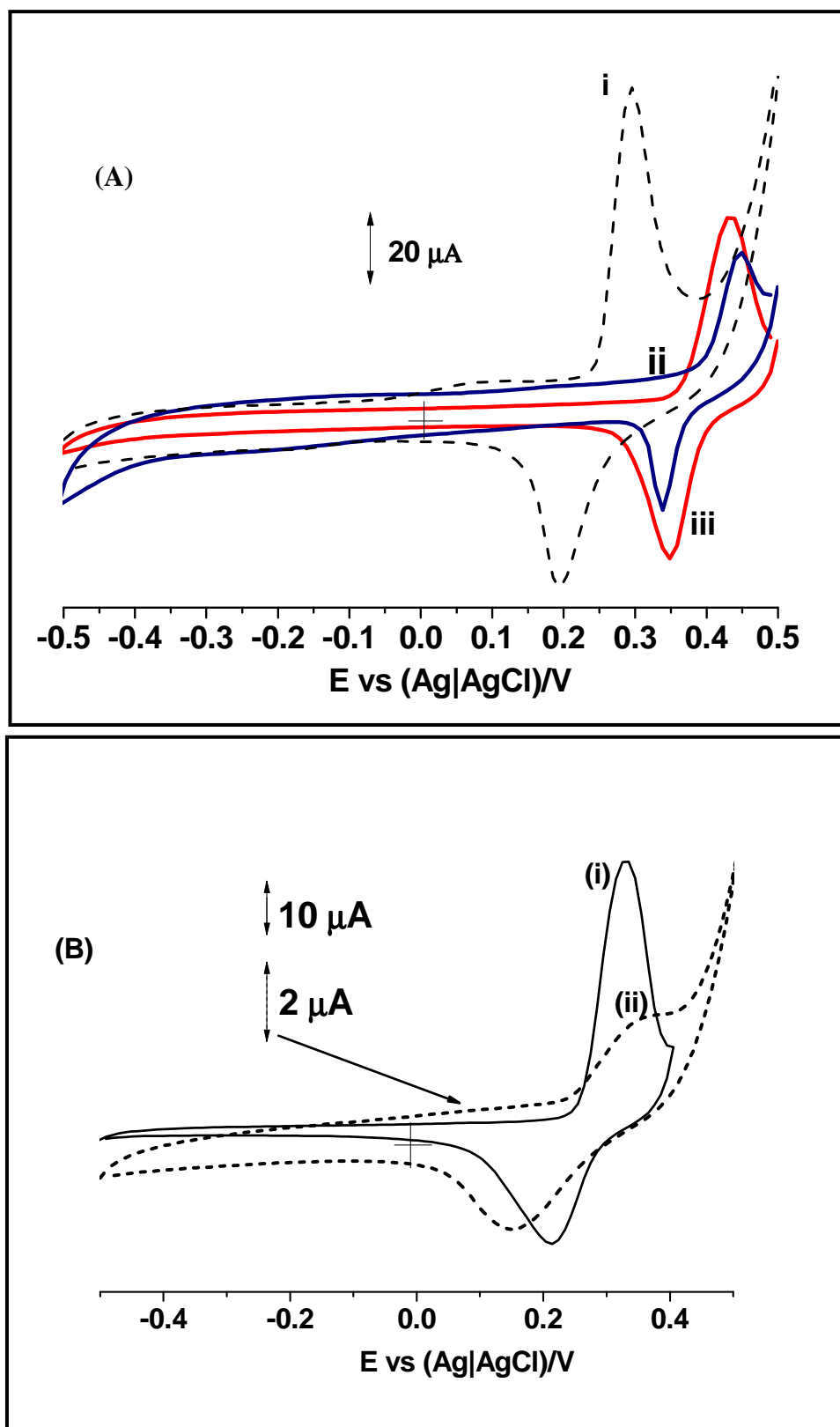
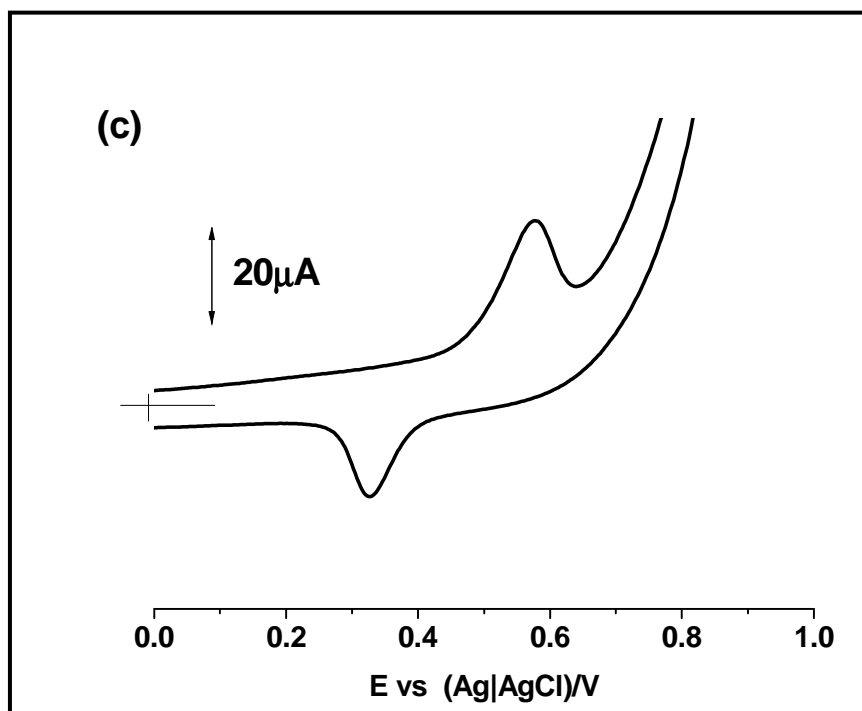


Figure 4.3: Cyclic voltammograms of (A)  $\alpha$ -NiPc(OH)<sub>4</sub>, and (B)  $\alpha$ -NiPc(OH)<sub>8</sub> adsorbed on the OPG electrode in 0.1 M NaOH, forming *poly- $\alpha$ -Ni(O)Pc(OH)<sub>4</sub>* and *poly- $\alpha$ -Ni(O)Pc(OH)<sub>8</sub>*, respectively, (C)  $\alpha$ -NiPc(C<sub>10</sub>H<sub>21</sub>)<sub>8</sub> adsorbed on the GC electrode and cycled in 0.1 M NaOH, forming *GCE-*poly- $\alpha$ -Ni(O)Pc(C<sub>10</sub>H<sub>21</sub>)<sub>8</sub>**, (D) NiPc adsorbed on the GC electrode in 0.1 M NaOH, forming *GCE-*poly-Ni(O)Pc**. Scan rate = 100 mVs<sup>-1</sup>

**Figure 4.4A** overlays the cyclic voltammograms of (i) *poly-β-Ni(O)Pc(OH)<sub>4</sub>*, (ii) *poly-α-Ni(O)Pc(OH)<sub>4</sub>* and (iii) *poly-α-Ni(O)Pc(OH)<sub>8</sub>* in 0.1 M NaOH. The peaks due to Ni<sup>III</sup>/Ni<sup>II</sup> are observed at  $E_{1/2} = 0.39$  V for *poly-α Ni(O)Pc(OH)<sub>8</sub>*, 0.40 V for *poly-α-Ni(O)Pc(OH)<sub>4</sub>* and at  $E_{1/2} = 0.28$  V for *poly-β-Ni(O)Pc(OH)<sub>4</sub>* in 0.1 M NaOH on OPGE, **Table 4.1**. The Ni<sup>III</sup>/Ni<sup>II</sup> peaks for *poly-α-Ni(O)Pc(OH)<sub>4</sub>* and *poly-α-Ni(O)Pc(OH)<sub>8</sub>* occur at more positive potentials compared to *poly-β-Ni(O)Pc(OH)<sub>4</sub>*, suggesting difficulty of oxidation for the former complexes which are non-peripherally substituted. **Figure 4.4B** shows a large peak separation for *poly-α-Ni(O)Pc(C<sub>10</sub>H<sub>21</sub>)<sub>8</sub>* (curve ii), suggesting that the formation of O-Ni-O oxo bridge is not favorable for *poly-α-Ni(O)Pc(C<sub>10</sub>H<sub>21</sub>)<sub>8</sub>* due to increased irreversibility of that process, with respect to *poly-Ni(O)Pc* and all other NiPc complexes. The irreversibility observed suggest that the OH<sup>-</sup> ions cannot easily penetrate the film in order to react with the Ni atom and form more O-Ni-O oxo bridge. **Figure 4.4C** shows the Ni<sup>III</sup>/Ni<sup>II</sup> peaks for *poly-β-Ni(O)Pc(NH<sub>2</sub>)<sub>4</sub>* ( $E_{1/2} = 0.45$  V, **Table 4.1**) to occur at less positive potentials compared to *poly-Ni(O)Pc(OH)<sub>n</sub>* complexes with the exception of *poly-β-Ni(O)Pc(OH)<sub>4</sub>*.





**Figure 4.4:** (A) Cyclic voltammograms of (i) *poly-β-Ni(O)Pc(OH)<sub>4</sub>*, (ii) *poly-α-Ni(O)Pc(OH)<sub>4</sub>* and (iii) *poly-α-Ni(O)Pc(OH)<sub>8</sub>* on OPG electrode, (B) Comparison of cyclic voltammogram of *poly-Ni(O)Pc* (i) with *poly-α-Ni(O)Pc(C<sub>10</sub>H<sub>21</sub>)<sub>8</sub>* (ii) on GCE, (C) Cyclic voltammograms of *poly-β-Ni(O)Pc(NH<sub>2</sub>)<sub>4</sub>* on GCE in 0.1 M NaOH. Scan rate = 100 mVs<sup>-1</sup>.

The effective electrodes area were estimated by using the  $[\text{Fe}(\text{CN})_6]^{3-/4-}$  redox system and applying the Randles–Sevick (**Equation 4.1**) for a reversible process [269]:

$$I_{pa} = (2.69 \times 10^5) n^{3/2} D^{1/2} \nu^{1/2} A C_o \quad 4.1$$

where  $D$  and  $C_o$  are the diffusion coefficient and bulk concentration of the redox probe 1 mM  $\text{K}_3[\text{Fe}(\text{CN})_6]$ , respectively,  $\nu$  is the scan rate and  $A$  is the effective electrode area and was determined to be 0.079 cm<sup>2</sup> for GCE. Cyclic voltammetry experiments at different scan rates were performed with each of the complexes stated above immersed in a solution of 1 mM  $\text{K}_3[\text{Fe}(\text{CN})_6]$  in 0.1 M KCl. The  $D$  value for  $\text{K}_3[\text{Fe}(\text{CN})_6]$  is  $7.6 \times 10^{-6}$  cm<sup>2</sup> s<sup>-1</sup> [269] and  $n$  is 1.

The surface coverages ( $\Gamma$ ,  $\text{mol}/\text{cm}^2$ ) for GCE-*poly*- $\beta$ -Ni(O)Pc(OH)<sub>4</sub>, GCE-*poly*- $\alpha$ -Ni(O)Pc(OH)<sub>4</sub>, GCE-*poly*- $\alpha$ -Ni(O)Pc(OH)<sub>8</sub>, GCE-*poly*- $\beta$ -Ni(O)Pc(NH<sub>2</sub>)<sub>4</sub>, GCE-*poly*- $\alpha$ -Ni(O)Pc(C<sub>10</sub>H<sub>21</sub>)<sub>8</sub>, GCE-*poly*-Ni(O)Pc and GCE-*poly*- $\beta$ -Ni(O)Pc(NH<sub>2</sub>)<sub>4</sub>-SWCNT (linked) were estimated from the charge under their relative oxidation peak using **Equation 4.2** [87, 270].

$$Q = nFA\Gamma \quad (4.2)$$

where  $Q$  is the total charge (C),  $A$  the effective surface area of the electrode and  $\Gamma$  is the surface coverage of the redox species. Using **Equation 4.2**, the total surface coverages of the electrodes of 2.46, 1.42, 4.74, 4.10, 4.81, 1.20 and 1.06  $\times 10^{-10}$  mol  $\text{cm}^{-2}$  were obtained for GCE-*poly*- $\alpha$ -Ni(O)Pc(OH)<sub>8</sub>, GCE-*poly*- $\alpha$ -Ni(O)Pc(OH)<sub>4</sub>, GCE-*poly*- $\beta$ -Ni(O)Pc(OH)<sub>4</sub>, GCE-*poly*- $\alpha$ -Ni(O)Pc(C<sub>10</sub>H<sub>21</sub>)<sub>8</sub>, GCE-*poly*-Ni(O)Pc and, GCE-*poly*- $\beta$ -Ni(O)Pc(NH<sub>2</sub>)<sub>4</sub> respectively, **Table 4.1**.

In the absence of O-Ni-O peaks, peaks due to the ring processes were employed. **Figure 4.5** shows the CV of adsorbed  $\beta$ -NiPc(OH)<sub>4</sub> species on GCE as an example. The quasi reversible peak is attributed to adsorbed NiPc derivative as observed before [140]. The surface coverages were calculated by using the charge under the adsorption peak in **Figure 4.5**, according to **Equation 4.2** [271].

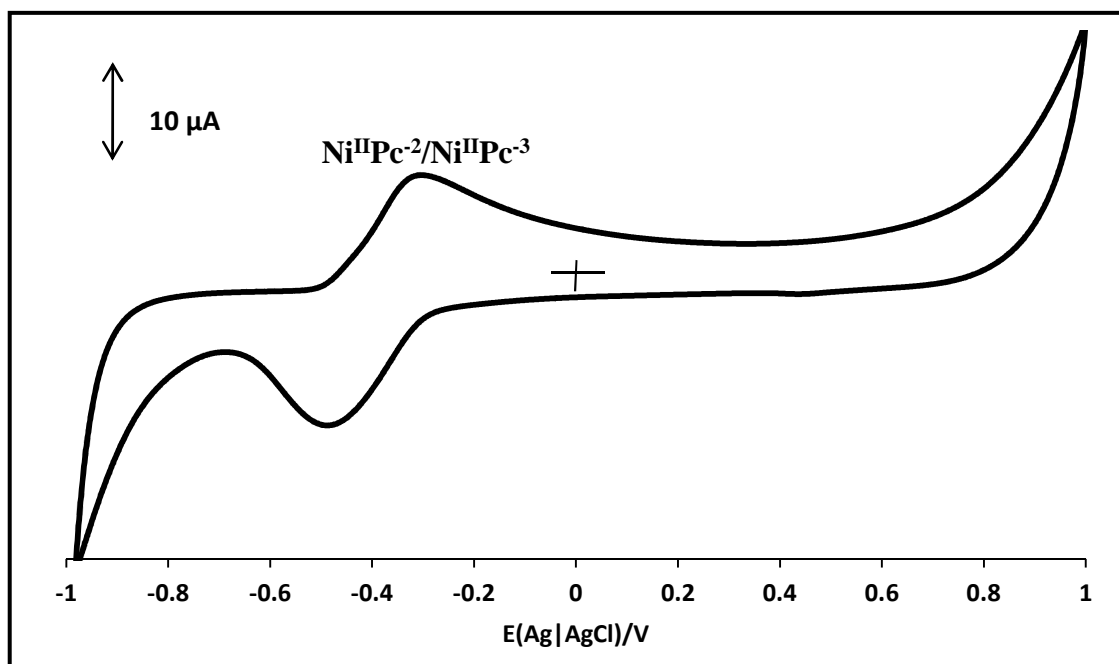


**Figure 4.5:** Cyclic voltammogram of GCE- $\beta$ -NiPc(OH)<sub>4</sub> electrode in buffer solution of pH 9.2.

**Table 4.1. Electrochemical parameters for NiPc derivatives in 0.1 M NaOH, on GCE unless otherwise stated.**

NiPc derivative	$E_{1/2}$ vs (Ag/AgCl)/V (Ni <sup>III</sup> /Ni <sup>II</sup> ) or (Pc <sup>-2</sup> /Pc <sup>-3</sup> )	$10^{-10} \times \Gamma / \text{mol cm}^{-2}$	Number of NiPc derivative molecules <sup>c</sup>
<i>poly</i> - $\beta$ -Ni(O)Pc(OH) <sub>4</sub>	(0.28) <sup>b</sup> 0.36	4.74	$2.37 \times 10^{13}$ ( $2.9 \times 10^{13}$ ) <sup>c</sup>
<i>poly</i> - $\alpha$ -Ni(O)Pc(OH) <sub>4</sub>	(0.40) <sup>b</sup> 0.48	1.42	$7.6 \times 10^{12}$ ( $2.9 \times 10^{13}$ ) <sup>c</sup>
<i>poly</i> - $\alpha$ -Ni(O)Pc(OH) <sub>8</sub>	(0.39) <sup>b</sup> 0.47	2.46	$1.23 \times 10^{13}$ ( $3.7 \times 10^{10}$ ) <sup>c</sup>
$\beta$ -NiPc(OH) <sub>4</sub> , <sup>a</sup>	-0.39	0.26	$1.3 \times 10^{12}$
NiPc <sup>a</sup>	-0.36	7.20	$3.6 \times 10^{13}$
$\alpha$ -NiPc(OH) <sub>4</sub> , <sup>a</sup>	-0.51	5.18	$2.5 \times 10^{13}$
$\alpha$ -NiPc(OH) <sub>8</sub> , <sup>a</sup>	-0.52	3.23	$1.6 \times 10^{13}$
$\beta$ -NiPc(NH <sub>2</sub> ) <sub>4</sub>	-0.76	1.02	$6.14 \times 10^{13}$
$\alpha$ -NiPc(C <sub>10</sub> H <sub>21</sub> ) <sub>8</sub> <sup>d</sup>	0.15	1.54	$7.7 \times 10^{12}$
<i>poly</i> - $\alpha$ -Ni(O)Pc(C <sub>10</sub> H <sub>21</sub> ) <sub>8</sub>	0.81	4.10	$1.9 \times 10^{12}$
<i>poly</i> -Ni(O)Pc	0.51	4.81	$2.0 \times 10^{13}$
<i>poly</i> - $\beta$ -Ni(O)Pc(NH <sub>2</sub> ) <sub>4</sub>	0.45	1.20	$7.2 \times 10^{13}$
<i>poly</i> - $\beta$ -Ni(O)Pc(NH <sub>2</sub> ) <sub>4</sub> -SWCNT(linked)	0.30	1.06	$5.1 \times 10^{12}$

<sup>a</sup> Values determined using Pc<sup>-2</sup>/Pc<sup>-3</sup> due to lack of Ni<sup>III</sup>/Ni<sup>II</sup> couple. <sup>b</sup> Values in brackets were determined using OPGE. <sup>c</sup> Numbers in brackets are calculated values. <sup>d</sup> Values determined using Pc<sup>-1</sup>/Pc<sup>-2</sup> peak.

The surface coverage values are within the order of magnitude of values expected for phthalocyanine molecule lying flat on the surface ( $10^{-10}$  mol cm<sup>-2</sup> [87]). All electrodes in the absence of SWCNT (except for  $\beta$ -NiPc(OH)<sub>4</sub>) gave values larger than a monolayer, suggesting multilayers [272].

The number of molecules covering the surface area of the electrode was estimated experimentally using the surface coverage above and the geometric area of the GCE, whereas the theoretical number of molecules (in brackets in **Table 4.1**) covering the surface area of the electrode were determined from optimized molecular structures (hence area of one molecule) using Gaussian at B3LYP/6-31G(d) level, **Table 4.1**. The number of molecules experimentally determined on GCE were of the order of  $10^{12}$  to  $10^{13}$ , typical of Pcs [272] compared to literature. The calculated (theoretical) number of molecules for *poly*- $\alpha$ -

$\text{Ni(O)Pc(OH)}_4$  and *poly*- $\beta\text{-Ni(O)Pc(OH)}_4$ , are larger than the experimentally determined values, which suggest that the surface coverage is less than a monolayer. For *poly*- $\alpha\text{-Ni(O)Pc(OH)}_8$  the calculated number of molecules is much lower than the experimental values, which suggests that the surface coverage exceeds that of a monolayer.

The surface coverages, in **Table 4.1**, obtained for GCE-NiPc, GCE- $\beta\text{-NiPc(NH}_2)_4$ , GCE- $\beta\text{-NiPc(OH)}_4$ , GCE- $\alpha\text{-NiPc(OH)}_4$ , GCE- $\alpha\text{-NiPc(OH)}_8$  and GCE- $\alpha\text{-NiPc(C}_{10}\text{H}_{21})_8$ ,  $\text{Pc}^{-2}/\text{Pc}^{-3}$  or  $\text{Pc}^{-1}/\text{Pc}^{-2}$  peaks were used to determine the surface coverage due to lack of  $\text{Ni}^{\text{III}}/\text{Ni}^{\text{II}}$  couple as indicated on **Table 4.1**. GCE-NiPc, GCE- $\alpha\text{-NiPc(OH)}_4$  and GCE- $\alpha\text{-NiPc(OH)}_8$  gave surface coverage values which are larger than a monolayer, suggesting multilayers. GCE- $\beta\text{-NiPc(OH)}_4$  and GCE- $\beta\text{-NiPc(NH}_2)_4$  gave surface coverage values which are lower or within a monolayer value.

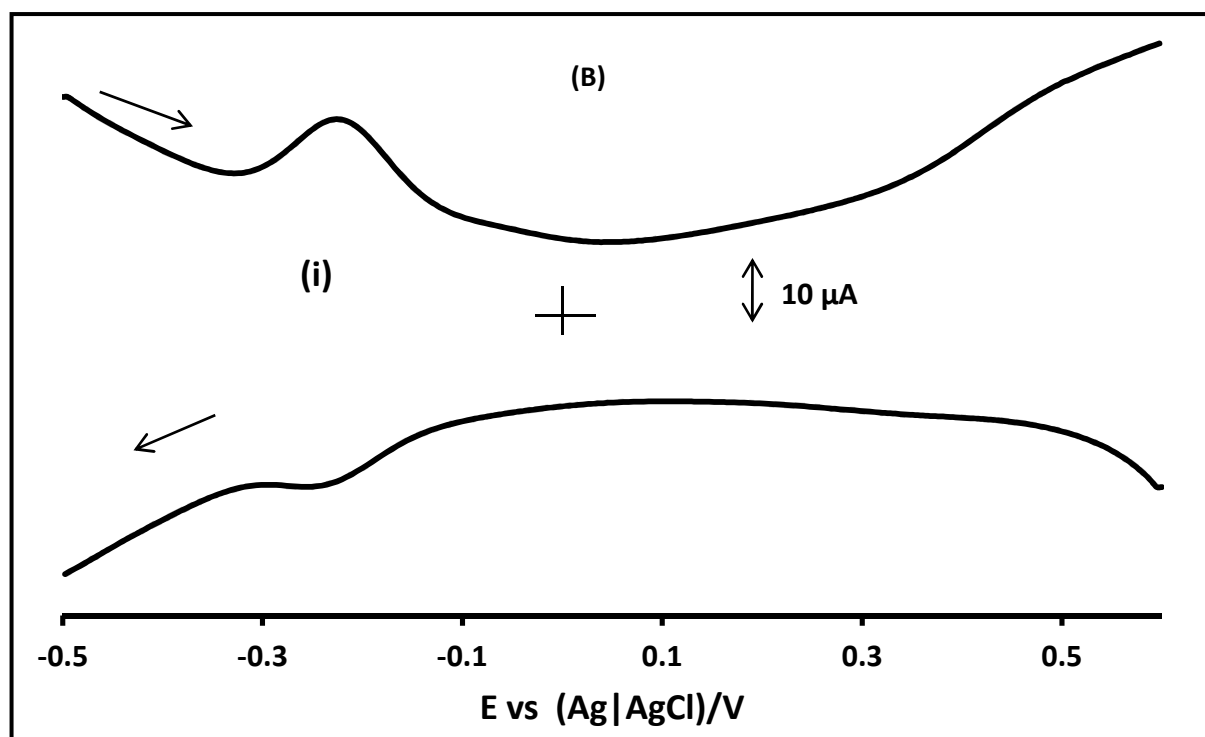
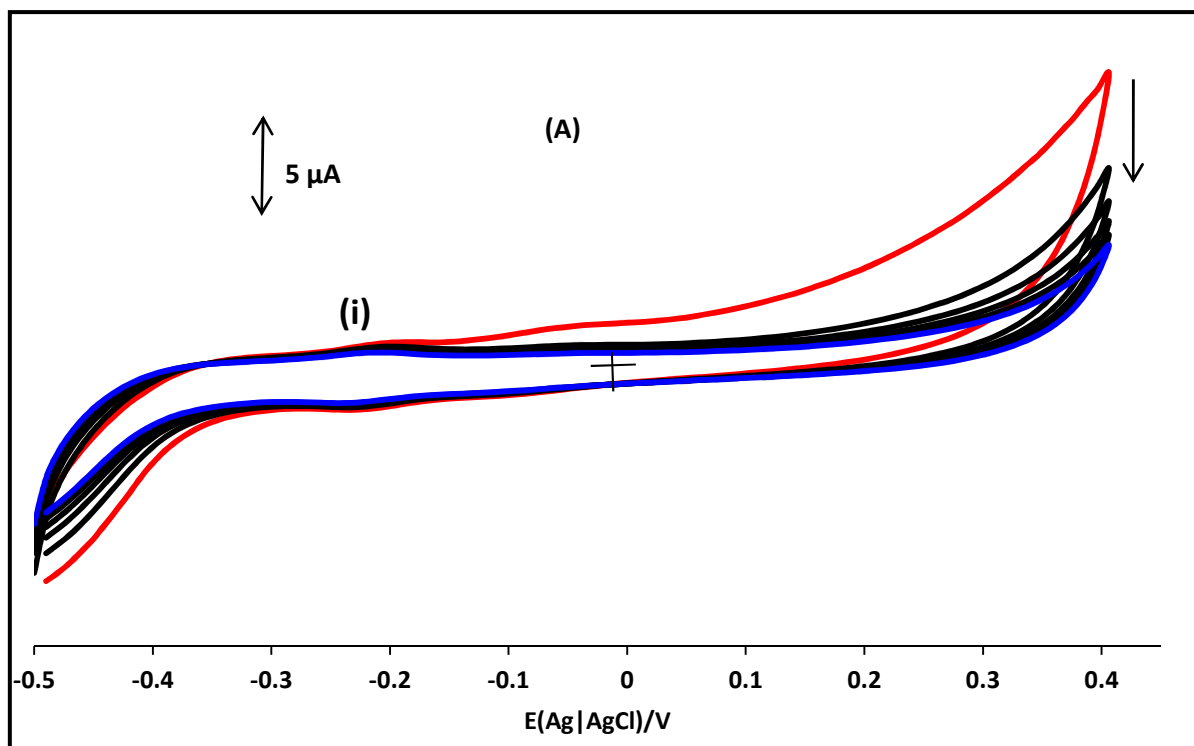
#### 4.1.2. NiPc-SWCNT conjugates

The adsorption of NiPc derivatives on the SWCNT was achieved by ultrasonication of the mixture of the two in DMF or THF followed by purification. The NiPc derivatives are expected to adsorb on SWCNT by  $\pi\text{-}\pi$  interactions. There is a chemical bond between the two, via an amide bond, only for  $\beta\text{-NiPc(NH}_2)_4\text{-SWCNT(linked)}$ . The GCE was modified with SWCNT, NiPc-SWCNT,  $\beta\text{-NiPc(NH}_2)_4\text{-SWCNT(linked)}$ ,  $\beta\text{-NiPc(NH}_2)_4\text{-SWCNT}$ ,  $\beta\text{-NiPc(OH)}_4\text{-SWCNT}$ ,  $\alpha\text{-NiPc(OH)}_4\text{-SWCNT}$ ,  $\alpha\text{-NiPc(OH)}_8\text{-SWCNT}$  and  $\alpha\text{-NiPc(C}_{10}\text{H}_{21})_8\text{-SWCNT}$  by the drop dry method, where by a drop of the colloidal solution of each modifier was placed onto the electrode and allowed to dry as explained in the experimental section. For complexes without SWCNTs, the GCE was modified by placing a drop of DMF solutions of NiPc,  $\beta\text{-NiPc(NH}_2)_4$ ,  $\beta\text{-NiPc(OH)}_4$ ,  $\alpha\text{-NiPc(OH)}_4$  or  $\alpha\text{-NiPc(OH)}_8$  and a drop of  $\alpha\text{-NiPc(C}_{10}\text{H}_{21})_8$  in THF on GCE followed by drying in nitrogen atmosphere. The modified electrodes are represented as GCE-SWCNT, GCE-NiPc, GCE- $\beta\text{-NiPc(NH}_2)_4$ , GCE- $\beta\text{-NiPc(OH)}_4$ , GCE- $\alpha\text{-NiPc(OH)}_4$ , GCE- $\alpha\text{-NiPc(OH)}_8$ , GCE- $\alpha\text{-NiPc(C}_{10}\text{H}_{21})_8$ , GCE- $\beta\text{-NiPc(NH}_2)_4\text{-SWCNT(linked)}$ , GCE- $\beta\text{-NiPc(NH}_2)_4\text{-SWCNT}$ , GCE- $\beta\text{-NiPc(OH)}_4\text{-SWCNT}$ , GCE- $\alpha\text{-NiPc(OH)}_4\text{-SWCNT}$ , GCE- $\alpha\text{-NiPc(OH)}_8\text{-SWCNT}$ , GCE-NiPc-SWCNT and GCE- $\alpha\text{-NiPc(C}_{10}\text{H}_{21})_8\text{-SWCNT}$ .

There was no clear peak due to the adsorbed NiPc derivative in the presence of SWCNT except for *poly*- $\beta$ -Ni(O)Pc(NH<sub>2</sub>)<sub>4</sub>-SWCNT (linked). As an example square wave voltammograms of GCE- $\alpha$ -NiPc(C<sub>10</sub>H<sub>21</sub>)<sub>8</sub>-SWCNT after 30 scans in 0.1 M NaOH are shown in **Figure 4.6B**. Cyclic or differential pulse voltammetry of GCE- $\alpha$ -NiPc(C<sub>10</sub>H<sub>21</sub>)<sub>8</sub>-SWCNT in 0.1 M NaOH, did not show typical peaks due to Ni<sup>III</sup>/Ni<sup>II</sup> redox process (**Figure 4.6A**). The square wave voltammogram (SWV) in **Figure 4.6B** shows a weak, but highly reversible, redox process observed at -0.24 V, with a peak separation ( $\Delta E$ ) near zero, typical of adsorbed species. The peak is also clear in the cyclic voltammogram in **Figure 4.6A**. This redox process is assigned to phthalocyanine ring reduction, because typical Ni<sup>III</sup>/Ni<sup>II</sup> redox process occurs at positive potentials. Similarly for all NiPc derivatives when adsorbed on SWCNT, and cycled in 0.1M NaOH, no Ni<sup>III</sup>/Ni<sup>II</sup> couple was observed. However Ni<sup>III</sup>/Ni<sup>II</sup> couple was observed only for  $\beta$ -NiPc(NH<sub>2</sub>)<sub>4</sub>-SWCNT(linked) (**Figure 4.6C**). The above suggests that, for  $\beta$ -NiPc(NH<sub>2</sub>)<sub>4</sub>-SWCNT(linked), the linking Ni central atom is still available to form O-Ni-O bonds, but when adsorbed on SWCNT this is not possible. The Ni<sup>III</sup>/Ni<sup>II</sup> peak was observed at 0.30 V for  $\beta$ -NiPc(NH<sub>2</sub>)<sub>4</sub>-SWCNT(linked) compared to 0.45 V in the absence of SWCNT (**Table 4.1**). The surface coverage for the linked was  $1.06 \times 10^{-10}$ , typical of a monolayer.

The shift of Ni<sup>III</sup>/Ni<sup>II</sup> process to lower oxidation potential for the linked complex compared to  $\beta$ -NiPc(NH<sub>2</sub>)<sub>4</sub> alone, further confirms the linking of  $\beta$ -NiPc(NH<sub>2</sub>)<sub>4</sub> to SWCNT. The shift to lower oxidation potential suggests that linking  $\beta$ -NiPc(NH<sub>2</sub>)<sub>4</sub> to SWCNT lowers the energy required to drive the Ni<sup>III</sup>/Ni<sup>II</sup> redox process. The  $\Delta E$  of Ni<sup>III</sup>/Ni<sup>II</sup> redox process is 0.15 V for the linked *poly*- $\beta$ -Ni(O)Pc(NH<sub>2</sub>)<sub>4</sub>-SWCNT and 0.25 V for  $\beta$ -NiPc(NH<sub>2</sub>)<sub>4</sub>. The small  $\Delta E$  value for *poly*- $\beta$ -Ni(O)Pc(NH<sub>2</sub>)<sub>4</sub>-SWCNT (linked) compared to *poly*- $\beta$ -Ni(O)Pc(NH<sub>2</sub>)<sub>4</sub> suggests that the rate of electron transfer for Ni<sup>III</sup>/Ni<sup>II</sup> redox process is enhanced when  $\beta$ -NiPc(NH<sub>2</sub>)<sub>4</sub> is linked to SWCNT. The above results suggest that SWCNT have an effect on the redox properties of Ni<sup>III</sup>/Ni<sup>II</sup> process, by lowering the oxidation potential where Ni<sup>III</sup>/Ni<sup>II</sup> redox process occurs with respect to *poly*- $\beta$ -Ni(O)Pc(NH<sub>2</sub>)<sub>4</sub>.





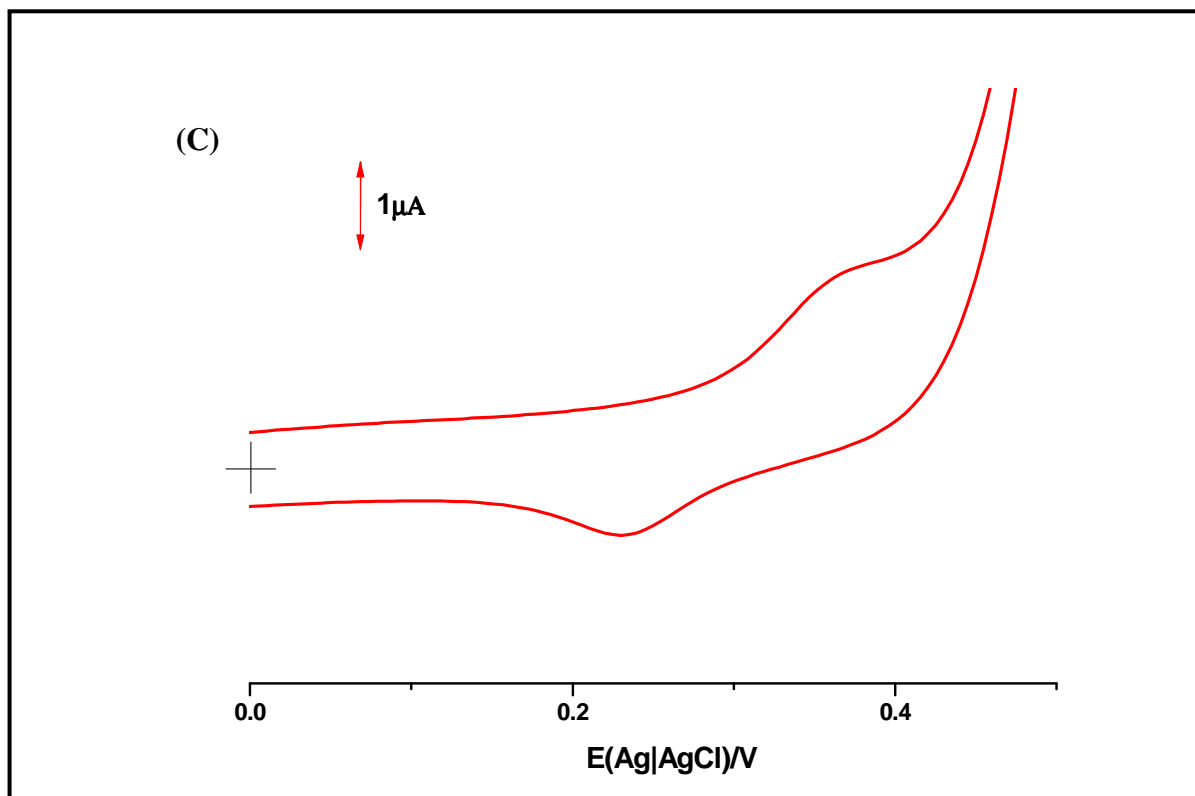


**Figure 4.6:** (A) Cyclic voltammogram of  $\alpha$ -NiPc(C<sub>10</sub>H<sub>21</sub>)<sub>8</sub>-SWCNT, (B) Square wave voltammogram of  $\alpha$ -NiPc(C<sub>10</sub>H<sub>21</sub>)<sub>8</sub>-SWCNT and (C) cyclic voltammogram of GCE- $\beta$ -Ni(O)Pc(NH<sub>2</sub>)<sub>4</sub>-SWCNT (linked) in 0.1 M NaOH solution, Scan rate 100 mVs<sup>-1</sup>

#### 4.1.3. Surfaces characterization of electrodes in [Fe(CN)<sub>6</sub>]<sup>3-/4-</sup>

The [Fe(CN)<sub>6</sub>]<sup>3-</sup>/[Fe(CN)<sub>6</sub>]<sup>4-</sup> couple is often employed to characterize the blocking ability of surfaces [272]. **Figure 4.7A** shows cyclic voltammograms of 1 mM [Fe(CN)<sub>6</sub>]<sup>3-</sup>/[Fe(CN)<sub>6</sub>]<sup>4-</sup> in 0.1 M KCl on GCE- $\beta$ -NiPc(OH)<sub>4</sub>-SWCNT (**15**), bare GCE (**1**), GCE- $\alpha$ -NiPc(OH)<sub>8</sub>-SWCNT (**12**) and GCE-SWCNT (**2**), as representatives of the rest of the electrodes listed in **Table 4.2**. All the modified electrodes showed the [Fe(CN)<sub>6</sub>]<sup>3-</sup>/[Fe(CN)<sub>6</sub>]<sup>4-</sup> redox probe, hence do not block the electrode effectively. **Table 4.2** shows the anodic to cathodic peak separations ( $\Delta E$ ) for the [Fe(CN)<sub>6</sub>]<sup>3-</sup>/[Fe(CN)<sub>6</sub>]<sup>4-</sup> redox probe on the various electrodes. Numbers are used in **Table 4.2** for ease of discussion.

The lack of blocking of [Fe(CN)<sub>6</sub>]<sup>3-</sup>/[Fe(CN)<sub>6</sub>]<sup>4-</sup> redox probe by MPc complexes has been reported previously for adsorbed cobalt tetraaminophthalocyanine films on glassy carbon electrode [273]. In terms of current, GCE- $\beta$ -NiPc(NH<sub>2</sub>)<sub>4</sub>-SWCNT (**5**), GCE- $\beta$ -NiPc(OH)<sub>4</sub>-

SWCNT (**15**) and GCE- $\alpha$ -NiPc(OH)<sub>4</sub>-SWCNT (**9**) (only (**15**) shown in **Figure. 4.7A**, for clarity of the figure) showed larger currents than bare GCE (**1**). GCE- $\beta$ -NiPc(NH<sub>2</sub>)<sub>4</sub>-SWCNT(linked) (**6**) (not shown in **Figure. 4.7A**), GCE- $\alpha$ -NiPc(OH)<sub>8</sub>-SWCNT (**12**) and GCE-SWCNT (**2**) showed lower currents than the bare GCE (**1**), the latter two showed highly distorted voltammograms, hence showing slow kinetics and some blocking of the [Fe(CN)<sub>6</sub>]<sup>3-</sup>/[Fe(CN)<sub>6</sub>]<sup>4-</sup> couple. The  $\Delta E$  value for the [Fe(CN)<sub>6</sub>]<sup>3-</sup>/[Fe(CN)<sub>6</sub>]<sup>4-</sup> couple are 0.09 V for bare GCE (**1**), 0.13 V for GCE- $\beta$ -NiPc(OH)<sub>4</sub>-SWCNT (**15**), 0.14 V for GCE- $\alpha$ -NiPc(OH)<sub>4</sub>-SWCNT (**9**) and GCE- $\beta$ -NiPc(NH<sub>2</sub>)<sub>4</sub>-SWCNT (**5**), 0.19 V for GCE- $\beta$ -NiPc(NH<sub>2</sub>)<sub>4</sub>-SWCNT (linked) (**6**), 0.27 V for GCE- $\alpha$ -NiPc(OH)<sub>8</sub>-SWCNT (**12**) and 0.50 V for GCE-SWCNT (**2**), **Table 4.2**. Thus the largest  $\Delta E$  value is for GCE-SWCNT (**2**). The  $\Delta E$  values suggest that adsorbing NiPc complexes on SWCNT improves the rate of electron transfer compared to SWCNT alone. GCE- $\beta$ -NiPc(NH<sub>2</sub>)<sub>4</sub>-SWCNT (**5**), GCE- $\beta$ -NiPc(OH)<sub>4</sub>-SWCNT (**15**) and GCE- $\alpha$ -NiPc(OH)<sub>4</sub>-SWCNT (**9**) have similar  $\Delta E$  values ( $\Delta E = 0.13$  or  $0.14$ ), suggesting similar rate of electron transfer which is faster compared to the rest of the electrodes.

The  $\Delta E$  values on  $\beta$ -NiPc(OH)<sub>4</sub>-SWCNT (**15**) and  $\alpha$ -NiPc(OH)<sub>4</sub>-SWCNT (**9**) are similar at 0.13 and 0.14, respectively, showing that the point of substitution has no effect on electrode kinetics. Comparing GCE- $\alpha$ -NiPc(OH)<sub>4</sub>-SWCNT (**9**) with GCE- $\alpha$ -NiPc(OH)<sub>8</sub>-SWCNT (**12**), with  $\Delta E = 0.14$  and  $0.27$ , respectively, shows that the latter has about double the  $\Delta E$  value of the former, suggesting that the number OH functional groups has an effect on the rate of electron transfer, when adsorbed on SWCNT. It is known that the rate of electron transfer depends on the orientation of aromatic complexes on SWCNT [274]. Thus the above results suggest that  $\beta$ -NiPc(OH)<sub>4</sub> and  $\alpha$ -NiPc(OH)<sub>4</sub> have similar orientation on SWCNT which is different from the orientation of  $\alpha$ -NiPc(OH)<sub>8</sub> containing a larger number of substituents. When GCE- $\beta$ -NiPc(OH)<sub>4</sub>-SWCNT (**15**) is compared to GCE- $\beta$ -NiPc(NH<sub>2</sub>)<sub>4</sub>-SWCNT (**5**), the  $\Delta E$  values obtained for both electrodes are very close to each other, 0.13 and 0.14 V respectively. This suggests that the rate of electron transfer, for NiPcs adsorbed on SWCNT, is not affected by the electron donating ability of the NH<sub>2</sub> group.  $\beta$ -NiPc(NH<sub>2</sub>)<sub>4</sub> was then covalently linked to SWCNT via amide bond and its electrochemical behavior compared to that of  $\beta$ -NiPc(NH<sub>2</sub>)<sub>4</sub> adsorbed on SWCNT. The  $\Delta E$  value of  $\beta$ -NiPc(NH<sub>2</sub>)<sub>4</sub>-SWCNT (linked) (**6**) is higher ( $\Delta E = 0.19$  V) compared to  $\beta$ -NiPc(NH<sub>2</sub>)<sub>4</sub>-SWCNT (**5**),  $\Delta E = 0.14$  V), suggesting that linking SWCNT to  $\beta$ -NiPc(NH<sub>2</sub>)<sub>4</sub> via covalent bond reduces the rate of electron transfer.

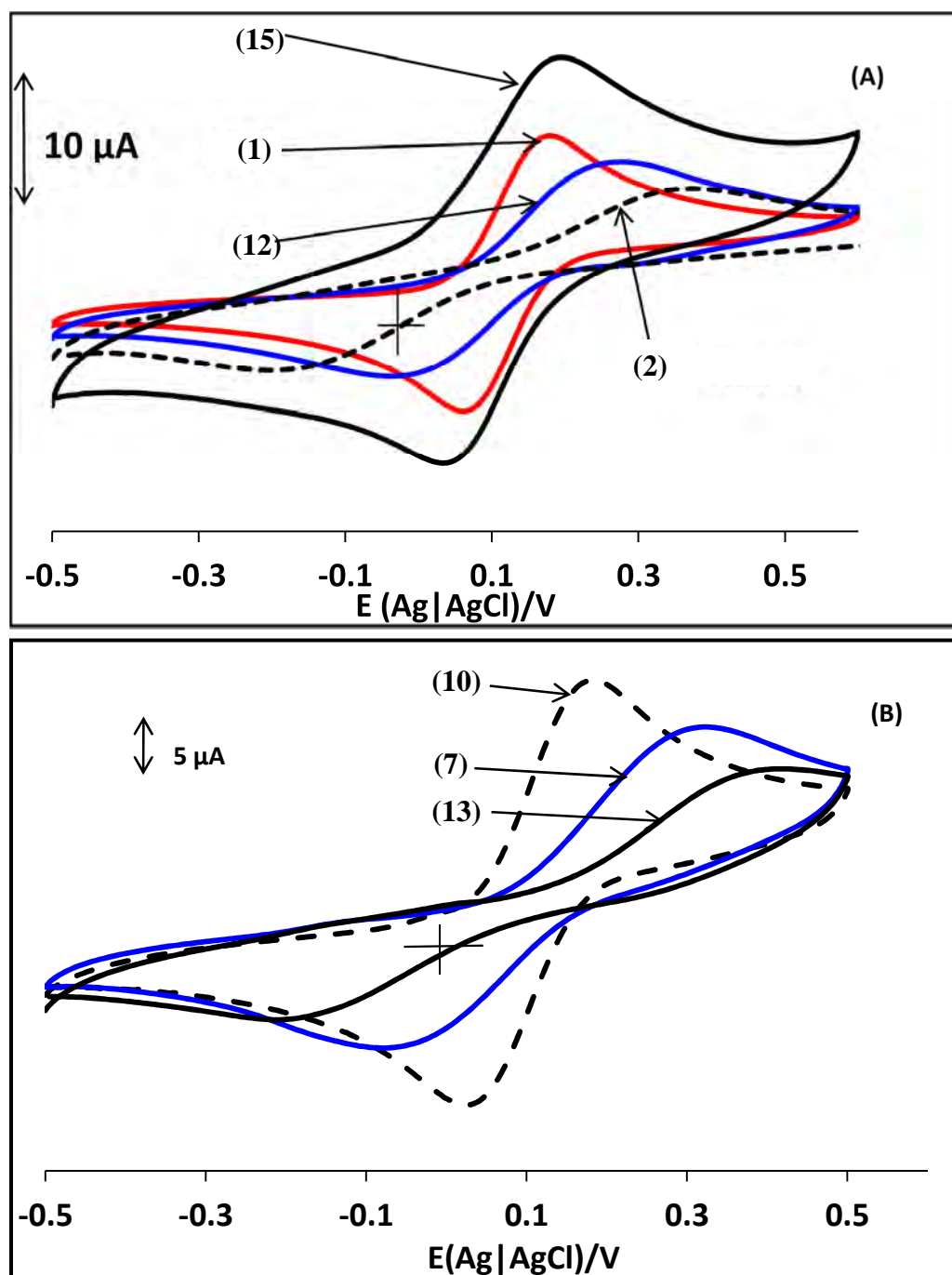


**Figure 4.7:** Cyclic voltammograms of 1mM  $[\text{Fe}(\text{CN})_6]^{3-}/[\text{Fe}(\text{CN})_6]^{4-}$  in 0.1 M KCl on (A) GCE- $\beta$ -NiPc(OH) $_4$ -SWCNT (15), bare GCE (1), GCE- $\alpha$ -NiPc(OH) $_8$ -SWCNT (12) and GCE-SWCNT (2); (B) GCE- $\alpha$ -NiPc(OH) $_8$  (10), GCE- $\alpha$ -NiPc(OH) $_4$  (7) and GCE- $\beta$ -NiPc(OH) $_4$  (13) Scan rate = 100  $\text{mVs}^{-1}$ . See Table 4.2 for numbering.

**Figure 4.7B** shows cyclic voltammograms (in the absence of SWCNT) for GCE- $\alpha$ -NiPc(OH) $_8$  (10), GCE- $\alpha$ -NiPc(OH) $_4$  (7) and GCE- $\beta$ -NiPc(OH) $_4$  (13), in 1 mM  $[\text{Fe}(\text{CN})_6]^{3-}/[\text{Fe}(\text{CN})_6]^{4-}$  in 0.1 M KCl, with  $\Delta E$  values of 0.18, 0.25 and 0.24 V, respectively (Table 4.2).

**Table 4.2: Electrochemical parameters for electrode characterization (using  $[\text{Fe}(\text{CN})_6]^{3-}$  /  $[\text{Fe}(\text{CN})_6]^{4-}$  in 0.1 M KCl. Potentials versus Ag|AgCl on GCE, Scan rate = 100 mVs<sup>-1</sup>)**

Electrodes	$\Delta E / \text{V}$
(1) bare GCE	0.09
(2) GCE-SWCNT	0.50
(3) GCE- $\beta$ -NiPc(NH <sub>2</sub> ) <sub>4</sub>	0.25
(4) GCE- <i>poly</i> - $\beta$ -Ni(O)Pc(NH <sub>2</sub> ) <sub>4</sub>	0.12
(5) GCE- $\beta$ -NiPc(NH <sub>2</sub> ) <sub>4</sub> -SWCNT	0.14
(6) GCE- $\beta$ -NiPc(NH <sub>2</sub> ) <sub>4</sub> -SWCNT (linked)	0.19
(7) GCE- $\alpha$ -NiPc(OH) <sub>4</sub>	0.25
(8) GCE- <i>poly</i> - $\alpha$ -Ni(O)Pc(OH) <sub>4</sub>	0.14
(9) GCE- $\alpha$ -NiPc(OH) <sub>4</sub> -SWCNT	0.14
(10) GCE- $\alpha$ -NiPc(OH) <sub>8</sub>	0.18
(11) GCE- <i>poly</i> - $\alpha$ -Ni(O)Pc(OH) <sub>8</sub>	0.15
(12) GCE- $\alpha$ -NiPc(OH) <sub>8</sub> -SWCNT	0.27
(13) GCE- $\beta$ -NiPc(OH) <sub>4</sub>	0.24
(14) GCE- <i>poly</i> - $\beta$ -Ni(O)Pc(OH) <sub>4</sub>	0.12
(15) GCE- $\beta$ -NiPc(OH) <sub>4</sub> -SWCNT	0.13
(16) GCE- $\alpha$ -NiPc(C <sub>10</sub> H <sub>21</sub> ) <sub>8</sub>	0.76
(17) GCE- <i>poly</i> - $\alpha$ -Ni(O)Pc(C <sub>10</sub> H <sub>21</sub> ) <sub>8</sub>	0.81
(18) GCE- $\alpha$ -NiPc(C <sub>10</sub> H <sub>21</sub> ) <sub>8</sub> -SWCNT	0.12
(19) GCE-NiPc	0.16
(20) GCE- <i>poly</i> -Ni(O)Pc	0.51
(21) GCE-NiPc -SWCNT	0.20

Again, the  $\Delta E$  values suggest that the number OH functional groups have an effect on the rate of electron transfer in the absence of SWCNT and again the point of substitution has no effect on the  $\Delta E$  values as was the case in the presence of SWCNT. As already stated, in the absence of SWCNT,  $\alpha$ -NiPc(OH)<sub>8</sub> (**10**) with  $\Delta E = 0.18$ , shows fast kinetics compared to  $\alpha$ -NiPc(OH)<sub>4</sub> (**7**) with  $\Delta E = 0.25$ . The opposite was true in the presence of SWCNT as discussed above.

### Long Chain vs unsubstituted NiPc

The  $\Delta E$  value for the  $[\text{Fe}(\text{CN})_6]^{3-}/[\text{Fe}(\text{CN})_6]^{4-}$  couple are 0.09 V (see **Table 4.2**) for the bare GCE ( $\Delta E = 0.09$  V for the ferrocene standard), 0.12 V for GCE- $\alpha$ -NiPc(C<sub>10</sub>H<sub>21</sub>)<sub>8</sub>-SWCNT (**18**) and 0.20 V for GCE-NiPc-SWCNT (**21**). The values suggest that the rate of electron transfer for GCE- $\alpha$ -NiPc(C<sub>10</sub>H<sub>21</sub>)<sub>8</sub>-SWCNT is slightly improved compared to GCE-NiPc-SWCNT. When  $\alpha$ -NiPc(C<sub>10</sub>H<sub>21</sub>)<sub>8</sub> and NiPc are not adsorbed on SWCNT,  $\Delta E$  value of 0.76 V for GCE- $\alpha$ -NiPc(C<sub>10</sub>H<sub>21</sub>)<sub>8</sub> (**16**), 0.16 V for GCE-NiPc (**19**) were obtained, **Table 4.2**. The  $\Delta E$  value for GCE- $\alpha$ -NiPc(C<sub>10</sub>H<sub>21</sub>)<sub>8</sub> ( $\Delta E = 0.76$  V) suggest that the  $[\text{Fe}(\text{CN})_6]^{3-}/[\text{Fe}(\text{CN})_6]^{4-}$  redox process is not reversible and shows slower rate of electron transfer compared to the fast rate of electron transfer for GCE-NiPc ( $\Delta E = 0.16$  V). The  $\Delta E$  values for GCE-NiPc (0.16 V) and GCE-NiPc-SWCNT (0.20 V) are very close to each other, showing that for NiPc, the effect of SWCNT is minimal unlike for  $\alpha$ -NiPc(C<sub>10</sub>H<sub>21</sub>)<sub>8</sub> where there is a huge improvement on electron transfer kinetics in the presence of SWCNT with  $\Delta E = 0.81$  V in the absence and 0.12 V in the presence of SWCNT. When  $\alpha$ -NiPc(C<sub>10</sub>H<sub>21</sub>)<sub>8</sub> or NiPc are transformed into *poly*- $\alpha$ -Ni(O)Pc(C<sub>10</sub>H<sub>21</sub>)<sub>8</sub> ( $\Delta E = 0.81$  V) or *poly*-Ni(O)Pc ( $\Delta E = 0.51$  V), the electron transfer becomes much worse for the latter, with only a small change for the former compared to the values in the absence of O-Ni-O at 0.16 V (NiPc) and 0.76 V for  $\alpha$ -NiPc(C<sub>10</sub>H<sub>21</sub>)<sub>8</sub>. The rate of electron transfer will depend on the orientation of the NiPc derivatives on SWCNT, as has been reported for the interaction of other aromatic complexes with SWCNT [274].

## 4.2. QDs and their conjugates with $\beta$ -NiPc(NH<sub>2</sub>)<sub>4</sub>

### 4.2.1. Pre-adsorbed CdTe-QDs on Au electrode

#### 4.2.1.1. CV

CdTe-QDs easily adsorb on Au electrode surface compared to OPGE and GCE, hence this electrode was used to study the redox properties of QDs. Modification of electrodes to form adsorbed CdTe-QDs or CdTe-QDs- $\beta$ -NiPc(NH<sub>2</sub>)<sub>4</sub> was performed by dipping a bare Au electrode into the CdTe-QDs colloidal solution for 1 h, followed by rinsing with pH 9.2 buffer solution, and allowing the electrode to dry under nitrogen atmosphere. The modified electrode was then rinsed with buffer solution to remove excess CdTe-QDs or CdTe-QDs- $\beta$ -NiPc(NH<sub>2</sub>)<sub>4</sub> on the electrode, as explained in the experimental section. These electrodes are referred to as pre-adsorbed.

In order to understand the effect of the  $\beta$ -NiPc(NH<sub>2</sub>)<sub>4</sub> on the electrochemical properties of CdTe-QDs, anodic and cathodic scans from the open circuit potential were recorded on gold electrode for pre-adsorbed CdTe-QDs (**Figure 4.8A**) and CdTe-QDs- $\beta$ -NiPc(NH<sub>2</sub>)<sub>4</sub> (**Figure 4.8B**). **Figure 4.8A (c)** and **Figure 4.8B (c)** shows a cyclic voltammogram of the bare Au electrode in buffer solution (pH = 9.2), scanned from the open circuit potential ( $E_{oc}$ ) in the positive direction. All the cyclic voltammogram experiments are first scan experiments. The gold oxidation and stripping peaks are observed at 0.56 V and 0.1 V vs Ag|AgCl on bare gold electrode at pH 9.2, **Figure 4.8A (c)** and **Figure 4.8B (c)**, as reported before at the same pH [225]. **Figure 4.8A(a)** and **(b)** shows a cyclic voltammogram scanned from the open circuit potential ( $E_{oc}$ ) in the positive direction (blue scan) from -0.19 to + 1.05, and from + 1.05 to - 1.2 V back to -0.19 V and in the negative direction (black scan) from - 0.19 to -1.20 V, and from -1.20 to + 1.05 V back to -0.19 V. Fresh CdTe-QDs were pre-adsorbed for both positive and negative scans. The cyclic voltammogram of CdTe-QDs capped with TGA has been reported in literature and three anodic peaks have been observed for CdTe-QDs [225, 266, 275, 276]. The two anodic peaks observed between 0 and 1.0 V are known to be due to oxidation of QDs (in pH 9.2 buffer solution). When the potential is swept in positive direction (**Figure 4.8A(a)**), the anodic scan shows one distinct peak at 0.51 V ( $A_1$ ) and one weak peak -0.50 V ( $A_3$ ). The peak at 0.51 V ( $A_1$ ) will have a contribution of both the Au and CdTe-QDs oxidation peaks hence the enhancement in currents compared to bare Au

electrode. The reverse scan shows two peaks at 0.04 V ( $C_1$ ) and -0.86 V ( $C_3$ ). Peak ( $C_1$ ) is shifted to more negative potentials compared the peak observed for gold electrode in blank buffer solution. Peak  $C_3$  is associated with the electrochemical reduction of CdTe-QDs oxidation products which are metallic in nature.

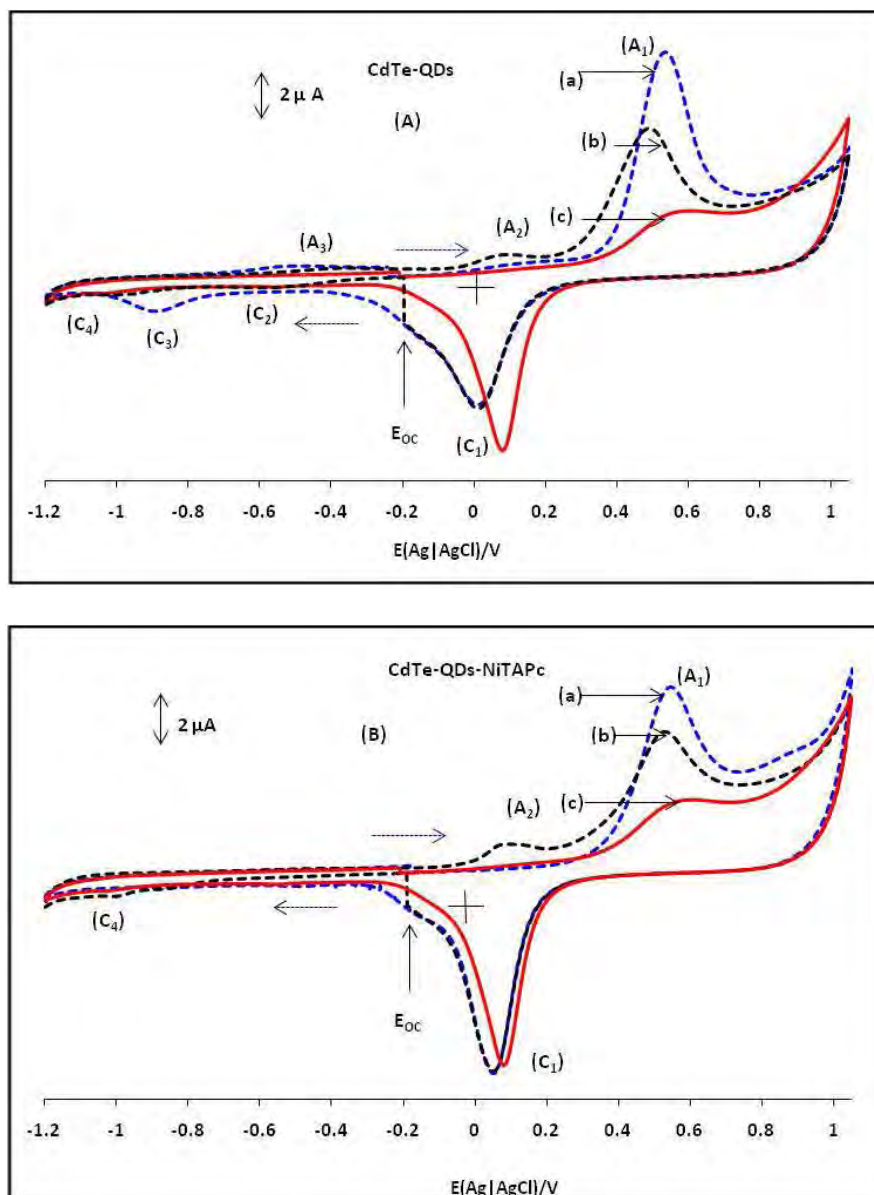
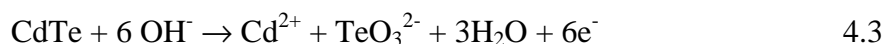


**Figure 4.8:** (A) ((a) and (b)) cyclic voltammograms of Au electrode with pre-adsorbed CdTe-QDs and (c) bare Au electrode in blank buffer pH 9.2; (B) ((a) and (b)) cyclic voltammograms of Au electrode with pre-adsorbed CdTe-QDs- $\beta$ -NiPc( $\text{NH}_2$ )<sub>4</sub> and (c) bare Au electrode in blank buffer pH 9.2. The potential sweep rate was  $50 \text{ mVs}^{-1}$ .  $E_{oc}$ : open circuit potential.



The metallic oxidation products which are obtained on oxidation of CdTe-QDs are shown by **Equation 4.3** [225]



As **Equation 4.3** shows the oxidation of QDs generates  $\text{Te}^{4+}$  and  $\text{Cd}^{2+}$ . Two DPV peaks have been reported for the reduction of  $\text{Te}^{4+}$  in pH 9.4 buffer [277]. The first is attributed to the reduction  $\text{Te}^{4+}$  to  $\text{Te}^0$ , the second to  $\text{Te}^0$  to  $\text{Te}^{2-}$ . The two peaks have been reported to be located at  $\sim -0.6$  and  $-0.9$  V in basic media [277] vs Ag|AgCl. There is only a weak peak near  $-0.6$  V in **Figure 4.8A(a)** ( $\text{C}_2$ ), but a stronger peak at  $\sim -0.86$  V ( $\text{C}_3$ ). Thus both  $\text{C}_2$  and  $\text{C}_3$  are associated with reduction of metallic oxidation products of QDs.

The electrochemistry of CdTe-QDs is highly influenced by the nature of the stabilisers, pH of solution and QD size [225, 236]. The relative intensities of the peaks are highly influenced by pH, with only two peaks  $\text{A}_1$  and  $\text{A}_2$  normally dominating the voltammograms in basic media [236]. In this work the dominating peak is  $\text{A}_1$  which is associated with the oxidation of intact QDs [225]. Peak  $\text{A}_2$  has been associated with the oxidation of surface defects of intact QDs [225], hence changes in its position and height may be an indicator of changes on the surface of the QDs.  $\text{A}_2$  is not pronounced when scanning in the positive direction from open circuit, **Figure 4.8A (a)**.

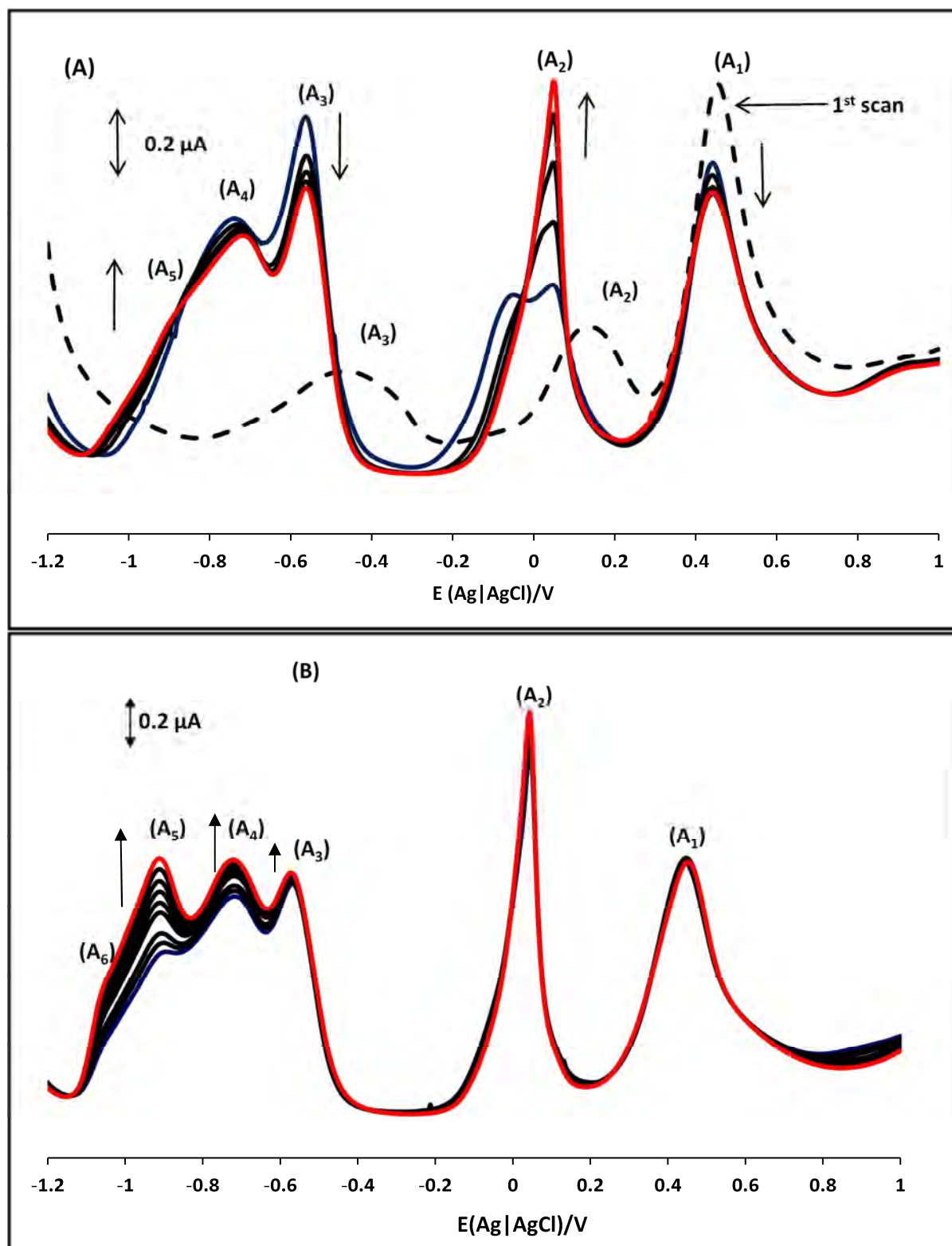
When the potential is swept in the negative direction from the  $E_{oc}$  (**Figure 4.8A (b)**), the cathodic scan does not show the  $\text{C}_3$  peak, associated with reduction of the oxidation products of CdTe-QDs which are  $\text{Te}^{4+}$  and  $\text{Cd}^{2+}$  according to **Equation 4.3**. As stated above,  $\text{C}_3$  was observed in the positive direction following oxidation of QDs, confirming that this peak is due to the reduction of oxidation products of QDs. The absence of  $\text{C}_3$  in the negative direction confirms the absence of oxidation products. On negative scan, weak peaks labelled  $\text{C}_2$  and  $\text{C}_4$  are observed which could be related to the reduction of free metallic ions which are not associated with the oxidation of QDs. Also on negative scan from open circuit potential, peak  $\text{A}_2$  is clearly observed. The increase in current, on negative scan, for peak  $\text{A}_2$  and a significant decrease in current for peak  $\text{A}_1$  with a shift towards lower potential as observed in **Figure 4.8A (b)**, is a typical behavior observed for CdTe-QDs in buffer pH 9.2 solution [225].

#### 4.2.1.2. DPV

The more sensitive DPV was further employed to characterize adsorbed QDs in solution and adsorbed on Au electrode. As stated above three voltammogram oxidation peaks are observed for CdTe-QDs, labelled  $A_1$ ,  $A_2$ ,  $A_3$  in **Figure 4.9A**. The relative intensities of the peaks are highly influenced by pH, with only two peaks  $A_1$  and  $A_2$  dominating the voltammograms in basic media as stated above [236, 239].

$A_1$  in **Figures 4.9A** and **B** may be associated to the oxidation of the CdTe core as has been suggested in the literature [239] and stated above. This leaves  $A_2$  to be discussed which as stated above is associated with the oxidation of surface QDs defects. In this work  $A_2$  increases in intensity with cycling and it becomes sharper probably due to conditioning of adsorbed species. Sharp peaks are associated with adsorption [278]. In general as  $A_2$  increases,  $A_1$  decreases in **Figure 4.9A**, suggesting the interrelation of the two. Since we associate  $A_1$  with CdTe core, it is logical to also associate  $A_2$  with CdTe. Thus we associate  $A_2$  with the oxidation of core CdTe-QDs surface defects, and the adsorption of the oxidation products. It is possible that as oxidation continues,  $A_1$  decreases as free QDs depletes and  $A_2$  increases as more surface defects are created due to QDs oxidation. **Figure 4.9B** is a continuation of **Figure 4.9A**. As discussed above we can assign  $A_3$  and  $A_4$  in **Figure 4.9A** (after the first scan) to the two telluride reduction processes. The final product of the reduction of  $\text{Te}^{4+}$  is thus anionic  $\text{Te}^{2-}$ .

During the second scan the shoulder which appears next to  $A_2$  in **Figure 4.9A** is probably due to the oxidation of free TGA molecules on the adsorbed QDs which form a film, this oxidation was reported [239] to occur at a lower potential than for free TGA on Au, **Figure 4.9D (ii)**. TGA oxidation products (most likely disulfides) can diffuse into the bulk solution. Thus, on cycling, the shoulder due to TGA oxidation disappears.



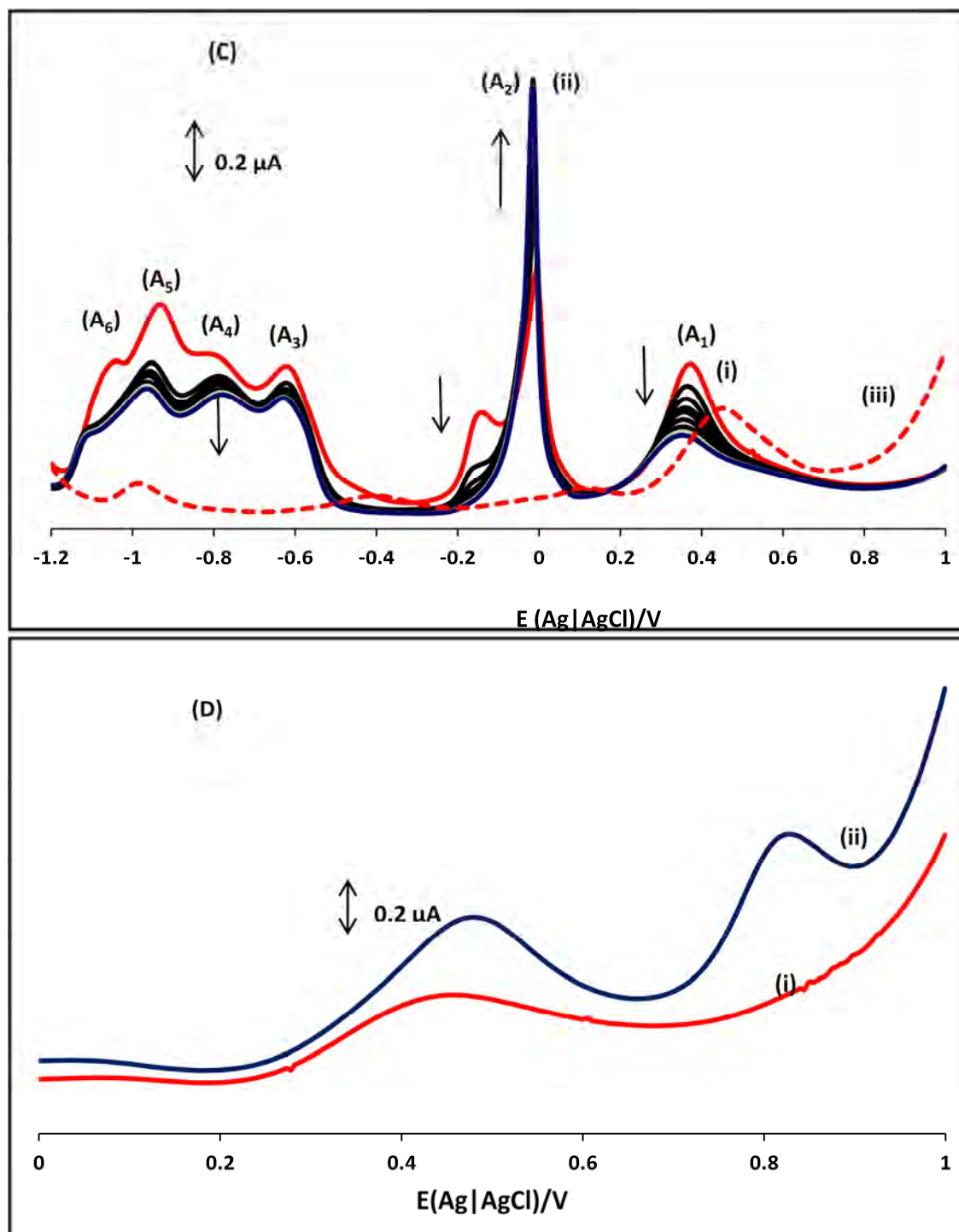


**Figure 4.9:** DPV scans of (A) CdTe-QDs 1<sup>st</sup> scan to 6<sup>th</sup> scan, (B) 6<sup>th</sup> scan to 14<sup>th</sup> scan. (C) the last scan in (B) following rinsing in pH 9.2 buffer and recording of 8 DPV scans in pH 9.2 buffer (i) 1<sup>st</sup> scan, (ii) 8<sup>th</sup> scan and (iii) bare Au electrode. (D) DPV scans of bare gold electrode in a blank solution (i) and solution containing TGA capping agent (ii). Electrolyte: pH 9.2 buffer solution containing Na<sub>2</sub>SO<sub>4</sub>.

Peaks in the potential range of A<sub>5</sub> and A<sub>6</sub>, **Figure 4.9B** have been reported before [279] for the reduction of Te<sup>4+</sup> on glassy carbon electrode and their presence was dependent on the media and the formation on new tellerium complexes which are further reduced at negative potentials. Thus A<sub>5</sub> and A<sub>6</sub> are associated with the reduction of Te products. It is also known [277] that at potentials more negative than -0.9 V, Te<sup>2-</sup> may interact with Cd<sup>2+</sup> near the electrode surface to form CdTe. Reduction of Cd<sup>2+</sup> in solution occurs at ~ -0.9 V [279] at pH 9.2 and on GCE. Cd<sup>2+</sup> peak was observed at -0.86 V on Au electrode at pH 9.2 (figure not shown). Thus the reduction of Cd<sup>2+</sup> will overlap with that of Te<sup>0</sup> to Te<sup>2-</sup> since they occur at about the same potential.

Following the last scan in **Figure 4.9B**, the electrode was rinsed in pH 9.2 solution and DPV scans (8) were recorded in the blank (pH 9.2 buffer), **Figure 4.9C**. There is appearance of the shoulder to A<sub>2</sub> due to free TGA, which soon disappears on cycling. It is important to note that A<sub>1</sub> decreases significantly with cycling as A<sub>2</sub> increases. Since the DPV scan were recorded in the absence of QDs in the solution, the observed voltammograms are associated with the oxidation of electrodeposited CdTe-QDs. Peak A<sub>1</sub> decays to currents below those of bare Au ( **Figure 4.9C (iii)**) suggesting the blocking of the Au oxidation peak by adsorbed QDs on Au, which is a known phenomena [239]. A closer look at **Figure 4.9C** shows that A<sub>1</sub> occurs at lower potentials (0.35 V) compared to **Figure 4.9B** at 0.44 V. This is due to the fact that QDs are electrodeposited in the former (hence oxidation occurs at a lower potential) than when QDs are adsorbed before oxidation (**Figure 4.9B**). A<sub>1</sub> shifts from 0.35 to 0.32 V (in **Figure 4.9C**) occurs with cycling suggesting change of surface. Similarly A<sub>2</sub> appears at -0.014 V in **Figure 4.9C** compared to 0.04 V in **Figure 4.9B**. The modified electrode shown in **Figure 4.9C** after the final scan (containing electrodeposited QDs) will be used for the electrocatalytic oxidation of dichlorophenol (DCP) and pentachlorophenol (PCP) and is represented as electrodepos-CdTe-QDs as opposed to electrodes which contain adsorbed CdTe-QDs (represented ads-CdTe-QDs), without cycling.

## 4.2.2. Pre-adsorbed CdTe-QDs- $\beta$ -NiPc(NH<sub>2</sub>)<sub>4</sub> conjugate

### 4.2.2.1. CV

**Figure 4.8B ((a) and (b))** shows a cyclic voltammograms of CdTe-QDs- $\beta$ -NiPc(NH<sub>2</sub>)<sub>4</sub> (linked). The cyclic voltammograms in **Figure 4.8B** are all first scans. **Figure 4.8B (a)** shows similar CVs as discussed for CdTe-QDs, **Figure 4.8A (a)**. No peaks due to  $\beta$ -NiPc(NH<sub>2</sub>)<sub>4</sub> are observed in **Figure 4.8B ((a) and (b))**. NiPc complexes show a very distinct peaks near +0.2 V vs Ag|AgCl due to the formation of O-Ni-O bridges in basic media [125, 265], See also **Figure 4.4**. However these peaks are only formed on continuous cycling for  $\beta$ -NiPc(NH<sub>2</sub>)<sub>4</sub> [250], hence do not contribute to the changes in voltammograms in **Figure 4.8B ((a) and (b))**. The first scan for  $\beta$ -NiPc(NH<sub>2</sub>)<sub>4</sub> shows featureless voltammogram scans [250]. **Figure 4.8B (a)** shows the absence of C<sub>3</sub> on return for CdTe-QDs- $\beta$ -NiPc(NH<sub>2</sub>)<sub>4</sub>, suggesting that  $\beta$ -NiPc(NH<sub>2</sub>)<sub>4</sub> stabilizes the QDs against oxidation, since C<sub>3</sub> is associated with the reduction of metallic oxidation products of QDs. The negative scan is similar to that of QDs alone, except C<sub>2</sub> is no longer evident.

In **Figure 4.10A** the positive scans for CdTe-QDs and CdTe-QDs- $\beta$ -NiPc(NH<sub>2</sub>)<sub>4</sub> are overlaid. C<sub>1</sub> occurs at a less negative potential for CdTe-QDs- $\beta$ -NiPc(NH<sub>2</sub>)<sub>4</sub> compared to CdTe QDs, resulting in a reduced peak separation (A<sub>1</sub> and C<sub>1</sub>) for the former, suggesting improved kinetics in the presence of  $\beta$ -NiPc(NH<sub>2</sub>)<sub>4</sub>. While there is very little change in potential for A<sub>1</sub>, the absence of C<sub>3</sub> for CdTe-QDs- $\beta$ -NiPc(NH<sub>2</sub>)<sub>4</sub> is very clear in **Figure 4.10A**, confirming the stabilization of QDs by  $\beta$ -NiPc(NH<sub>2</sub>)<sub>4</sub> against oxidation to metallic products, similar behaviour as for overlaid nenegative scans in **Figure 4.10B**.

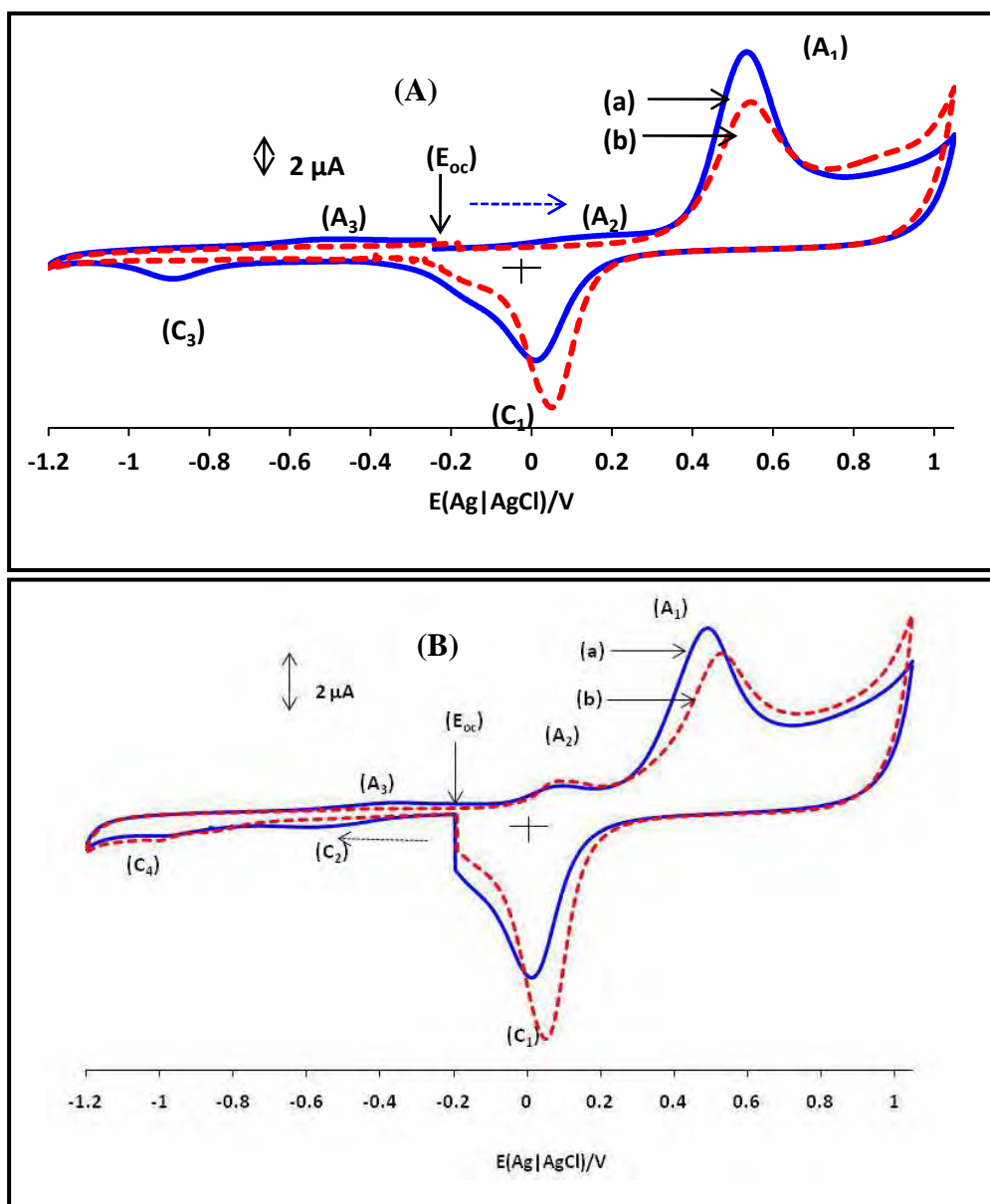


**Figure 4.10:** (A) Cyclic Voltammograms of Au electrode with pre-adsorbed (a) CdTe-QDs and (b) CdTe-QDs- $\beta$ -NiPc(NH<sub>2</sub>)<sub>4</sub> in blank buffer pH 9.2. The positive potential sweep direction was from -0.19 V to 1.05 V, then from 1.05 V to -1.20 V and back to -0.19 V. (B) Cyclic Voltammograms of Au electrode with pre-adsorbed (a) CdTe-QDs and (b) CdTe-QDs- $\beta$ -NiPc(NH<sub>2</sub>)<sub>4</sub> in blank buffer pH 9.2. The potential sweep rate was  $50 \text{ mVs}^{-1}$ .

#### 4.2.2.2. DPV studies

**Figure 4.11** shows DPV scans of CdTe-QDs- $\beta$ -NiPc(NH<sub>2</sub>)<sub>4</sub> in pH 9.2 buffer. Only A<sub>1</sub> and A<sub>2</sub> are present with significant intensities, **Figure 4.11A**. Both of these are associated with intact CdTe-QDs, the former the oxidation of QDs core, the latter the oxidation of surface defects. There is no sign of the peaks due to the reduction of Te<sup>4+</sup> and Cd<sup>2+</sup> observed between -0.6 V and -1.0 V in **Figure 4.9A**. This shows that  $\beta$ -NiPc(NH<sub>2</sub>)<sub>4</sub> stabilizes the QDs against disintegration into metallic products on oxidation. Only a weak peak appears with cycling near -0.6 V, **Figure 4.11A**.

On continuous cycling in CdTe-QDs- $\beta$ -NiPc(NH<sub>2</sub>)<sub>4</sub>, an increase in anodic peak A<sub>2</sub> and a simultaneous decrease in anodic peak A<sub>1</sub> are observed, similar to CdTe-QDs. As also discussed above, there is an interrelation between the two peaks. Thus, again A<sub>2</sub> is associated with the oxidation of QDs surface defects on CdTe-QDs- $\beta$ -NiPc(NH<sub>2</sub>)<sub>4</sub>, and A<sub>1</sub> to the CdTe core.  $\beta$ -NiPc(NH<sub>2</sub>)<sub>4</sub> shows Ni<sup>III</sup>/Ni<sup>II</sup> redox process when cycled in basic media. This process is usually observed between 0 V and 0.5 V, hence will overlap with the redox processes of the CdTe-QDs in this potential range. Comparing of DPVs of CdTe-QDs with CdTe-QDs- $\beta$ -NiPc(NH<sub>2</sub>)<sub>4</sub>, **Figure 4.12** clearly shows the lack of metallic oxidation products in the latter.



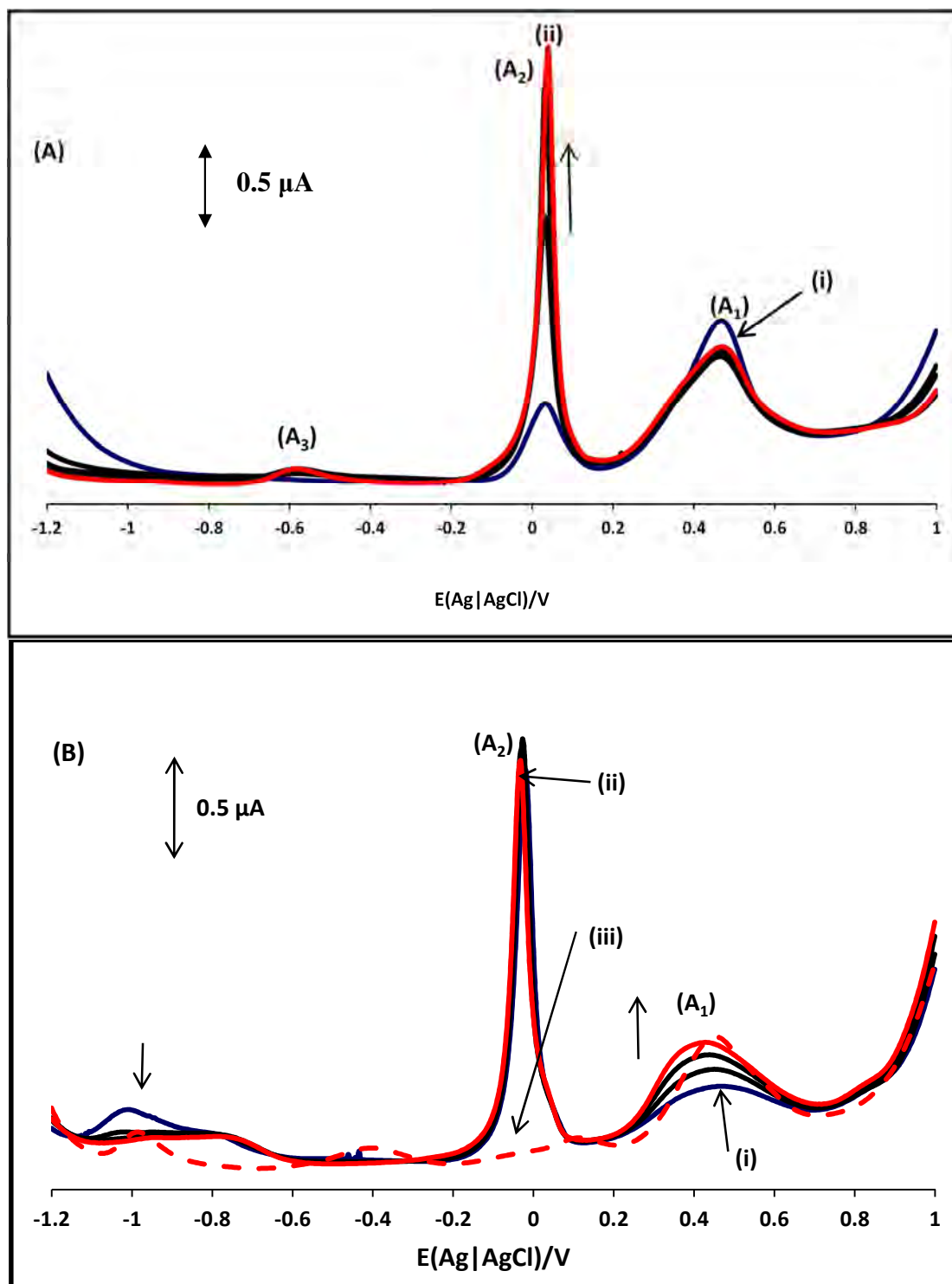
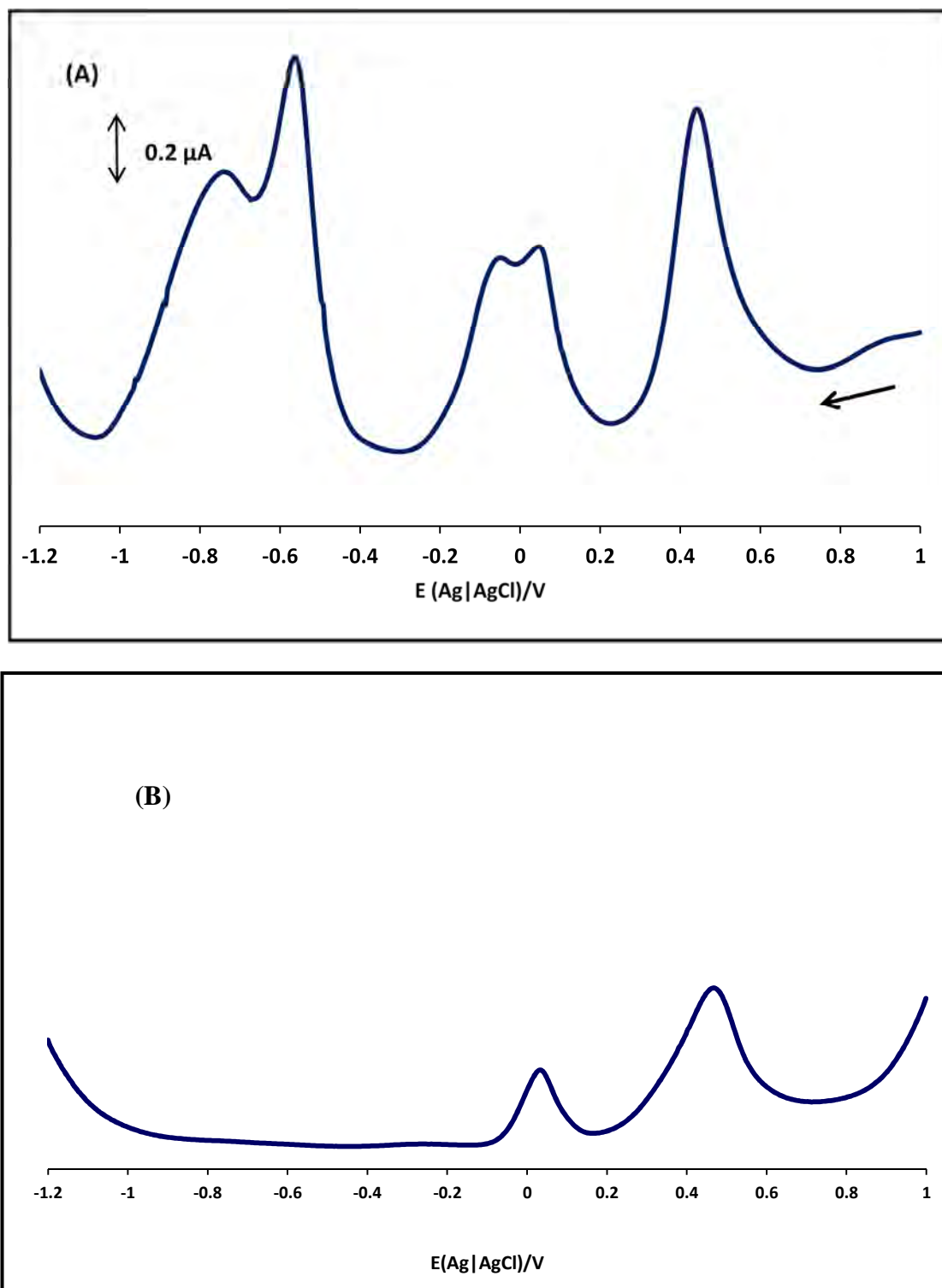


Figure 4.11: (A) DPV scans of CdTe-QDs- $\beta$ -NiPc(NH<sub>2</sub>)<sub>4</sub> in pH 9.2 buffer solution with 0.1 M Na<sub>2</sub>SO<sub>4</sub> as an electrolyte, (i) 1<sup>st</sup> scan and (ii) 4<sup>th</sup> scan. (B) CdTe-QDs- $\beta$ -NiPc(NH<sub>2</sub>)<sub>4</sub> adsorbed on the Au electrode and cycled in pH 9.2 buffer, (i) 1<sup>st</sup> scan, (ii) last scan and (iii) bare Au in pH 9.2 buffer.



**Figure 4.12:** DPV scans of (A) CdTe-QDs and (B) CdTe-QDs- $\beta$ -NiPc(NH<sub>2</sub>)<sub>4</sub> in pH 9.2 buffer solution containing Na<sub>2</sub>SO<sub>4</sub>.

Following the last scan in **Figure 4.11A**, the electrode was rinsed in buffer solution of pH 9.2 and DPV scans (4) were recorded in the blank (pH 9.2 buffer), **Figure 4.11B**. Unlike in the case of CdTe-QDs,  $A_1$  increases and  $A_2$  decreases slightly with scanning, showing

stabilization of CdTe-QDs. There is also a slight increase in current on the metallic reduction parts but not nearly as intense as for CdTe-QDs alone. It is clear from **Figure 4.11B** that the CdTe-QDs- $\beta$ -NiPc(NH<sub>2</sub>)<sub>4</sub> oxidation products are electrodeposited onto the electrode, hence the oxidation peaks are present. Again, the modified electrode shown in **Figure 4.11B** after the final scan (modified by electrodeposition) will be used for the electrocatalytic oxidation of DCP and PCP and is represented as electrodep-CdTe-QDs- $\beta$ -NiPc(NH<sub>2</sub>)<sub>4</sub> as opposed to electrodes which contain adsorbed without DPV scans CdTe-QDs- $\beta$ -NiPc(NH<sub>2</sub>)<sub>4</sub> (represented as ads-CdTe-QDs- $\beta$ -NiPc(NH<sub>2</sub>)<sub>4</sub>).

### 4.2.3. Electrochemical impedance spectroscopy

In this work electrochemical impedance spectroscopy (EIS) was used to monitor the effects of adsorbed CdTe-QDs and CdTe-QDs- $\beta$ -NiPc(NH<sub>2</sub>)<sub>4</sub> on the rate of electron transfer process. EIS experiments were carried out under potentiostatic polarization. The quality of the impedance data were validated by applying the Voigt model to the data, which is equivalent to the Kramers-Kronig transforms [280]. The suitable equivalent circuit for the observed electrode behaviour under study is shown in **Figure 4.13c**, where  $R_s$  is the resistance of the electrolyte solution between the reference and the working electrodes,  $R_{CT}$  is the charge transfer resistance,  $Z_w$  is the mass-transfer or Warburg impedance and CPE is the constant phase element [109]. The values of these quantities are shown in **Table 4.3**. **Figure 4.13a** shows the Nyquist plots of bare (A), adsorbed CdTe-QDs (B), and adsorbed CdTe-QDs- $\beta$ -NiPc(NH<sub>2</sub>)<sub>4</sub> conjugate (C) obtained in 1 mM [Fe(CN)<sub>6</sub>]<sup>3-</sup>/[Fe(CN)<sub>6</sub>]<sup>4-</sup> in 0.1M KCl. [Fe(CN)<sub>6</sub>]<sup>3-</sup>/[Fe(CN)<sub>6</sub>]<sup>4-</sup> redox system was chosen because of its fast reaction kinetics. The experiments were done at an applied potential of 0.12 V versus Ag|AgCl. The diameter of the semicircle **Figure 4.13a** give charge transfer resistance ( $R_{ct}$ ). Adsorbed CdTe-QDs has the larger semicircle, **Table 4.3** and **Figure 4.13a**, hence a large  $R_{ct}$  than CdTe-QDs- $\beta$ -NiPc(NH<sub>2</sub>)<sub>4</sub> and therefore the former shows the slowest rate of charge transfer. The apparent electron-transfer rate constant  $k_{app}$  was obtained from  $R_{ct}$  using the conventional **Equation 4.4**, [281]:

$$k_{app} = \frac{RT}{n^2 F^2 R_{ct} C} \quad 4.4$$

where C is a concentration of the [Fe(CN)<sub>6</sub>]<sup>3-/4-</sup>, n is the number of electrons, R, T and F have their usual meanings. The order in terms of  $k_{app}$  is as follows (**Table 4.3**): bare Au electrode

$(2.1 \times 10^{-3} \text{ cm/s}) > \text{adsorbed CdTe-QDs-}\beta\text{-NiPc(NH}_2\text{)}_4 (7.1 \times 10^{-5} \text{ cm/s}) > \text{adsorbed CdTe-QDs} (3.5 \times 10^{-6} \text{ cm/s})$ . Thus adsorbed CdTe-QDs- $\beta$ -NiPc(NH<sub>2</sub>)<sub>4</sub> gave a higher  $k_{app}$  than CdTe-QDs due to the smaller  $R_{CT}$ .

**Figure 4.13b** (Bode plot of phase angle versus  $\log f$ ) shows that the bare Au electrode, has a maximum phase angle at a higher frequency compared to CdTe-QDs. The shift for CdTe-QDs- $\beta$ -NiPc(NH<sub>2</sub>)<sub>4</sub> is minimal. However the shifts confirm that [Fe(CN)<sub>6</sub>]<sup>3-</sup>/[Fe(CN)<sub>6</sub>]<sup>4-</sup> redox process takes place on the modified electrode surfaces rather than directly on the bare gold. The phase angle remains less than 90° for all the electrodes [282]. A phase angle greater or equal to 90° means that the modified surface behaves like an ideal capacitor. Whereas, a phase angle less than 90°, the modified surface is viewed as a contaminated capacitor meaning the modified surface is permeable to solution ions [282].

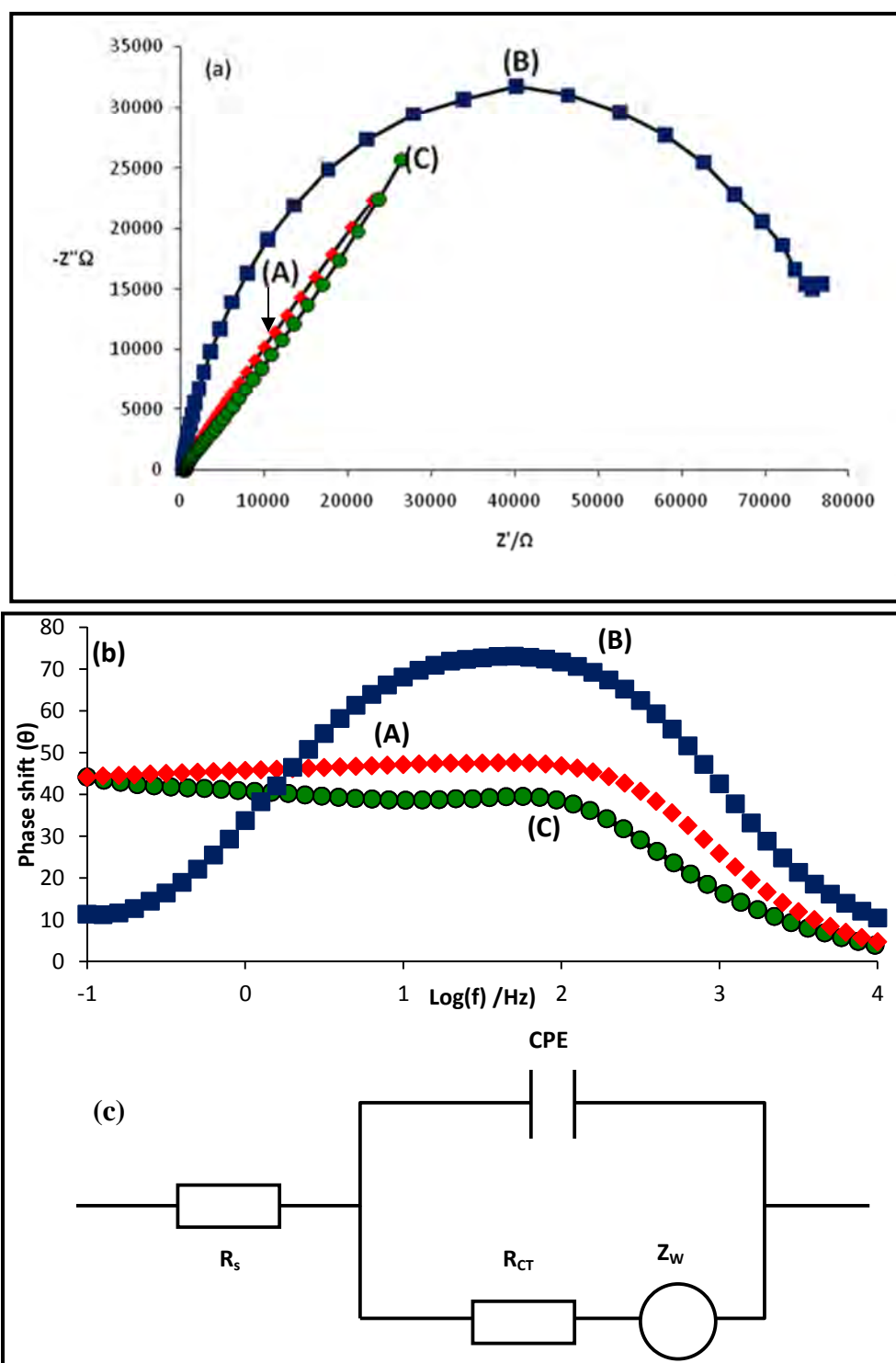


**Figure 4.13:** (a) Nyquist plots, (b) Bode plots of (A) bare Au, (B) Au/CdTe-QDs (adsorbed) and (c) Au/CdTe-QDs- $\beta$ NiPc(NH<sub>2</sub>)<sub>4</sub> (adsorbed) (c) Equivalent circuit used in this work and. Electrolyte = 0.1M [Fe(CN)<sub>6</sub>]<sup>4-</sup>/[Fe(CN)<sub>6</sub>]<sup>3-</sup> in 1M KCl solution with equilibrium potential of 0.045 V. Applied potential = 0.12 V versus Ag|AgCl. (C) (Randle cell: Equivalent circuit with mixed kinetic and charge transfer).

**Table 4.3: Impedance data of adsorbed CdTe-QDs and CdTe-QDs- $\beta$ -NiPc(NH<sub>2</sub>)<sub>4</sub> in pH 9.2 buffer. Fe(CN)<sub>6</sub><sup>4-</sup>/[Fe(CN)<sub>6</sub>]<sup>3-</sup> in 1M KCl solution with equilibrium potential of 0.045 V.**

Electrode	$k_{app}/\text{cm s}^{-1}$	$\theta$	$R_{ct} (\text{K}\Omega)\text{cm}^{-2}$
Au-CdTeQDs	$3.5 \times 10^{-6}$	73	75.3
Au- $\beta$ -NiPc(NH <sub>2</sub> ) <sub>4</sub> -CdTeQDs	$7.1 \times 10^{-5}$	39	3.74
Au-bare	$2.1 \times 10^{-3}$	44	0.13

# Chapter 5

## Electrocatalysis

## 5.1. 4-Chlorophenol (4-CP)

### 5.1.1. NiPc derivatives in the absence of nanomaterials

OPGE was employed for all NiPc(OH)<sub>n</sub> complexes and GCE used for the rest of the complexes, see section 4.1 for reasons.

#### 5.1.1.1. $\beta$ -NiPc(OH)<sub>4</sub>

**Figure 5.1** shows the CVs of 1mM 4-CP (a) in 0.1 M NaOH at (i) unmodified OPGE electrode; (ii) OPGE- $\beta$ -NiPc(OH)<sub>4</sub> before cycling in NaOH but Ni<sup>III</sup>/Ni<sup>II</sup> peaks already present, and (iii) OPGE-*poly*- $\beta$ -Ni(O)Pc(OH)<sub>4</sub>. Electrocatalysis is characterized by a shift of potential to lower values and/or increase in current with respect to an unmodified electrode. **Figure 5.1** show that OPGE- $\beta$ -NiPc(OH)<sub>4</sub> shifts the 4-chlorophenol peak to much lower potential when compared to bare OPGE or OPGE-*poly*- $\beta$ -Ni(O)Pc(OH)<sub>4</sub>. The peak observed on the bare OPGE is less defined than the peaks on OPGE- $\beta$ -NiPc(OH)<sub>4</sub> or OPGE-*poly*- $\beta$ -Ni(O)Pc(OH)<sub>4</sub>, **Figure 5.1**. The peak potentials observed in **Figure 5.1** for 4-chlorophenol at 0.26 V on OPGE- $\beta$ -NiPc(OH)<sub>4</sub> and 0.41 on GCE- $\beta$ -NiPc(OH)<sub>4</sub> are lower than reported for this analyte on GCE in literature [125, 241] at 0.62 V, using the same reference electrode (Ag|AgCl), showing that this NiPc complex has potential in terms of analysis of phenols. The onset of the 4-chlorophenol peak occurs at a lower potential compared to the Ni<sup>III</sup>/Ni<sup>II</sup> peak, **Figure 5.2**, showing catalytic response of OPGE-*poly*- $\beta$ -Ni(O)Pc(OH)<sub>4</sub>. The ratio of anodic to cathodic peak currents was ~ 28 for oxidation of 4-CP on OPGE-*poly*- $\beta$ -Ni(O)Pc(OH)<sub>4</sub> and 2 for the latter alone, hence showing the catalytic nature of the complex. The fact that there is a return peak (cathodic) for detection of 4-chlorophenol on OPGE-*poly*- $\beta$ -Ni(O)Pc(OH)<sub>4</sub> shows that 4-chlorophenol is incapable of reducing the entire Ni<sup>III</sup> species [283].



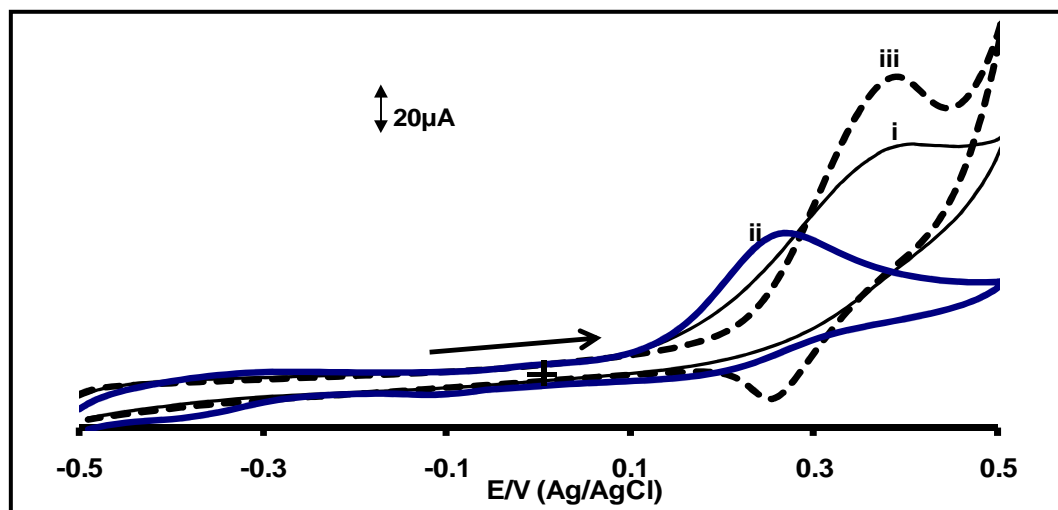


Figure 5.1: Cyclic voltammograms of 0.7 mM 4-chlorophenol in 0.1 M NaOH on (i) bare OPGE, (ii) OPGE- $\beta$ -NiPc(OH)<sub>4</sub> before cycling but Ni<sup>III/II</sup> peaks already present and (iii) OPGE-*poly*- $\beta$ -Ni(O)Pc(OH)<sub>4</sub>.

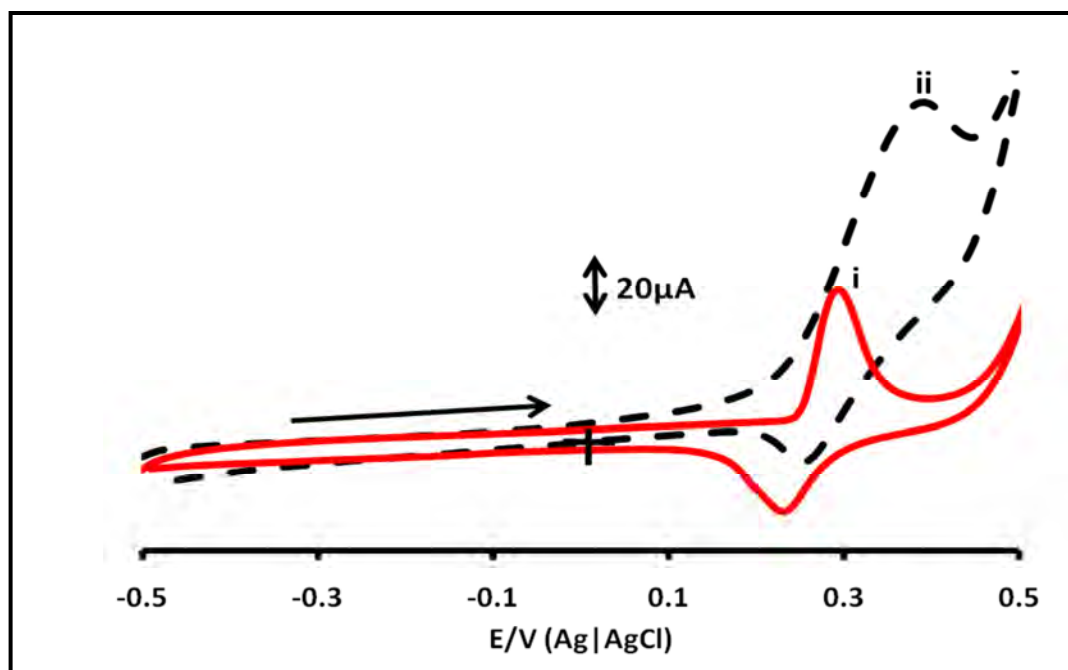


Figure 5.2: Comparison of cyclic voltammogram of OPGE-*poly*- $\beta$ -Ni(O)Pc(OH)<sub>4</sub> in the absence (i) and presence (ii) of 4-chlorophenol in 0.1 M NaOH.

Background corrected currents (66  $\mu$ A) for 4-chlorophenol oxidation on the OPGE-*poly*- $\beta$ -Ni(O)Pc(OH)<sub>4</sub> were higher than those of adsorbed  $\beta$ -NiPc(OH)<sub>4</sub> (13  $\mu$ A), showing better catalytic behaviour of the former in terms of current. Thus in terms of potential, adsorbed OPGE-NiPc(OH)<sub>4</sub> is superior to OPGE-*poly*- $\beta$ -Ni(O)Pc(OH)<sub>4</sub>, but in terms of current enhancement, the latter is better.

### 5.1.1.2. $\alpha$ -NiPc(OH)<sub>4</sub>

**Figure 5.3A** shows the cyclic voltammograms of 4-chlorophenol on bare (i), OPGE- $\alpha$ -NiPc(OH)<sub>4</sub> (ii) and OPGE-*poly*- $\alpha$ -Ni(O)Pc(OH)<sub>4</sub> (iii). There is no peak observed for the oxidation 4-chlorophenol on OPGE- $\alpha$ -NiPc(OH)<sub>4</sub> even though there is one on bare OPGE. However an oxidation peak for 4-chlorophenol is clearly observed on GCE- $\alpha$ -NiPc(OH)<sub>4</sub> and it occurs at 0.36 V, (figure not shown) suggesting different interaction between 4-chlorophenol and the two electrode systems (**Table 5.1**). The peaks observed near -0.2 for OPGE- $\alpha$ -NiPc(OH)<sub>4</sub> and near -0.3 for OPGE-*poly*- $\alpha$ -Ni(O)Pc(OH)<sub>4</sub> are due to ring reduction (NiPc<sup>2-</sup>/NiPc<sup>3-</sup>) process, as discussed above. This process is not involved in the catalysis of 4-chlorophenol since it is at a much more negative potential than expected for the catalytic oxidation of this species. It has been reported that for the oxidation of 2-chlorophenol on *poly*-NiTSPc (tetrasulfonated phthalocyanine) two anodic peaks are observed [284]. The first anodic peak (for oxidation of 2-chlorophenol) appears at the same potential as on the bare electrode, it is followed by a second peak (with higher currents) located at about 30 mV more positive than the potential of Ni<sup>III</sup>/Ni<sup>II</sup> couple in the absence of 2-chlorophenol. The two peaks are observed in **Figure 5.3A** for the oxidation of 4-chlorophenol on (iii) OPGE-*poly*- $\alpha$ -Ni(O)Pc(OH)<sub>4</sub> at 0.42 and 0.45 V, **Table 5.1**. The first peak observed in **Figure 5.3A (iii)** is due to oxidation of 4-chlorophenol on the part of the bare electrode not covered with the NiPc and the second peak is due its oxidation on OPGE-*poly*- $\alpha$ -Ni(O)Pc(OH)<sub>8</sub>.

Oxidation of 4-chlorophenol on OPGE-*poly*- $\alpha$ -Ni(O)Pc(OH)<sub>4</sub> occurs with currents which are lower than those on bare OPGE, suggesting no catalytic activity. However, there is an enhancement in the anodic currents of the Ni<sup>III</sup>/Ni<sup>II</sup> couple in the presence of 4-chlorophenol (**Figure 5.3A (iv)**), compared with the cyclic voltammogram of OPGE-*poly*- $\alpha$ -Ni(O)Pc(OH)<sub>4</sub> in the absence of 4-chlorophenol, suggesting the involvement of the former species in the oxidation process of the latter. However, since the currents for oxidation of 4-chlorophenol on bare OPGE are higher than on OPGE-*poly*- $\alpha$ -Ni(O)Pc(OH)<sub>4</sub>, catalytic activity cannot be proved convincingly.

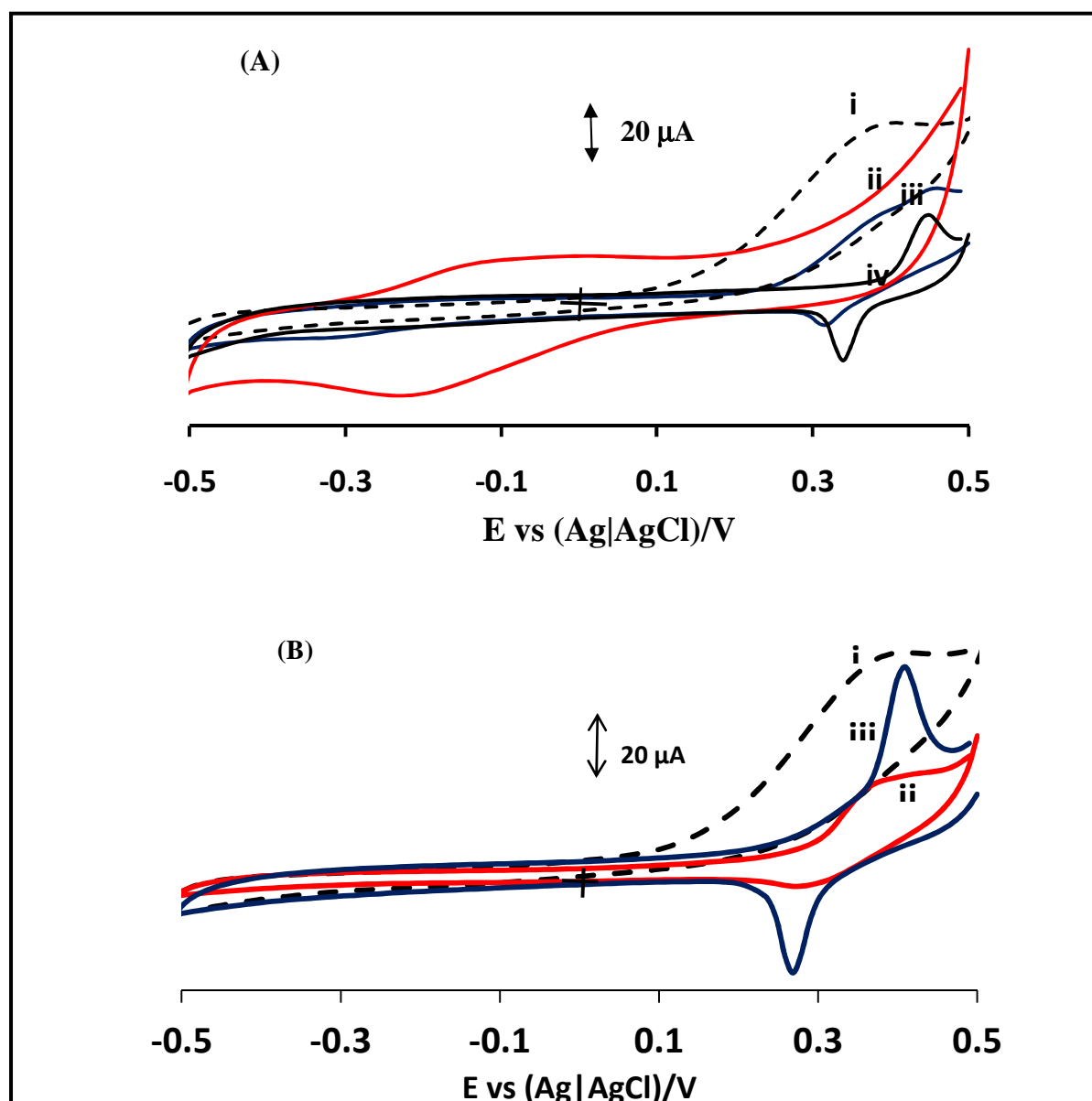


Figure 5.3: Cyclic voltammograms of 0.7 mM 4-chlorophenol in 0.1 M NaOH on OPGE modified with (A)  $\alpha\text{-NiPc(OH)}_4$  and (B)  $\alpha\text{-NiPc(OH)}_8$ . (i) bare OPGE, (ii) adsorbed complexes and (iii) polymerized complexes containing O-Ni-O bridges. (iv) in (A) is for OPGE-*poly*- $\alpha\text{-Ni(O)Pc(OH)}_4$  in the absence of 4-chlorophenol (in 0.1 M NaOH). Scan rate =  $100 \text{ mVs}^{-1}$ .

**Table 5.1: Electrochemical parameters for the detection 0.7 mM 4-chlorophenols in 0.1 M NaOH. Potentials versus Ag|AgCl on GCE and on OPGE.**

Electrode	4-CP/V	4-CP peak current ( $\mu\text{A}$ )	Regeneration %
bare	0.40(0.40) <sup>a</sup>	18(95) <sup>a</sup>	67(61) <sup>a</sup>
SWCNT	0.40	25	57
$\beta$ -NiPc(OH) <sub>4</sub>	(0.26) <sup>a</sup>	(60) <sup>a</sup>	(70) <sup>a</sup>
<i>poly</i> - $\beta$ -Ni(O)Pc(OH) <sub>4</sub>	(0.39) <sup>a</sup>	(122) <sup>a</sup>	(70) <sup>a</sup>
$\alpha$ -NiPc(OH) <sub>4</sub>	No peak detected	No peak detected	-
<i>poly</i> - $\alpha$ -Ni(O)Pc(OH) <sub>4</sub>	(0.42, 0.45) <sup>a</sup>	(47, 67) <sup>a</sup>	(70) <sup>a</sup>
$\alpha$ -NiPc(OH) <sub>8</sub>	(0.41) <sup>a</sup>	(40) <sup>a</sup>	(70) <sup>a</sup>
<i>poly</i> - $\alpha$ -Ni(O)Pc(OH) <sub>8</sub>	(0.37) <sup>a</sup>	(90) <sup>a</sup>	(70) <sup>a</sup>
<i>poly</i> - $\alpha$ -Ni(O)Pc(C <sub>10</sub> H <sub>21</sub> ) <sub>8</sub>	0.39	17	32 <sup>b</sup>
$\alpha$ -NiPc(C <sub>10</sub> H <sub>21</sub> ) <sub>8</sub> -SWCNT	0.41	28	30 <sup>b</sup>
<i>poly</i> - $\beta$ -Ni(O)Pc(NH <sub>2</sub> ) <sub>4</sub>	0.41	39	60
$\beta$ -NiPc(NH <sub>2</sub> ) <sub>4</sub> -SWCNT(linked)	0.40 (0.41) <sup>c</sup>	20 (35.4) <sup>c</sup>	70 (35) <sup>c</sup>
$\beta$ -NiPc(NH <sub>2</sub> ) <sub>4</sub> -SWCNT	0.36 (0.41) <sup>c</sup>	24 (35) <sup>c</sup>	68 (35) <sup>c</sup>
$\beta$ -NiPc(OH) <sub>4</sub> -SWCNT	0.38 (0.43) <sup>c</sup>	20 (18) <sup>c</sup>	86 (81) <sup>c</sup>
$\alpha$ -NiPc(OH) <sub>4</sub> -SWCNT	0.36 (0.36) <sup>c</sup>	23 (29) <sup>c</sup>	76 (69) <sup>c</sup>

GCE- $\alpha$ -NiPc(OH) <sub>8</sub> -SWCNT	0.37 (36) <sup>c</sup>	41 (29) <sup>c</sup>	96 (70) <sup>c</sup>
GCE- <i>poly</i> -Ni(O)Pc	0.36	20	84
GCE-NiPc-SWCNT	0.35	22.6	24 <sup>b</sup>

<sup>a</sup>Oxidation potential or current (in brackets) of 4-CP on OPGE and <sup>b</sup> decrease in current after the first scan was used. <sup>c</sup> values in brackets are for complexes on GCE in the absence of SWCNT

### 5.1.1.3. $\alpha$ -NiPc(OH)<sub>8</sub>

**Figure 5.3B** shows that the anodic currents on bare OPGE (i) are higher than for OPGE- $\alpha$ -NiPc(OH)<sub>8</sub> before cycling in NaOH, but with Ni<sup>III</sup>/Ni<sup>II</sup> peaks already present (ii) and OPGE-*poly*- $\alpha$ -Ni(O)Pc(OH)<sub>8</sub> (iii) modified electrodes for 0.7 mM 4-chlorophenol oxidation. For the OPGE- $\alpha$ -NiPc(OH)<sub>8</sub> (ii), the currents for 4-chlorophenol are lower than for OPGE-*poly*- $\alpha$ -Ni(O)Pc(OH)<sub>8</sub> (iii). **Figure 5.3B** (iii) shows that the anodic currents for OPGE-*poly*- $\alpha$ -Ni(O)Pc(OH)<sub>8</sub> in the presence of 4-chlorophenol are higher than the cathodic currents confirming the involvement of the Ni<sup>III</sup>/Ni<sup>II</sup> couple in the oxidation of 4-chlorophenol. The 4-chlorophenol oxidation peak is observed at 0.41 V for  $\alpha$ -NiPc(OH)<sub>8</sub> and at 0.37 V for *poly*- $\alpha$ -NiPc(OH)<sub>8</sub> on OPGE, **Table 5.1**. The 4-chlorophenol oxidation peak is observed at 0.36 V on GCE- $\alpha$ -NiPc(OH)<sub>8</sub> with lower currents (29  $\mu$ A) compared to OPGE- $\alpha$ -NiPc(OH)<sub>8</sub> (41  $\mu$ A). This oxidation potential is lower compared to OPGE- $\alpha$ -NiPc(OH)<sub>8</sub>.

In summary, for the oxidation of 4-chlorophenol on OPGE-*poly*- $\alpha$ -Ni(O)Pc(OH)<sub>4</sub> and OPGE-*poly*- $\alpha$ -Ni(O)Pc(OH)<sub>8</sub>, the observed currents are less than those of the bare OPGE, with no improvement in potential. However for OPGE-*poly*- $\beta$ -Ni(O)Pc(OH)<sub>4</sub> higher currents for 4-chlorophenol oxidation are observed than on bare OPGE showing good electrocatalytic activity compared to OPGE-*poly*- $\alpha$ -Ni(O)Pc(OH)<sub>4</sub> and OPGE-*poly*- $\alpha$ -Ni(O)Pc(OH)<sub>8</sub>.

It can thus be concluded that non-peripheral substitution ( $\alpha$ ) does not favour electrocatalytic oxidation of 4-chlorophenols. The behaviour could be related to the ease of formation and nature of the O-Ni-O bridges, which form more readily for *poly*- $\beta$ -Ni(O)Pc(OH)<sub>4</sub> compared to either *poly*- $\alpha$ -Ni(O)Pc(OH)<sub>4</sub> or *poly*- $\alpha$ -Ni(O)Pc(OH)<sub>8</sub>. The better catalysis observed for *poly*- $\beta$ -Ni(O)Pc(OH)<sub>4</sub> could also be due to the fact the Ni<sup>III</sup>/Ni<sup>II</sup> peaks are observed at a much lower potential (0.28 V) when compared to OPGE-*poly*- $\alpha$ -Ni(O)Pc(OH)<sub>4</sub> and OPGE-*poly*- $\alpha$ -Ni(O)Pc(OH)<sub>8</sub> (0.40 and 0.39 V, respectively), **Table 4.1**.

### 5.1.1.4. $\alpha$ -NiPc(C<sub>10</sub>H<sub>21</sub>)<sub>8</sub>, $\beta$ -NiPc(NH<sub>2</sub>)<sub>4</sub> and NiPc

There was instant formation of Ni<sup>III</sup>/Ni<sup>II</sup> peaks, which did not improve on cycling for *poly*- $\alpha$ -Ni(O)Pc(C<sub>10</sub>H<sub>21</sub>)<sub>8</sub>, hence adsorbed species are not discussed. Ni<sup>III</sup>/Ni<sup>II</sup> peaks did not form instantly for NiPc or  $\beta$ -NiPc(NH<sub>2</sub>)<sub>4</sub>, however for comparative purposes with *poly*- $\alpha$ -Ni(O)Pc(C<sub>10</sub>H<sub>21</sub>)<sub>8</sub>, only *poly*-Ni(O)Pc and *poly*- $\beta$ -Ni(O)Pc(NH<sub>2</sub>)<sub>4</sub> will be discussed in this section. Even though the GCE-*poly*- $\alpha$ -Ni(O)Pc(C<sub>10</sub>H<sub>21</sub>)<sub>8</sub> is not catalytic towards 4-

chlorophenol, as judged by the low currents compared to bare GCE, the onset of the 4-chlorophenol peak is at about the same potential as the  $\text{Ni}^{\text{III}}/\text{Ni}^{\text{II}}$  peak, **Figure 5.4A**. The peak for 4-chlorophenol is observed at 0.39 V, **Table 5.1**.

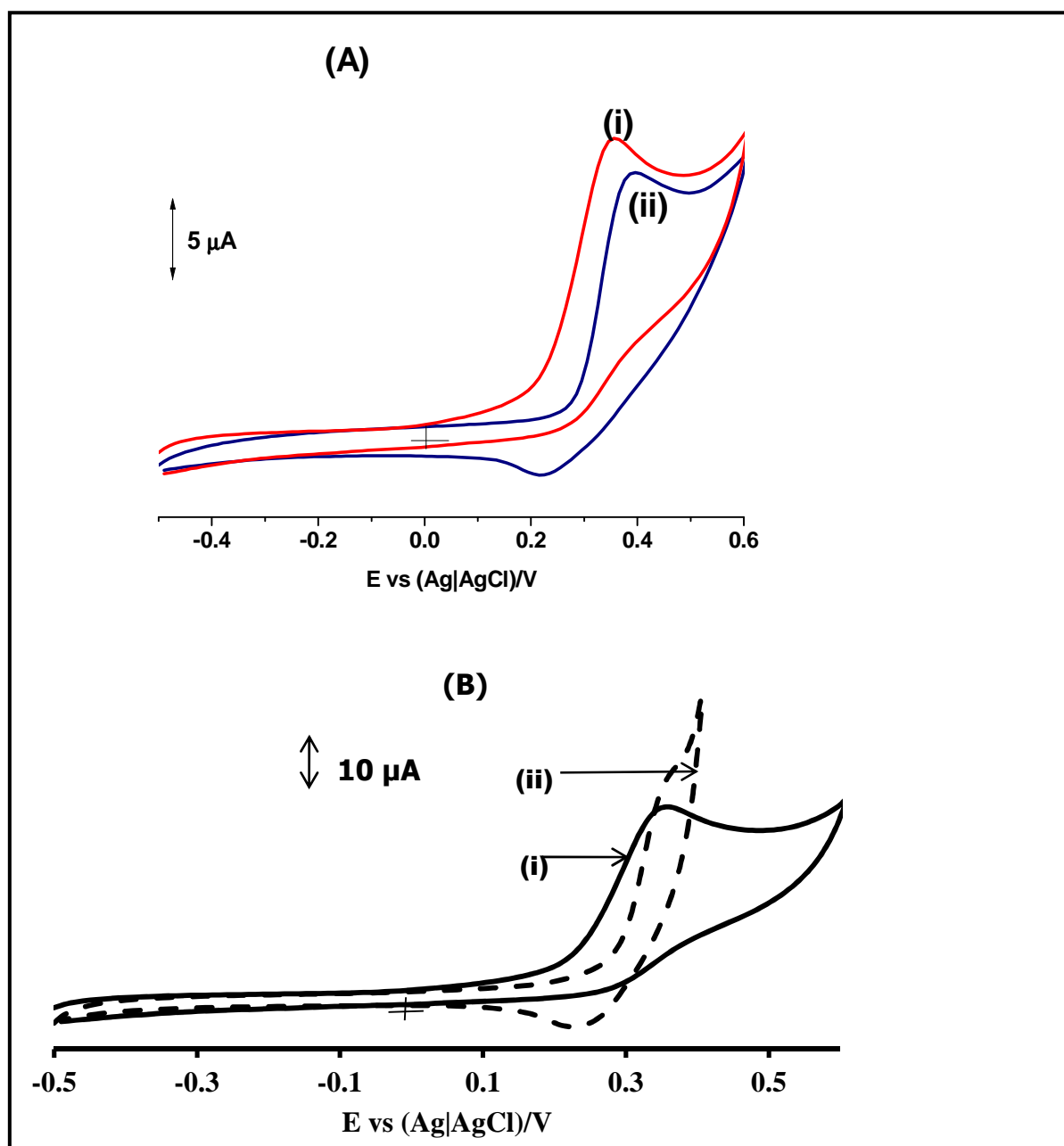


**Figure 5.4:** Cyclic voltammograms of 0.7 mM 4-chlorophenol in 0.1 M NaOH on (A) (i) bare GCE and (ii) GCE-*poly-α-Ni(O)Pc(C<sub>10</sub>H<sub>21</sub>)<sub>8</sub>* and (B) (i) bare GCE and (ii) GCE-*poly-Ni(O)Pc*.

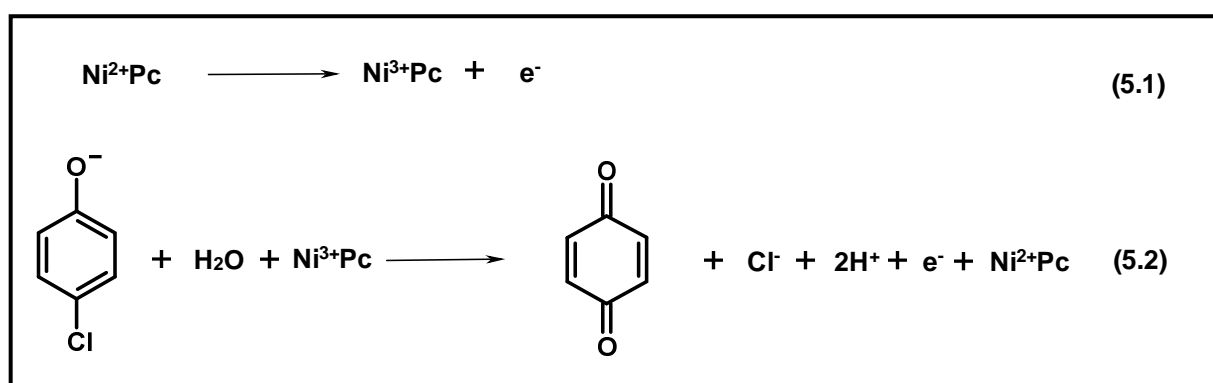
The above observation suggests that the involvement of  $\text{Ni}^{\text{III}}/\text{Ni}^{\text{II}}$  process, and the fact that there is only a small return peak (cathodic) for detection of 4-chlorophenol on GCE-*poly-α-Ni(O)Pc(C<sub>10</sub>H<sub>21</sub>)<sub>8</sub>* shows that 4-chlorophenol is capable of reducing almost all of the  $\text{Ni}^{\text{III}}$

species. **Table 5.1** shows the oxidation potential for 4-chlorophenol on GCE-NiPc(NH<sub>2</sub>)<sub>4</sub> occurs at 0.41 V (35 μA) which is at the same potential as GCE-*poly*-Ni(O)Pc(NH<sub>2</sub>)<sub>4</sub> (38.5 μA), thus showing no improvement for electrocatalytic oxidation of 4-chlorophenol in terms of potential.

**Figure 5.4B** shows oxidation of 0.7 mM of 4-chlorophenol in 0.1 M NaOH solution on bare GCE (curve i) and GCE-*poly*-Ni(O)Pc (curve ii). The redox process corresponding to oxidation of 4-chlorophenol was observed at 0.36 V on GCE-*poly*-Ni(O)Pc, **Table 5.1**. GCE-*poly*-Ni(O)Pc (19.8 μA) shows slightly larger currents compared to bare GCE suggesting that this electrode shows minimal electrocatalysis but better than GCE-*poly*-α-Ni(O)Pc(C<sub>10</sub>H<sub>21</sub>)<sub>8</sub> (16.6 μA), **Table 5.1**. GCE-*poly*-α-Ni(O)Pc(C<sub>10</sub>H<sub>21</sub>)<sub>8</sub> showed lower currents compared to bare GCE. Again the onset of the 4-chlorophenol peak, for GCE-*poly*-Ni(O)Pc is at about the same potential as the Ni<sup>III</sup>/Ni<sup>II</sup> peak suggesting the involvement of this process with only a small return peak (cathodic) suggesting that 4-chlorophenol is capable of reducing most of the Ni<sup>III</sup> species. Oxidation peak of 4-CP on GCE-*poly*-β-Ni(O)Pc(NH<sub>2</sub>)<sub>4</sub> was observed at 0.41 V (**Table 5.1**), which is worse than GCE-*poly*-Ni(O)Pc (0.36 V).

### 5.1.1.5. Mechanism

The mechanism for the oxidation of 4-chlorophenol in basic media may be proposed as shown by **Scheme 5.1**, **Equation 5.1**, [284] on *poly*-β-Ni(O)Pc(OH)<sub>4</sub> where clear catalytic activity was involved.



**Scheme 5.1.** Proposed mechanism for the catalytic oxidation of 4-chlorophenols by *poly*-β-Ni(O)Pc(OH)<sub>4</sub> or *poly*-α-Ni(O)Pc(OH)<sub>8</sub> derivatives.

In highly basic media (such as 0.1 M NaOH), 4-chlorophenol is deprotonated. The first step is the electrochemical oxidation of Ni<sup>II</sup> to Ni<sup>III</sup> for *poly*-Ni(O)Pc (**Equation 5.1**), followed by



the reaction of  $\text{Ni}^{\text{III}}$  with deprotonated 4-chlorophenol in the presence of water molecules from electrolyte to form benzoquinone (**Equation 5.2**). Quinones are well known as products of electrocatalytic oxidation of chlorophenols [267]. For the nonpolymerized species, it is possible that ring based processes of the NiPc derivatives are involved since  $\text{Ni}^{\text{III}}/\text{Ni}^{\text{II}}$  are not known when NiPc derivatives are not polymerized.

### 5.1.2. NiPc-SWCNT conjugates on GCE

As already stated under basic conditions, NiPc derivatives readily transform into O-Ni-O when adsorbed, however the O-Ni-O bridges did not form for NiPc adsorbed on SWCNT. Only covalently linked  $\beta\text{-NiPc}(\text{NH}_2)_4$  to SWCNT was able to transform into O-Ni-O bridge when cycled in 0.1 M NaOH solution (discussed below). In the absence of SWCNT, O-Ni-O bridges formed.

#### 5.1.2.1. NiPc(NH<sub>2</sub>)<sub>4</sub> and NiPc(OH)<sub>n</sub> derivatives

**Figure 5.5** shows oxidation of 0.7 mM of 4-chlorophenol in 0.1 mM NaOH aqueous solution on GCE- $\beta\text{-NiPc}(\text{NH}_2)_4\text{-SWCNT}$ , GCE- $\beta\text{-NiPc}(\text{NH}_2)_4\text{-SWCNT}(\text{linked})$ , GCE- $\alpha\text{-NiPc}(\text{OH})_4\text{-SWCNT}$  and bare GCE, as representatives of all electrodes. **Table 5.1** lists the peak potentials and currents for the oxidation of 4-chlorophenol on the various electrodes. The irreversible redox process, which corresponds to oxidation of 4-chlorophenol, is observed at potentials of 0.36 V for GCE- $\alpha\text{-NiPc}(\text{OH})_4\text{-SWCNT}$  and GCE- $\beta\text{-NiPc}(\text{NH}_2)_4\text{-SWCNT}$ , 0.37 V for GCE- $\alpha\text{-NiPc}(\text{OH})_8\text{-SWCNT}$ , 0.38 V for GCE- $\beta\text{-NiPc}(\text{OH})_4\text{-SWCNT}$ , and 0.40 V for bare GCE, GCE-SWCNT and GCE- $\beta\text{-NiPc}(\text{NH}_2)_4\text{-SWCNT}(\text{linked})$ , **Table 5.1**. Thus in terms of potential (and in the presence of SWCNT), all electrodes performed equally or better than the bare GCE. Comparing GCE- $\beta\text{-NiPc}(\text{OH})_4\text{-SWCNT}$  and GCE- $\alpha\text{-NiPc}(\text{OH})_4\text{-SWCNT}$  shows no major difference in terms of potential for 4-chlorophenol oxidation, hence showing no effect of the point of substitution. Comparing GCE- $\alpha\text{-NiPc}(\text{OH})_4\text{-SWCNT}$  and GCE- $\alpha\text{-NiPc}(\text{OH})_8\text{-SWCNT}$  in terms of potential also shows no effects of the number of substituents on 4-chlorophenol oxidation, the same applies to GCE- $\beta\text{-NiPc}(\text{NH}_2)_4\text{-SWCNT}$  and GCE- $\beta\text{-NiPc}(\text{OH})_4\text{-SWCNT}$ , where the effects of the different substituents is not clear. In terms of current, GCE- $\alpha\text{-NiPc}(\text{OH})_8\text{-SWCNT}$  (41  $\mu\text{A}$ ) performed better compared to all other electrodes containing SWCNT in **Table 5.1**. Even though for  $\alpha\text{-NiPc}(\text{OH})_4$  and  $\alpha\text{-NiPc}(\text{OH})_8$  adsorbed on SWCNT catalytic activity in terms of potential remains approximately the same,

the current for 4-chlorophenol improved considerably for the latter suggesting that the number of substituents, which will affect orientation, result in improved catalytic activity in terms of current. The bare GCE (17.9  $\mu\text{A}$ ) and GCE-*poly- $\alpha$* -Ni(O)Pc(C<sub>10</sub>H<sub>21</sub>)<sub>8</sub> (16.6  $\mu\text{A}$ ) gave the lowest current for 4-chlorophenol detection.

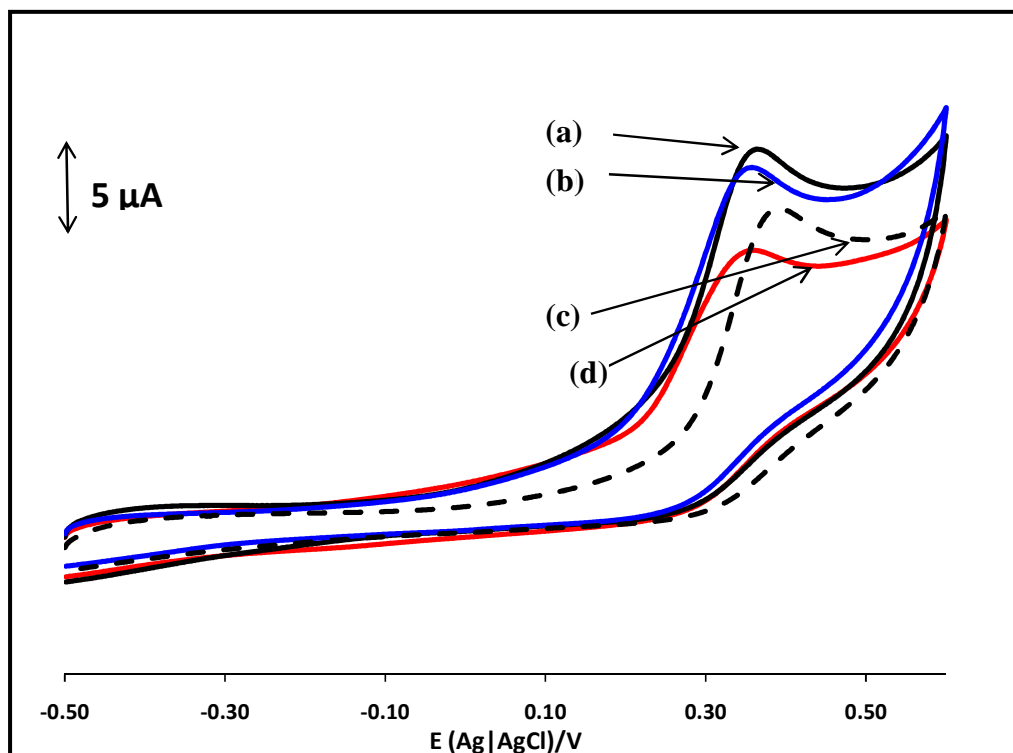


**Figure 5.5:** Oxidation of 0.7 mM of 4-chlorophenol in 0.1 mM NaOH aqueous solution on GCE- $\beta$ -NiPc(NH<sub>2</sub>)<sub>4</sub>-SWCNT (a), GCE- $\alpha$ -NiPc(OH)<sub>4</sub>-SWCNT (b), GCE- $\beta$ -NiPc(NH<sub>2</sub>)<sub>4</sub>-SWCNT(linked) (c) and bare GCE (d), Scan rate = 100 mVs<sup>-1</sup>.

Peaks observed in the absence of SWCNT are also listed in **Table 5.1**. These values are 0.36 V, 0.36 V, 0.41 V and 0.43 V for GCE- $\alpha$ -NiPc(OH)<sub>4</sub>, GCE- $\alpha$ -NiPc(OH)<sub>8</sub>, GCE- $\beta$ -NiPc(NH<sub>2</sub>)<sub>4</sub> and GCE- $\beta$ -NiPc(OH)<sub>4</sub>, respectively. Non-peripherally substituted derivatives showed improved potential in the absence of SWCNT compared to peripherally substituted derivatives (compare GCE- $\beta$ -NiPc(OH)<sub>4</sub> and GCE- $\alpha$ -NiPc(OH)<sub>4</sub>), contradicting results in the presence of SWCNT where there was no significant change in potential. However change of substituent from NH<sub>2</sub> (GCE- $\beta$ -NiPc(NH<sub>2</sub>)<sub>4</sub>) to OH (GCE- $\beta$ -NiPc(OH)<sub>4</sub>) did not affect the potential for 4-chlorophenol oxidation in the absence of SWCNT as was the case in its presence.

**Table 5.1** suggests that the catalytic activity of  $\beta$ -NiPc(OH)<sub>4</sub> towards the oxidation for 4-chlorophenol is improved in terms of potential when adsorbed on SWCNT (peak potential,  $E_p = 0.38$  V for GCE- $\beta$ -NiPc(OH)<sub>4</sub>-SWCNT compared to  $E_p = 0.43$  V in the absence of SWCNT (GCE- $\beta$ -NiPc(OH)<sub>4</sub>). Similar behavior was observed also for  $\beta$ -NiPc(NH<sub>2</sub>)<sub>4</sub> in terms of potential (comparing GCE- $\beta$ -NiPc(NH<sub>2</sub>)<sub>4</sub> with  $E_p = 0.41$  V compared to GCE- $\beta$ -NiPc(NH<sub>2</sub>)<sub>4</sub>-SWCNT with  $E_p = 0.36$  V). It can be concluded that non-peripheral substitution improves catalytic behavior in terms of current compared to peripheral substitution in the presence of SWCNT (compare GCE- $\beta$ -NiPc(OH)<sub>4</sub>-SWCNT and GCE- $\alpha$ -NiPc(OH)<sub>4</sub>-SWCNT). In terms of potential, SWCNT do not improve the catalytic behavior of non-peripherally substituted derivatives, but improve that of peripherally substituted ones. This could be related to the orientation of the differently substituted derivatives onto the SWCNT.

#### 5.1.2.2. $\alpha$ -NiPc(C<sub>10</sub>H<sub>21</sub>)<sub>8</sub> and NiPc

**Figure 5.6A** shows oxidation of 0.7 mM of 4-chlorophenol in 0.1 M NaOH aqueous solution on bare GCE (curve i), GCE-SWCNT (curve ii) and GCE- $\alpha$ -NiPc(C<sub>10</sub>H<sub>21</sub>)<sub>8</sub>-SWCNT (curve iii). The irreversible redox process which corresponds to the oxidation of 4-chlorophenol occurs at 0.40, 0.40 and 0.41 V for GCE, GCE-SWCNT and GCE- $\alpha$ -NiPc(C<sub>10</sub>H<sub>21</sub>)<sub>8</sub>-SWCNT, respectively, **Table 5.1**. GCE- $\alpha$ -NiPc(C<sub>10</sub>H<sub>21</sub>)<sub>8</sub>-SWCNT showed poor electrocatalytic response in terms of potential, but good electrocatalytic response in terms of current with respect to the bare GCE and GCE-SWCNT. The onset of the 4-CP oxidation peak occurs at a lower potential for GCE- $\alpha$ -NiPc(C<sub>10</sub>H<sub>21</sub>)<sub>8</sub>-SWCNT (**Figure 5.6**), showing good catalytic activity.

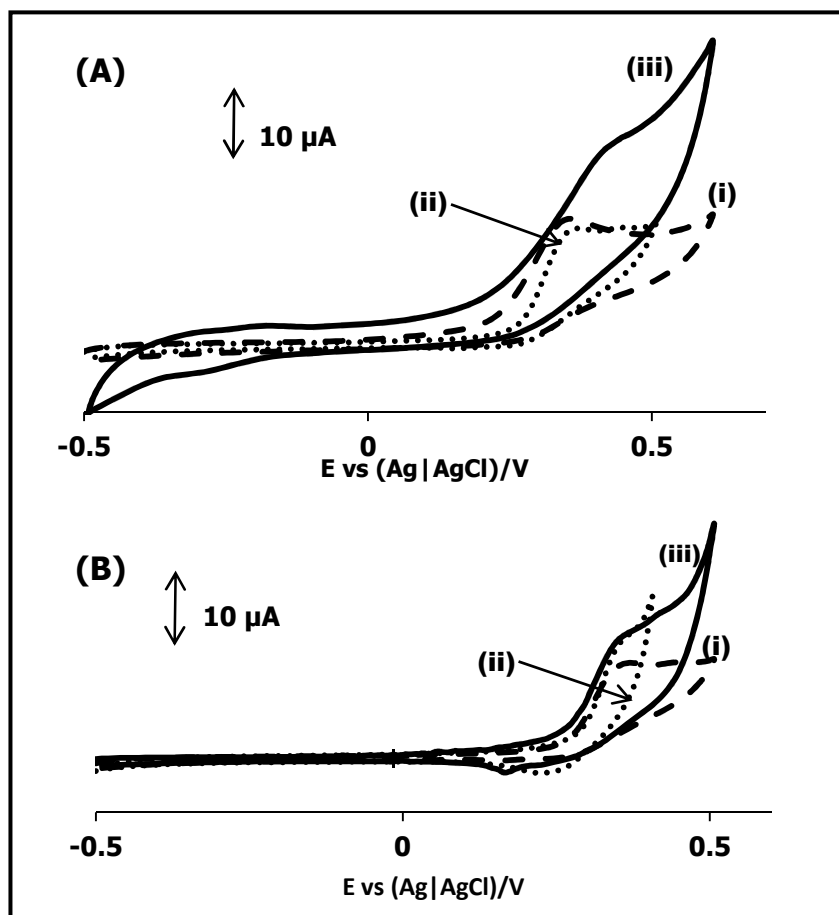


**Figure 5.6:** Cyclic voltammograms of 0.7 mM 4-chlorophenol in 0.1 M NaOH on (A) (i) bare GCE, (ii) GCE-SWCNT and (iii) GCE- $\alpha$ -NiPc( $\text{C}_{10}\text{H}_{21}$ )<sub>8</sub>-SWCNT and (B) (i) GCE-SWCNT, (ii) GCE-*poly*-Ni(O)Pc and (iii) GCE-NiPc-SWCNT

**Figure 5.6B** shows oxidation of 0.7 mM of 4-chlorophenol in 0.1 M NaOH solution on GCE-SWCNT (curve i), GCE-*poly*-Ni(O)Pc (curve ii) and GCE-NiPc-SWCNT (curve iii). **Figure 5.6B** shows that GCE-SWCNT electrode does not respond well to 4-chlorophenol in terms of current, with respect to other modified electrodes. This was also the case in **Figure 5.6A**. However once NiPc is adsorbed on the SWCNT there is some improvement in current for the detection of 4-chlorophenol (curve iii). When NiPc is adsorbed on the SWCNT, the onset of the 4-CP oxidation is at a lower potential compared to GCE-*poly*-Ni(O)Pc. Comparing GCE-*poly*-Ni(O)Pc with GCE-NiPc-SWCNT, **Figure 5.6B** shows that the presence of SWCNT does not improve electrocatalysis, in terms of current and potential whereas, catalysis is improved when  $\alpha$ -NiPc( $\text{C}_{10}\text{H}_{21}$ )<sub>8</sub> is adsorbed on SWCNT. A closer look at **Figure 5.6B**, shows a weak but sharp return peak between 0.1 ~ 0.2 V for GCE-NiPc-SWCNT in **Figure 5.6B** (iii) and *poly*-Ni(O)Pc in **Figure 5.6B** (ii). This peak can thus be related to the NiPc

complex. Even though the  $\text{Ni}^{\text{III}}/\text{Ni}^{\text{II}}$  couple is not evident in **Figure 5.6B** for adsorbed GCE-NiPc-SWCNT, the small peak in **Figure 5.6B** suggests traces of this redox process for both GCE-*poly*-Ni(O)Pc and GCE-NiPc-SWCNT.

### 5.1.3. Electrode stability

Surface fouling and restoration of electrodes during electrochemical detection of phenolic compounds is a major concern. Electrode passivation is illustrated by a drastic decrease in current, shown **Figure 5.7** where a drop in  $I_p$  with increase in scan number is observed, indicating passivation. For complexes adsorbed on OPGE, there was a ~ 70% regeneration of the electrodes on rinsing with water on both OPGE-*poly*- $\beta$ -Ni(O)Pc(OH)<sub>4</sub> and OPGE- $\beta$ -NiPc(OH)<sub>4</sub>. GCE- $\beta$ -NiPc(OH)<sub>4</sub> regeneration is 81% compared to 70% on OPGE, see **Table 5.1**. This result suggest that when  $\beta$ -NiPc(OH)<sub>4</sub> is adsorbed on GCE it offers greater resistance to passivation compared to when it is adsorbed on OPGE, possibly due to different interaction and orientation of  $\beta$ -NiPc(OH)<sub>4</sub> on the surface of GCE and OPGE.

**Figure 5.8** shows cyclic voltammograms of 0.7 mM 4-chlorophenol in 0.1 M NaOH solution catalysed by GCE- $\alpha$ -NiPc(OH)<sub>4</sub>-SWCNT electrode. The second scan in **Figure 5.8(c)** shows a considerable decrease in current compared to the first scan, **Figure 5.8(a)**. **Figure 5.8(b)** shows the the scan obtained after rinsing the modified electrode with millipore water. **Figure 5.8(b)** shows that there was recovery of the oxidation currents following rinsing with millipore water. **Table 5.1** shows the % recoveries obtained for all other electrodes studied. Of all the modified electrodes shown in **Table 5.1**, GCE- $\alpha$ -NiPc(OH)<sub>8</sub>-SWCNT (96% recovery) gave the best recovery against electrode fouling, followed by GCE- $\beta$ -NiPc(OH)<sub>4</sub>-SWCNT at 86% recovery. In all cases, the % recovery considerably improves in the presence of SWCNT, showing the huge influence of SWCNT on the stability of the electrode.

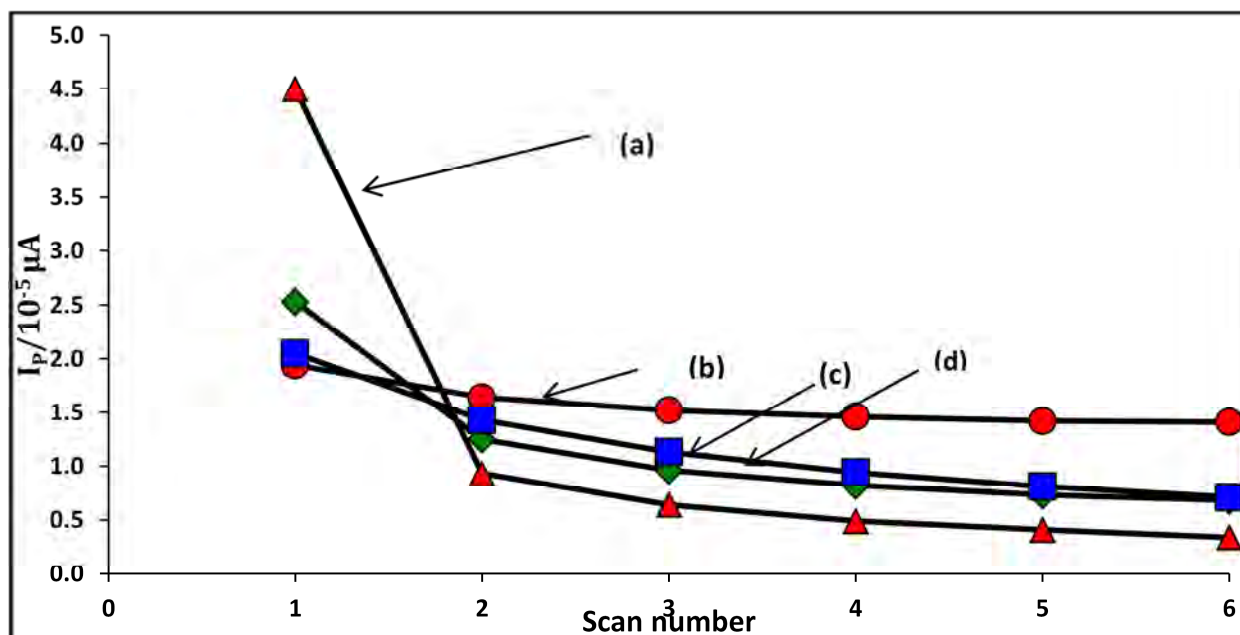


Figure 5.7: Variation of peak current with scan number for the voltammetric responses in 0.7 mM 4-chlorophenol in 0.1 M NaOH for (A) (a) bare GC, (b) GCE- $\beta$  NiPc(OH)<sub>4</sub>, (c) GCE- $\beta$ -NiPc(OH)<sub>4</sub>-SWCNT(ads), (d) SWCNT.

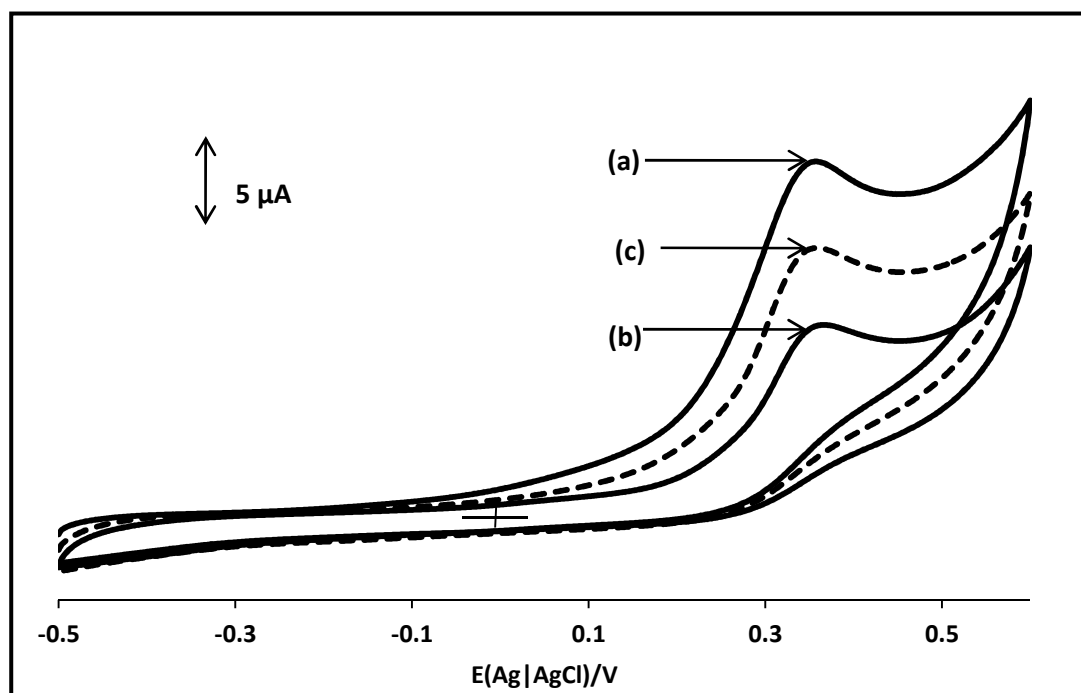


Figure 5.8: Cyclic voltammograms of 0.7 mM 4-chlorophenol in 0.1 M NaOH solution catalysed by GCE- $\alpha$ -NiPc(OH)<sub>4</sub>-SWCNT electrode showing the first (a), second (b) and the scan(c) obtained after rinsing the modified electrode with Millipore water.

The linked  $\beta$ -NiPc(NH<sub>2</sub>)<sub>4</sub>-SWCNT(linked) showed the same passivation pattern compared to adsorbed  $\beta$ -NiPc(NH<sub>2</sub>)<sub>4</sub>-SWCNT modified electrode, but both are improved compared to bare electrode. Electrode regeneration, after rinsing with water, for GCE- $\beta$ -NiPc(NH<sub>2</sub>)<sub>4</sub>-SWCNT (linked) electrode was calculated to be 70% compared to 68% for  $\beta$ -NiPc(NH<sub>2</sub>)<sub>4</sub>-SWCNT electrode, **Table 5.1**. Thus, comparing the linked and adsorbed  $\beta$ -NiPc(NH<sub>2</sub>)<sub>4</sub> there is no huge advantage of linking in terms of improvement in electrode regeneration. GCE- $\beta$ -NiPc(NH<sub>2</sub>)<sub>4</sub>-SWCNT (linked) and  $\beta$ -NiPc(NH<sub>2</sub>)<sub>4</sub>-SWCNT electrode showed better resistance to electrode fouling compared to *poly*- $\beta$ -Ni(O)Pc(NH<sub>2</sub>)<sub>4</sub> and  $\beta$ -NiPc(NH<sub>2</sub>)<sub>4</sub> electrodes in the absence of SWCNT, which gave 60% and 35% regeneration respectively. Thus *poly*- $\beta$ -Ni(O)Pc(NH<sub>2</sub>)<sub>4</sub> electrode showed improved stability towards electrode fouling compared to  $\beta$ -NiPc(NH<sub>2</sub>)<sub>4</sub> electrode.

The GCE-*poly*-Ni(O)Pc could be regenerated to 84% of its original current while bare GCE could be regenerated only to 67%, after using followed by rinsing in water. In terms of electrode passivation, GCE - $\alpha$ -NiPc(C<sub>10</sub>H<sub>21</sub>)<sub>8</sub>-SWCNT showed a 30% decrease (**Table 5.1**) in current between the first and second scans which is lower than for bare GCE at 36% (not in **Table 5.1**).

## 5.2. 2,4-Dichlorophenol (DCP)

### 5.2.1. NiPc derivatives without SWCNT

Only  $\alpha$ -NiPc(C<sub>10</sub>H<sub>21</sub>)<sub>8</sub> and NiPc are employed as examples for this analyte. **Figure 5.9A** shows oxidation of 0.7 mM of 2, 4-dichlorophenol in 0.1 M NaOH aqueous solution on bare GCE (curve i), and GCE-*poly*- $\alpha$ -Ni(O)Pc(C<sub>10</sub>H<sub>21</sub>)<sub>8</sub> (curve ii). Again the GCE-*poly*- $\alpha$ -Ni(O)Pc(C<sub>10</sub>H<sub>21</sub>)<sub>8</sub> does not show activity (in terms of current and potential) towards the oxidation of 2,4-dichlorophenol (as was the case for 4-CP) compared to GCE. The small return peak (cathodic, for GCE-*poly*- $\alpha$ -Ni(O)Pc(C<sub>10</sub>H<sub>21</sub>)<sub>8</sub>) suggests that 2,4-dichlorophenol is capable of reducing most of the Ni<sup>III</sup> species. GCE-*poly*- $\alpha$ -Ni(O)Pc(C<sub>10</sub>H<sub>21</sub>)<sub>8</sub> showed a good stability towards electrode fouling following the detection of 2, 4-dichlorophenol with a current decrease of 15% compared to 23% for bare GCE (**Table 5.2**).

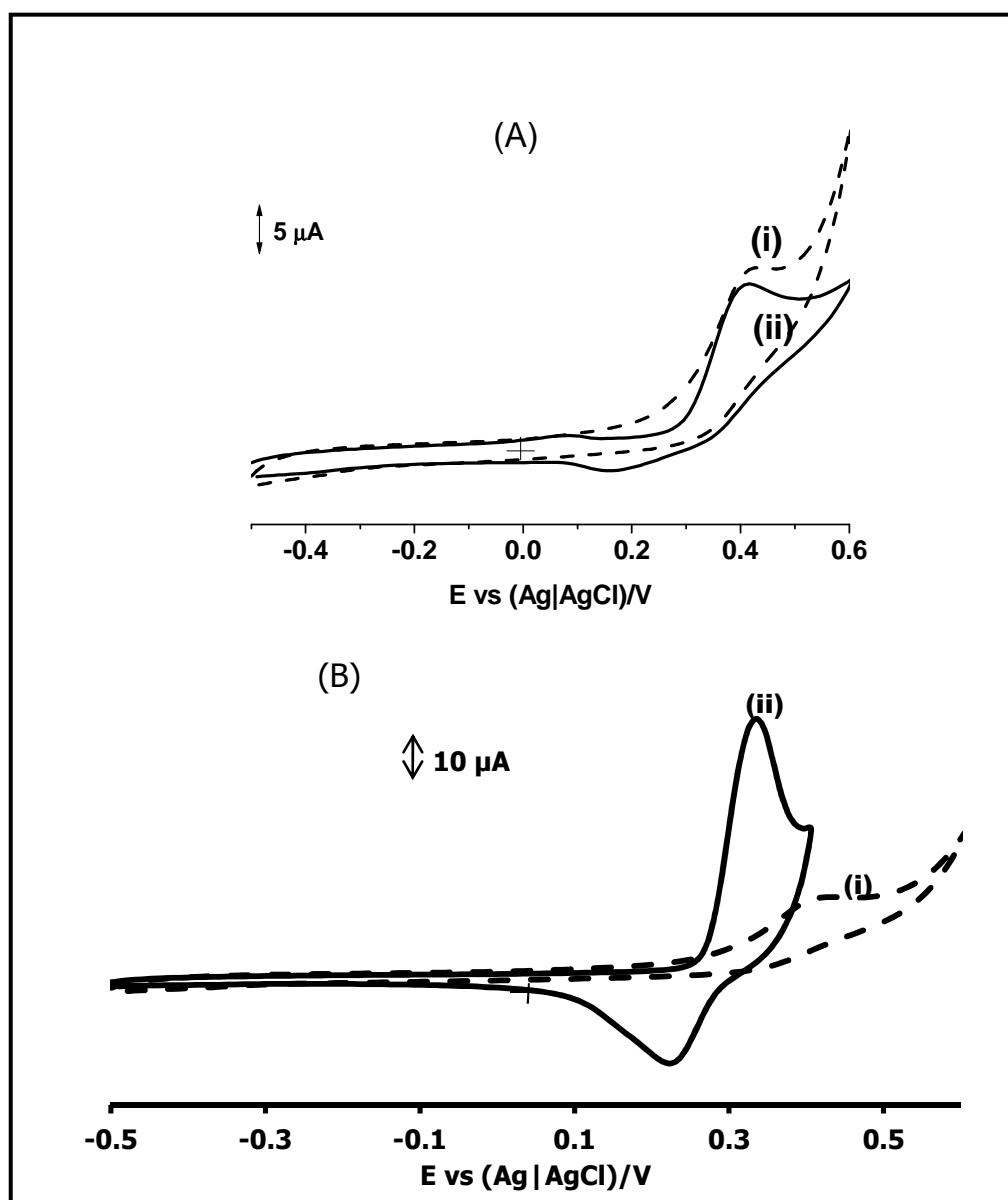


**Figure 5.9:** Cyclic voltammograms of 0.7 mM 2,4-dichlorophenol in 0.1 M NaOH on (A) (i) bare GCE and (ii) *poly- $\alpha$ -Ni(O)Pc(C<sub>10</sub>H<sub>21</sub>)<sub>8</sub>* and (B) (i) bare GCE and (ii) *GCE-poly-Ni(O)Pc*.

**Figure 5.9B** shows oxidation of 0.7 mM of 2, 4-dichlorophenol in 0.1 M NaOH aqueous solution on bare GCE (curve i) and *GCE-poly-Ni(O)Pc* (curve ii). *GCE-poly-Ni(O)Pc* showed an excellent response towards 2, 4-dichlorophenol oxidation in terms of enhanced currents and low potential. The stability test showed that the 2,4-DCP current drops to 12% after the first scan compared to 23% on bare GCE, **Table 5.2**. The return peak (cathodic) for detection of 2, 4-dichlorophenol on *GCE-poly-Ni(O)Pc* (**Figure 5.9B**) shows that 2, 4-dichlorophenol



is less capable of reducing the entire  $\text{Ni}^{\text{III}}$  species compared to GCE-*poly- $\alpha$ -Ni(O)Pc(C<sub>10</sub>H<sub>21</sub>)<sub>8</sub>* (Figure 5.9A).

**Table 5.2: Electrochemical parameters for the detection dichlorophenol in 0.1 M NaOH. Potentials versus Ag|AgCl.**

Electrode	2, 4-dichlorophenol /V	% decrease in current after the first scan
Bare	0.41	23
GCE-SWCNT	0.42	14
GCE- <i>poly-<math>\alpha</math>-Ni(O)Pc(C<sub>10</sub>H<sub>21</sub>)<sub>8</sub></i>	0.41	15
GCE- $\alpha$ -NiPc(C <sub>10</sub> H <sub>21</sub> ) <sub>8</sub> -SWCNT	~0.40	15
GCE- <i>poly-Ni(O)Pc</i>	0.33	12
GCE-NiPc -SWCNT	0.42	18

### 5.2.2. NiPc-SWCNT conjugates: $\alpha$ -NiPc(C<sub>10</sub>H<sub>21</sub>)<sub>8</sub> and NiPc used as examples

Figure 5.10A shows oxidation of 0.7 mM of 2, 4-dichlorophenol in 0.1 M NaOH solution on bare GCE (curve i), GCE-SWCNT (curve ii), GCE-*poly- $\alpha$ -Ni(O)Pc(C<sub>10</sub>H<sub>21</sub>)<sub>8</sub>* (curve iii) and GCE- $\alpha$ -NiPc(C<sub>10</sub>H<sub>21</sub>)<sub>8</sub>-SWCNT (curve iv). The potentials for 2,4-dichlorophenol oxidation are shown in Table 5.2 at 0.41, 0.42, 0.41 and ~0.4 V, for bare GCE, GCE-SWCNT, GCE-*poly- $\alpha$ -Ni(O)Pc(C<sub>10</sub>H<sub>21</sub>)<sub>8</sub>* and GCE- $\alpha$ -NiPc(C<sub>10</sub>H<sub>21</sub>)<sub>8</sub>-SWCNT, respectively. GCE- $\alpha$ -NiPc(C<sub>10</sub>H<sub>21</sub>)<sub>8</sub>-SWCNT- performed the best (compared to all electrodes in Figure 5.10A) in terms of current. The onset of the 2,4-DCP oxidation peak occurs at a lower potential for GCE- $\alpha$ -NiPc(C<sub>10</sub>H<sub>21</sub>)<sub>8</sub>-SWCNT electrode showing good catalytic activity. This electrode showed stability towards electrode fouling with a percentage decrease in current between first and second cycles of 15% (Table 5.2), which is similar to GCE- $\alpha$ -NiPc(C<sub>10</sub>H<sub>21</sub>)<sub>8</sub> without SWCNT and lower than for bare at 23%. The GCE- $\alpha$ -NiPc(C<sub>10</sub>H<sub>21</sub>)<sub>8</sub>-SWCNT electrode could be regenerated to 84% after rinsing in water following use. On their own SWCNT showed a good stability for 2,4-dichlorophenol detection with 14% decrease in current between the first and second cycles.

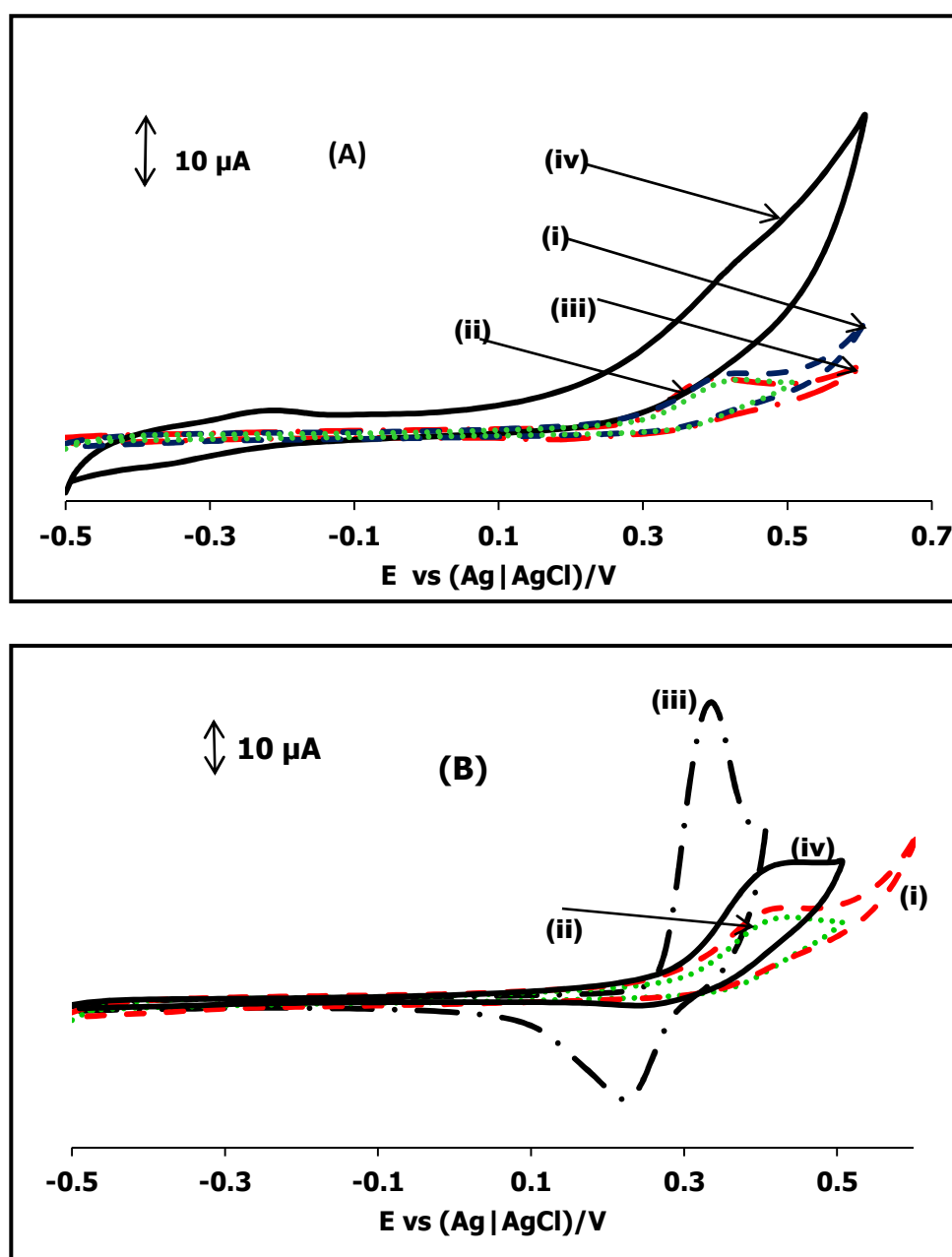


**Figure 5.10:** Cyclic voltammograms of 0.7 mM 2,4-dichlorophenol in 0.1 M NaOH on (A) (i) bare GCE, (ii) GCE-SWCNT, (iii) GCE-*poly- $\alpha$ -Ni(O)Pc(C<sub>10</sub>H<sub>21</sub>)<sub>8</sub>* and (iv) GCE- *$\alpha$ -NiPc(C<sub>10</sub>H<sub>21</sub>)<sub>8</sub>-SWCNT* and (B) (i) bare GCE, (ii) GCE-SWCNT, (iii) GCE-*poly-Ni(O)Pc* and (iv) GCE-NiPc-SWCNT.

**Figure 5.10B** shows oxidation of 0.7 mM of 2, 4-dichlorophenol in 0.1 M NaOH solution on bare GCE (curve i), GCE-SWCNT (curve ii), GCE-*poly-Ni(O)Pc* (curve iii) and GCE-NiPc-SWCNT (curve iv). When NiPc is adsorbed on the SWCNT there is some improvement in current for the detection of 2, 4-dichlorophenol (curve iv) compared to bare GCE and GCE-

SWCNT. However compared to GCE-*poly*-Ni(O)Pc without SWCNT, CGE-NiPc-SWCNT is less effective for detection of 2,4-DCP.

Thus, in the presence of SWCNT,  $\alpha$ -NiPc(C<sub>10</sub>H<sub>21</sub>)<sub>8</sub> shows good catalytic activity towards both 4-CP and 2,4-DCP in terms of current and onset of potential, whereas, the activity of NiPc does not improve in the presence of SWCNT. In terms of stability towards the detection of 2,4-DCP, all electrodes showed an improvement compared to bare GCE, **Table 5.2**. The combination of NiPc and SWCNT showed slightly worst behaviour in terms of stability compared to the rest of the modified electrodes.

### 5.2.3. CdTe-QDs and its conjugates

Please refer to section 4.2 for explanation of ads vs electrodeposition.

#### 5.2.3.1. CdTe-QDs without $\beta$ -NiPc(NH<sub>2</sub>)<sub>4</sub>

**Figures 5.11 A(b)** show that the oxidation peak for DCP occurs at 0.33 V (**Table 5.3**) on bare Au electrode. **Figure 5.11A(a)** represents the bare Au electrode in buffer. The peak for the oxidation of DCP is shifted to 0.38 V (**Table 5.3**) on electrodeposited CdTe-QDs **Figure 5.11B(b)**. The DCP peak is more intense on electrodeposited CdTe-QDs, showing the catalytic activity of the CdTe-QDs following oxidation. Thus the electrodeposited CdTe-QDs show electrocatalytic activity towards the oxidation of DCP in terms of current but not lower overpotential. The current for the oxidation potential of DCP on adsorbed CdTe-QDs at 0.34 V (**Figure 5.11B (c)**) is slightly more enhanced, with respect to the bare (**Figure 5.11B(d)**), suggesting some electrocatalytic activity. Adsorbed CdTe-QDs shows better electrocatalytic response in terms of lower oxidation potentials compared to electrodeposited CdTe-QDs, but exhibits poor catalytic currents for DCP.

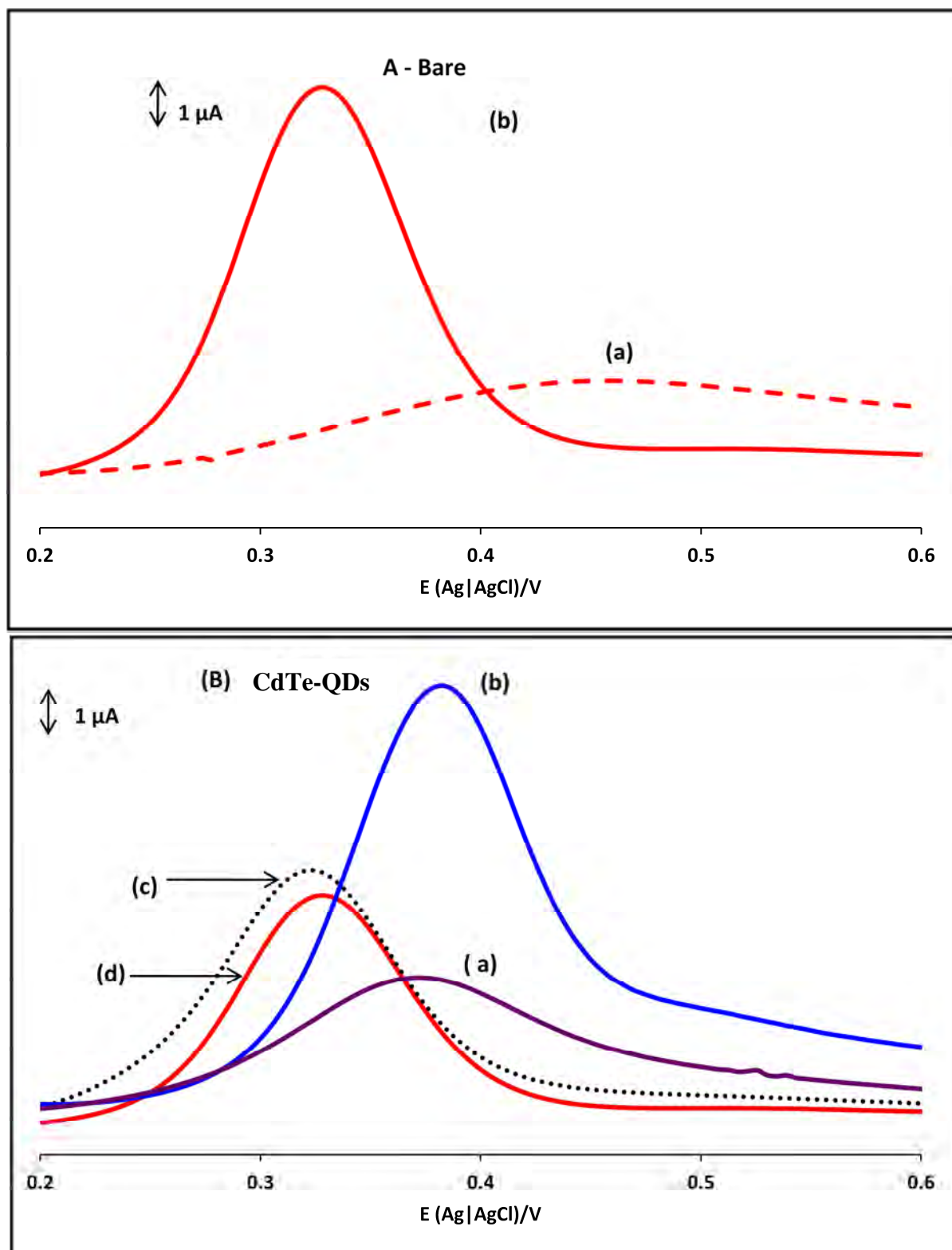


**Figure 5.11:** DPV scans for detection of 0.7 mM 2, 4-dichlorophenol in pH 9.2 buffer on: (A) bare Au electrode in the absence (a) and presence (b) of 2, 4-dichlorophenol. (B) electrodeposited-CdTe-QDs in the absence (a) and presence (b) of 2, 4-dichlorophenol. (c) and (d) in B are DPV scans for 2, 4-dichlorophenol on adsorbed-CdTe-QDs and bare Au electrode respectively.

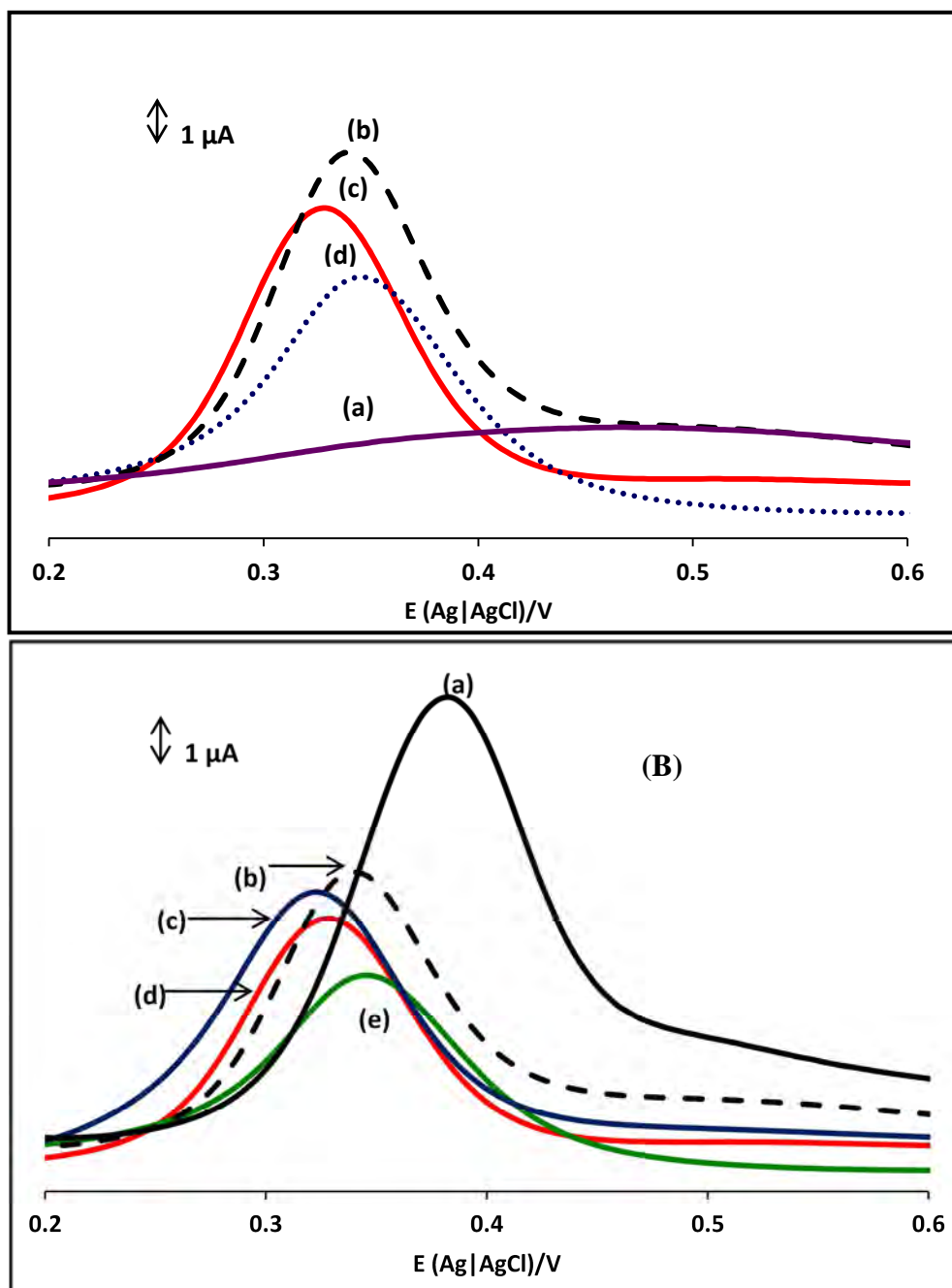


**Figure 5.12:** (A) electrodeposited CdTe-QDs- $\beta$ -NiPc(NH<sub>2</sub>)<sub>4</sub> in the absence (a) and presence (b) of 0.7 mM 2,4-dichlorophenol. (c) and (d) in (A) are DPV scans for 2,4-dichlorophenol on ads-CdTe-QDs- $\beta$ -NiPc(NH<sub>2</sub>)<sub>4</sub>, and bare Au electrode respectively. (B) An overlay of the DPV scans for the detection of 2,4-dichlorophenol on (a) electrodeposited CdTe-QDs, (b) electrodeposited CdTe-QDs- $\beta$ -NiPc(NH<sub>2</sub>)<sub>4</sub>, (c) ads-CdTe-QDs, (d) ads-CdTe-QDs- $\beta$ -NiPc(NH<sub>2</sub>)<sub>4</sub> and bare Au (e).

### 5.2.3.2. CdTe-QDs- $\beta$ -NiPc(NH<sub>2</sub>)<sub>4</sub> conjugates

**Figure 5.12A (b)** shows the oxidation peak for DCP at 0.36 V (**Table 5.3**) on electrodeposited CdTe-QDs- $\beta$ -NiPc(NH<sub>2</sub>)<sub>4</sub>. **Figure 5.12A (c)** shows that ads-CdTe-QDs- $\beta$ -NiPc(NH<sub>2</sub>)<sub>4</sub> exhibited low electrocatalytic activity (in terms of current). However it gave the best response in terms of oxidation potential (lower potentials of 0.28 V) for DCP with respect to the bare and electrodeposited CdTe-QDs- $\beta$ -NiPc(NH<sub>2</sub>)<sub>4</sub>, hence shows improved electrocatalytic activity. In summary, **Figure 5.12B** shows that electrodeposited CdTe-QDs exhibits much higher catalytic activity (in terms of current) followed by electrodeposited CdTe-QDs- $\beta$ -NiPc(NH<sub>2</sub>)<sub>4</sub>. Even though the latter stabilises QDs against oxidation, it shows poor performance in terms of current and a good response in terms of oxidation potential for DCP compared to electrodeposited CdTe-QDs. Ads-CdTe-QDs- $\beta$ -NiPc(NH<sub>2</sub>)<sub>4</sub> and ads-CdTe-QDs showed the best electrocatalytic activity in terms of oxidation potential for DCP, but poor performance in terms of current with respect to the electrodeposited electrodes (**Figure 5.12B**). In all cases the oxidation potentials for DCP are in the potential range of the oxidation of CdTe QDs core, and are thus catalysed by it. The involvement of Ni<sup>III</sup>/Ni<sup>II</sup> couple cannot be ruled out since, as stated above, this couple is observed in the region for DCP oxidation.

**Table 5.3** shows relative stabilities of all the electrodes discussed towards DCP detection. In terms of stability the electrodeposited CdTe-QDs showed less fouling compared to other electrodes and ads-CdTe-QDs showed the worst behavior.

**Table 5.3: Oxidation potentials for 2, 4-dichlorophenol and pentachlorophenol and current percentage loss after first scan in pH 9.2 buffer.**

Electrode	$E_p$ (DCP)/V	$E_p$ (PCP)/V	DCP Current loss after the first scan	PCP Current loss after the first scan
Bare (Au)	0.33	0.46	-	-
ads-CdTe-QDs	0.34	0.44	36%	38%
Electrodep-CdTe-QDs	0.38	0.48	27%	28%
ads-CdTe-QDs- $\beta$ -NiPc(NH <sub>2</sub> ) <sub>4</sub>	0.28	0.42	31%	29%
Electrodep-CdTe-QDs- $\beta$ -NiPc(NH <sub>2</sub> ) <sub>4</sub>	0.36	0.47	31%	42%

### 5.3. Pentachlorophenol (PCP)

#### 5.3.1. CdTe-QDs

**Figure 5.13A** show the oxidation peak for PCP at 0.46 V (**Table 5.3**) on bare Au electrode. The peak for the oxidation of PCP is shifted to 0.48 V (**Table 5.3**) on Au electrode modified with electrodep-CdTe-QDs, **Figure 5.13B (b)** and is slightly enhanced in current compared to PCP detection on bare Au electrode, hence showing weak electrocatalytic activity in terms of current. For ads-CdTe-QDs there is no electrocatalytic activity, **Figure 5.13 B (c)** (in terms of current), performing worse than bare Au electrode. However ads-CdTe-QDs gave a lower oxidation potential for PCP peak (0.44 V) compared to electrodep-CdTe-QDs at 0.48 V. Electrodep-CdTe-QDs appears at potential more positive of the of the oxidation of CdTe-QDs core (**Figure 5.13B (a)**), hence are catalysed by the CdTe-QDs.

### 5.3.2. CdTe-QDs- $\beta$ -NiPc(NH<sub>2</sub>)<sub>4</sub> conjugates

The peak for the oxidation of PCP is observed at 0.47 V (**Table 5.3**) on Au electrode modified with electrodeposited-CdTe-QDs- $\beta$ -NiPc(NH<sub>2</sub>)<sub>4</sub>. The PCP oxidation potential on electrodeposited-CdTe-QDs- $\beta$ -NiPc(NH<sub>2</sub>)<sub>4</sub> is at about the same potential as for electrodeposited-CdTe-QDs, but in terms of current enhancement, the latter shows slightly better activity. Adsorbed CdTe-QDs- $\beta$ -NiPc(NH<sub>2</sub>)<sub>4</sub> (**Figure 5.14B (e)**) shows improved electrocatalytic activity for PCP, due to low oxidation potential for this analyte at 0.42 V compared to the bare (0.46 V) and electrodeposited-CdTe-QDs- $\beta$ -NiPc(NH<sub>2</sub>)<sub>4</sub> (0.47 V) with very low currents. As with DCP, adsorbed CdTe-QDs- $\beta$ -NiPc(NH<sub>2</sub>)<sub>4</sub> showed the best catalytic activity in terms of potential but not currents. In terms of stability, **Table 5.3**, adsorbed-CdTe-QDs- $\beta$ -NiPc(NH<sub>2</sub>)<sub>4</sub> and electrodeposited-CdTe-QDs showed less fouling compared to other electrodes.



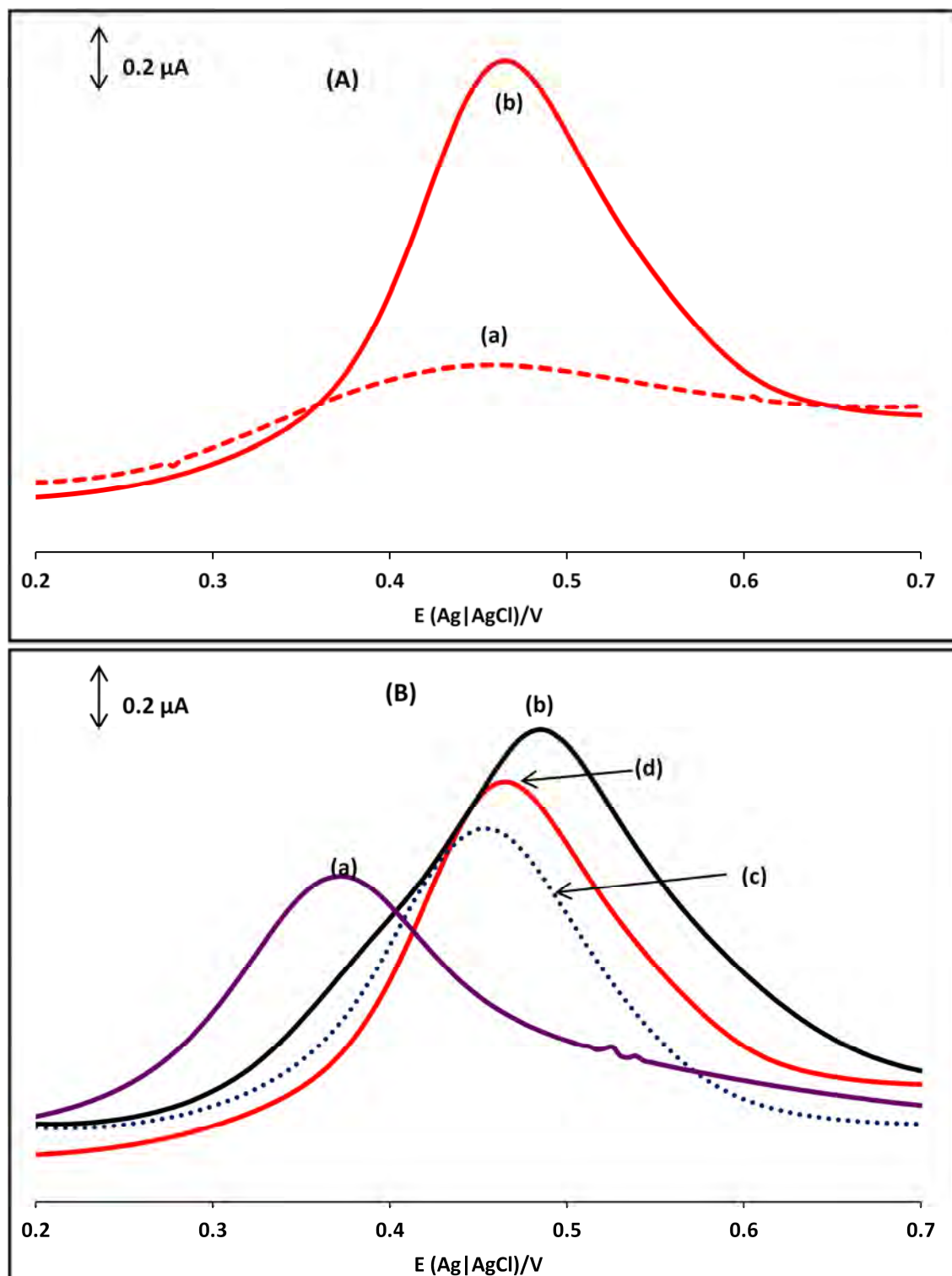


**Figure 5.13:** DPV scans for detection of 0.7 mM pentachlorophenol in pH 9.2 buffer on: (A) bare Au electrode in the absence (a) and presence (b) of 2, 4-dichlorophenol. (B) electrodeposited CdTe-QDs in the absence (a) and presence (b) of pentachlorophenol. (c) and (d) in B are DPV scans for pentachlorophenol on adsorbed CdTe-QDs and bare Au electrode respectively.

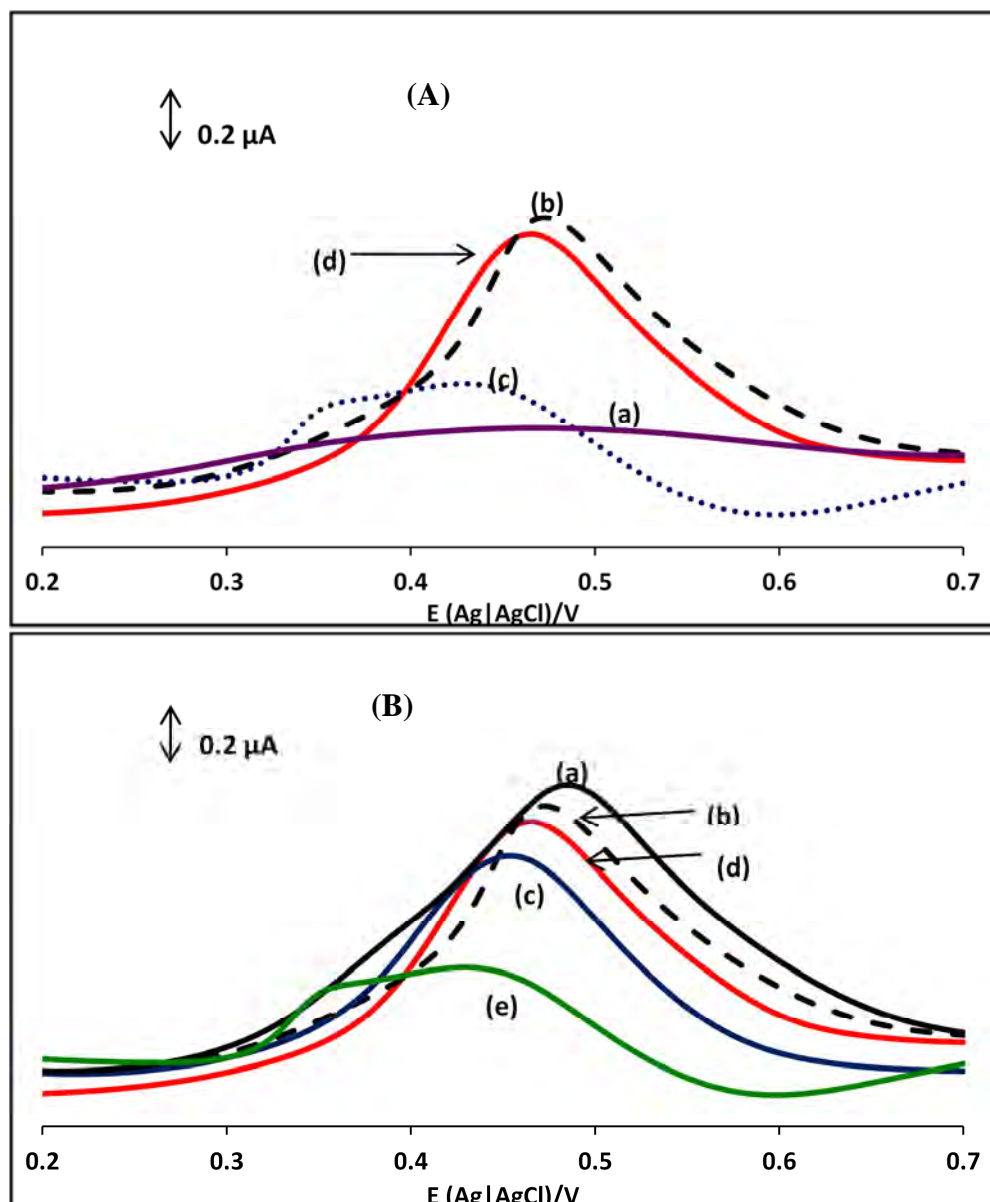


**Figure 5.14:** DPV scans for detection of  $0.7 \text{ mM}$  pentachlorophenol in pH 9.2 buffer on (A) electrodeposited  $\text{CdTe-QDs-}\beta\text{-NiPc(NH}_2)_4$  in the absence (a) and presence (b) of pentachlorophenol. (c) and (d) in (A) are DPV scans for pentachlorophenol on adsorbed  $\text{CdTe-QDs-}\beta\text{-NiPc(NH}_2)_4$  and bare Au electrode respectively. (B) An overlay of the DPV scans for the detection of pentachlorophenol on (a) electrodeposited  $\text{CdTe-QDs}$ , (b) electrodeposited  $\text{CdTe-QDs-}\beta\text{-NiPc(NH}_2)_4$ , (c) adsorbed  $\text{CdTe-QDs}$ , (d) bare Au and (e) adsorbed  $\text{CdTe-QDs-}\beta\text{-NiPc(NH}_2)_4$ .

### 5.3.3. NiPc-SWCNT-QDs conjugate

**Figure 5.15.** compares oxidation of 0.7 mM of pentachlorophenol in 0.1 M NaOH aqueous solution on GCE- $\alpha$ -NiPc(C<sub>10</sub>H<sub>21</sub>)<sub>8</sub>-SWCNT-QDs (a), GCE- $\alpha$ -NiPc(C<sub>10</sub>H<sub>21</sub>)<sub>8</sub>-SWCNT (b) and GCE- $\alpha$ -NiPc(C<sub>10</sub>H<sub>21</sub>)<sub>8</sub> (c). These studies were performed by making use of  $\alpha$ -NiPc(C<sub>10</sub>H<sub>21</sub>)<sub>8</sub> only. As explained already CdTe-QDs were adsorbed on  $\alpha$ -NiPc(C<sub>10</sub>H<sub>21</sub>)<sub>8</sub>-SWCNT and the conjugate was adsorbed on GCE. The aim was to confirm the effect of the combined nanomaterials on the catalytic behaviour of NiPc. The irreversible redox process, which corresponds to oxidation of pentachlorophenol, is observed at potentials of 0.58 V for GCE- $\alpha$ -NiPc(C<sub>10</sub>H<sub>21</sub>)<sub>8</sub>-SWCNT-QDs, 0.58 V for GCE-SWCNT, 0.51 V for GCE- $\alpha$ -NiPc(C<sub>10</sub>H<sub>21</sub>)<sub>8</sub>-SWCNT, 0.48 V for *poly*-GCE- $\alpha$ -Ni(O)Pc(C<sub>10</sub>H<sub>21</sub>)<sub>8</sub> and 0.52 V for bare GCE, **Table 5.4**. The bare GCE and GCE- $\alpha$ -NiPc(C<sub>10</sub>H<sub>21</sub>)<sub>8</sub> have similar oxidation potential values for pentachlorophenol oxidation, similarly GCE- $\alpha$ -NiPc(C<sub>10</sub>H<sub>21</sub>)<sub>8</sub>-SWCNT-QDs and GCE-SWCNT have similar oxidation potential values, which were the worst values. However, in terms of current, the GCE- $\alpha$ -NiPc(C<sub>10</sub>H<sub>21</sub>)<sub>8</sub>-SWCNT-QDs electrode gave the highest current compared to all other electrodes in **Figure 5.15**. The bare GCE and GCE-*poly*- $\alpha$ -Ni(O)Pc(C<sub>10</sub>H<sub>21</sub>)<sub>8</sub> gave the lowest current for pentachlorophenol detection. The above results suggest that the combination of SWCNT,  $\alpha$ -NiPc(C<sub>10</sub>H<sub>21</sub>)<sub>8</sub> and QDs improves the detection current.

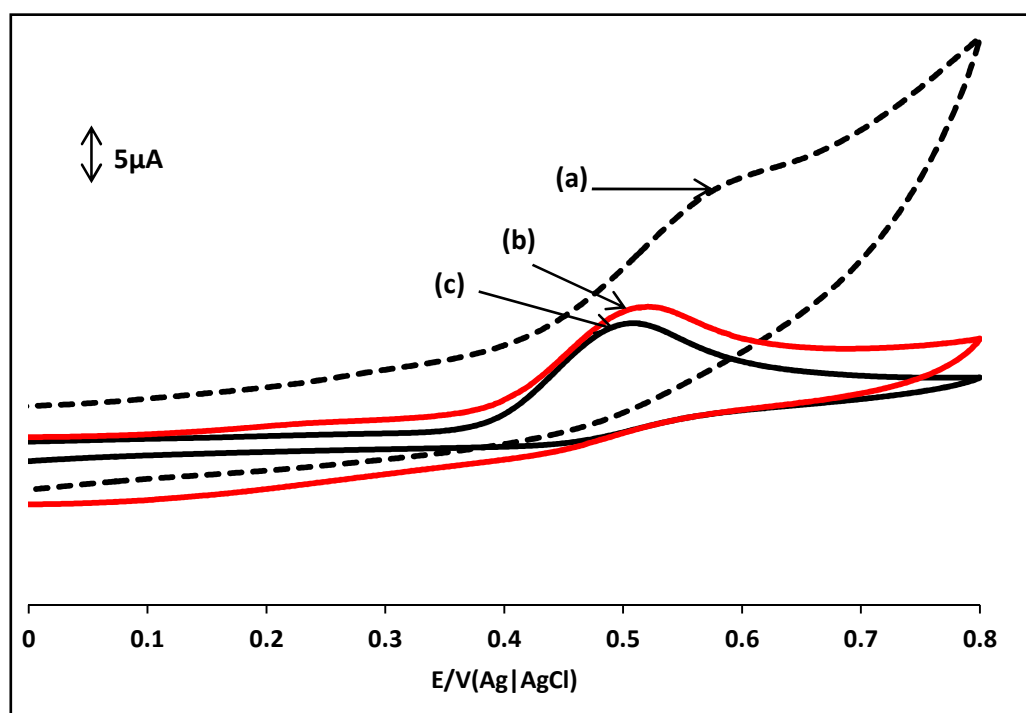


**Figure 5.15:** Oxidation of 0.7 mM of pentachlorophenol in 0.1 M NaOH aqueous solution on (a) GCE- $\alpha$ -NiPc(C<sub>10</sub>H<sub>21</sub>)<sub>8</sub>-SWCNT-QDs, (b) GCE- $\alpha$ -NiPc(C<sub>10</sub>H<sub>21</sub>)<sub>8</sub>-SWCNT and (c) *poly*-GCE- $\alpha$ -Ni(O)Pc(C<sub>10</sub>H<sub>21</sub>)<sub>8</sub>.

**Figure 5.16** shows the change in the peak current (background corrected) of pentachlorophenol with increase in the number of scans for GCE- $\alpha$ -NiPc(C<sub>10</sub>H<sub>21</sub>)<sub>8</sub>-SWCNT-QDs (a), GCE-SWCNT (b), bare GCE (c), GCE- $\alpha$ -NiPc(C<sub>10</sub>H<sub>21</sub>)<sub>8</sub>-SWCNT (d) and GCE-*poly*- $\alpha$ -Ni(O)Pc(C<sub>10</sub>H<sub>21</sub>)<sub>8</sub> (e) electrodes respectively. Electrode passivation is illustrated by a drastic decrease in current, shown **Figure 5.16** where a drop in  $I_p$  with increase in scan number is observed, indicating passivation. GCE- $\alpha$ -NiPc(C<sub>10</sub>H<sub>21</sub>)<sub>8</sub>-SWCNT-QDs stabilised at a higher current compared to the rest of the electrodes.

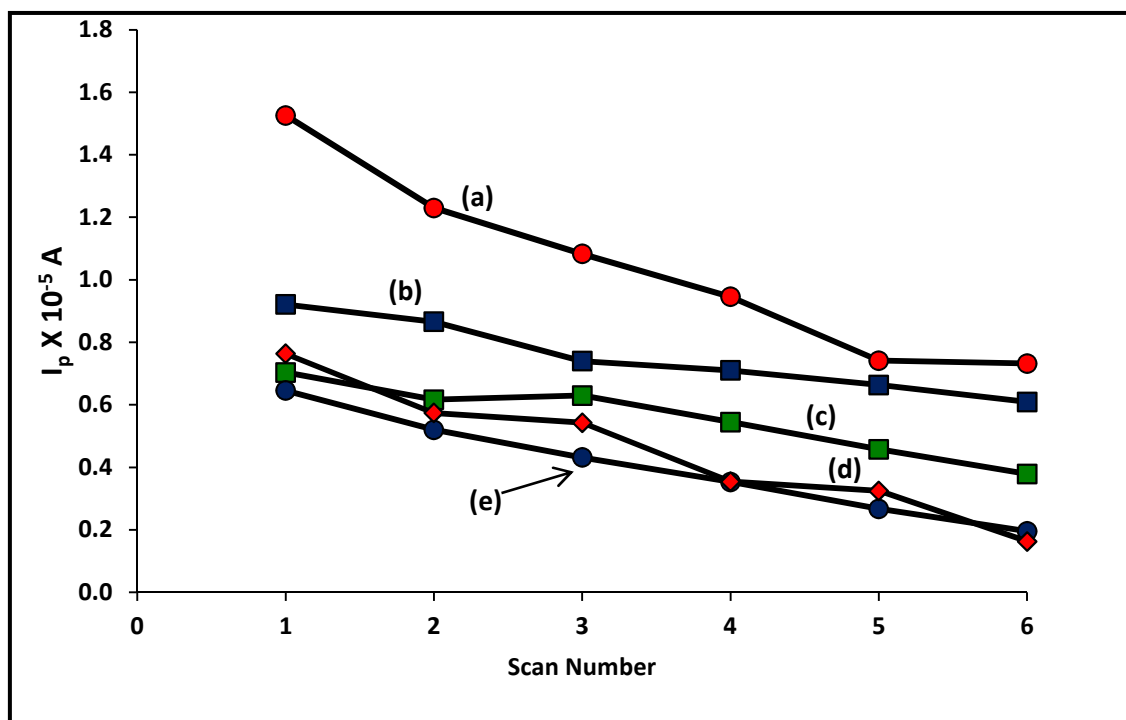


**Figure 5.16:** Plot of the change in peak current,  $I_p$ , versus cycle number for GCE- $\alpha$ -NiPc(C<sub>10</sub>H<sub>21</sub>)<sub>8</sub>-SWCNT-QDs (a), GCE-SWCNT (b), GCE bare (c), GCE- $\alpha$ -NiPc(C<sub>10</sub>H<sub>21</sub>)<sub>8</sub>-SWCNT (d) and GCE- $\alpha$ -Ni(O)Pc(C<sub>10</sub>H<sub>21</sub>)<sub>8</sub> (e) in 0.7 mM pentachlorophenol in 0.1 M NaOH.

**Table 5.4** lists the current percentage drop (after subtraction of background current) from the first scan for the electrodes studied. GCE-SWCNT gave the lowest percentage drop of 6%, followed by *poly*-GCE- $\alpha$ -Ni(O)Pc(C<sub>10</sub>H<sub>21</sub>)<sub>8</sub>, GCE-bare and GCE- $\alpha$ -NiPc(C<sub>10</sub>H<sub>21</sub>)<sub>8</sub>-SWCNT-QDs and with current percentage drop of 19 %, 12 % and 16% respectively. The highest current drop percentage was obtained for GCE- $\alpha$ -NiPc(C<sub>10</sub>H<sub>21</sub>)<sub>8</sub>-SWCNT(ads) and *poly*-GCE- $\alpha$ -Ni(O)Pc(C<sub>10</sub>H<sub>21</sub>)<sub>8</sub> electrode with percentage of 25% and 19 % respectively. Comparing GCE- $\alpha$ -NiPc(C<sub>10</sub>H<sub>21</sub>)<sub>8</sub>-SWCNT with GCE- $\alpha$ -NiPc(C<sub>10</sub>H<sub>21</sub>)<sub>8</sub>-SWCNT-QDs, the electrode stability is drastically improved upon adsorption of QDs to  $\alpha$ -NiPc(C<sub>10</sub>H<sub>21</sub>)<sub>8</sub>-SWCNT conjugate.

**Table 5.4: Peak potential for pentachlorophenol (PCP) oxidation and Current drop percentage from first scan for the detection of pentachlorophenol in 0.7 mM in 0.1M NaOH.**

Electrode	Peak potential for PCP detection	Current drop % after first scan
GCE-SWCNT	0.58	6
Bare	0.52	12
<i>Poly-GCE-<math>\alpha</math>-Ni(O)Pc(C<sub>10</sub>H<sub>21</sub>)<sub>8</sub></i>	0.48	19
GCE- $\alpha$ -NiPc(C <sub>10</sub> H <sub>21</sub> ) <sub>8</sub> -SWCNT	0.51	25
GCE- $\alpha$ -NiPc(C <sub>10</sub> H <sub>21</sub> ) <sub>8</sub> -SWCNT-QDs	0.58	16

#### 5.4. Theoretical prediction of the interaction between NiPc complexes and 4-chlorophenol.

The reactivity of  $\beta$ -NiPc(OH)<sub>4</sub> and  $\beta$ -Ni(O)Pc(OH)<sub>4</sub> electrodes towards the electrocatalytic oxidation of 4-chlorophenol is described by theoretical calculations. These calculations give information on electron transfer when the acceptor (NiPc complex) interacts with the donor (4-chlorophenol).

Optimization (**Figure 5.17**) and molecular orbital (MO) calculations of the HOMO (highest occupied MO) and LUMO (lowest unoccupied MO) of  $\beta$ -NiPc(OH)<sub>4</sub> (**Figure 5.18A**) and  $\beta$ -Ni(OH)Pc(OH)<sub>4</sub> (**Figure 5.18B**) and 4-chlorophenol (**Figure 5.19**) were obtained at the B3LYP/6-31G(d) level of calculation. Theoretical calculations of frontier MOs are known to provide information about molecular reactivity, which usually occurs in the frontier orbitals of a system [64]. The most probable reactive sites, which have a major probability to be involved in an oxidation or reduction process, are represented by the local regions where the frontier MOs are localized. It was observed that for  $\beta$ -NiPc(OH)<sub>4</sub> the frontier MO of the HOMO is localized on the ligand rather than on the nickel atom (**Figure 5.18A**), as judged by the high electron density on the ligand. This means that redox processes would occur on the ligand. Metal atom contribution to some molecular orbitals near the frontier of the system were also investigated. Nickel contribution was predicted from HOMO-1 to HOMO-2 and from LUMO+1 to LUMO+2 which both showed a strong contribution of nickel atom. The results indicate that if the complex studied were chosen for a redox process, the charge

transfer would occur between the donor (4-chlorophenol) and acceptor (NiPc) species, based mainly on the ring, but with a participation of the central metal atom.

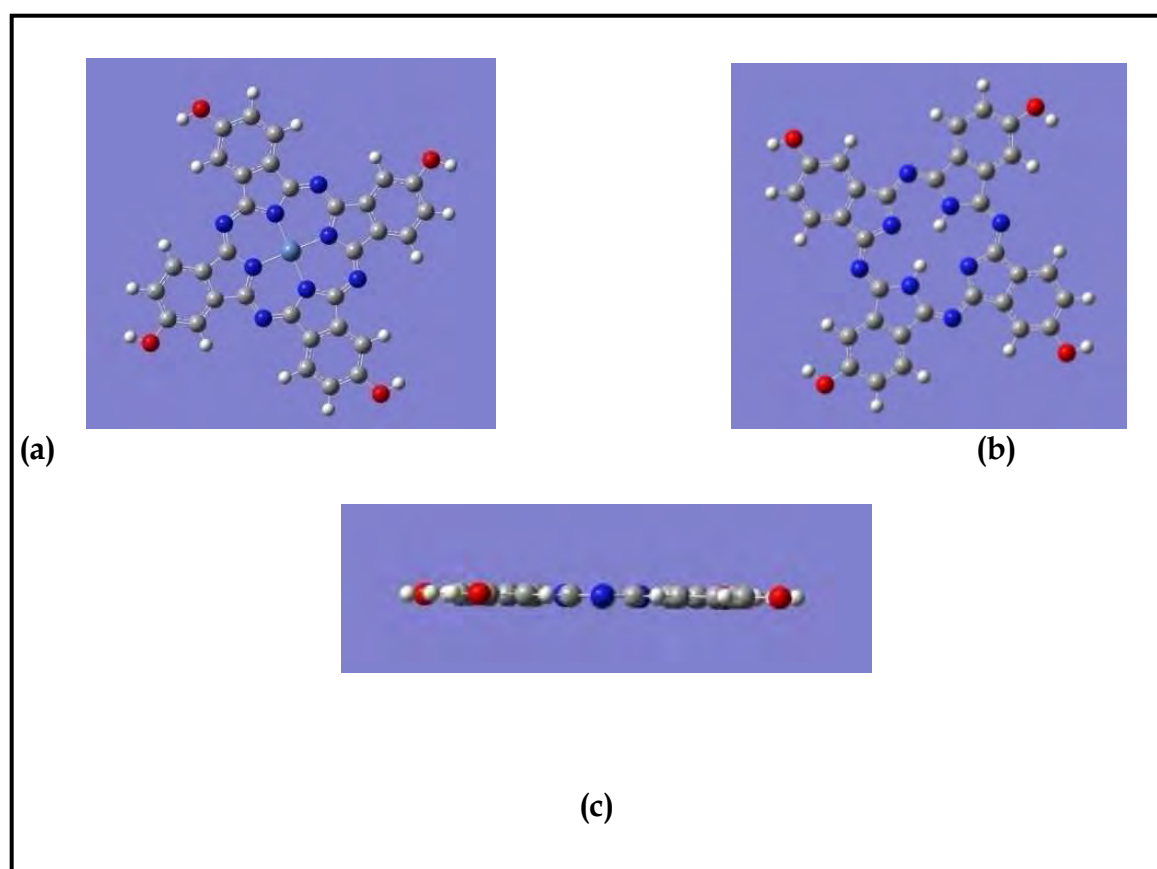


**Figure 5.17:** Fully optimized molecular structures at the B3LYP/DFT 6-31G(d) level of calculations of (a)  $\beta\text{-H}_2\text{Pc(OH)}_4$ , (b)  $\beta\text{-NiPc(OH)}_4$  and (c) side view of (b).

The absolute molecular hardness ( $\eta$ ) is defined by **Equation 5.3** [62, 285]

$$\eta = (\text{IP} - \text{EA})/2 \quad 5.3$$

where IP is the ionization potential and EA is the ionization energy. A good approximation of the EA is the lowest unoccupied molecular orbital (LUMO), the IP is approximated by highest occupied molecular orbital (HOMO).

The molecular hardness gives account of the molecular reactivity and is associated with the energy gap between the LUMO and the HOMO in a DFT framework. A higher  $\eta$  implies that a molecule has a higher ability to attract electrons, hence a good catalytic activity

towards oxidation. The concept of hardness is used in this work to explain the reactivity in electrodic reactions occurring on the OPGE modified with  $\beta$ -NiPc(OH)<sub>4</sub> and  $\beta$ -Ni(O)Pc(OH)<sub>4</sub> as redox mediators.

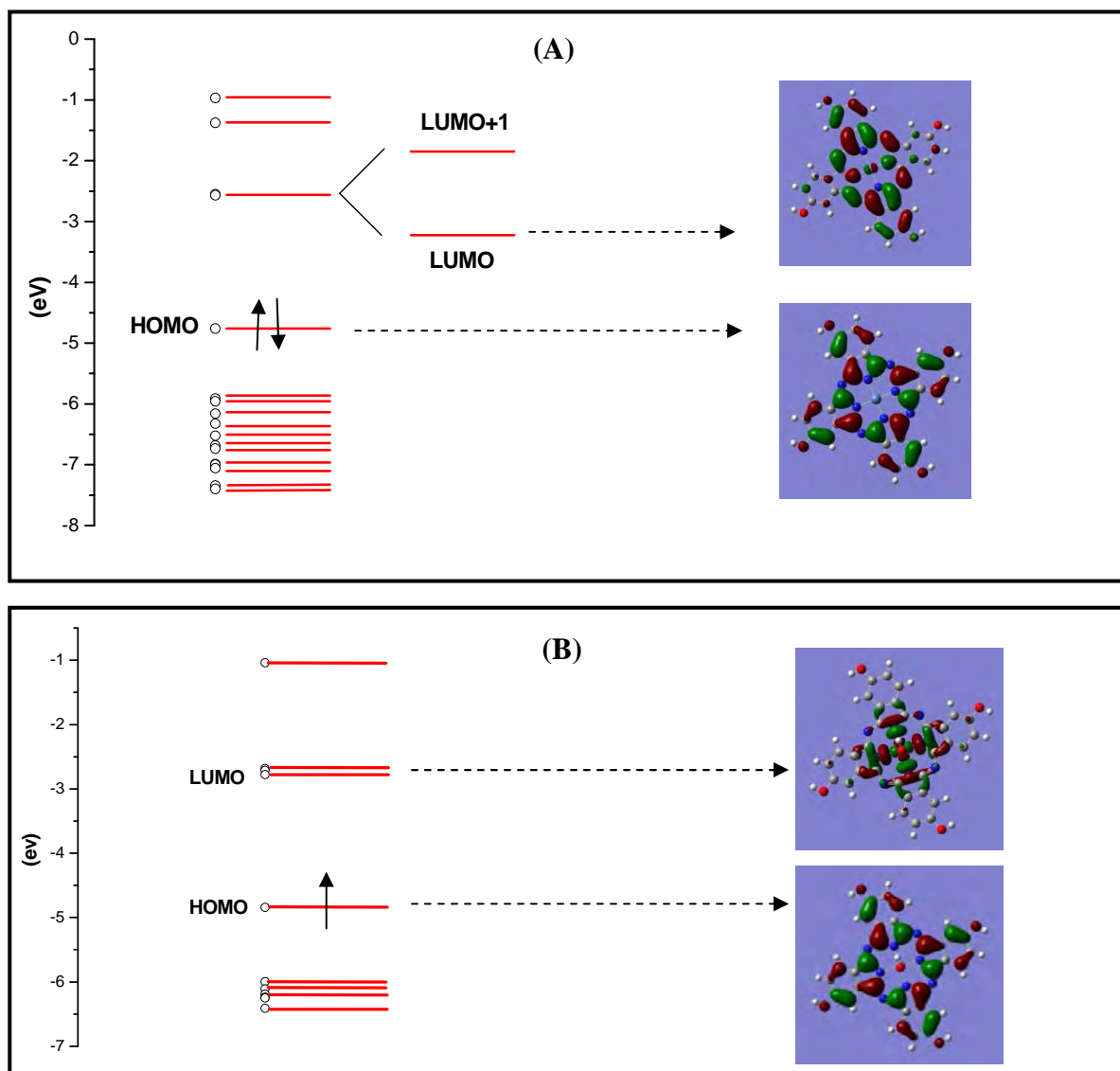
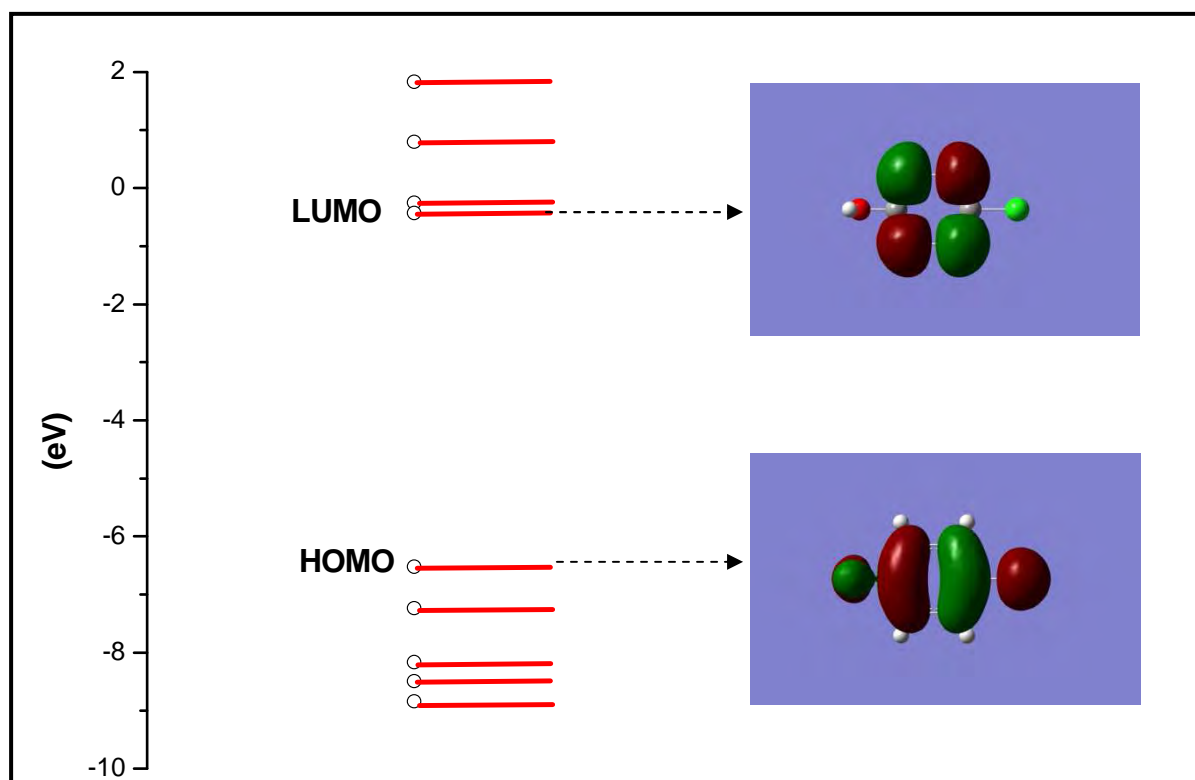


Figure 5.18: Orbital energy diagrams for  $D_{4h}$  configuration of (A)  $\beta$ -NiPc(OH)<sub>4</sub> and (B)  $\beta$ -Ni(O)Pc(OH)<sub>4</sub>.





**Figure 5.19: Orbital energy diagrams for 4-chlorophenol**

Molecular hardness calculated for  $\beta$ -NiPc(OH)<sub>4</sub> is 1.10 eV and  $\beta$ -Ni(O)Pc(OH)<sub>4</sub> is 1.03 eV (Table 5.5) compared to values ranging from 1.3 eV to 2.0 eV for similar macrocycles [66] suggesting that NiPc complexes discussed in this work have lower ability to attract electrons, due to the electron donating nature of the hydroxyl groups. Koopman's approximation [159] was used to estimate the electronic coupling of  $\beta$ -NiPc(OH)<sub>4</sub> and 4-chlorophenol by taking one half of the difference between the energy of the LUMO of  $\beta$ -NiPc(OH)<sub>4</sub> and the energy of the HOMO of 4-chlorophenol. The donor–acceptor molecular hardness ( $\eta_{DA}$ ), **Equation 5.4**

$$\eta_{DA} = (IP_D - EA_A)/2 \quad 5.4$$

where  $IP_D$  is the ionization energy of the donor and  $EA_A$  is the ionization energy of the acceptor. The smaller the  $\eta_{DA}$  value, the larger the interaction between the donor and the acceptor, and hence the smaller the energy gap between the donor HOMO and the acceptor LUMO. The calculated  $\eta_{DA}$  values for  $\beta$ -NiPc(OH)<sub>4</sub>/4-chlorophenol (1.98 eV) and for  $\beta$ -

Ni(O)Pc(OH)<sub>4</sub>/4-chlorophenol (1.87 eV) are smaller than the values reported for other macrocycles such as CoPc ( $\eta_{DA} = 2.98$  eV in the gaseous phase) for their interaction with 2-mercaptoethanol. Thus NiPc interacts better with 4-chlorophenol than CoPc does with 2-mercaptoethanol [66].

**Table 5.5: Calculated energy gaps (eV) between HOMO and LUMO and Molecular hardness( $\eta$ ) in gas phase.**

	$\beta$ -NiPc(OH) <sub>4</sub>	$\beta$ -Ni(O)Pc(OH) <sub>4</sub>
$ HOMO - LUMO $	2.19	2.06
$\eta = (E_{LUMO} - E_{HOMO})/2$	1.10	1.03
	$\beta$ -NiPc(OH) <sub>4</sub> /4-chlorophenol	$\beta$ -Ni(O)Pc(OH) <sub>4</sub> /4-chlorophenol
$\eta_{DA} = (E_{LUMO(A)} - E_{HOMO(D)})/2$	1.98	1.87

As shown by **Figures 5.18A** the LUMO of the  $\beta$ -NiPc(OH)<sub>4</sub> has substantial contributions located on the metal center, and possesses the correct symmetry to interact with the HOMO orbital of the extra planar ligand 4-chlorophenol. The lower value of  $\eta_{DA}$  for  $\beta$ -Ni(O)Pc(OH)<sub>4</sub>/4-chlorophenol compared to the value for  $\beta$ -NiPc(OH)<sub>4</sub>/4-chlorophenol, shows that the  $\beta$ -Ni(O)Pc(OH)<sub>4</sub> interacts more strongly with 4-chlorophenol, resulting in better catalytic activity in terms of increased currents compared to the former. Also compared to NiPc(OH)<sub>4</sub>, the LUMO of  $\beta$ -Ni(O)Pc(OH)<sub>4</sub> (**Figure 5.18B**) shows a substantial contribution located on the metal, therefore interaction of this HOMO with the LUMO of 4-chlorophenol is more pronounced. This confirms the cyclic voltammetry experiments which showed poly- $\beta$ -Ni(O)Pc(OH)<sub>4</sub> to be a better catalyst than adsorbed NiPc(OH)<sub>4</sub> in terms of currents. Theoretical calculations also shows that  $\beta$ -Ni(O)Pc(OH)<sub>4</sub> is paramagnetic, because there is an unpaired electron in the HOMO orbital, this implies that poly- $\beta$ -Ni(O)Pc(OH)<sub>4</sub> on the surface of the electrode is paramagnetic.

The larger electronic coupling between the donor and the acceptor results in the lowering of the activation energy which means a higher reaction rate constant and redox reactions will occur at lower potentials [65].

### Application of the Fukui function

Molecular orbital calculations together with Fukui functions, hardness and softness indices, were used to analyse the chemical interaction of  $\beta$ -NiPc(OH)<sub>4</sub> and  $\beta$ -Ni(O)Pc(OH)<sub>4</sub> with p-chlorophenol. The condensed Fukui function ( $f_{Ak}^+$ ) is used in order to further understand the electron transfer process. The theoretical calculations are compared with experimental results.

**Figure 5.20A** shows optimized structure of  $\beta$ -NiPc(OH)<sub>4</sub> and p-chlorophenol adduct. The energy levels of  $\beta$ -H<sub>2</sub>Pc(OH)<sub>4</sub>,  $\beta$ -NiPc(OH)<sub>4</sub> and  $\beta$ -Ni(O)Pc(OH)<sub>4</sub> and the interaction of the latter two with 4-chlorophenol were calculated, **Table 5.6**. The HOMO-LUMO energy gaps of  $\beta$ -H<sub>2</sub>Pc(OH)<sub>4</sub>,  $\beta$ -NiPc(OH)<sub>4</sub> and  $\beta$ -Ni(O)Pc(OH)<sub>4</sub> HOMO-LUMO gap are 2.11 eV, 2.19 eV and 2.06 eV respectively.

**Table 5.6. Calculated HOMO-LUMO energy gaps (eV) in gas phase.**

Molecules	HOMO – LUMO   (eV)
$\beta$ -H <sub>2</sub> Pc(OH) <sub>4</sub>	2.11
$\beta$ -NiPc(OH) <sub>4</sub>	2.19
$\beta$ -Ni(O)Pc(OH) <sub>4</sub>	2.06
$\beta$ -NiPc(OH) <sub>4</sub> / p-chlorophenol	2.17
$\beta$ -Ni(O)Pc(OH) <sub>4</sub> / p-chlorophenol	1.64
p-chlorophenol	6.01

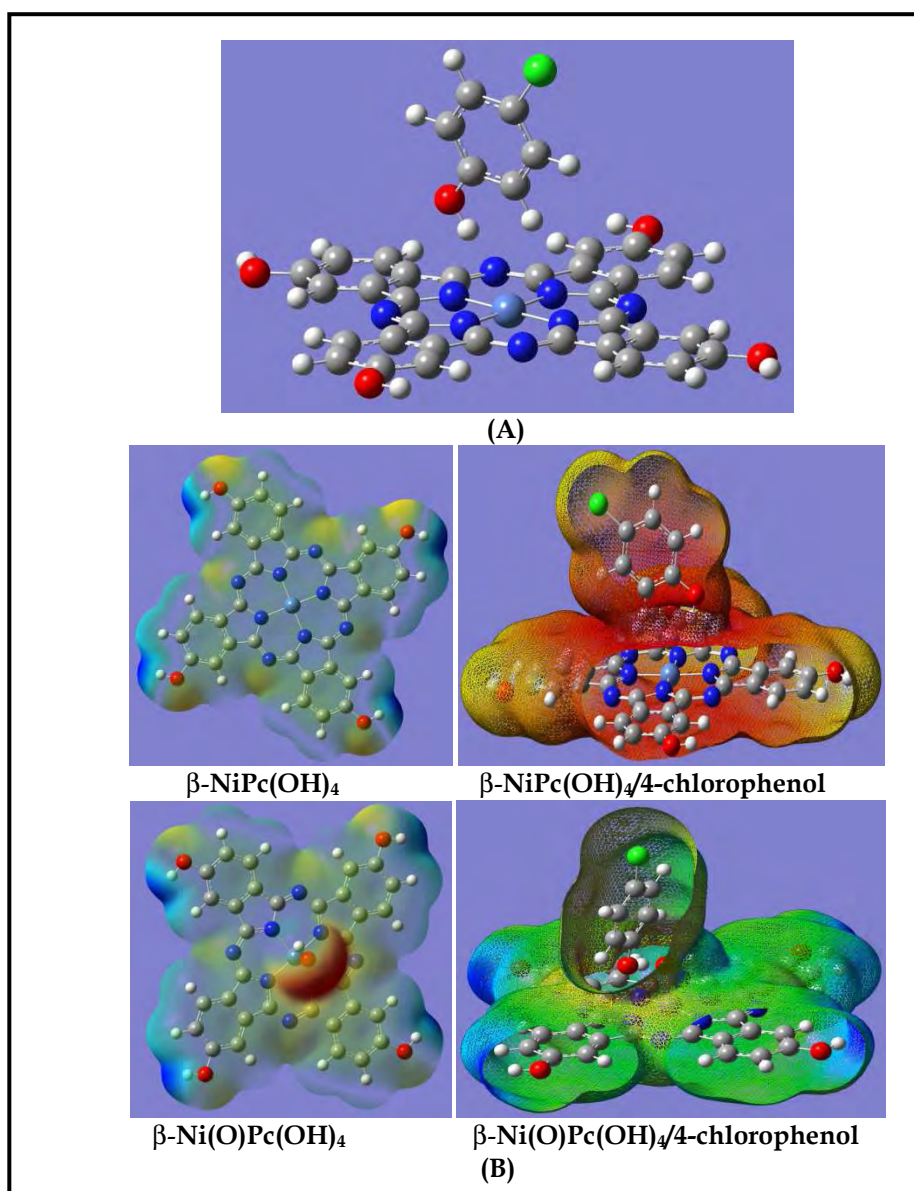


**Figure 5.20: (A) Optimised structure of  $\beta$ -NiPc(OH)<sub>4</sub> and 4-chlorophenol using B3LYP/6-3g(d). (B) Electron density distribution of  $\beta$ -NiPc(OH)<sub>4</sub> in the absence and presence of and  $\beta$ -Ni(O)Pc(OH)<sub>4</sub> in the absence and presence of 4-chlorophenol.**

The donor acceptor molecular hardness ( $\eta_{DA}$ ) factor was employed to study the interaction of 4-chlorophenol and the NiPc complexes, the result obtained suggested that the  $\beta$ -Ni(O)Pc(OH)<sub>4</sub> ( $\eta_{DA} = 1.87$  eV) interacted better with 4-chlorophenol compared to  $\beta$ -NiPc(OH)<sub>4</sub> ( $\eta_{DA} = 1.98$  eV). To further understand the interaction between 4-chlorophenol and the NiPc complexes a supramolecular approach method is used. The method gives more explicit and quantitative description of the interaction energy between the NiPc complexes and 4-chlorophenol which correlates better with experimental data. The intermolecular

interaction energy calculations were obtained using the supramolecular approach, using **Equation 5.5**

$$E_{\text{int}} = E_{\text{complex}} - \sum E_{\text{molecules}} \quad 5.5$$

where  $E_{\text{int}}$  is the interaction energy of the molecules,  $E_{\text{complex}}$  the energy of the complex (NiPc/4-chlorophenol) and  $\sum E_{\text{molecules}}$  is the sum total energy of isolated NiPc and p-chlorophenol. Interaction energy of 4-chlorophenol and NiPc complexes was calculated using DFT calculations to be -20.59 kcal/mol ( $\beta$ -NiPc(OH)<sub>4</sub>) and 19.1 kcal/mol ( $\beta$ -Ni(O)Pc(OH)<sub>4</sub>). **Figure 5.20B** shows the electron density distribution before and after the formation of the adduct. The interaction energy suggests that there is greater interaction of p-chlorophenol with  $\beta$ -NiPc(OH)<sub>4</sub> than with  $\beta$ -Ni(O)Pc(OH)<sub>4</sub>. This is evidenced by shifting of the oxidative peak towards less positive potentials for  $\beta$ -NiPc(OH)<sub>4</sub>, **Table 5.1** compared to *poly*- $\beta$ -Ni(O)Pc(OH)<sub>4</sub> in the presence of chlorophenol. The opposite was observed when we employed  $\eta_{DA}$  values. The results suggest that one has to be very careful when using molecular indices to study interaction between supramolecular complexes.

**Figure 5.21** shows that for  $\beta$ -NiPc(OH)<sub>4</sub> the frontier MO (LUMO) is localised on the ligand and partly on the Ni atom. When  $\beta$ -NiPc(OH)<sub>4</sub> interacts with p-chlorophenol (**Figure 15.21b**) the LUMO shows extensive localization of MO mainly on the Pc ligand with some on the Ni atom. For to  $\beta$ -Ni(O)Pc(OH)<sub>4</sub> in the presence p-chlorophenol (**Figure 15.21d**), there is less extensive delocalization on the Pc ring compared to when  $\beta$ -NiPc(OH)<sub>4</sub> interacts with p-chlorophenol. This suggests that for  $\beta$ -NiPc(OH)<sub>4</sub> the ring is more extensively involved in the oxidation of 4-chlorophenol when compared to  $\beta$ -Ni(O)Pc(OH)<sub>4</sub>. When adsorbed specie (without cycling or conditioning in 0.1 M NaOH) are employed for the catalytic oxidation of 4-chlorophenol, the oxidation potentials are observed at different values compared to when the electrode has been cycled in 0.1 M NaOH, suggesting that there are different catalytic sites involved. Following cycling in 0.1 M NaOH, there will be sites containing Ni<sup>III</sup>/Ni<sup>II</sup>, hence the central metal will be involved in the catalytic reaction.

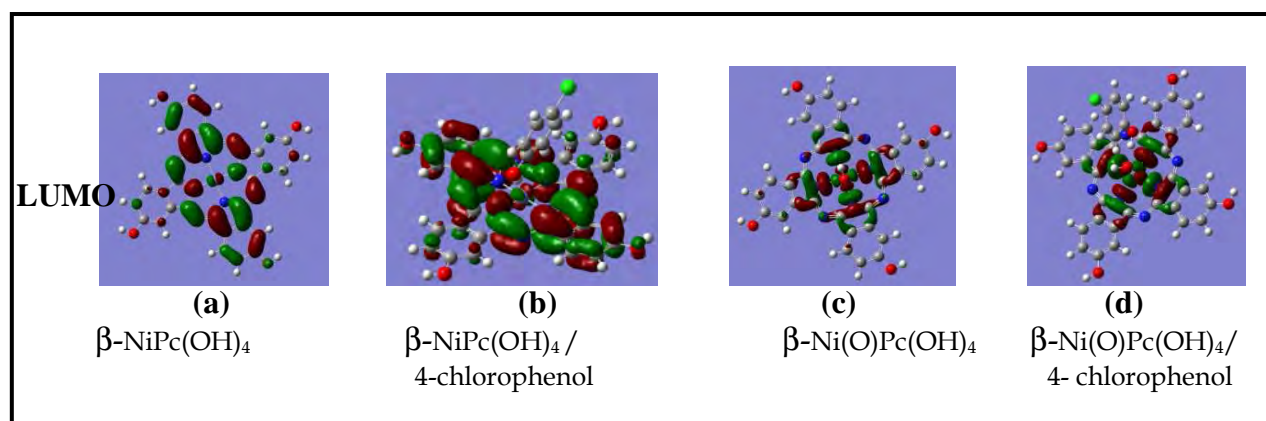
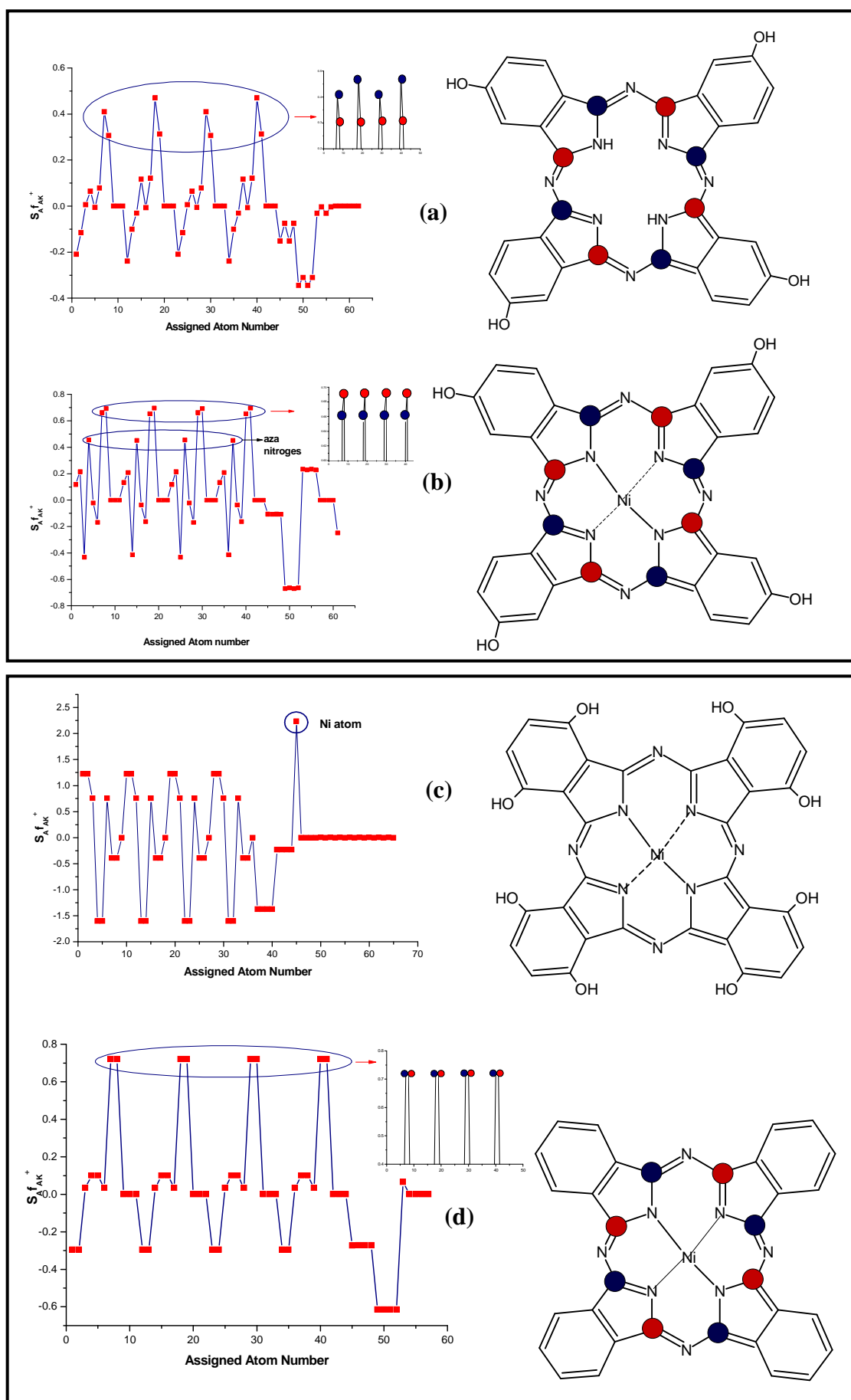


**Figure 5.21:**  $\beta$ -NiPc(OH)<sub>4</sub> (a),  $\beta$ -NiPc(OH)<sub>4</sub>/4-chlorophenol (b),  $\beta$ -Ni(O)Pc(OH)<sub>4</sub>/4-chlorophenol (c) and  $\beta$ -Ni(O)Pc(OH)<sub>4</sub> (d) frontier molecular orbitals (LUMO).

The oxidation process of p-chlorophenol is viewed as a nucleophilic attack of  $\beta$ -NiPc(OH)<sub>4</sub> by p-chlorophenol. According to **Equations 1.21-1.23** and **1.29-1.34**, in order to calculate the Fukui function and condensed Fukui function ( $f(r)$  and  $f_{Ak}^+$ ), one needs to determine the electron density of the molecule and the charges of the atoms in the molecule. In this work the Mulliken gross population analysis have been used for  $q_{AK}$ , **Equations 1.29 and 1.32** to determine the condensed Fukui function and the condensed local softness.

Tetrasubstituted phthalocyanine derivatives contain a mixture of four possible structural isomers, with the position of the substituents being at 2(3), 9(10), 16(17) and 23(24) for the peripherally substituted derivatives and at 1(4), 6(11), 15(18) and 22(25) for non-peripherally substituted derivatives (see numbering in **Figure 5.22 (f)**). However for the purposes of the current calculations, the substituents have been fixed to one position on each benzene group. **Figure 5.22(a–e)** gives a clearer picture of what is actually happening to the carbons attached to nitrogens when  $\beta$ -H<sub>2</sub>Pc(OH)<sub>4</sub> is metallated. Comparing **Figure 5.22a** and **b**, shows the condensed local softness (less reactive) values for carbons at 5,12,19,26 (red region) lie below the ones at 7,14,21,28 (blue regions), for unmetallated  $\beta$ -H<sub>2</sub>Pc(OH)<sub>4</sub>, (**Figure 5.22a**). Upon metallation (**Figure 5.22b**) the condensed local softness values for carbons at 5,12,19,26 (red region) have increased (more reactive) to a point where they have surpassed the values for carbons at 7,14,21,28 (blue regions).

**Figure 5.22a** and **b** suggest that when Ni is inserted into the ring, the carbon atoms at 5,12,19,26 (red region) are activated differently compared to unmetallated. The 5,12,19,26 (red region) carbons are situated on the side where the OH is substituted and show greater local softness (hence greater reactivity). The carbons at 7,14,21,28 (blue regions) are situated on the side where there are no OH substituents and have lower local softness values (less reactive compared to 5,12,19,26 carbons). This suggests that even though the OH substituents have no effect on the bond length between the Ni atom and the N, it has some destabilization effect on the 5,12,19,26 carbons for  $\beta$ -NiPc(OH)<sub>4</sub>. **Figure 5.22**, shows that for unsubstituted NiPc all the carbons are activated equally compared to  $\beta$ -NiPc(OH)<sub>4</sub>. **Figure 5.22c** suggest that, for  $\alpha$ -NiPc(OH)<sub>8</sub>, the Ni atom is made softer or more reactive relative to all other atoms. The Fukui plots of  $\alpha$ -NiPc(OH)<sub>8</sub> suggests that if this complex were to be used for electrocatalytic oxidation of p-chlorophenol, catalysis through the nickel atom would be favoured over the ring. **Figure 5.22e** show the Fukui plots of  $\alpha$ -NiPc(OH)<sub>4</sub>, showing that only the carbons are activated. It is observed experimentally that  $\alpha$ -NiPc(OH)<sub>4</sub> and  $\alpha$ -NiPc(OH)<sub>8</sub> shows the bad catalytic activity towards the oxidation of 4-chlorophenol compared to  $\beta$ -NiPc(OH)<sub>4</sub> in terms of catalytic currents.





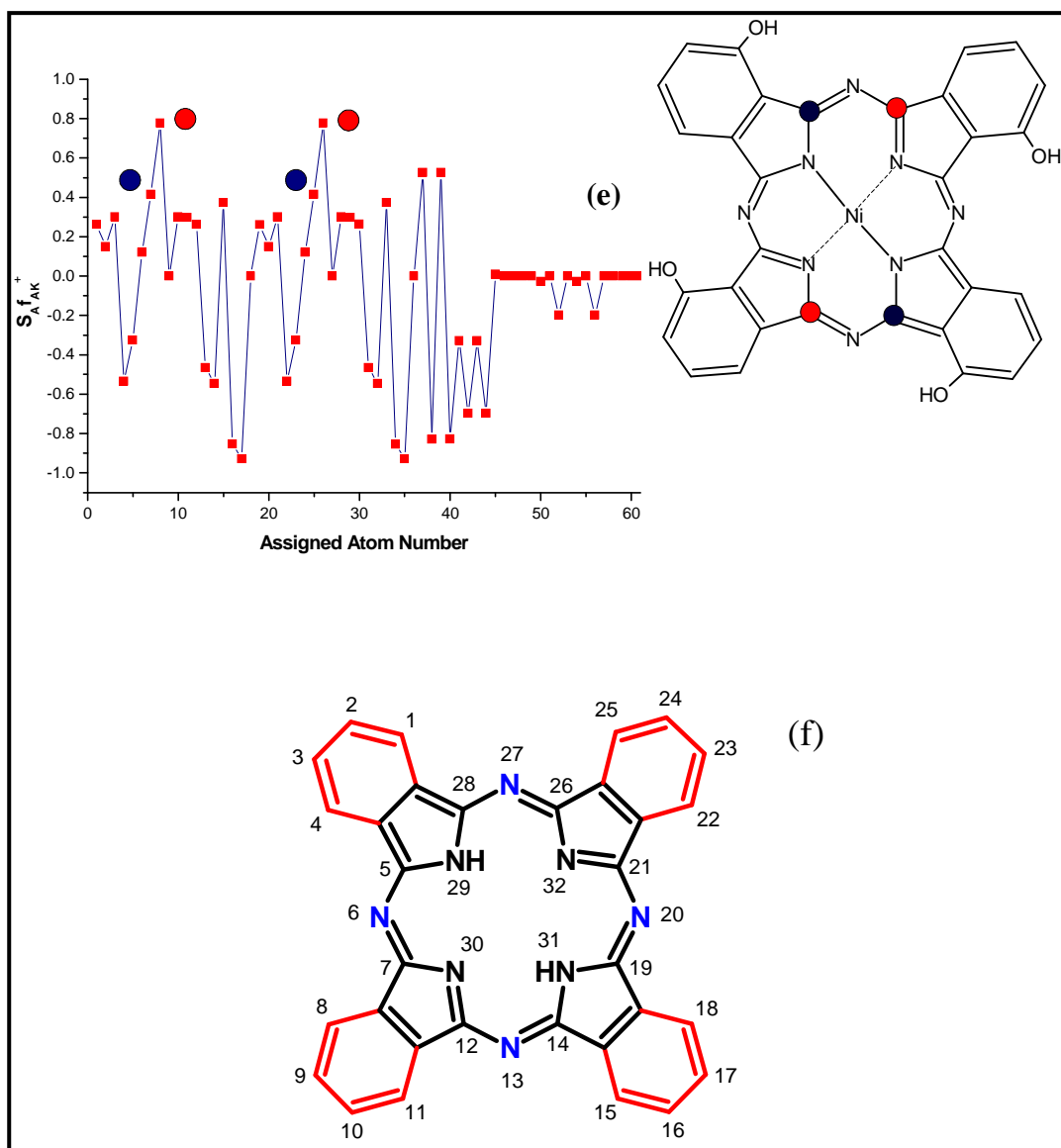


**Figure 5.22: Fukui 2D plots of condensed softness for maximum softness,  $\beta$ - $H_2Pc(OH)_4$  (a),  $\beta$ - $NiPc(OH)_4$  (b),  $\alpha$ - $NiPc(OH)_8$  (c),  $NiPc$  (d), and  $\alpha$ - $NiPc(OH)_4$  (e), (f) shows the atomic numbering in the phthalocyanine molecule which is used for describing peripheral and non-peripheral positions.**

# **Chapter 6**

## **Conclusions**

### 6.1. General Conclusion

In conclusion this work has shown that FTIR and Raman spectra of NiPc complexes can be predicted accurately using DFT calculations. We have also shown that both  $\beta$ -NiPc(OH)<sub>4</sub>, adsorbed on an OPGE electrode, its polymerization product *poly*- $\beta$ -Ni(O)Pc(OH)<sub>4</sub> (forming Ni-O-Ni bridges), show catalytic activity towards the oxidation of 4-chlorophenol. Electrocatalysis is characterized by a shift of potential to lower values and/or increase in current with respect to an unmodified electrode.  $\beta$ -NiPc(OH)<sub>4</sub> shows lowering in oxidation potentials while *poly*- $\beta$ -Ni(O)Pc(OH)<sub>4</sub> shows enhanced currents compared to unmodified OPGE. DFT calculations show the *poly*- $\beta$ -Ni(O)Pc(OH)<sub>4</sub> to be paramagnetic. Using donor acceptor molecular hardness ( $\eta_{DA}$ ) values, we have shown that both complexes interact strongly with 4-chlorophenol, with the  $\beta$ -Ni(O)Pc(OH)<sub>4</sub> showing a larger interaction hence a better catalytic activity towards the oxidation of 4-chlorophenol, hence the larger catalytic currents.

This work has shown that fused benzene rings at the  $\alpha$ , and  $\beta$  positions of SubPcs enabled the successful separation and characterization of one of the diastereomers and enantiomers for the first time in the chemistry of inherently chiral SubPcs. Electronic absorption and MCD measurements, in addition to theoretical calculations, reveal that the annelation of the benzene rings causes minor alterations in the energy levels of the HOMO, LUMO, and LUMO+1, but major changes in the HOMO-3, which leads to the appearance of characteristic bands in the Soret band region. The CD spectra of chiral SubNPcs exhibited similar shapes to those of the absorption spectra apart from their signs.

NiPc derivatives: OPGE-*poly*- $\alpha$ -Ni(O)Pc(OH)<sub>4</sub>, OPGE-*poly*- $\alpha$ -Ni(O)Pc(OH)<sub>8</sub> and OPGE-*poly*- $\beta$ -Ni(O)Pc(OH)<sub>4</sub> and their adsorbed counterparts (OPGE- $\alpha$ -NiPc(OH)<sub>4</sub>, OPGE- $\alpha$ -NiPc(OH)<sub>8</sub> and OPGE- $\beta$ -NiPc(OH)<sub>4</sub>) were studied for their catalytic activity towards the oxidation of 4-chlorophenol. In terms of electrocatalytic activity, OPGE-*poly*- $\alpha$ -Ni(O)Pc(OH)<sub>4</sub> and OPGE-*poly*- $\alpha$ -Ni(O)Pc(OH)<sub>8</sub>, showed evidence for the involvement of the Ni<sup>III</sup>/Ni<sup>II</sup> couple in the oxidation of 4-chlorophenol, but the catalytic currents were less than those of the bare OPGE. OPGE-*poly*- $\beta$ -Ni(O)Pc(OH)<sub>4</sub> showed higher currents than the bare OPGE showing good electrocatalytic activity compared to for OPGE-*poly*- $\alpha$ -Ni(O)Pc(OH)<sub>4</sub> and OPGE-*poly*- $\alpha$ -Ni(O)Pc(OH)<sub>8</sub>. Interaction energy values suggest that p-chlorophenol interacts better with  $\beta$ -NiPc(OH)<sub>4</sub> than *poly*- $\beta$ -Ni(O)Pc(OH)<sub>4</sub>, hence the former is a better

catalyst in terms of lowering of overpotential. We have used the condensed Fukui function to determine the reactive sites where electron transfer would take place between 4-chlorophenol and the nickel phthalocyanine complexes.

CdTe-QDs and CdTe-QDs- $\beta$ -NiPc(NH<sub>2</sub>)<sub>4</sub> conjugate were synthesised and characterised. Fluorescence lifetime studies showed the QDs remain intact within the CdTe-QDs- $\beta$ -NiPc(NH<sub>2</sub>)<sub>4</sub> conjugate. Thus the conjugates of the two have potential for use in electrocatalysis with CdTe-QDs remaining intact.

The work demonstrates that CdTe-QDs can be stabilised against electrochemical oxidation, to some extent, by linking them with  $\beta$ -NiPc(NH<sub>2</sub>)<sub>4</sub> molecules. The work further demonstrate that oxidation products of CdTe-QDs adsorbed on Au electrode can be used to electrochemically detect chlorophenols. When electrodeposited-CdTe-QDs and electrodeposited-CdTe-QDs- $\beta$ -NiPc(NH<sub>2</sub>)<sub>4</sub> electrodes were used for electrocatalysis of 2, 4-dichlorophenol and pentachlorophenol, larger currents were observed on electrodeposited-CdTe-QDs than on electrodeposited-CdTe-QDs- $\beta$ -NiPc(NH<sub>2</sub>)<sub>4</sub> electrode. Electrodeposited-CdTe-QDs and electrodeposited-CdTe-QDs- $\beta$ -NiPc(NH<sub>2</sub>)<sub>4</sub> showed the best performance with respect to currents and ads-CdTe-QDs- $\beta$ -NiPc(NH<sub>2</sub>)<sub>4</sub> gave the best response in terms of potential. This study shows that when CdTe-QDs are employed for electrocatalysis, the electrodeposited form performs better in terms of currents (hence sensitivity) compared to simple adsorption which is often employed in electrocatalysis.

This work has shown that GCE electrode modified with  $\beta$ -NiPc(NH<sub>2</sub>)<sub>4</sub>-SWCNT(linked),  $\beta$ -NiPc(NH<sub>2</sub>)<sub>4</sub>-SWCNT,  $\beta$ -NiPc(OH)<sub>4</sub>-SWCNT,  $\alpha$ -NiPc(OH)<sub>4</sub>-SWCNT and  $\alpha$ -NiPc(OH)<sub>8</sub>-SWCNT exhibit electrocatalytic activity towards the oxidation of 4-chlorophenol. The study demonstrates that in general SWCNT improves the electrocatalytic activity of NiPc complexes, when adsorbed on SWCNT. SWCNT improves the resistance to electrode fouling when used in conjunction with NiPc complexes. Catalytic activity of NiPc adsorbed on SWCNT is affected by substitution of electron donating substituents at the  $\alpha$  or  $\beta$  position.

$\alpha$ -NiPc(C<sub>10</sub>H<sub>21</sub>)<sub>8</sub> was synthesised and characterised. The complex was adsorbed on SWCNT and fully characterised the conjugate with UV/Vis, IR and Raman spectroscopies, as well as AFM and TEM. The  $\alpha$ -NiPc(C<sub>10</sub>H<sub>21</sub>)<sub>8</sub>-SWCNT film was used to modify GCE for electrocatalysis of 4-chlorophenol and 2,4-dichlorophenol and stability of the electrode studied. GCE- $\alpha$ -NiPc(C<sub>10</sub>H<sub>21</sub>)<sub>8</sub>-SWCNT showed the best response, in terms of current, towards 4-chlorophenol and 2, 4-dichlorophenol compared to the absence of SWCNT. Electrocatalytic activity for  $\alpha$ -NiPc(C<sub>10</sub>H<sub>21</sub>)<sub>8</sub> is improved in the presence of SWCNT, showing the favourable effects of the substituents.

$\alpha$ -NiPc(C<sub>10</sub>H<sub>21</sub>)<sub>8</sub> and CdTe-QDs were adsorbed on SWCNT and fully characterised the conjugate with XRD, IR and Raman spectroscopies. The  $\alpha$ -NiPc(C<sub>10</sub>H<sub>21</sub>)<sub>8</sub>-SWCNT-QDs conjugate film was used to modify GCE for electrocatalysis of pentachlorophenol and stability of the electrode studied.  $\alpha$ -NiPc(C<sub>10</sub>H<sub>21</sub>)<sub>8</sub>-SWCNT-QDs electrode showed the best response, in terms of current, towards pentachlorophenol compared to SWCNT,  $\alpha$ -NiPc(C<sub>10</sub>H<sub>21</sub>)<sub>8</sub>-SWCNT,  $\alpha$ -NiPc(C<sub>10</sub>H<sub>21</sub>)<sub>8</sub> and *poly*-Ni(O)Pc(C<sub>10</sub>H<sub>21</sub>)<sub>8</sub> electrode.  $\alpha$ -NiPc(C<sub>10</sub>H<sub>21</sub>)<sub>8</sub>-SWCNT-QDs showed better stability from the first scan to the second scan in pentachlorophenol.

### References:

1. K. C. Honeychurch, L. Gilbert, J. P. Hart, *Anal. Bioanal. Chem.* 2010, **396**, 3103.
2. R. Bonnett, in *Chemical Aspects of Photodynamic Therapy*, D. Phillips (Ed.), Gordon and Breach Science, Canada, 2000.
3. C. J. Walsh, B. K. Mandal, *J. Mater.* 2000, **12**, 287.
4. S. Vilakazi, T. Nyokong, *Polyhedron*, 2000, **19**, 229.
5. K. Morishige, S. Tomoyasu, G. Iwani, *Langmuir*, 1997, **3**, 5184.
6. H. Eichhorn, *J. Porphy. Phthalocya.* 2000, **4**, 88.
7. R. P. Linstead, *J. Chem. Soc.* 1934, 1016.
8. C. G. Claessens, D. González-Rodríguez, T. Torres, *Chem. Rev.* 2002, **102**, 835.
9. A. Meller, A. Ossoko, *Monatsh. Chem.* 1972, **103**, 150.
10. H. Kietai, *Monatsh. Chem.* 1972, **105**, 405.
11. C. G. Claessens, D. González-Rodríguez, T. Torres, G. Martin, F. Agullo-Lopez, I. Ledoux, J. Zyss, V. R. Ferro, J. M. G. de la Vega, *J. Phys. Chem. B* 2005, **109**, 3800.
12. D. Dini, S. Vagin, M. Hanack, V. Amendola, M. Meneghetti, *Chem. Commun.* 2005, 3796.
13. A. S. Medina, C. G. Claessens, G. M. A. Rahman, A. M. Lamsabhi, O. Mo, M. Yanez, D. M. Guldi, T. Torres, *Chem. Commun.* 2008, 1759.
14. M. S. Rodriguez-Morgade, C. G. Claessens, A. Medina, D. González-Rodríguez, E. Gutierrez-Puebla, A. Monge, I. Alkorta, J. Elguero, T. Torres, *Chem.-Eur. J.* 2008, **14**, 1342.
15. H. Xu, D. K. P. Ng, *Inorg. Chem.* 2008, **47**, 7921.
16. Z. X. Zhao, A. N. Cammidge, M. J. Cook, *Chem. Commun.* 2009, 7530.
17. G. E. Morse, A. S. Paton, A. Lough, T. P. Bender, *Dalton. Trans.* 2010, **39**, 3915
18. H. Gommans, T. Aernouts, B. Verreet, P. Heremans, A. Madina, C. G. Claessens, T. Torres, *Adv. Funct. Mater.* 2009, **19**, 3435.
19. B. Verreet, S. Schols, D. Cheyns, B. P. Rand, H. Gommans, T. Aernouts, P. Heremans, J. Genoe, *J. Mater. Chem.* 2009, **19**, 5295.
20. G. L. Pakhomov, V.V. Travkin, A. Y. Bogdanova, T. F. Guo, *J. Porphyrins Phthalocyanines* 2008, **12**, 1182.
21. Y. Rio, P. Vazquez, E. Palomares, *J. Porphyrins Phthalocyanines* 2009, **13**, 645.
22. C. C. Matheus, W. Michaelis, C. Kelting, W. S. Durfee, D. Wöhrle, D. Schlettwein, *D. Synthetic. Met.* 2004, **146**, 335.

## References

---

23. R. S. Iglesias, C. G. Claessens, G. M. A. Rahman, M. A. Herranz, D. M. Guldi, T. Torres, *Tetrahedron*, 2007, **63**, 12396.
24. M. E. E-Khouly, S. H. Shim, Y. Araki, O. Ito, K. Y. Kay, *Phys. Chem. B* 2008, **112**, 3910.
25. C. G. Claessens, T. Torres, *J. Am. Chem. Soc.* 2002, **124**, 14522.
26. S. Shimizu, S. Nakano, T. Hosoya, N. Kobayashi, *Chem. Commun.* 2011, **47**, 316.
27. J. G. Young, W. Onyebuagu, *J. Org. Chem.* 1990, **55**, 2155.
28. V. M. Vlasov, *Russ. Chem. Rev.* 2003, **72**, 681.
29. R. D. George, A. W. Snow, *J. Heterocyclic Chem.* 1995, **32**, 495.
30. D. Wöhrle, M. Eskes, K. Shigehara, A. Yamada, *Synthesis* 1993, 194.
31. M. J. Cook, N. B. McKeown, I. Chambrier, *J. Chem. Soc. Perkin Trans. I*, 1990, 1169.
32. M. J. Cook, I. Chambrier, S. J. Cracknell, D. A. Mayes, D. A. Russell, *Photochem. Photobiol.* 1995, **62**, 542.
33. F. Nekelson, Novel oligomeric phthalocyanines and new synthesis of tetrabenzotriazaporphyrin, University of East Anglia, 2005, thesis
34. P. M. Burnham, M. J. Cook, L. A. Gerrard, M. J. Heeney, D. L. Hughes *Chem. Comm.* 2003, 2064.
35. A. Suzuki, *Synth. Commun.* 1981, **11**, 513.
36. E. I. Negishi, A. O. King, N. Okukado, *J. Org. Chem.* 1977, **42**, 1821.
37. P. Knochel, R. D. Singer, *Chem. Rev.* 1993, **93**, 2117.
38. P. Knochel, J. J. A. Perea, P. Jones, *Tetrahedron* 1998, **54**, 8275.
39. B. N. Achar, P. K. Jayasree, *Synthetic Metals* 1999, **104**, 101.
40. M. P. Somashekarapa, J. Keshavayya, *Synth. React. Inorg. Met.-Org. Chem.* 2001, **31**, 811.
41. G. P. Shaposhnikov, V. E. Maizlish, V. P. Kulinich, *Russian Journal of general chemistry.* 2005, **75**, 1830.
42. A. V. Ivanov, P. A. Svinareva, L. G. Tomilova, N. S. Zefirov, *Russian Chemical Bulletin (Translation of Izvestiya Akademii Nauk, Seriya Khimicheskaya).* 2003, **52**, 1562.
43. M. Hanack, M. Geyer, *J. Chem. Soc. Chem. Commun.* 1994, 2253.
44. G. C. Claessens, T. Torres, *Eur. J. Org. Chem.* 2000, 1603.
45. G. C. Claessens, T. Torres, *Tetrahedron Lett.* 2000, **41**, 6361.
46. N. Kobayashi, T. Nonomura, *Tetrahedron Lett.* 2002, **43**, 4253.

## References

---

47. M. Hanack, J. Rauschnabel, *Tetrahedron Lett.* 1995, **36**, 1629.
48. M. Geyer, F. Plenzig, J. Rauschnabel, M. Hanack, B. del Rey, A. Sastre, T. Torres, *Synthesis* 1996, 1139.
49. J. R. Stork, R. J. Potucek, W. S. Durfee, B. C. Noll, *Tetrahedron Lett.* 1999, **40**, 8055.
50. C. D. Zyskowski, V. O. Kennedy, *J. Porphyrins Phthalocyanines* 2000, **4**, 707.
51. N. Kobayashi, T. Ishizaki, K. Ishii, H. Konami, *J. Am. Chem. Soc.* 1999, **121**, 9096.
52. N., Kobayashi, R. Kondo, S.-I. Nakajima, T. Osa, *J. Am. Chem. Soc.* 1990, **112**, 9640.
53. Y. Wang, D. Gu, F. Gan, *Opt. Commun.* 2000, **183**, 445.
54. S. V. Kudrevich, S. Gilbert, J. E. van Lier, *J. Org. Chem.* 1996, **61**, 5706.
55. B. del Rey, M.-V. Martinez-Diaz, J. Barbera', T. Torres, *J. Porphyrins Phthalocyanines* 2000, **4**, 569.
56. M. V. Marti'nez-Di'az, B. del Rey, T. Torres, Agricola, B. C. Mingotaud, N. Cu villier, G. Rojo, F. Agullo'-Lopez, *J. Mater. Chem.* 1999, **9**, 1521.
57. M. J. Cook, A. N. Dunn, S. D. Howe, A. J. Thompson, K. J. Harrison, *J. Chem. Soc. Perkin Trans. I*, 1988, 2453.
58. D. W. Clack, M. Monshi, *Inorg. Chim Acta* 1977, **22**, 261.
59. E. Orti, J. L. Bredas, *J. Am. Chem. Soc.* 1992, **114**, 8669.
60. A. Ghosh, P. G. Gassman, J. Almlof, *J. Am. Chem. Soc.* 1994, **116**, 1932.
61. M.-S. Liao, S. Scheiner, *J. Chem. Phys.* 2001, **114**, 9780.
62. C. Berrios, G. I. Cardenas-Jiron, J. F. Marco, C. Gutierrez, M. S. Ureta- Zañartu, *J. Phys. Chem. A* 2007, **111**, 2706.
63. X. Cai, N. Sheng, Y. Zhang, D. Qi, J. Jiang, *Spectrochim. Acta* 2009, **A 72**.
64. J. H. Zagal, G. I. Cardenas-Jiron, *J. Electroanal. Chem.* 2000, **489**, 96.
65. I. Ciofini, F. Bedioui, J. H. Zagal, C. Adamo, *Chem. Phys. Lett.* 2003, **376**, 690.
66. S. Griveau, F. Bedioui, C. Adamo, *J. Phys. Chem.* 2001, **105**, 11304.
67. M. J. Pelletier, *Analytical Applications of Raman Spectroscopy*, Michigan, USA, 1999.
68. J. Popp, W. Kiefer, *Encyclopedia of Analytical Chemistry: Applications, Theory and Instrumentation*, (Eds) R. A. Meyer, John Wiley & Sons, New York, 2000, Vol. 15.
69. T. Kobayashi, Y. Fujiyoshi, N. Uyeda, *Acta Cryst.* 1982, **A38**, 356.
70. G. Dent, F. Farrell, *Spectrochim. Acta A*, 1997, **53**, 21.
71. D. R. Tackley, G. Dent, W. E. Smith, *Phys. Chem. Chem. Phys.* 2001, **3**, 1419.
72. D. R. Tackley, G. Dent, W. E. Smith, *Phys. Chem. Chem. Phys.* 2000, **2**, 3949.



## References

---

73. Z. Liu, Z.-X. Chen, B. Jin, X. Zhang, *Vibrational Spectroscopy* 2011, **56**, 210.
74. T. V. Basova, V. G. Kiselev, B.-E. Schuster, H. Peisert, T. Chasse, *J. Raman Spectrosc.* 2009, **40**, 2080.
75. Z. Liu, X. Zhang, Y. Zhang, J. Jiang, *Spectrochimica Acta Part A* 2007, **67**, 1232.
76. T. Basova, F. Latteyer, D. Atilla, A. G. Gurek, A. Hassan, V. Ahsen, H. Peisert, T. Chasse, *Thin Solid Film* 2010, **518**, 5745.
77. N. Kobayashi, *J. Chem. Soc, Chem. Commun.* 1991, 1203.
78. N. Kobayashi, *J. Porphyrins Phthalocyanines* 1999, **3**, 453.
79. P. J. Stephens, *Adv. Chem. Phys.* 1976, **35**, 197.
80. J. Mack, M.J. Stillman, N. Kobayashi, *Coord. Chem. Rev.* 2007, **251**, 429.
81. S. Higashibayashi, H. Sakurai, *J. Am. Chem. Soc.* 2008, **130**, 8592.
82. C. Thilgen, F. Diederich, *Chem. Rev.* 2006, **106**, 5049.
83. G. Dukovic, M. Balaz, P. Doak, N. D. Berova, M. Zheng, R. S. Mclean, L. E. Brus, *J. Am. Chem. Soc.* 2006, **128**, 9004.
84. R. K. Smith, P. A. Lewis, P. S Weiss, *Prog. Surf. Sci.* **2004**, 75, 1.
85. I. Chambrier, M.J. Cook, D.A. Russell, *Synthesis*, 1995, 1283.
86. T. R. E. Simpson, D. J. Revell, M.J. Cook, D.A. Russell, *Langmuir*, 1997, **13**, 460.
87. Z. Li, M. Lieberman, W. Hill, *Langmuir*, 2001, **17**, 4887.
88. Z. Li, M. Lieberman, *Supramol. Science*, 1998, **5**, 485.
89. C. Li, *Microchim Acta.* 2007, **157**, 21.
90. Y. Zhang, T. F. Kang, Y.-W. Wan, S.-Y. Chen. *Microchim Acta*, 2009, **165**, 307.
91. A. E. Kaifer, M. G-Kaifer, *Supramolecular electrochemistry*, WILEY-VCH, New York, 1999, pg 14.
92. D. Wohrle, G. Schnurpfeil, G. Knothe, *Dyes and Pigments.* 1992, **18**, 91.
93. A. Lützen, S. D. Starnes, D. M. Rudkevich, J. Rebeck Jr, *Tet. Lett.* 2000, **41**, 3777.
94. J. Wang, T. Golden, K. Varughese, I. El-Rayes, *Anal. Chem.*, 1989, **61**, 509.
95. M. B. Gilbert, D. J. Curran, *Anal. Chem.* 1986, **58**, 1028.
96. J. Oni, P. Westbroek, T. Nyokong, *Electrochem. Commun.* 2001, **3**, 524.
97. A. H. Schroeder, F. B. Kaufman, *J. Electroanal. Chem.* 1980, **133**, 209.
98. M. F. Dautartas, J. F. Evans, T. Kuwana, *Anal. Chem.* 1978, **51**, 104.
99. J.B. Kerr, L.L. Miller, M.R. Van De Mark, *J. Am. Chem. Soc.* 1980, **102**, 3383.
100. C. A. Caro, F. Bedioui, J. H. Zagal, *Electrochim. Acta* 2002, **47**, 1489.
101. S. Griveau, F. Bedioui, *Electroanalysis.* 2001, **13**, 253.

## References

---

102. D. Losic, J. G. Shapter, J. J. Gooding, *Langmuir* 2001, **17**, 3307.
103. H. O. Finklea, D. D. Hanshew, *J. Am. Chem. Soc.* 1992, **114**, 3173.
104. C. W. Dirk, T. Inabe, K. F. Schoch, T. J. Marks. *J. Am. Chem. Soc.* 1983, **105**, 1539.
105. W. J. Kroenke, M. E. Kenney, *Inorg. Chem.* 1964, **3**, 251.
106. W. Freyer, S. Mueller, K. Teuchner, *J. Photochem. Photobiol. A: Chem.* 2004, **163**, 231.
107. A. E. Kaifer, M. G-Kaifer, *Supramolecular electrochemistry*, WILEY-VCH, New York, 1999, pg 42.
108. P. Westbroek, G. Priniotakis, P. Kiekens, *Analytical electrochemistry in textiles*, Woodhead publishing Limited and CRC Press LLC, Cambridge 100 England, 2005.
109. E. Barsoukov, J. R. Macdonald, *Impedance spectroscopy*, second edition, John Wiley & Sons, New Jersey, 2005.
110. B.-Y. Chang, S.-M. Park, *Anal. Chem.* 2006, **78**, 1052
111. P. Millet, *J. Phys. Chem. B* 2005, **109**, 24025.
112. S. G. Wang, C. B. Shen, K. Long, T. Zhang, F. H. Wang, Z. D. Zang, *J. Phys. Chem. B* 2006, **110**, 377.
113. J. D. Jacobs, H. Koerner, H. Heinz, B. L. Farmer, P. Mirau, P. H. Garrett, R. A. Vaia, *J. Phys. Chem.* 2006, **110**, 20143.
114. A. Y. Ku, J. A. Ruud, T. A. Early, R. R. Corderman, *Langmuir* 2006, **22**, 8277.
115. J. H. Zagal, *Coord. Chem. Rev.* 1992, **119**, 89.
116. F. Beck, *J. Appl. Electrochem.* 1977, **7**, 191.
117. R. Jalinsky, *J. Electrochem. Soc.* 1965, **112**, 526.
118. N. Kobayashi, W. A. Nevin, *Appl. Organomet. Chem.* 1996, **10**, 579.
119. C. A. Caro, F. Bedioui, M. A. Páez, G.I. Cárdenas-Jirón, J. H. Zagal, *J. Electrochem. Soc.* 2004, **151**, E32.
120. G. I. C. Jiron. C. A. Caro, D. V.-Yazigi, J. H. Zagal, *J. Molecular Structure (Theochem)* 2002, **580**, 193.
121. M. Gulppi, F. Bedioui, J.H. Zagal, *Electroanalysis* 2001, **13**, 1136.
122. N.B. McKeown, *Chem. Ind.* 1999, 92.
123. D. R. Tackley, G. Dent, W. E. Smith, *Phys. Chem. Chem. Phys.* 2001, **2**, 1419.
124. M. S. Ureta-Zanartu, P. Bustos, C. Berrios, M. C. Diez, M. L. Mora, C. Guitierrez, *Electrochim. Acta.* 2002, **47**, 2399.

## References

---

- 125.M. S. Ureta- Zañartu, A. Alarcon, C, Berrios, G. I. Cardenas-Jiron, J. Zagal, C. Gutierrez, J. *Electroanal. Chem.* 2005, **580**, 94.
- 126.M. Gattrell, D. W. Kirk, J. *Electrochem. Soc.* 1992, **139**, 2736.
- 127.J. Manriquez, J. L. Bravo, S. Guitierrez-Granados, S. S. Succar, C. Bied-Charreton, A. A. Ordaz, F. Bedioui, *Anal. Chim. Acta.* 1999, **378**, 159.
- 128.Environmental Protection Agency (EPA, USA). *Federal Register*, 2004, **69**, 130
- 129.L.H. Keith and W.A. Tellard Priority pollutants I: a perspective view. *Environ. Sci. Technol.* 1979, **13**, 416.
- 130.D. Liu, K. Thompson, K. L. E. Kaiser, *Bull. Environ. Contam. Toxicol.* 1982, **24**, 130.
- 131.H. Saito, M. Sudo, T. Shigeoka, F. Yamauchi, *Envir. Toxic. Chem.* 1991, **10**, 235.
- 132.M. Czaplicka, *Sci. Total Environ.* 2004, **322**, 21.
- 133.M. Gattrell, D. W. Kirk, J. *Electrochem. Soc.* 1992, **139**, 2736.
- 134.M. Gattrell, B. MacDougall, J. *Electrochem. Soc.* 1999, **146**, 3335.
- 135.Z. Ezerskis, Z. Jusys, J. *Appl. Electrochem.* 2001, **31**, 1117.
- 136.Z. Ezerskis, Z. Jusys, J. *Appl. Electrochem.* 2002, **32**, 49.
- 137.M. S. Ureta-Zanartu, P. Bustos, M. C. Diez, M.L. Mora, C. Gutierrez, *Electrochim. Acta.* 2001, **46**, 2545.
- 138.A. Merz, in: *Topics in Current Chemistry, Electrochemistry IV*, vol. **152**, E. Steckhan Eds., Springer, Berlin, 1990, pg 49.
- 139.P. Guo, T.-W. Hui, K.-C. Wong , K.-K. Shiu, J. *Electroanal. Chem.* 2001, **498**, 142.
- 140.A. Goux, F. Bedioui, L. Robbiola, M. Pontie, *Electroanalysis*, 2003, **15**, 696.
- 141.G. Roslonek, J. Taraszewska, J. *Electroanal. Chem.* 1992, **325**, 285.
- 142.T.R.I. Cataldi, D. Centonze, G. Ricciardi, *Electroanalysis*. 1995, **7**, 312.
- 143.T.R. I. Cataldi, E. Desimoni, G. Ricciardi, L. Francesco, *Electroanalysis* 1995, **7**, 435.
- 144.J. Obirai, F. Bedioui, T. Nyokong, J. *Electroanal. Chem.* 2005, **576**, 323.
- 145.C. de la Fuente, M.D. Vazquez, M. L. Tascon, M. I. Gomez, S. Batanero, *Talanta.* 1997, **44**, 685.
- 146.B. Agboola, T. Nyokong, *Electrochim. Acta.* 2007, **52**, 5039.
- 147.J. Obirai, T. Nyokong, J. *Electroanal. Chem.* 2005, **576**, 323.
- 148.T. Nyokong, F. Bedioui, J. *Porphyryns Phthalocyanines* 2006, **10**,110.
- 149.A. R. Leach, *Molecular modelling principles and applications*, second edition, Pearson Education Limited, England, 2001, pg. 61-73.

## References

---

150. M. Springborg, *Density-functional methods in chemistry and material science*, John Wiley & Sons, New York, 1997, pg 2-3.
151. Parr, R. G. *Annu. Rev. Phys. Chem.* 1983, **34**, 631.
152. Parr, R. G.; Donnelly, R. A.; Levy, M.; Palke, W. E. *J. Chem. Phys.* 1978, **68**, 3801.
153. Perdew, J. P.; Parr, R. G.; Levy, M.; Balduz, J. L., Jr. *Phys. Rev. Lett.* 1982, **49**, 1691.
154. Parr, R. G.; Pearson, R. G. *J. Am. Chem. Soc.* 1983, **105**, 7512.
155. P. Geerlings, F. de Proft, W. Langenaeker, *Density-functional methods in chemistry and material science*, John Wiley & Sons, New York, 1997, pg 19-23.
156. P. Hohenberg, W. Kohn, *Phys. Rev.* 1964, **136**, B864.
157. A. D. Becke, *J. Chem. Phys.* 1993, **98**, 5648.
158. C. Lee, W. Yang, R. G. Parr, *Phys. Rev. B* 1988, **37**, 785.
159. R. G. Pearson, *Acc. Chem. Res.* 1993, **26**, 250.
160. Y. Li, J. N. S. Evans, *J. Am. Chem. Soc.* 1995, **117**, 7756.
161. R. G. Parr, Z. Zhou, *Acc. Chem. Res.* 1993, **26**, 256.
162. M. Berkowitz, *J. Am. Chem. Soc.* 1987, **109**, 4823.
163. Méndez, F.; Gázquez, J.L.; *J. Am. Chem. Soc.*; 1994, **116**, 9298.
164. Gaussian 03, Revision E.01, M. J. Frisch, G. W. Trucks, H. B. Schlegel, G. E. Scuseria, M. A. Robb, J. R. Cheeseman, J. A. Montgomery, Jr., T. Vreven, K. N. Kudin, J. C. Burant, J. M. Millam, S. S. Iyengar, J. Tomasi, V. Barone, B. Mennucci, M. Cossi, G. Scalmani, N. Rega, G. A. Petersson, H. Nakatsuji, M. Hada, M. Ehara, K. Toyota, R. Fukuda, J. Hasegawa, M. Ishida, T. Nakajima, Y. Honda, O. Kitao, H. Nakai, M. Klene, X. Li, J. E. Knox, H. P. Hratchian, J. B. Cross, V. Bakken, C. Adamo, J. Jaramillo, R. Gomperts, R. E. Stratmann, O. Yazyev, A. J. Austin, R. Cammi, C. Pomelli, J. W. Ochterski, P. Y. Ayala, K. Morokuma, G. A. Voth, P. Salvador, J. J. Dannenberg, V. G. Zakrzewski, S. Dapprich, A. D. Daniels, M. C. Strain, O. Farkas, D. K. Malick, A. D. Rabuck, K. Raghavachari, J. B. Foresman, J. V. Ortiz, Q. Cui, A. G. Baboul, S. Clifford, J. Cioslowski, B. B. Stefanov, G. Liu, A. Liashenko, P. Piskorz, I. Komaromi, R. L. Martin, D. J. Fox, T. Keith, M. A. Al-Laham, C. Y. Peng, A. Nanayakkara, M. Challacombe, P. M. W. Gill, B. Johnson, W. Chen, M. W. Wong, C. Gonzalez, J. A. Pople, Gaussian, Inc., Wallingford CT, 2004.
165. S. Iijima, *Nature* 1991, **354**, 56.
166. S. Iijima, T. Ichihashi, *Nature* 1993, **363**, 603.

## References

---

- 167.D. S. Bethune, C. H. Klang, M. S. de Vries, G. Gorman, R. Savoy, J. Vazquez, *Nature*, 1993, **363**, 605.
- 168.A. Oberlin, M. Endo, T. Koyama, *J. Cryst. Growth*, 1976, **32**, 335.
- 169.M. M. Treachy, T. W. Ebbesen, J. M. Gibson, *Nature*. 1996, **381**, 678.
- 170.W.A. de Heer, A. Chatelaine, D. Ugarte, *Science* 1995, **270**, 1179.
- 171.J. M. Bonard, *Solid State Electron* 2001, **45**, 893.
- 172.S. J. Tans, A. R. M. Verschueren, C. Dekker *Nature* 1998, **393**, 49.
- 173.R. Martel, T. Schmidt, H. R. Shea, T. Hertel, P. Avouris, *Appl Phys Lett* 1998, **73**, 2447.
- 174.H. Dai, J. H. Hafner, A. G. Rinzler, D. T. Colbert, R. E. Smalley, *Nature* 1996, **384**, 147.
- 175.M. S. Shaffer, X. Fan, A.-H. Windle, *Carbon* 1998, **36**, 1603.
- 176.A. Merkoci, *Microchim. Acta* 2006, **152**, 157.
- 177.G.L. Hornyak, J. Dutta, H.F. Tibbals, A. K. Rao, in *Introduction to Nanoscience*, CRC Press, Taylor and Francis Group, Boca Raton, (2008).
- 178.B. Rogers, S. Pennathur, J. Adams, in *Nanotechnology: Understanding small systems*, CRC Press, Taylor and Francis Group, Boca Raton, (2008).
- 179.S. A. Mamuru, K. I. Ozoemena, T. Fukuda, N. Kobayashi, T. Nyokong, *Electrochim. Acta*. 2010, **55**, 6367.
- 180.A. Kongkanand, P. V. Kamat. *ACS Nano*. **1**, 2007, 13-21.
- 181.L. Chen, C. L. Cheung, P. D. Ashby, C. N. Lieber, *Nano Lett*. **4**, 2004, 1725.
- 182.Y. Chen, Y. Lin, Y. Liu, J. Doyle, N. He, X. D. Zhuang, J.R. Bai, W.J. Blau, J. *Nanosci. Nanotech*. 2007, **7**, 1268.
- 183.J.P. Lukaszewic, *Sensors Lett*. 2006, **4**, 53.
- 184.P. R. Bandaru, J. *Nanosci. Nanotech*. 2007, **7**, 1239.
- 185.M. Inagaki, K. Kaneko, T. Nishizawa, *Carbon*. 2004, **42**, 1401.
- 186.J. H. Zagal, S. Griveau, K. Ozoemena, T. Nyokong, F. Bedioui, J. *Nanosci. Nanotech*. **9**, 2009, 2201.
- 187.K.I. Ozoemena, T. Nyokong, D. Nkosi, I. Chambrier, M. J. Cook, *Electrochim Acta*. 2007, **52**, 4132.
- 188.M. S. Siswana, K. I. Ozoemena, T. Nyokong, *Electrochim. Acta*. 2006, **52**, 114.
- 189.W. Chidawanyika, C. Litwinski, E. Antunes T. Nyokong, J. *Photochem. Photobiol. A: Chem*. 2010, **212**, 027.

## References

---

190. D. A. Geraldo, C. A. Togo, J. Limson, T. Nyokong, *Electrochim. Acta.* 2008, **53**, 8051.
191. H. Hu, B. Zhao, M. E. Itkis, R. C. Haddon, *J. Phys. Chem. B* 2003, **107**, 13838.
192. H. Murakami, G. Nakamura, T. Nomura, T. Miyamoto, N. Nakashima, *J. Porph. Phthal.* 2007, **11**, 418
193. J. Liu, A.G. Rinzler, H. Dai, J.H. Hafner, R. K. Bradley, P. J. Boul, A. Lu, T. Iverson, K. Shelimov, C. B. Huffman, F. Rodriguez-Macias, T. Y-Seon Shon, R. Lee, D.T. Colbert, R.E. Smalley, *Science.* 1998, **280**, 1253.
194. B. Ballesteros, S. Campidelli, G. de la Torre, C. Ehli, D. M. Guldi, M. Prato, T. Torres, *Chem. Commun.* 2007, 2950.
195. G. de la Torre, W. Blau, T. Torres, *Nanotechnology.* 2003, **14**, 765.
196. Z.-L. Yang, H.-Z. Chen, L. Cao, H.-Y. Li, M. Wang, *Mater. Sci. Eng. B* 2004, **106**, 73.
197. H.-B. Xu, H.-Z. Chen, M.-M. Shi, R. Bai, M. Wang, *Mater. Chem. Phys.* 2005, **94**, 342.
198. J. L. Bahr, J. Y. Dmitry, V. Kosynkin, M. J. Bronikowski, R. E. Smalley, J. M. Tour, *J. Am. Chem. Soc.* 2001, **123**, 6536.
199. D. J. Nelson, H. Rhoads, C. Brammer, *J. Phys. Chem. C* 2007, **111**, 17872.
200. S. M. Bachilo, M. S. Strano, C. Kittrell, R.H. Hauge, R. E. Smalley, R. B. Weisman, *Science* 2002, **298**, 2361.
201. M. S. Dresselhaus, G. Dresselhaus, A. Jorio, *J. Phys. Chem. C* 2007, **111**, 17887.
202. F. Hennrich, R. Kupke, S. Lebedkin, K. Arnold, R. Fisher, D. Resasco, M. Kappes, *J. Phys. Chem. B* 2005, **109**, 10567.
203. B. Ballesteros, G. de la Torre, C. Ehli, G.M. Aminur Rahman, F. Agullo-Rueda, D.M. Guldi, T. Torres, *J. Am. Chem. Soc.* 2007, **129**, 5061.
204. C. A. Dyke, J. M. Tour, *J. Am. Chem. Soc.* 2003, **125**, 1156.
205. J. L. Bahr, J. M. Tour, *J. Mater. Chem.* 2002, **12**, 1952.
206. E. P. Dillon, C. A. Crouse, A. R. Barron, *ACS Nano* 2008, **2**, 156.
207. J. Kastner, T. Pichler, H. Kuzmany, S. Curran, W. Blau, D.N. Weldon, M. Delamesiere, S. Draper, H. Zandbergen, *Chem. Phys. Lett.* 1994, **221**, 53.
208. W. C. W. Chan, D. J. Maxwell, X. H. Gao, R. E. Bailey, M. Y. Han, S. M. Nie, *Curr. Opin. Biotechnol.* 2002, **13**, 40.

## References

---

209. E. Jubete, K. Zelechowska, O. A. Loaiza, P. J. Lamas, E. Ochoteco, K. D. Farmer, K. P. Roberts, J. F. Biernat, *Electrochim. Acta* 2011, **56**, 3988.
210. A. P. Gutierrez, S. Griveau, C. Richard, A. Pailleret, S. G. Granados, F. Bedioui, *Electroanalysis* 2009, **21**, 2303.
211. J. F. Silva, S. Griveau, C. Richard, J. H. Zagal, F. Bedioui, *Electrochem. Commun.* 2007, **9**, 1629.
212. T. Mugadza, T. Nyokong, *Electrochim. Acta* 2010, **55**, 6049.
213. T. Mugadza, T. Nyokong, *Electrochim. Acta* 2010, **55**, 2606.
214. T. Mugadza, T. Nyokong, *Electrochim. Acta* 2011, **56**, 1995
215. T. Mugadza, T. Nyokong, *Synthetic Metals* 2010, **160**, 2089.
216. K. I. Ozoemena, T. Nyokong, D. Nkosi, I. Chambrier, M. J. Cook, *Electrochim. Acta* 2007, **52**, 4132.
217. B. O. Agboola, K. I. Ozoemena, T. Nyokong, T. Fukuda, N. Kobayashi, *CARBON*, 2010, **48**, 763.
218. B. Agboola, P. Westbroek, K. I. Ozoemena, T. Nyokong, *Electrochem. Commun.* 2007, **9**, 310-316.
219. W. C. W. Chan, D. J. Maxwell, X.H. Gao, R.E. Bailey, M.Y. Han, S.M. Nie, *Curr. Opin. Biotechnol.* 2002, **13**, 40.
220. T. Jamieson, R. Bakhshi, D. Petrova, R. Pocock, M. Imani, A.M. Seifalian, *Biomaterials* 2007, **28**, 4717.
221. T. J. Bukowski, *Critical Reviews in Solid State and Materials Sciences* 2002, **27**, 119.
222. S. V. Gaponenko, *Optical Properties of Semiconductor Nanocrystals*; Cambridge University Press: Cambridge, U.K., 1998.
223. A. P. Alivisatos, *J. Phys. Chem.* 1996, **100**, 13226.
224. S. Ogawa, K. Hu, F.-R. F. Fan, A. J. Bard, *J. Phys. Chem. B* 1997, **101**, 5707.
225. S. K. Poznyak, N. P. Osipovich, A. Shavel, D. V. Talapin, M. Gao, A. Eychmiiller, N. Gaponik, *J. Phys. Chem. B.* 2005, **109**, 1094.
226. Y. Bae, N. Myung, A. J. Bard. *Nano Lett.* 2004, **4**, 1153.
227. S. Chen, L. A. Truax, J. M. Sommers, *Chem. Mater.* 2000, **12**, 3864.
228. S. K. Haram, B. M. Quinn, A. J. Bard, *J. Am. Chem. Soc.* 2001, **123**, 8860.
229. E. Kucur, J. Riegler, G. A. Urban, T. Nann, *J. Chem. Phys.* 2003, **119**, 2333.
230. Z. Ding, B. M. Quinn, S. K. Haram, L. E. Pell, B. A. Korgel, A. J. Bard, *Science* 2002, **296**, 1293.

## References

---

231. U. T. D. Thuy, P. S. Toan, T. T. K. Chi, D. D. Khang, N. Q. Liem, *Adv. Nat. Sci.: Nanosci. Nanotechnol.* 2010, **1**, 2043.
232. V. I. Klimov, *Alamos Science*. 2003, **28**, 214.
233. M. Kuno, J.K. Lee, B.O. Dabbousi, F.V. Mikulec, M.G. Bawendi, *J. Chem. Phys.* 1997, **106**, 9869.
234. C. J. Murphy, J.L. Coffey, *Appl. Spectrosc.* 2002, **56**, 16A.
235. L. S. Li, J. Hu, W. Yang, A. P. Alivisatos, *Nanolett.* 2001, **1**, 349.
236. J. Li, G. Zou, X. Hu, X. Zhang, *J. Electroanal. Chem.* 2009, **625**, 88.
237. T. Longhau, C. Haixin, Li. Jinghong, *Anal. Chem.* 2009, **81**, 9710.
238. Q. Liu, X. Lu, J. Li, X. Yao, J. Li, *Biosens. Bioelectr.* 2007, **22**, 3203.
239. S. K. Poznyak, N. P. Osipovich, A. Shavel, D. V. Talapin, M. Gao, A. Eychmiiller, N. Gaponik, *J. Phys. Chem. B.* 2005, **109**, 1094.
240. C. Berríos, M.S. Ureta-Zañartu, C. Gutiérrez, *Electrochim. Acta* 2007, **53**, 792.
241. T. Nyokong, in J. H. Zagal, F. Bedioui, J.-P. Dodelet (Eds.), *N4-Macrocyclic Metal Complexes*, Springer, New York, (2006).
242. J. Britton, E. Antunes, T. Nyokong, *Inorganic Chemistry Communications* 2009, **12**, 828.
243. S. D'Souza, E. Antunes, C. Litwinski, T. Nyokong, *J. Photochem. Photobiol. A: Chemistry* 2011, **220**, 11.
244. S. D'Souza, E. Antunes, T. Nyokong, *Inorganica Chimica Acta* 2001, **367**, 173.
245. A. C. S. Samia, S. Dayal, C. Burda, *Photochem. Photobiol.* 2006, **82**, 617.
246. A. C. S. Samia, X. Chen, C. Burda, *J. Am. Chem. Soc.* 2003, **125**, 15736.
247. G. Mbambisa, P. Tau, E. Atunes and T. Nyokong. *Polyhedron*, 2007, **26**, 5355.
248. M. Idowu, J. -Y. Chen, T. Nyokong, *New J. Chem.*, 2008, **32**, 290
249. C. C. Leznoff, D. M. Drew, *Can. J. Chem.* 1996, **74**, 307.
250. V. Chauke, F. Matemadombo, T. Nyokon, *J. Hazard. Mat.* 2010, **178**, 180.
251. Y. H. Tse, P. Janda, H. Lam, W.J. Pietro, A.B.P. Lever. *J. Porphyrins Phthalocyanines*. 1997, **1**, 3.
252. C. Murray, N. Dozova, J.G. McCaffrey, S. FitzGerald, N. Shafizadeh, C. Crepin, *Phys. Chem. Chem. Phys.* 2010, **12**, 10406.
253. X. Zhang, Y. Zhang, J. Jiang, *Spectrochim. Acta A.* 2004, **60**, 2195-2200.
254. T. Kobayashi, F. Kurokawa, N. Uyeda, E. Suito, *Spectrochim. Acta.* 1970, **26A**, 1305.
255. A. Hirsch, *Angew. Chem. Int. Ed.* 2009, **48**, 5403.



## References

---

- 256.S. Moeno, E. Antunes, S. Khene, C. Litwinski, T. Nyokong, Dalton Trans. 2010, **39**, 3460.
- 257.W. W. Yu, E. Cheng, R. Drezek, V. L. Colvin, Biochem. Biophys. Res. Comm. 2006, **348**, 781.
- 258.X. Wang, L. Qu, J. Zhang, X. Peng, M. Xiao, Nano Lett. 2003, **3**, 1103.
- 259.M. Sanz, M.A. Correa-Duarte, L.M. Liz-Marzan, A. Douhal, J. Photochem. Photobiol A: Chem. 2008, **196**, 51.
- 260.E. Z. Chong, D.R. Matthews, H.D. Summers, K.L. Njoh, R.J. Errington, P.J. Smith, J. Biomed. Biotechnol. 2007, **1**, 54169.
- 261.A. Javier, D. Magana, T. Jennings, G.F. Strouse, Appl. Phys. Lett. 2003, **83**, 1423.
- 262.J. Zhang, X. Wang, M. Xiao, Opt. Lett. 2002, **27**, 1253.
- 263.M. Lunz, A. Louise Bradley, J. Phys. Chem. C 2009, **113**, 3084.
- 264.S. Moeno, M. Idowu, T. Nyokong, Inorg. Chim. Acta. 2008, **361**, 2950.
- 265.T. Kobayashi, Spectrochim. Acta, 1970, **26A**, 1313.
- 266.A. G. Rolo, M.I. Vasilevskiy, N. P. Gaponik, A. L. Rogach, M. J. M. Gomes, Phys. Stat. Sol 2002, **229**, 433.
- 267.M. S. Ureta-Zañartu, C. Berríos, J. Pavez, J. Zagal, C. Gutiérrez, J.F. Marco, J. Electroanal. Chem. 2003, **553**, 147.
- 268.C. Berríos, M.S. Ureta-Zañartu, C. Gutiérrez, Electrochim. Acta 2007, **53**, 792.
- 269.J. J. Gooding, V.G. Praig, E.A.H. Hall, Anal. Chem. 1998, **70**, 2396.
- 270.H. O. Finklea, in Electroanalytical Chemistry, A. J. Bard, I. Rubinstein (Eds.), Marcel Dekker, New York, Volume **19**, 1996, pg 109 – 335.
- 271.A. J. Bard and L. R. Faulkner, Electrochemical Methods, John Wiley and Sons, New York, 2001
- 272.K. Ozoemena, T. Nyokong, Electrochim. Acta. 2002, **47**, 4035.
- 273.S. Griveau, J. Pavez, J. H. Zagal, F. Bedioui. J. Electroanal. Chem. 2001, **497**, 75.
- 274.J. Lu, S. Nagase, X. Zhang, D. Wang, M. Ni, Y. Maeda, T. Wakahara, T. Nakahondo, T. Tsuchiya, T. Akasaka, Z. Gao, D. Yu, H. Ye. W. M. Mei, Y. Zhou, J. Am. Chem. Soc. 2006, **128**, 5114.
- 275.D. Du, W. Chen, J. Cai, J. Zhang, F. Qu, H. Li, J. Electroanal. Chem. 2008, **623**, 81.
- 276.P. Wu, Y. Li, X.-P. Yan, Anal. Chem. 2009, **81**, 6252.
- 277.M. B. Dergacheva, V.N. Statsyuk, L.A. Fogel, J Electroanal. Chem. 2005, **579**, 43.

## References

---

- 278.P. T. Kissinger, C.R. Preddy, R.E. Shoup, W.R. Heineman, in Laboratory techniques in Electroanalytical Chemistry, O.T. Kissinger, W.R. Heineman (Eds.). 2<sup>nd</sup> Ed. (1996) Marcel Dekker, New York.
- 279.G. Riveros, H. Gómez, R. Henríquez, R. Schrebler, R.Córdova, R. E. Marotti, E.A. Dalchiele, Bol. Soc. Chil. Quím. 2002, **47**, 411.
- 280.P. Agarwal, M.E. Orazem, L.H. Garcia-Rubio, J Electrochem. Soc. 1992, **139**, 1917.
- 281.E. Sabatani, I. Rubinstein, J. Phys. Chem. 1987, **91**, 6663.
- 282.V. Lakshminarayanan and Sur U.K. Pramana J. Phys. 2003, **61**, 361.
- 283.S. Majdi, A. Jabbari, H. Heli, A.A. Moosavi-Movahedi, Electrochim. Acta. 2007, **52**, 4622.
- 284.C. Berrios, J. F. Marco, C. Gutierrez, M. S. Ureta-Zañartu, Electrochim. Acta, Electrochim. Acta. 2009, **54**, 6425.
- 285.B. E. Douglas, D. H. McDaniels, J. J. Alexander, Concepts and models of inorganic chemistry, John Wiley and Sons, Inc, New York, 1994, 193-195.